technische universität
dortmund

Excitation Spectrum and Quantum Phase Transitions in the One-Dimensional Ionic Hubbard Model

Continuous Unitary Transformations Approach

Ph.D. Thesis

Lehrstuhl für Theoretische Physik I
Fakultät Physik
Technische Universität Dortmund

Mohsen Hafez Torbati

Supervised by: Prof. Dr. G.S. Uhrig

July 2014

Abstract

Strongly correlated electron systems are one of the most fascinating problems in current physics. The strong electron-electron interaction in these materials leads to the emergence of nontrivial elementary excitations (quasiparticles, QPs) above the ground state ranging from fractional spins in quasi-one-dimensional materials to magnetic monopole in the pyrochlore lattice. The condensation of these quasiparticles upon changing some external parameters may stabilize new exotic states of matter. Experimental measurements such as inelastic neutron scattering provide us with valuable information about the excitation spectrum of such systems which require microscopic models to be described. This thesis is devoted to a detailed analysis of the excitation spectrum and of the quantum phase transitions in the one-dimensional (1D) ionic Hubbard model (IHM). The IHM consists of a nearest-neighbor (n.n.) hopping, onsite Hubbard interaction, and an ionic (staggered) potential separating the odd and even sites energetically.

The model exhibits two continuous phase transitions on increasing the Hubbard interaction identified by a low-energy effective field theory and confirmed by a rigorous density matrix renormalization group (DMRG) analysis after several attempts. The first transition occurs from band insulator (BI) phase to the 2-fold degenerate spontaneously dimerized insulator (SDI) phase. The transition is in the Ising universality class as is plausible from symmetry considerations. The SDI phase becomes unstable towards a quasi-long-range order Mott insulator (MI) phase at a second transition point resembling the Kosterlitz-Thouless (KT) transition in the frustrated Heisenberg chain.

We employ continuous unitary transformations (CUT) to systematically map the IHM to effective Hamiltonians (almost) conserving the number of QPs in the system. Using an analysis in the BI regime where electrons and holes define QPs, the low-energy excitation spectrum of the model is quantitatively determined in the BI phase almost up to the first transition point. The transition from the BI to the SDI phase is signaled by the vanishing of an $S = 0$ exciton mode at the total momentum $K = \pi$. The condensation of these excitons beyond the first transition point is described by a BCS-type-theory showing the stabilization of the SDI phase. The mean-field solution indicates no second phase transition to the quasi-long-range order MI phase. This is interpreted as the effect of strong quantum fluctuations in one dimension.

We consider the IHM in the dimer limit where the uniform chain is separated into independent dimers. The different phases of the IHM are studied by increasing the interdimer hopping and reaching the uniform limit. This dimer limit satisfactorily produces the excitation spectrum of the BI phase confirming the vanishing of an $S = 0$ exciton mode at the first transition point. It is found that the SDI-to-MI transition takes place by softening of a magnetic $S = 1$ excitation, *i.e.*, a triplon. We report rigorous results for the gapless triplon dispersion in the MI phase and discuss the binding effects in the 2-triplon sector.

Contents

Abstract 3

Acknowledgment 9

1 Introduction 11
- 1.1 Two Insulators . . . 11
- 1.2 The Hubbard Model . . . 12
- 1.3 Spinon Versus Triplon . . . 13
- 1.4 Outlines . . . 15

2 The Ionic Hubbard Model 17
- 2.1 Experimental Observations . . . 17
  - 2.1.1 Neutral-Ionic Transition . . . 17
  - 2.1.2 Ferroelectricity in TTF-CA . . . 18
- 2.2 Hamiltonian and Solvable Limits . . . 19
  - 2.2.1 The Model Hamiltonian . . . 19
  - 2.2.2 Gaps and Order Parameters . . . 19
  - 2.2.3 Special Limits . . . 21
- 2.3 Some Previous Results . . . 24
  - 2.3.1 Phase Diagram . . . 24
  - 2.3.2 Excitation Spectrum . . . 31
- 2.4 Chapter Summary . . . 32

3 Method 35
- 3.1 The CUT method . . . 35
  - 3.1.1 The Basic Concept . . . 35
  - 3.1.2 Wegner's Generator . . . 36
  - 3.1.3 Particle-Conserving Generator . . . 37
  - 3.1.4 Reduced Generator . . . 38
- 3.2 The deepCUT method . . . 39
  - 3.2.1 Flow Equations . . . 39
  - 3.2.2 Truncation Scheme . . . 41
  - 3.2.3 Simplification Rules . . . 43
  - 3.2.4 Residual Off-Diagonality . . . 43

3.3 Few-Particle Problems . . . 44
3.3.1 Basis States . . . 44
3.3.2 Hamiltonian Matrix . . . 45
3.4 Chapter Summary . . . 47

4 Band Insulator Limit **49**
4.1 A Pure deepCUT Analysis . . . 50
4.1.1 Preliminary Considerations . . . 50
4.1.2 Low-Energy Effective Hamiltonian . . . 52
4.1.3 The 1-Quasiparticle Sector . . . 55
4.1.4 The 2-Quasiparticle Sector . . . 58
4.2 Thermodynamic Exact Diagonalization . . . 62
4.2.1 Construction of the Hamiltonian Matrix . . . 62
4.2.2 Low-lying Excitation Spectrum . . . 63
4.3 Beyond the Transition Point: A Mean Field Study . . . 66
4.4 Chapter Summary . . . 71

5 Dimer Limit Analysis **73**
5.1 Preliminary Considerations . . . 74
5.1.1 Restricted IHM . . . 74
5.1.2 Dimer limit . . . 75
5.1.3 Technical Points . . . 78
5.2 Ground Energy and Energy Gaps . . . 78
5.2.1 Ground State Energy . . . 78
5.2.2 Gaps to Excited States . . . 80
5.3 Excitation Spectrum . . . 85
5.3.1 Band Insulator Phase . . . 85
5.3.2 Spontaneously Dimerized Phase . . . 87
5.3.3 Mott Insulator Phase . . . 89
5.4 Chapter Summary . . . 95

Summary and Outlook **97**

A Analysis of Effective Hamiltonians **101**
A.1 $H_{1:1}$ . . . 101
A.2 $H_{2:2}$ . . . 103
A.3 $H_{3:3}$ . . . 107
A.4 $H_{4:4}$ . . . 108
A.5 $H_{2:1}$ . . . 109
A.6 $H_{3:1}$ . . . 111
A.7 $H_{4:1}$ . . . 112
A.8 $H_{3:2}$ . . . 112
A.9 $H_{4:2}$ . . . 114
A.10 $H_{4:3}$ . . . 114

B Simplification Rules **115**
B.1 Simplification Rules for BI Limit . . . 115
B.1.1 The *A-Posteriori* Simplification Rules . . . 116

B.1.2 The *A-Priori* Simplification Rules 117
B.2 Simplification Rules for Dimer Limit 119
B.2.1 The Basic Simplification Rule 120
B.2.2 The Extended Simplification Rule 122

C Spin States **125**
C.1 Fermions 125
C.2 Triplons 125

Bibliography **129**

Acknowledgment

This thesis could not have been accomplished without help, collaboration, and encouragements of a number of people whose contributions I gratefully acknowledge.

First of all, I would like to thank my supervisor Prof. Dr. Götz S. Uhrig who always led me to the right direction by his creative and systematic way of thinking. He carefully listened to the subsequent questions which I asked in any discussion and answered all of them patiently. He encouraged me to apply also my own ideas giving me self-confidence for my future research. He provides his students a friendly environment making them always happy and satisfied. I am deeply grateful for all he has taught me and helping me to grow as a research scientist – God bless you Götz.

I wish to thank the scientific committee Prof. Dr. Metin Tolan, Dr. Kai P. Schmidt, and Dr. Alex Greilich for their useful comments and feedback, which helped me to improve this manuscript. It was a great opportunity to communicate with Dr. Kai P. Schmidt during my Ph.D period in the Chair of Theoretical Physics I, Technical University of Dortmund.

I would like to thank my colleagues in the Chair of Theoretical Physics I, Technical University of Dortmund who I spent a pleasant time with. Their friendly behavior made me feel right at home although I had no knowledge of German language. My deepest gratitude goes to Nils A. Drescher who was a point of hope whenever I was in difficulties. I appreciate Holger Krull for his useful comments and suggestions to my thesis. I find myself lucky to have friends like them in my life – Thank you all.

I wish to thank my parents who this thesis is a result of their encouragements and supports. I know that you have been praying for me all the time. I hope this tiny work makes you proud of me.

This thesis is dedicated to the dearly loved Elham, who has been waiting patiently for three long years, who has been a pillar of strength in the most difficult times.

Chapter 1

Introduction

1.1 Two Insulators

In independent-electron approximations such as Hartree-Fock theory the electron-electron interactions and the electron-ion interactions are regarded as an effective static potential. In crystalline materials, such an independent-particle description leads to energy bands that each *single* electron is allowed to occupy.[1] Consequently, the ground state of the system is obtained by putting all the electrons in the lowest band eigenstates with up and down spins each. The energy level between the highest filled band and the lowest empty band defines the Fermi energy. If the Fermi energy lies between two bands where the density of states is zero, there is a gap to the excited states and the substance is recognized as insulator. This kind of insulator predicted by the band theory is known as "band insulator" (BI). If the Fermi energy lies inside an energy band, there is no gap in the system and the substance is a metal [AM76, GP00].

The band theory was formulated in the late 1920s and in the years following its formulation it successfully classified a large class of solids into insulators and metals. In 1937, however, it was found by Boer and Verwey that many transition metal oxides with a partially filled band are insulators contrary to band theory prediction [Mot90]. A famous example is CoO. This compound has an odd number of electrons per unit cell and the band theory immediately identifies it to be a metal. Contrarily, CoO is in fact a strong insulator. We want to point out that due to spontaneously symmetry breaking and enlarging the size of the unit cell, the band theory has some way to escape from this contradiction. But it remains highly questionable how satisfactorily the band theory can describe insulators such as CoO [Faz99]. The compound La_2CuO_4 is another example which contains an odd number of electrons per unit cell but shows an insulating behavior at low temperatures. La_2CuO_4 is an important material in the context of high temperature superconductivity.

[1] We like to emphasize the difference between the energy bands that each single electron in the independent-electron approximations is allowed to occupy and the energy excitation spectrum of a solid as a whole.

The importance of electron-electron interaction in the insulating behavior of transition metal oxides was first proposed by Mott. He argued that strong interaction between the two electrons occupying the same atomic orbital might be the major reason which makes the electrons localized in these compounds. Such an insulating state which stems from strong electron-electron correlations is called "Mott insulator" (MI). Magnetically, Mott insulators can be divided into two broad classes: with or without magnetic order. Mott insulators with magnetic order are usually antiferromagnet [Mot90, IFT98]. Since the discovery of high-temperature superconductivity, much more attention has been paid to the understanding of Mott insulators and to the effect of strong electron-electron correlations in these materials. This originates from the fact that the high-temperature superconductors are mainly Mott insulators doped with electrons and holes [LNW06].

1.2 The Hubbard Model

The Hubbard model is one of the simplest model which describes the effect of electron-electron interactions in quantum many-particle systems. The model was proposed in 1963 simultaneously by Gutzwiller [Gut63], Hubbard [Hub63], and Kanamori [Kan63] to explain the origin of ferromagnetism in transition metal oxides. The Hubbard model is given by

$$H = -t \sum_{<i,j>,\sigma} \left(c^{\dagger}_{i,\sigma} c_{j,\sigma} + \text{h.c.} \right) + U \sum_{i} n_{i,\uparrow} n_{i,\downarrow} \tag{1.1}$$

where $c^{\dagger}_{i,\sigma}$ and $c_{i,\sigma}$ create and annihilate an electron at site i with spin σ, respectively. The operator $n_{i,\sigma} = c^{\dagger}_{i,\sigma} c_{i,\sigma}$ counts the number of electrons at site i with spin σ. The notation $<i, j>$ on the first summation means that sites i and j are always nearest neighbors. The kinetic and the interaction terms in the Hamiltonian (1.1) have opposite tendencies. The first term describes the hopping process of electrons which is in favor of a metallic behavior. The second term contributes when two electrons with opposite spins occupy the same site. This interaction term makes the electrons localized leading to an insulating behavior.

The Hubbard model (1.1) in one dimension at zero temperature is exactly solvable by Bethe Ansatz [LW68, EFG+05]. At half-filling, the model shows no phase transition in the whole parameter region. The ground state of the system is a Mott insulator (MI) without any order parameter known as "spin liquid". Regarding the gaps, there is no spin gap while there is a finite charge gap which is called "Mott gap". For small values of the Hubbard interaction U, the charge gap is proportional to $\sqrt{tU}e^{-\frac{2\pi t}{U}}$. This indicates that in one dimension the metallic phase for $U = 0$ is unstable versus the Hubbard interaction. An infinitesimal value for the interaction U makes the system gapped. In the large-U limit, the charge gap is proportional to the Hubbard interaction U. This is natural because adding an electron to the half-filled ground state leads to the creation of double occupancy. Such a double occupancy costs an energy proportional to U which is the dominant term in the system. The charge excitation spectrum of the MI phase can be interpreted in terms of the quasiparticles "holon" and "doublon". The quasiparticle relevant for the low-energy spin spectrum is called "spinon" which carries total spin half. The spinon dispersion is gapless with a linear momentum dependence near the edge of the Brillouin Zone (BZ).

The Hubbard model away from half-filling and at higher dimensions has no exact solution and it is a difficult problem to be treated. However, it can be simplified to other effective Hamiltonians in some special limits. The interesting physics of the Hubbard model happens at large values of the Hubbard interaction U. In this case, all the states with a finite number of double occupancies are very high in energy and the states with no double occupancy determine the low energy physics of the system. The off-diagonal elements connecting these two parts of the Hilbert space are also small and proportional to the hopping parameter t. By a unitary transformation, it is possible to eliminate the off-diagonal terms up to second order in t [Hir85]. The resulting low-energy effective Hamiltonian ignoring all the three and higher particle interactions is given by

$$H_{t-J} = -t \sum_{<i,j>} \sum_{\sigma} \left(c^{\dagger}_{i,\sigma} c_{j,\sigma} + \text{h.c.} \right) + J \sum_{<i,j>} \left(\boldsymbol{S}_i \cdot \boldsymbol{S}_j - \frac{n_i n_j}{4} \right), \tag{1.2}$$

where $J = \frac{4t^2}{U}$, $n_i = \sum_{\sigma} n_{i,\sigma}$, and $\boldsymbol{S}_i$ is the spin operator at site i. We stress that the Hamiltonian (1.2) is a low-energy Hamiltonian defined in the sector with no double occupancy. To release this constraint, the fermion operators have to be replaced by hardcore operators. The Hamiltonian (1.2) is known as $t-J$ model with a long historical background [HL67, CSO77, Hir85]. The attractive electron-electron interaction which has appeared in the second term is quite remarkable [Hir85]. It displays the tendency of holes for being on the nearest-neighbor (n.n.) sites and forming bound states, *i.e.*, Cooper pairs. The $t-J$ model plays an important role in the context of high-temperature superconductivity. The model is considered not only as an effective Hamiltonian derived from the Hubbard model but also as an original Hamiltonian with independent parameters t and J. The $t-J$ model (1.2) at the half-filling condition reduces to the Heisenberg model

$$H = J \sum_{<i,j>} \boldsymbol{S}_i \cdot \boldsymbol{S}_j \tag{1.3}$$

with the antiferromagnetic prefactor $J = \frac{4t^2}{U}$. Therefore, we have found an initial fermion Hamiltonian which reduces to the (antiferromagnetic) Heisenberg model for large U.

1.3 Spinon Versus Triplon

The concept of elementary excitations or quasiparticles (QPs) is commonly used in low temperature condensed matter physics to calculate the excitation spectrum of a given system. The type of QP, of course, changes from one phase to another. However, there might be different possible QPs to describe a specific phase. Which QP is more suitable for understanding the properties of a specific phase remains an important issue. In a MI phase, elementary excitations are fundamentally different from a band insulator where electrons and holes are the appropriate QPs. The excitation spectrum of the one-dimensional Heisenberg model is usually discussed in terms of the spin-1/2 quasiparticle spinon [dCP62, FT81]. In addition to the spinon, the magnetic excitations in a MI phase are addressed in terms of spin-1 QPs called “triplon” or “magnon”. The magnons are well-defined spin excitations when

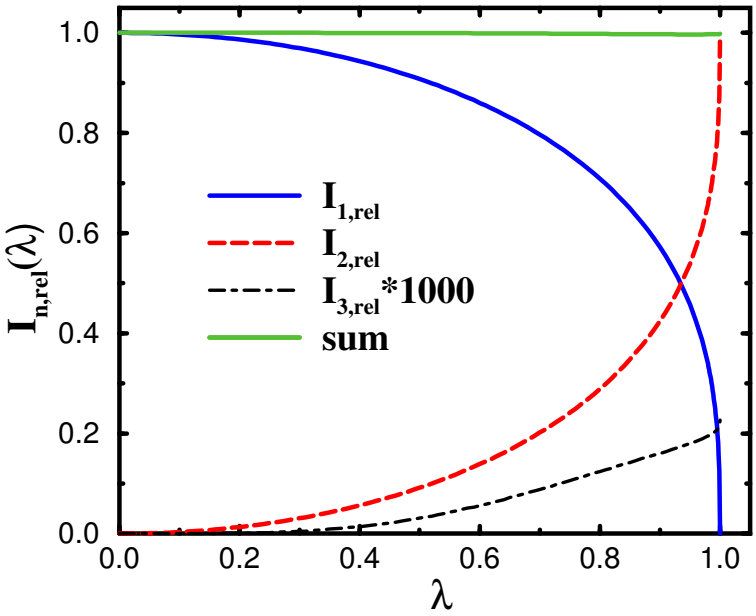

Figure 1.1: Relative spectral weights $I_{n,\mathrm{rel}}$ of the one-dimensional dimerized Heisenberg model plotted versus the interdimer interaction λ. $I_{1,\mathrm{rel}}$, $I_{2,\mathrm{rel}}$, and $I_{3,\mathrm{rel}}$ correspond to the contribution of 1-, 2-, and 3-triplon sectors, respectively. The figure is taken from Ref. [SU03].

the ground state is a magnetized MI as in the Neel-ordered phase in the two-dimensional Heisenberg model. The triplon language, on the other hand, is widely used to analyze dimerized MI phases where the ground state is composed of singlet pairs of spins in strong and weak orders [KU00, SKU04] or to describe ladder structures [SU05, USG04]. Since spinon is a spin-1/2 particle, triplon and magnon can be seen as a bound state between two spinons [KSGU01].

The properties of the 1D dimerized Heisenberg model for large enough dimerization can be well understood in terms of triplons [SKU04]. In the limit of zero dimerization, however, it is an interesting question to see whether the triplon picture can be still valid or not. If it is, we are provided with an alternative beside the spinons to investigate the spin liquid MI phase in 1D. The fact that which language is more suitable to study a specific phase depends on the distribution of total spectral weight into different QP sectors [SU03]. In an appropriate description, the major part of the spectral weight lies in the first few QP sectors. The picture is inappropriate if sectors with a large number of QPs have to be taken into account which is hard to realize. The analysis of the 1D dimerized Heisenberg model indicates that even in the limit of vanishing dimerization, 0.99% of the total spectral wight lies in the 2-triplon sector. Fig. 1.1 taken from Ref. [SU03] displays the relative spectral weights versus the interdimer interaction λ, see Ref. [SU03] for details. The results are obtained using the perturbative continuous unitary transformation method starting from the dimer limit. The contribution of the 2-triplon sector to the spectral weight is even larger than the contribution of 2-spinon sector which is 72.89% [KMB+97]. This brings us to the conclusion that the triplon language can also be used indeed to understand the 1D

spin liquid MI phase.

1.4 Outlines

In this thesis, we explore the one-dimensional (1D) ionic Hubbard model (IHM) using the continuous unitary transformation (CUT) technique. The phase diagram of the model and the position of the transition points are known at present although there has been some controversial results reported in the past. We discuss not only the phase transitions of the model but also its low-lying excitation spectrum in different phases.

The IHM is introduced in the next chapter. The chapter starts with the experimental motivation behind the IHM. Then, the Hamiltonian of the model is presented and some special limits are analyzed. We also review some of the previous results for the phase transitions and the excitation spectrum which are obtained by applying different methods to the IHM.

Chapter 3 is devoted to the methodological aspects. Mainly, we have used the CUT method combined with an exact diagonalization technique which is valid in the thermodynamic limit. This exact diagonalization enables us to solve few-particle problems. At first, the general concept of the CUT method is illustrated with special attention to the renormalization approach *directly evaluated enhanced perturbative CUT* (deepCUT). The subsequent solution of few-particle problems is required to analyze the effective Hamiltonians derived from the deepCUT.

The IHM is investigated in chapter 4 by the deepCUT method starting from the BI limit. The BI limit is defined by writing the initial Hamiltonian in terms of excitation operators of the BI phase. We use the deepCUT in two subsequent steps to obtain effective Hamiltonians. At first, we derive an effective Hamiltonian describing the low-energy physics of the system. In this way, we reduce the size of the local Hilbert space from four to three. The effective low-energy Hamiltonian is mapped by a second application of the deepCUT method to various effective Hamiltonians using different generators. Finally, it remains a few particle problem to solve providing us with accurate results for the low-energy spectrum of the model in the BI phase. It is found that a singlet exciton mode becomes soft at the critical value of the Hubbard interaction. Beyond this critical interaction, excitons condense and the quasiparticle picture that we started with breaks down. The low-energy physics of the system can no longer be captured by solving a few-particle problem. Instead, we evaluated the effective Hamiltonian extracted from the deepCUT by a BCS-type-theory to go beyond the transition point. Our calculations indicate the stabilization of a spontaneously dimerized insulator (SDI) phase. No second transition to the MI phase in this mean-field level could be observed.

In chapter 5, we start from the dimer limit where the system is composed of isolated dimers and consider the effect of interdimer hopping based on the renormalization scheme of the deepCUT method. The advantage of the dimer limit, compared to the BI limit, is

that it allows us to have access to different phases of the IHM when the deepCUT method is employed. We address the transition points of the model by analyzing both the ground state energy and different gaps. In addition, we discuss the low-energy excitation spectrum of the model in the BI, in the SDI, and in the MI phases. In the BI phase, it is revealed that the dimer limit can satisfactorily reproduce the deepCUT results obtained from the BI limit in chapter 4. In the MI phase, it is found that the low-energy physics of the IHM for large enough Hubbard interaction can be described by an effective Hamiltonian *purely* in terms of triplon operators. The analysis of this effective triplon Hamiltonian leads to quantitative results for the gapless triplon dispersion of the IHM in the MI phase.

We conclude this thesis by giving a summary and outlook.

Chapter 2

The Ionic Hubbard Model

The ionic Hubbard model (IHM) is introduced in this chapter. In the first section, we briefly present some experimental observations which represent the fundamental motivation behind the IHM. The model Hamiltonian is given in section 2.2. We discuss previous investigations on the ionic Hubbard model in section 2.3 and conclude this chapter with a summary.

2.1 Experimental Observations

2.1.1 Neutral-Ionic Transition

Organic charge transfer compounds are classified into two major categories. In one category, the donor and the acceptor molecules make their own stack, separately. This class of organic compounds has attracted much interest because of exhibiting a large conductivity. The other category includes the mixed-stack compounds where the donor and the acceptor molecules change alternatively along the stack. These compounds are always insulators due to the double periodicity of the lattice. The donor and the acceptor molecules in the mixed-stack compounds appear either as nominally ionic or nominally neutral [TVML81].

It was discovered by Torrance *et al.* in 1981 that some of the mixed-stack organic compounds, which are near the neutral-ionic boundary, undergo a reversible phase transition between the nominally ionic and the nominally neutral phases [TVML81]. This neutral-ionic transition occurs upon changing pressure [TVML81] or temperature [TGM$^+$81]. TTF-chloranil (TTF-CA) is a concrete example which shows such a phase transition. This compound is nominally neutral above $\approx$84K under atmospheric pressure. But below this temperature, there is a broad temperature range of about 30K where both neutral and ionic molecules coexist. By decreasing the temperature even further, it is found that all the neutral molecules are gone and the compound is nominally ionic. This neutral-ionic transition is accompanied with a color change in the sample [TGM$^+$81].

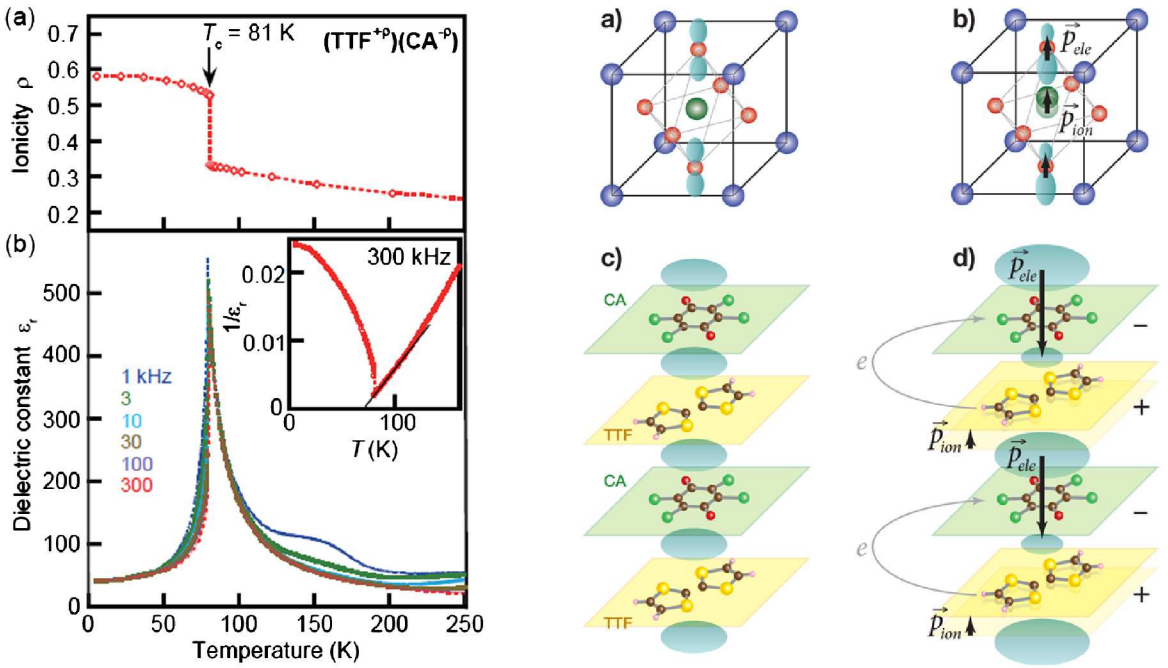

Figure 2.1: Left figure: The degree of charge transfer ρ between the donor ($TTF^{+\rho}$) and the acceptor ($CA^{-\rho}$) molecules (a) and the dielectric constant (b) versus temperature measured in TTF-CA by Kobayashi *at al.* [KHK+12]. Right figure: Comparison between ferroelectricity in $BaTiO_3$ (panles a and b) and TTF-CA (panels c and d) illustrated by Matthew Dawber [Daw12].

2.1.2 Ferroelectricity in TTF-CA

It is reported by Kobayashi *et al.* [KHK+12] that the neutral-ionic transition in TTF-CA is accompanied by

- A dimerization along the molecular stacking chain.
- An ionization of about $\pm 0.6e$ of the donor (TTF) and the acceptor (CA) molecules.

The dimerization of the compound leads to an ionic polarization pointing in the same direction as the ionic displacement. The large intermolecular charge transfer $\pm 0.6e$ induces also an electronic contribution to the ferroelectricity which is 20 times larger than the ionic polarization. This electronic ferroelectricity is antiparallel to the the ionic displacement switching the direction of the total polarization in the compound. The left figure of Fig. 2.1 taken from Ref. [KHK+12] shows the ionization degree ρ of the donor ($TTF^{+\rho}$) and the acceptor ($CA^{-\rho}$) molecules (a) and the behavior of the dielectric constant (b) versus temperature.

The above described process is very different from what happens in usual ferroelectrics where the polarization is mainly governed by a shift in the ion positions. The right figure of Fig. 2.1 sketched by Matthew Dawber [Daw12] illustrates the difference between ferroelec-

tricity in a conventional ferroelectric like $BaTiO_3$ and in a mixed-stack organic compound such as TTF-CA. Panel (a) in the right figure of Fig. 2.1 shows the perovskite structure of $BaTiO_3$ with the barium ions at the corners, oxygens at the faces, and the titanium ion at the center. Panel (b) on the right-side of Fig. 2.1 indicates how the titanium ion moves off the center of the cube by cooling the system below 120°K leading to the electronic $\boldsymbol{P}_{\text{ele}}$ and the ionic $\boldsymbol{P}_{\text{ion}}$ polarization. The ferroelectric process in TTF-CA is depicted in panels (c) and (d). The charge transfer between the donor TTF and the acceptor CA molecules induced by the neutral-ionic transition gives rise to a large electronic polarization which is directed antiparallel to the ionic displacement.

2.2 Hamiltonian and Solvable Limits

2.2.1 The Model Hamiltonian

The IHM was first proposed by Soos and his coworkers to study charge transfer in donor-acceptor crystals [SS70, SM78]. Nagaosa and Takimoto in 1986 [NT86] considered the model as a prototype to describe the neutral-ionic transition which was observed in the mixed-stack organic compounds [TVML81, TGM+81]. Egami, Ishihara, and Tachiki in 1993 also suggested that the model has the potential to illustrate the ferroelectricity in transition metal oxides such as $BaTiO_3$ [EIT93]. Giovannetti *et al.* in 2009 added the electron-lattice interaction to the IHM in order to confirm the presence of multiferroicity state in TTF-CA predicted throw *ab initio* calculations [GKS+09].

The IHM consists of a n.n. hopping term, the onsite Hubbard interaction, and an ionic (staggered) potential which stands for the energy difference between the highest occupied orbital of the donor and the lowest unoccupied orbital of the acceptor molecules. The Hamiltonian of the model in the electron-hole symmetric form is given by

$$H = \frac{\delta}{2}\sum_{i,\sigma}(-1)^i n_{i,\sigma} + t\sum_{i,\sigma}\left(c^{\dagger}_{i,\sigma}c_{i+1,\sigma} + \text{h.c.}\right) + U\sum_{i}\left(n_{i,\uparrow} - \frac{1}{2}\right)\left(n_{i,\downarrow} - \frac{1}{2}\right), \qquad (2.1)$$

where $c^{\dagger}_{i,\sigma}$ and $c_{i,\sigma}$ are the usual creation and annihilation fermion operators at site i and spin σ, respectively. The operator $n_{i,\sigma} := c^{\dagger}_{i,\sigma}c_{i,\sigma}$ counts the number of electrons with spin σ at site i. The ionic potential in the Hamiltonian (2.1) breaks the full translational symmetry of the model and enlarges the size of the unit cell from one site to two sites. The IHM (2.1) is invariant under site-parity but not under bond-parity for any finite value of δ. The three different terms present in the IHM (2.1) are schematically depicted in Fig. 2.2.

2.2.2 Gaps and Order Parameters

It is useful to define three different gaps which measure the excitation energies in the IHM. The charge gap Δ_c is defined as the energy that we need to add an electron to the system

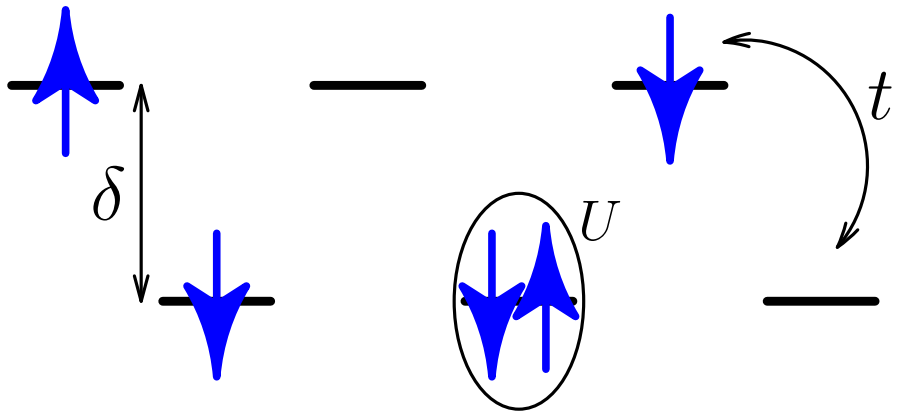

Figure 2.2: Schematic representation of the one-dimensional ionic Hubbard model (2.1). The parameter t shows the nearest-neighbor hopping, the Hubbard interaction is denoted by U, and δ indicates the energy separation between odd and even sites.

plus the energy to take an electron from the system. The charge gap is given by

$$\Delta_c \equiv E_0(N+1) + E_0(N-1) - 2E_0(N), \tag{2.2}$$

where $E_0(N)$ stands for the ground state energy of the system with N particles. The exciton (singlet) gap Δ_e and the spin gap Δ_s are defined as the excitation energy to the states with the same particle number as the ground state but with total spin zero and one, respectively. The exciton and spin gaps read

$$\Delta_e \equiv E_1(N, S=0) - E_0(N, S=0), \tag{2.3}$$
$$\Delta_s \equiv E_1(N, S=1) - E_0(N, S=0), \tag{2.4}$$

where $E_1(N,S)$ denotes the first excited state with N particle and total spin S. Because we are interested in half-filling, we put $N = L$ where L is the lattice size.

We define the ionicity I as the difference between the density of particle on the odd sites and the density of particles on the even sites. The ionicity is given by

$$I \equiv -\frac{1}{L}\sum_{i,\sigma}(-1)^i \langle n_{i,\sigma}\rangle. \tag{2.5}$$

where $\langle\cdots\rangle$ is the expectation value with respect to the ground state. This quantity can be used as measure of the degree of charge transfer between the donor and the acceptor molecules. The ionicity is unity if all the odd sites are occupied and all the even sites are empty. It is zero on the other limit where each site is occupied with one electron. The ionicity can be calculated from the ground state energy of the IHM (2.1) via the Hellmann-Feynman theorem

$$\begin{aligned} I = -\frac{2}{L}\left\langle \frac{\partial H}{\partial \delta}\right\rangle &= -\frac{2}{L}\frac{\partial \langle H\rangle}{\partial \delta} \\ &= -2\frac{\partial \epsilon_0}{\partial \delta}, \end{aligned} \tag{2.6}$$

where ϵ_0 denotes the ground state energy per site.

The translational symmetry in the model can be spontaneously broken leading to a bond order or spontaneously dimerized insulator (SDI) phase. The relevant order parameter to detect such a dimerized phase is the spontaneous dimerization $\mathcal{D}$ given by

$$\mathcal{D} \equiv \frac{1}{L}\sum_{i,\sigma}(-1)^i \langle c^\dagger_{i,\sigma} c_{i+1,\sigma} + \text{h.c.}\rangle. \tag{2.7}$$

This quantity is zero if all bonds in a chain are equivalent and becomes finite if the site-parity is broken and a bond order appears in the system.

2.2.3 Special Limits

Let us consider the IHM in some special limits in order to obtain a general idea about the phase diagram of the model. The simplest case is without hopping in the system, $t = 0$. In this limit, we have a classical Hamiltonian to deal with. For $U < \delta$, the ground state is unique with all odd sites occupied and all even sites empty. For $U > \delta$, each site is occupied with one electron which is free to choose up or down spin. This leads to the degeneracy 2^L of the ground state. These BI and MI phases are separated by a first order transition point at $U = \delta$. The ionicity (2.5) changes discontinuously from one to zero at this first order transition point.

The Hamiltonian (2.1) in the non-interacting limit $U = 0$ is also easily solvable by a Bogoliubov transformation in momentum space. One finds two energy bands given by

$$E_\pm(k) = \pm\sqrt{\left(\frac{\delta}{2}\right)^2 + 4t^2\cos^2(k)}, \tag{2.8}$$

where the momentum k is defined in the reduced BZ, $-\frac{\pi}{2} < k \leq +\frac{\pi}{2}$. The lower band $E_-(k)$ and the upper band $E_+(k)$ are separated by an energy gap δ which occurs at momentum $k = \frac{\pi}{2}$. At half-filling, the lower band $E_-(k)$ is completely filled with up and down spins. The charge gap (2.2), the exciton gap (2.3), and the spin gap (2.4) are all identical and equal to δ. This is natural because with no interaction in the system, electron and hole pairs can never form bound states and therefore the exciton gap and the spin gap are always identical to the charge gap. The ionicity can be obtained from the ground state energy via equation (2.6). One finds

$$I^{(0)} = \frac{2}{\pi}\int_0^{\frac{\pi}{2}} \frac{\mathrm{d}k}{\sqrt{1+\left(\frac{4t}{\delta}\right)^2\cos^2(k)}} = \frac{2}{\pi\sqrt{1+\left(\frac{4t}{\delta}\right)^2}} K\left(\sqrt{\frac{16t^2}{\delta^2+16t^2}}\right), \tag{2.9}$$

where $K(\cdots)$ is the complete elliptic integral of the first kind. In the limit $t \ll \delta$, we can expand the square root expression to obtain

$$I^{(0)} = 1 - \left(\frac{2t}{\delta}\right)^2 + O\left(\frac{t^4}{\delta^4}\right). \tag{2.10}$$

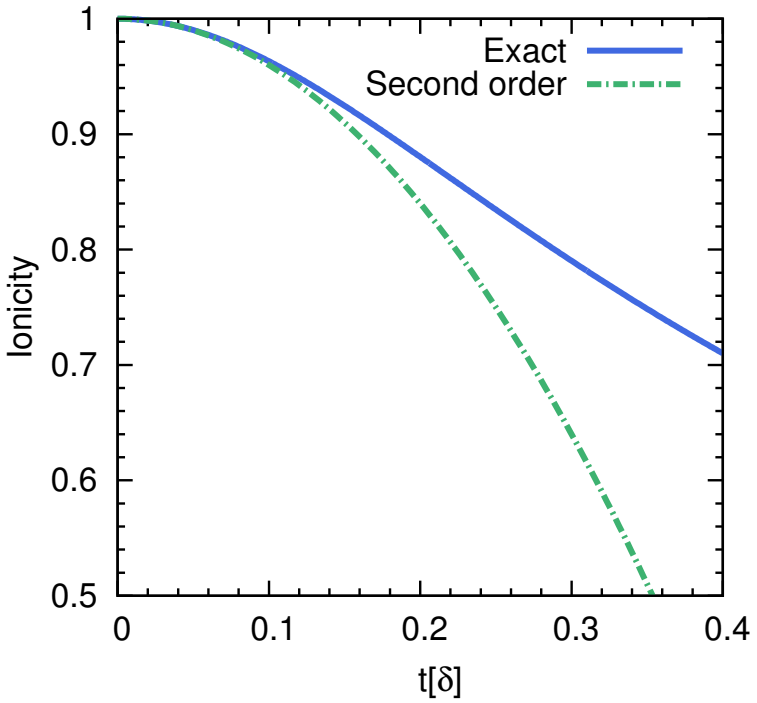

Figure 2.3: The exact result of ionicity (2.9) compared with the result of second order in t/δ.

The ionicity decreases from unity as square of $\left(\frac{t}{\delta}\right)$ upon introducing the hopping parameter in the system. The exact result of ionicity is compared with the second order result in Fig. 2.3.

We expect that in the presence of the Hubbard interaction, the ionicity will reduce due to the onsite interaction between the electrons on the odd sites. The effect of the Hubbard interaction U on the ionicity up to first order in U can be taken into account using first order perturbation theory. The ground state energy per site up to first order in U is given by

$$\epsilon_0^{(1)} = \epsilon_0^{(0)} + \frac{U}{2}\left(\langle n_{\mathrm{e},\sigma}\rangle^2 + n_{\mathrm{o},\sigma}\rangle^2\right) \tag{2.11}$$

where $\langle n_{\mathrm{e},\sigma}\rangle$ and $\langle n_{\mathrm{o},\sigma}\rangle$ are the density of particles with spin $\sigma = \uparrow, \downarrow$ on even and odd sites, respectively. The expectation values are with respect to the non-interacting ground state. The right-side of Eq. (2.11) can be written in terms of ionicity $I^{(0)}$ using the relations

$$I^{(0)} = \langle n_{\mathrm{o},\sigma}\rangle - \langle n_{\mathrm{e},\sigma}\rangle, \tag{2.12a}$$
$$1 = \langle n_{\mathrm{o},\sigma}\rangle + \langle n_{\mathrm{e},\sigma}\rangle. \tag{2.12b}$$

Finally, one finds the ionicity up to first order in U using Eq. (2.6)

$$I^{(1)} = I^{(0)}\left(1 - U\frac{\partial I^{(0)}}{\partial \delta}\right), \tag{2.13}$$

where $I^{(0)}$ is given in Eq. (2.9). The ionicity reduces linearly in the Hubbard interaction.

In the limit that doubly occupied sites are very high in energy, the IHM (2.1) at half-filling can be mapped to an effective low-energy spin Hamiltonian. The procedure is similar to the derivation of the Heisenberg model from the Hubbard model. However, we should notice that such a mapping is valid if $U-\delta \gg t$ and not for $U \gg t$ as in the usual Hubbard model. This stems from the fact that in the IHM (2.1) the electrons on the odd sites gain a negative energy of order δ. The effective spin Hamiltonian up to fourth order in the hopping parameter t is given by [NT86]

$$H = J_1 \sum_i \boldsymbol{S}_i \cdot \boldsymbol{S}_{i+1} + J_2 \sum_i \boldsymbol{S}_i \cdot \boldsymbol{S}_{i+2} \tag{2.14}$$

where the prefactors J_1 and J_2 are defined as

$$J_1 \equiv \frac{4t^2}{U}\frac{1}{1-x^2} - \frac{16t^4}{U^3}\frac{1+4x^2-x^4}{\left(1-x^2\right)^3}, \tag{2.15a}$$

$$J_2 \equiv \frac{4t^4}{U^3}\frac{1+4x^2-x^4}{\left(1-x^2\right)^3}, \tag{2.15b}$$

with $x \equiv \delta/U$. We notice that the spin Hamiltonian (2.14) has the full translational symmetry although the original IHM (2.1) has two sites per unit cell. It can be shown that the effective spin Hamiltonian up to infinite order in the hopping parameter t is invariant under the full translational symmetry [NT86].

The Hamiltonian (2.14) is the Heisenberg model with a frustrated next nearest-neighbor (n.n.n.) interaction J_2 and it is known as J_1-J_2 Heisenberg model. This Hamiltonian has been investigated by several methods such as exact diagonalization [TH87], field theory [ON92, Egg96], density matrix renormalization group [CPK+95, WA96], series expansion [Hon99, SW99], and perturbative CUT [KU00]. In the limit $J_2 = 0$, the Hamiltonian simplifies to the n.n. Heisenberg model which is exactly solvable [Bet31]: The ground state is a spin liquid phase and the excitations are spinons with the dispersion

$$\omega_{\text{spinon}}(k) = J_1 \frac{\pi}{2} \sin(k). \tag{2.16}$$

The system is stable versus the n.n.n. interaction and remains gapless up to $J_2/J_1 = 0.241167$ [Egg96]. At this point, a second order phase transition from the gapless spin liquid phase to the dimerized MI phase occurs. The transition is identified as Kosterlitz-Thouless (KT) transition where the opening of the gap is exponentially slow. In the dimerized phase, the doubly degenerate ground state is characterized by strong and weak bonds which alternate along the chain. The value $J_2 = J_1/2$ corresponds to the Majumdar-Gosch point [MG69] where the system is fully dimerized: The 2-fold degenerate ground state is given by the direct product of singlets on independent dimers with $\boldsymbol{S}_1 \cdot \boldsymbol{S}_2 = -3/4$.

Nevertheless, as far as the spin Hamiltonian (2.14) is derived from the IHM in the limit $U-\delta \gg t$ and the interactions J_1 and J_2 are given by equations (2.15), we are deep inside the gapless spin liquid phase of J_1-J_2 Heisenberg model. This is because $U-\delta \gg t$ implies $J_1 \gg J_2$, see Eqs. (2.15). Therefore we expect the IHM to be in large-U limit a MI with gapless spinons. While the spin gap (2.4) is zero in this phase, the charge gap (2.2) increases linearly in the interaction U like in the usual Hubbard model for large

U. The Hamiltonian (2.14) up to second order in the hopping parameter t reduces to the Heisenberg model with the exact ground state energy per site

$$\epsilon_0 = \left(\frac{1}{4} - \ln(2)\right) J, \tag{2.17}$$

where $J := 4t^2U/(U^2 - \delta^2)$ is the prefactor of the n.n. interaction. Hence, the leading order in t of the ionicity in the limit $U - \delta \gg t$ is given by

$$I = +\frac{16t^2U\delta}{\left(U^2 - \delta^2\right)^2}\ln(2). \tag{2.18}$$

This relation indicates that in the large-U limit, the ionicity decreases as power law ($\sim 1/U^3$) upon increasing Hubbard interaction. Therefore, it remains finite for any finite value of the interaction U.

The general behavior of the IHM at half-filling can be deduced from the above special limits. The ground state of the IHM (2.1) at small values of the Hubbard interaction U is a BI and at the large-U limit it is a gapless MI phase. The natural question appears: What is between these two BI and MI phases? Are they separated by a transition point or is there an intermediate phase? In the latter case, what is the nature of this intermediate state? What is the excitation spectrum of the system in the different phases?

In the next section, we review some of the previous investigations on the phase diagram of the IHM as well as on its excitation spectrum.

2.3 Some Previous Results

In this section, we try to follow the historical order especially for the results which concern the phase diagram of the 1D IHM. There have been several attempts to determine the phase diagram of the IHM using different approaches. In the following, however, we will focus only on methods such as QMC and DMRG as well as bosonization. The results obtained by approximate techniques like (slave-particle) mean-field theory [RS95, OOMC96, CAN00] and renormalization group methods [GSB01, HJA09] are not discussed. The mean-field analyses ignore quantum fluctuations which expect to be essential in one dimension. We also do not address the exact diagonalization calculations performed on finite size clusters [Anu01, GST00]. There are some difficulties in exact diagonalization results to be extrapolated to the thermodynamic limit, cf. [GST00].

2.3.1 Phase Diagram

Nagaosa and Takimoto using Quantum Monte Carlo (QMC) simulations investigated the phase diagram of the 1D IHM in 1986 [NT86]. Different integrated correlation functions

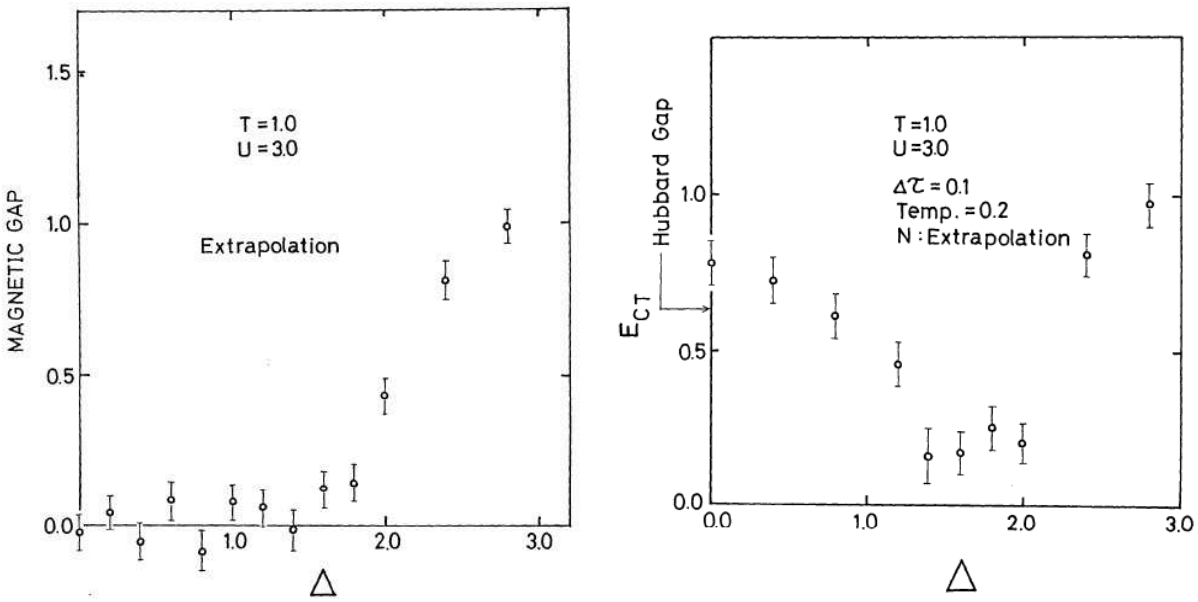

Figure 2.4: The results of quantum Monte Carlo simulations for the spin gap (left panel) and the charge gap (right panel) plotted versus the ionic potential. The parameters Δ and T in this figure correspond to the ionic potential δ and the hopping parameter t of the ionic Hubbard model (2.1). The parameter U stands for the Hubbard interaction. The results are for $t = 1.0$ and $U = 3.0$. The figure is taken from Ref. [NT86].

corresponding the charge density wave, spin density wave, and bond order wave are evaluated. We focus here only on their results for the spin gap and the charge gap. The exciton gap (2.3) is not considered in the analysis by Nagaosa and Takimoto. The spin gap (called magnetic gap) and the charge gap (denoted by E_{CT}) are plotted in the left panel and in the right panel of Fig. 2.4, respectively. The parameter Δ stands for the ionic potential δ and T equals the hopping parameter t. The hopping parameter and the Hubbard interaction in these figures are fixed to $t = 1.0$ and $U = 3.0$. From the left panel of Fig. 2.4, it is concluded that the spin gap remains zero up to $\delta \simeq 1.4$ and rises continuously beyond this point suggesting a phase transition. There have been more problems to extrapolate the charge gap from finite temperature to zero temperature compared to the spin gap. The error due to the finiteness of temperature (Temp.=$0.2t$) in the right panel of Fig. 2.4 is estimated based on two facts: First, the charge gap at $\delta = 0$ should be identical to the Hubbard gap but it is about 0.15 higher than this exact value. Second, the spin gap should be equal or less than the charge gap. This is because two free fermions can always form a singlet or triplet state. The exciton gap (2.3) and/or the spin gap (2.4) may get a value less than the charge gap (2.2) if the two fermions form a bound state. This can occur due to some effective attractive interactions in the system. Thus, comparing the results of the spin gap and the charge gap at $\delta = 2.0$ gives us another estimate for the error present in the charge gap. The right panel of Fig. 2.4 shows that the charge gap has a minimum near the transition point $\delta = 1.4$. Within the accuracy of the results the authors do not exclude the appearance of a metallic state at the transition point from the MI to the BI.

Fabrizio, Gogolin, and Nersesyan in 1999 employed the bosonization technique to investigate the phase diagram of the 1D IHM (2.1) [FGN99]. They claim that the BI and MI

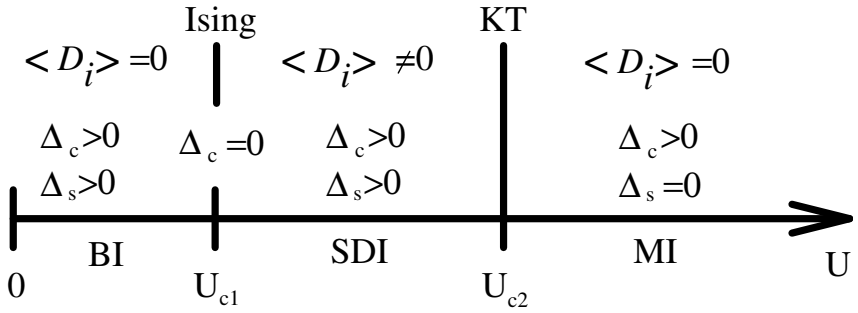

Figure 2.5: The phase diagram of the ionic Hubbard model (2.1) obtained by bosonization technique. There is a spontaneously dimerized insulator (SDI) phase between the band insulator (BI) and the Mott insulator (MI) phases. The dimer operator has a non-zero expectation value in this intermediate phase. The figure is taken from Ref. [FGN99].

phases are separated by an intermediate phase. The nature of this middle phase is identified as a SDI where the dimer operator (2.7) defines the order parameter and acquires a finite expectation value. Upon increasing the Hubbard interaction U for fixed values of t and δ, the exciton gap vanishes at the first transition point U_{c1} from BI to SDI. This transition is recognized to be of Ising type. Hence, the first phase transition is a charge transition at which no qualitative effect occurs in the spin sector. The second transition point U_{c2} from the SDI to the MI phase takes place by softening of the spin gap. It is asserted to be of Kosterlitz-Thouless (KT) type. This resembles the 1D $J_1 - J_2$ Heisenberg model where the system undergoes a KT transition from the dimerized MI phase to the gapless spin liquid phase by reducing the n.n.n. interaction.

The position of the second transition point in the limit $t \gg (\delta, U)$ estimated by Fabrizio *et. al.* [FGN99] is given by

$$U_{c2} = \frac{2\pi t}{\ln(2t/\delta)} \left[1 + O\left(\frac{\ln\ln(2t/\delta)}{\ln(2t/\delta)} \right) \right]. \tag{2.19}$$

The finite width of the SDI phase is also determined by the relation

$$\frac{U_{c2}}{U_{c1}} - 1 = \frac{\text{const.}}{\ln(2t/\delta)}, \tag{2.20}$$

where the positive constant on the right hand side is a number of order 1. Fig. 2.5 summarizes the phase diagram of the IHM obtained by the low-energy effective field theory [FGN99].

We now discuss the DMRG results presented by Takada and Kido in 2001 [TK01]. The charge gap and the spin gap are calculated for chains up to 400 sites and the thermodynamic limit is approached by a finite-size scaling. No attention has been paid to the exciton gap (2.3). In addition to the charge and spin gaps, the authors consider the localization length to identify the transition point(s), see Ref. [TK01]. Fig. 2.6 extracted from Ref. [TK01] shows the charge gap Δ_c and the spin gap Δ_s (left panel) and the localization length D_L (right panel) plotted versus the Hubbard interaction. In this figure, the Hubbard interaction U is denoted by u and t stands for the hopping parameter. The parameter v is

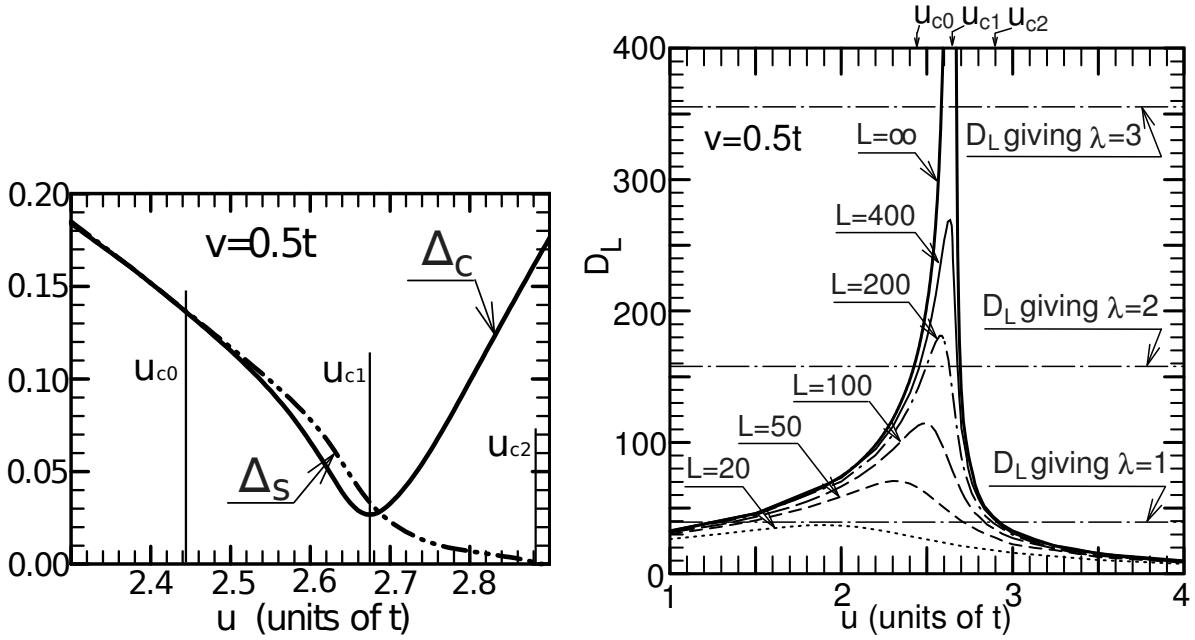

Figure 2.6: The charge gap Δ_c and the spin gap Δ_s (left panel) and the localization length D_L (right panel) obtained by Takada and Kido using density matrix renormalization group method [TK01]. The parameters t and u in this figure stand for the hopping parameter and the Hubbard interaction. The parameter v corresponds to $\delta/2$ in our notation of the ionic Hubbard model (2.1). These figures are extracted from Ref. [TK01].

equivalent to $\delta/2$ in our representation of the IHM (2.1). Therefore $v = 0.5t$ corresponds to $\delta = t$. Let us focus on the left panel of Fig. 2.6 which clarifies the behavior of the spin gap (dotted-dashed line) and the charge gap (solid line) near the critical points. For fixed values of t and δ, three characteristic points are distinguished upon increasing the Hubbard interaction U. The spin gap and the charge gap are equal up to the first point called U_{c0}. Beyond this point, the authors find a spin gap larger than the charge gap. Both the spin and charge gaps decrease up to the second critical point U_{c1} where the charge gap takes its finite minimum. Beyond this minimum, the charge gap starts to increase while the spin gap continues to decrease. The third critical point U_{c2} is characterized as the point where the spin gap vanishes. The authors identify a transition at U_{c1} by observing a divergency in the localization length D_L although they never find a gap vanishing at this point. The non-zero minimum of the charge gap at U_{c1} is interpreted as the error due to the open boundary condition which tends to overestimate the charge gap. They think that in a more reliable calculations the gap would vanish. From the behavior of the charge gap and the localization parameter, Takada and Kido suggest a Luttinger-liquid-type quasi-metallic phase with the order parameter $(\Delta_s - \Delta_c)$ for the region $U_{c0} < U < U_{c1}$ and an insulating phase for the range $U_{c1} < U < U_{c2}$. It is concluded that the insulating phase for $U_{c1} < U < U_{c2}$ is most likely a SDI as proposed by Fabrizio, Gogolin, and Nersesyan [FGN99].

In 2001 Wilkens and Martin performed a variational QMC study of the phase diagram of the 1D IHM [WM01]. Their main focus is the bond order parameter (2.7) and the polarization. By increasing the Hubbard interaction, it is found that the dimerization becomes finite at a critical interaction indicating a phase transition from the BI to the SDI phase.

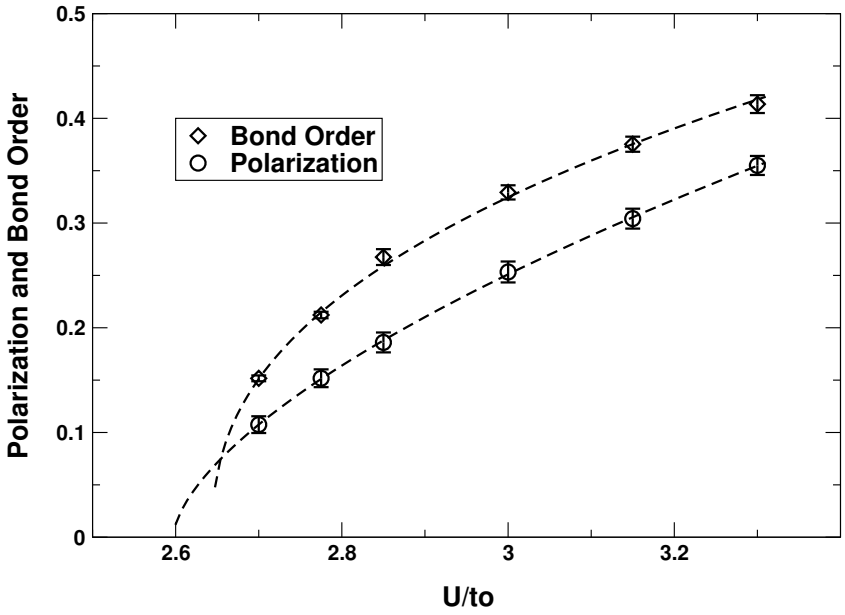

Figure 2.7: The bond order parameter and polarization of the ionic Hubbard model obtained from quantum Monte Carlo (QMC) calculations. The dashed lines indicate a fit function of the form $A\left[U-U_c\right]^{\xi}$ to the QMC results. For the bond order parameter $\xi = 0.39(4)$ and for the polarization $\xi = 0.60(10)$. The figure is taken from Ref. [WM01].

Surprisingly, no second transition from the SDI phase to the MI phase is identified. The dimerization parameter remains finite even for very large values of the Hubbard interaction. Fig. 2.7 shows the behavior of the bond order parameter and polarization versus the Hubbard interaction U near the transition point from the BI phase to the SDI phase. The QMC results are fitted by a function of the form $A\left[U-U_c\right]^{\xi}$ where ξ is the critical exponent. The critical exponent for the bond order parameter and polarization are found to be 0.39(4) and 0.60(10), respectively. These numbers are close to 1/2, the mean-field critical exponent, and differs significantly from 1/8 which was suggested by Fabrizio, Gogolin, and Nersesyan [FGN99]. For the phase diagram of the IHM, Wilkens and Martin conclude that the MI phase is unstable versus the ionic potential δ and appears only for $\delta \equiv 0$ [WM01].

Another DMRG analysis of the IHM was implemented by Lou *et al.* in 2003 [LQX+03]. The exciton gap (2.3), the charge gap (2.2), and the spin gap (2.4) are all investigated. The finite size results are carefully extrapolated to the thermodynamic limit. For fixed values of t and δ, two transition points are identified upon increasing the Hubbard interaction U. One from the BI phase to the SDI at U_{c1} and the other from the SDI to the MI at $U_{c2} > U_{c1}$. Fig. 2.8 taken from Ref. [LQX+03] denotes the extrapolated results obtained for the charge gap (solid circles), the spin gap (empty circles), and the exciton gap (empty squares) at $\delta = 0.6t$ (panels a and b) and $\delta = 2.0t$ (panels c and d). It is found that a charge-neutral spin-singlet mode develops in the BI phase which closes at the first transition point beyond which the SDI phase stabilizes. The charge gap and the spin gap remain equal up to the *second* transition point U_{c2} where they both vanish. Beyond this point, the charge gap rises linearly while the spin gap remains zero. The equality of the spin gap and the charge gap in the SDI phase reported in this paper contradicts the findings by Fabrizio [FGN99] and Takada [TK01] discussed above.

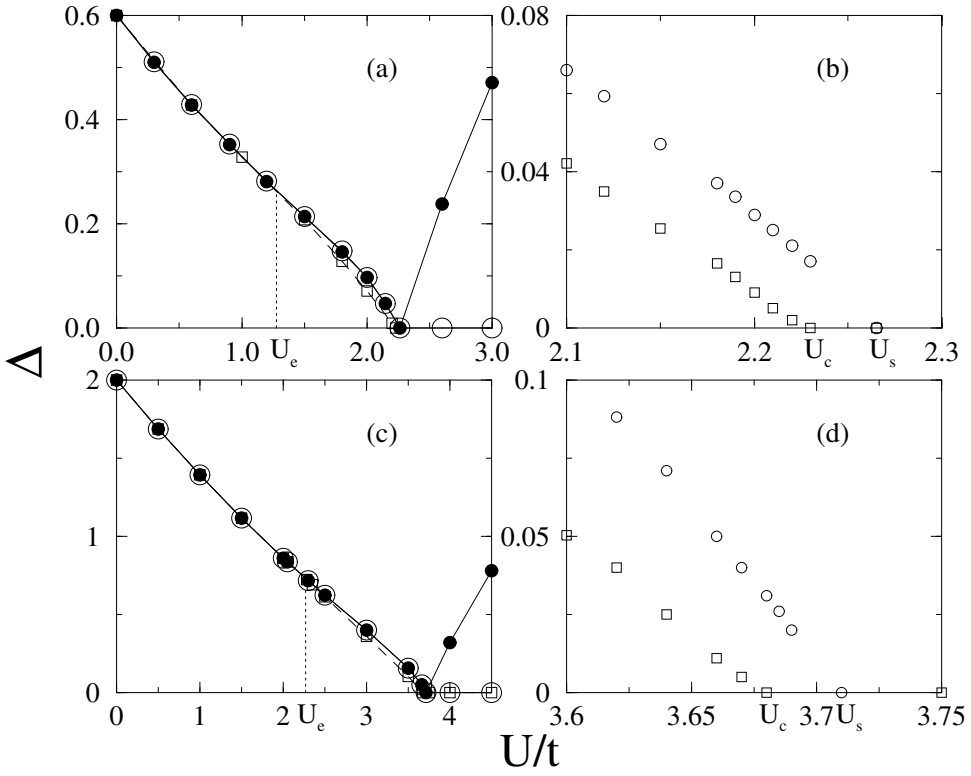

Figure 2.8: The extrapolated DMRG results obtained by Lou *et al.* for the charge gap (solid circles), the spin gap (empty circles), and the exciton gap (empty squares) at $\delta = 0.6t$ (panels a and b) and $\delta = 2.0t$ (panels c and d). This figure is taken from Ref. [LQX+03]. The first transition point from BI to SDI is shown by $U_c = U_{c1}$ and the second transition point from the SDI to the MI is displayed by $U_s = U_{c2}$. U_e is the position where the charge-neutral spin-singlet mode appears.

In the same year 2003, Kampf *et al.* [KSJB03] come to a rather different conclusion than Lou *et al.* [LQX+03] using the DMRG method. One phase transition from the BI phase to the SDI phase is recognized where the exciton gap vanishes. The authors mention that within the accuracy of the DMRG results and the accessible chain lengths, it is not possible to judge whether the spin gap is zero or not for large U. The charge gap Δ_c and the spin gap Δ_s derived by Kampf *et al.* are plotted in Fig. 2.9 versus the Hubbard interaction. The parameter δ is fixed to $0.5t$ in this figure. The authors emphasize the role of the extrapolation of the results for large enough chain lengths. The main plot indicates the extrapolated results for the chain lengths $L = \{30, 40, 50, 60\}$ and the inset is obtained after increasing the lattice size to $L = 512$. From the main plot, it is seen that the spin gap and the charge gap become different before the transition to the SDI phase and the spin gap vanishes at large Hubbard interaction. The more rigorous results in the inset, however, indicate a considerably different picture. The spin gap and the charge gap are identical up to the BI-to-SDI transition point where the sharp finite minimum of the charge gap takes place. Beyond this minimum, the spin gap decreases and becomes unresolvably small above $U \sim 2.5t$ within the achievable numerical accuracy, the authors state. The results in the inset of Fig. 2.9 challenge both previous DMRG findings by Takada and Lou sketched in Figs. 2.6 and 2.8.

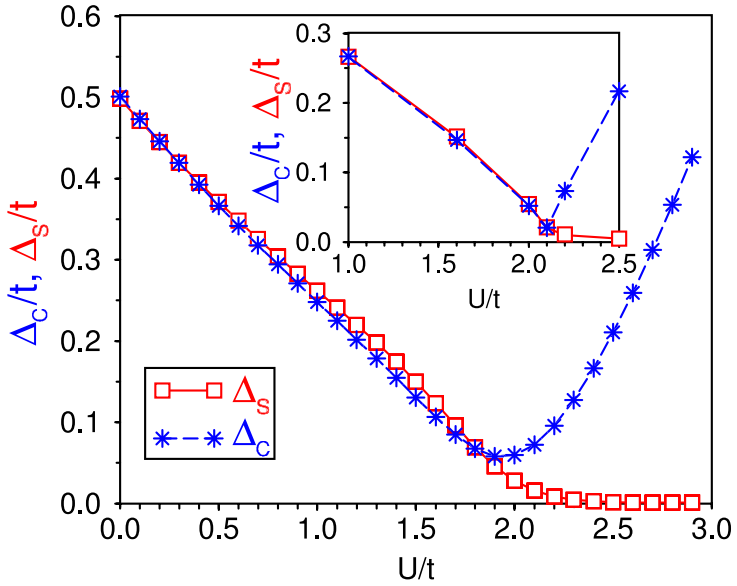

Figure 2.9: The spin gap Δ_s and the charge gap Δ_c for $\delta = 0.5t$ obtained by Kampf *et al.* using the DMRG method [KSJB03]. The main plot shows the extrapolated results obtained from the lattice sizes $L = \{30, 40, 50, 60\}$. The inset is derived after the lattice size is increased to $L = 512$. The figure is taken from Ref. [KSJB03].

By employing again the DMRG method and by a careful finite-size scaling, Manmana *et al.* [MMNS04] in 2004 confirm the phase diagram of Fig. 2.5 that was initially proposed by Fabrizio, Gogolin, and Nersesyan. The extrapolated DMRG results obtained by Manmana *et. al.* are sketched in Fig. 2.10. The left panel of this figure shows the charge gap (empty circle), the exciton gap (empty square), and the spin gap (asterisk) near the critical region for $\delta = 20$ and $t = 1$. For the same set of parameters, the right panel of Fig. 2.10 denotes the dimerization versus the Hubbard interaction near the transition points. It is found that the spin gap and the charge gap remain equal up to the first transition point where the exciton gap closes. The minimum of the charge gap, within the accuracy of the results, coincides with the first transition point. Beyond this point, the charge gap increases while the spin gap continues to decrease and becomes soft at the second transition point to the MI phase. The extrapolated values for the dimerization parameter indicates that the middle phase is a SDI with a finite dimerization. The dimerization is zero in both the BI and MI phases.

There are other DMRG-based investigations ofthe phase diagram of the 1D IHM by Otsuka and Nakamura in 2005 [ON05], Legeza *et al.* in 2006 [LBS06], and Tincani *et al.* in 2009 [TNB09] which confirm the qualitative picture sketched in Fig. 2.5. In the next chapters, we will compare our findings for the charge, spin, and exciton gaps to the DMRG results obtained by Manmana *et al.* [MMNS04] as the most advanced one in our view.

In two dimensions, the phase diagram of the IHM is still highly disputed. Because this thesis is devoted to the 1D IHM, we just mention the outcomes of recent investigations on the 2D IHM. Although the presence of the band and Mott insulators for the small and large values of the Hubbard interaction are established [GKR06, PBH+07, BPH+07, CLH+08, KD07, CZLW10], the existance and the nature of the intermediate phase is not clear yet.

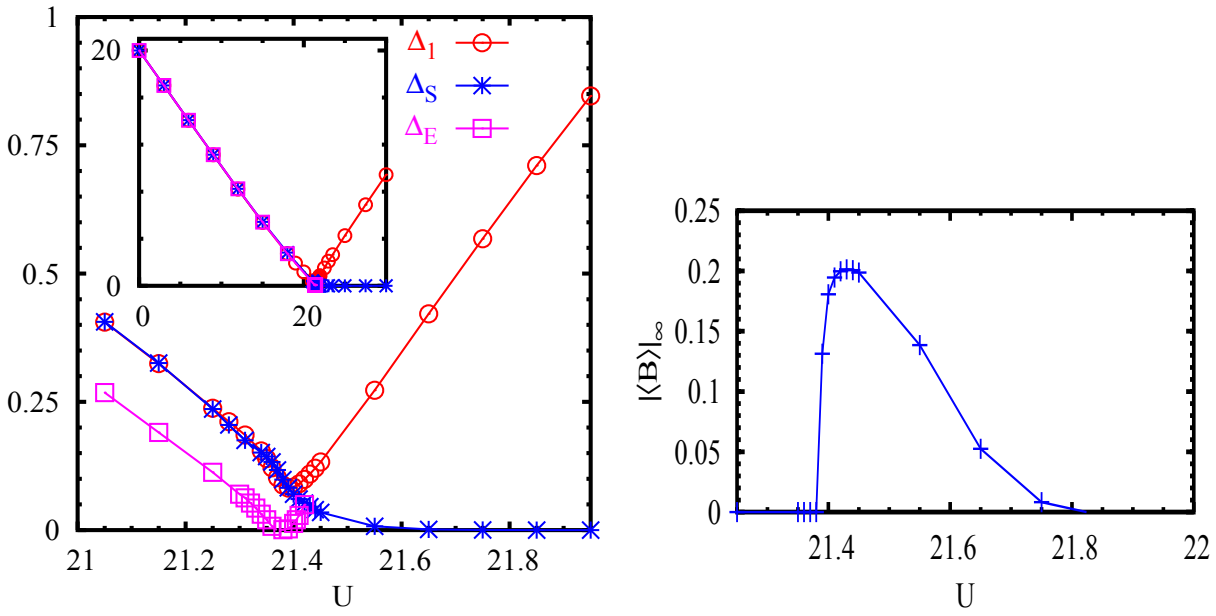

Figure 2.10: The extrapolated DMRG results for the gaps (left panel) and the dimerization parameter $|\langle B\rangle|$ (right panel) near the critical region obtained by Manmana *et al.*. The charge gap, the exciton gap, and the spin gap in the left panel are denoted by empty circle, empty square, and asterisk, respectively. The results are for $\delta = 20$ and $t = 1$. The figures are taken from Ref. [MMNS04].

A single-site dynamic mean-field theory (DMFT) indicates an intermediate metallic phase between BI and MI [GKR06] which is confirmed by determinant QMC method [PBH+07, BPH+07]. In another single-site DMFT study [CLH+08], in addition to a metallic phase, coexistence of MI with metallic and coexistence of MI with BI are found, see Ref. [CLH+08]. However, an investigation based on cluster-DMFT shows that the middle phase is a SDI similar to the 1D case [KD07]. In the variational cluster approach, it is a bond-located spin density wave with a magnetic order which has the lowest energy in the intermediate region [CZLW10]. We want to emphasize that our analysis of the 1D IHM in chapter 4 is conceptually not restricted to one dimension and can in principle be applied to the 2D lattices as well.

2.3.2 Excitation Spectrum

The excitation spectrum and the spectral properties of the IHM in spite of its phase diagram have attracted less attention. These physical quantities provide valuable information relevant to experimental measurements such inelastic neutron scattering experiments and electron-energy loss spectroscopy. To our knowledge, the only known results for the excitation spectrum [HJ10] and the spectral properties [HA11] of the IHM are obtained by perturbative CUT method in the BI phase. Due to the perturbative nature of the method, the authors have not been able to approach the BI-to-SDI transition point for the 2-particle excitations. The results are presented deep in the BI phase. The left panel of Fig. 2.11 shows the excitation spectrum of the 1D IHM in the reduced BZ for $\delta = 1.0$, $t = 0.125$, and

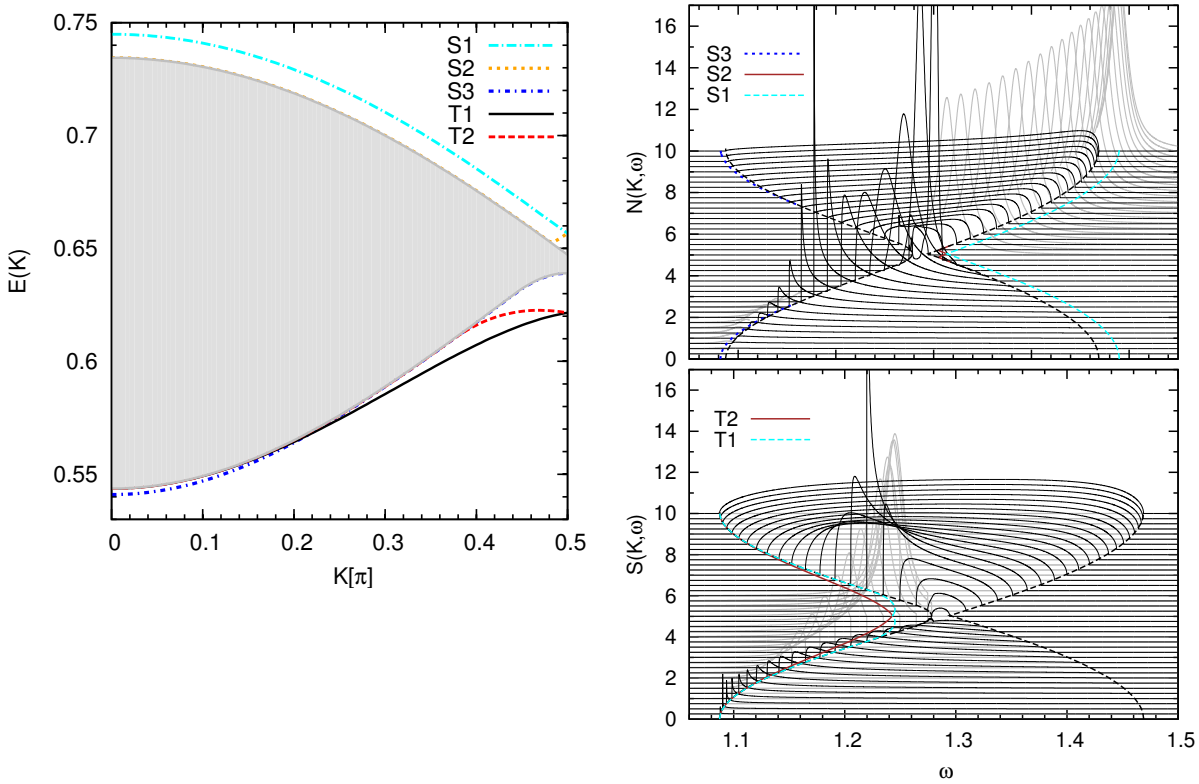

Figure 2.11: Left panel: The excitation spectrum of the one-dimensional ionic Hubbard model in the band insulator phase for $\delta = 1$, $t = 0.125$, and $U = 0.5$ [HJ10]. Right panel: The charge-charge $N(K,\omega)$ and the spin-spin $S(K,\omega)$ correlation functions of the ionic Hubbard model for $\delta = 2.0$, $t = 0.25$, and $U = 1.0$ [HA11].

$U = 0.5$ [HJ10]. The right panel of this figure indicates the charge-charge $N(K,\omega)$ and the spin-spin $S(K,\omega)$ dynamical correlation functions for $\delta = 2.0$, $t = 0.25$, and $U = 1.0$. The right panel is extracted from Ref. [HA11]. Because the IHM has two sites per unit cell, the excitation spectrum should be considered in the reduced BZ, $-\pi/2 < K \leq \pi/2$. In the singlet channel of the 2-fermion sector, two anti-bound states and one bound state is found. The singlet bound state $S3$ at the total momentum $K = 0$ is the mode which condenses at the transition point to the SDI phase. There are also two triplet bound states which are degenerate at the edge of the BZ, $K = \pm\frac{\pi}{2}$. We notice the large exciton gap $\Delta_e \approx 0.54\delta$ in Fig. 2.11 indicating that we are still far away from the transition point to the SDI phase.

2.4 Chapter Summary

This chapter is devoted to a general understanding of the 1D IHM. Starting with the experimental motivation behind the IHM. The model is used as a prototype to describe the neutral-ionic transition observed in the mixed-stack charge-transfer organic compounds such as TTF-chloranil [NT86] and the ferroelectricity in perovskite transition metal oxides such as $BaTiO_3$ [EIT93]. Next we present the model Hamiltonian which consists of the usual Hubbard model plus an ionic potential. This ionic potential separates the odd and

even sites by an energy shift enlarging the size of the unit cell from one to two lattice sites. The charge gap, the spin gap, and the exciton gap are defined to measure different excitation energies in the system. These gaps help us to identify the phase transitions which occur in the IHM. Some other relevant quantities such as the ionicity and the spontaneous dimerization (bond order parameter) are also introduced. In some special limits the IHM is analyzed to give us a general view of the phase diagram of the model. We review some of the previous investigations of the IHM with a main focus on one dimension. The large discrepancy between the results of different analyses is discussed and the likely phase diagram of the model in one dimension is sketched. Finally, it is pointed out that there is much less known about the excitation spectrum of the model, especially near the critical region.

Chapter 3

Method

This chapter is devoted to the methodological aspects of the present thesis. We have mostly used the recently formulated method called *directly evaluated enhanced perturbative continuous unitary transformation* (deepCUT) [KDU12] to obtained effective Hamiltonians. The deepCUT is a renormalization approach based on continuous unitary transformation (CUT) [Weg94, GW93]. The basic idea in the deepCUT is to map a given many-particle Hamiltonian to a few-particle problem by working in a suitable quasiparticle (QP) picture. We evaluate the final few-particle problem by an exact diagonalization (ED) technique which is valid in the thermodynamic limit.

This chapter is divided to three sections: In the first section 3.1 the basic concept of CUT is introduced. Then, the deepCUT is briefly illustrated in section 3.2. Finally, the ED method, which works in the thermodynamic limit, is explained in the last section 3.3.

3.1 The CUT method

3.1.1 The Basic Concept

The CUT or flow equation approach was proposed by Wegner [Weg94] and independently by Głazek and Wilson [GW93]. In this method a given Hamiltonian H is mapped, by a unitary transformation, to a diagonal or block diagonal effective Hamiltonian in a systematic fashion [Keh06]. The unitary transformation $U(\ell)$ depends on an auxiliary continuous parameter ℓ which defines the flow under which the Hamiltonian transforms from its initial form $H = H(\ell)\big|_{\ell=0}$ to its final effective form $H_{\text{eff}} = H(\ell)\big|_{\ell=\infty}$. The transformed Hamiltonian is given by

$$H(\ell) = U^{\dagger}(\ell) H U(\ell). \tag{3.1}$$

The Hamiltinian $H(\ell)$ is determined from the following differential equation called flow equation

$$\partial_\ell H(\ell) = [\eta(\ell), H(\ell)], \tag{3.2}$$

where the anti-hermitian operator

$$\eta(\ell) = -U^\dagger(\ell)\partial_\ell U(\ell) \tag{3.3}$$

is the generator of the flow. It is seen from Eq. (3.2) that we can directly deal with the generator instead of the unitary transformation $U(\ell)$. What is needed is the the generator $\eta(\ell)$ as function of the Hamiltonian operator. Then, the Hamiltonian $H(\ell)$ can be determined from the differential equation (3.2) and the initial condition $H(\ell)\big|_{\ell=0} = H$. The unitary transformation $U(\ell)$, if it is needed, can be determined from Eq. (3.3) in an iterative way [LW96].

The aim is to choose the generator $\eta(\ell)$ such that the off-diagonal elements become zero in the limit $\ell \to \infty$. Which term is diagonal and which is not, of course, depends on the effective Hamiltonian that we want to derive at $\ell \to \infty$. It is an arbitrary decision, but it should not affect the physics going on in the system. For instance, if the purpose is to replace the electron-phonon interaction with an effective electron-electron interaction, then all the terms which change the number of phonon in the system will consider as off-diagonal elements [LW96]. One may reach an effective Hamiltonian which conserves the number of double occupancies, in the Hubbard model for example, by properly separating the operators into diagonal and off-diagonal parts [Ste97, RMHU04, HDU10]. In a gapped phase, one may think of integrating out the terms which change the number of QPs in the system [KU00, DU04]. In this last case, the low-energy part of a many-particle Hamiltonian can be calculated by solving a few-particle problem [KSU03b]. Below we discuss some common choices of generators.

3.1.2 Wegner's Generator

We start with the simple observation that the trace of an operator does not change under a unitary transformation. Therefore, one can write

$$\partial_\ell \mathrm{Tr}\left(H^2(\ell)\right) = \partial_\ell \mathrm{Tr}\left(H^2\right) = 0. \tag{3.4}$$

This relation leads to the differential equation for the summation of the norm of the off-diagonal elements

$$\begin{aligned} \partial_\ell \sum_{i\neq j} \left|h_{i,j}(\ell)\right|^2 &= -\partial_\ell \sum_i \left|h_{i,i}(\ell)\right|^2 \\ &= -2\sum_i h_{i,i}(\ell)\partial_\ell h_{i,i}(\ell), \end{aligned} \tag{3.5}$$

where we have defined $h_{i,j}(\ell) := \langle i|H(\ell)|j\rangle$. $\{|i\rangle\}$ stands for a complete basis. The matrix representation of the flow equation (3.2) is given by

$$\partial_\ell h_{i,j}(\ell) = \sum_k \left(\eta_{i,k}(\ell)h_{k,j}(\ell) - h_{i,k}(\ell)\eta_{k,j}(\ell)\right). \tag{3.6}$$

This relation can be used to substitute the quantity $\partial_\ell h_{i,i}(\ell)$ on the right-hand side of Eq. (3.5). We obtain

$$\begin{aligned}\partial_\ell \sum_{i\neq j} \left|h_{i,j}(\ell)\right|^2 &= -2\sum_{i,j} h_{i,i}(\ell)\left(\eta_{i,j}(\ell)h_{j,i}(\ell) - h_{i,j}(\ell)\eta_{j,i}(\ell)\right) \\ &= -2\sum_{i,j} h_{j,i}(\ell)\left(h_{i,i}(\ell) - h_{j,j}(\ell)\right)\eta_{i,j}(\ell). \end{aligned} \tag{3.7}$$

Wegner suggested to take the generator as [Weg94]

$$\eta_{i,j}(\ell) = \left(h_{i,i}(\ell) - h_{j,j}(\ell)\right) h_{i,j}(\ell). \tag{3.8}$$

In the operator form this reads

$$\eta_W(\ell) = [H^d(\ell), H(\ell)], \tag{3.9}$$

where $H^d(\ell)$ is the diagonal part of the Hamiltonian $H(\ell)$. Clearly, this choice makes each term on the right-hand side of Eq. (3.7) non-positive. Because the norm of the off-diagonal elements

$$\sum_{i\neq j} \left|h_{i,j}(\ell)\right|^2 \geq 0, \tag{3.10}$$

is limited from below, the right-hand side of Eq. (3.7) must vanish for $\ell \to \infty$. Hence, we obtain

$$\left(h_{i,i}(\infty) - h_{j,j}(\infty)\right) h_{i,j}(\infty) = 0. \tag{3.11}$$

This relation shows that the off-diagonal elements are zero at $\ell \to \infty$ except for degenerate states $h_{i,i}(\infty) = h_{j,j}(\infty)$.

The disadvantage of Wegner's generator is that if the matrix of the initial Hamiltonian has a band-diagonal structure, *i.e.*,

$$h_{i,j}(0) = 0 \quad \text{For} \quad \left|i-j\right| > M, \tag{3.12}$$

this property is lost during the flow. This point can be seen from the shape of the flow equation (3.6) for Wegner's choice of generator.

3.1.3 Particle-Conserving Generator

Mielke introduced a modified generator that was especially useful for band diagonal matrices [Mie98]. In the many-particle context, Stein [Ste97] and Knetter and Uhrig [UN98, KU00] introduced an analogous generator to derive an effective block-diagonal Hamiltonian which preserves the number of quasiparticles (QPs) in the system. This generator, called particle-conserving (pc) generator, is widely used to simplify many-particle Hamiltonians. To be concrete, we work in QP representation where each state $|i\rangle$ includes a definite number of QP labelled as q_i. We suppose without loss of generality that $i \geq 1$ and $q_j \geq q_i$ if $j > i$. The matrix elements of the pc generator is given by

$$\eta_{i,j}(\ell) = \text{sign}(q_i - q_j) h_{i,j}(\ell), \tag{3.13}$$

with sign(0) := 0. Only the elements which link *different* QP sectors contribute to the generator. The flow equation (3.6) for the pc generator takes the form

$$\begin{aligned}\partial_\ell h_{i,j}(\ell) = \; & - \; \operatorname{sign}(q_i - q_j)\left(h_{i,i}(\ell) - h_{j,j}(\ell)\right) h_{i,j}(\ell) \\ & + \sum_{k\neq i,j} \left(\operatorname{sign}(q_i - q_k) + \operatorname{sign}(q_j - q_k)\right) h_{i,k}(\ell) h_{k,j}(\ell). \end{aligned} \tag{3.14}$$

The two sign functions appearing in the second term cancel each other for $q_i < q_k < q_j$[1]. This garantees that no off-diagonal element outside the band is linked to the matrix elements inside the band. Therefore the Hamiltonian remains band-diagonal even during the flow,

$$\text{If } h_{i,j}(0) = 0 \text{ for } \left|q_i - q_j\right| > M \quad \Longrightarrow \quad h_{i,j}(\ell) = 0 \text{ for } \left|q_i - q_j\right| > M. \tag{3.15}$$

We have not yet proved that the pc generator makes all off-diagnoal elements zero in the limit $\ell \to \infty$. The derivative of the first r diagonal elements of the Hamiltonian $H(\ell)$ is given by

$$\partial_\ell \sum_{i=1}^{r} h_{i,i}(\ell) = -2 \sum_{i=1}^{r} \sum_{j>r} \left|h_{i,j}(\ell)\right|^2 \operatorname{sign}(q_j - q_i) < 0. \tag{3.16}$$

If we suppose the Hamiltonian H is bounded from below, the quantity $\sum_{i=1}^{r} h_{i,i}(\ell)$ will be bounded as well. Therefore, the right-hand side of Eq. (3.16) must vanish in the limit $\ell \to \infty$ leading to

$$\operatorname{sign}(q_j - q_i) \left|h_{i,j}(\infty)\right|^2 = 0. \tag{3.17}$$

This relation means that $h_{i,j}(\infty) = 0$ if i and j belong to different QP sectors. Thus, the final effective Hamiltonian conserves the number of QPs in the system. Because the off-diagonal elements tend to zero at large values of ℓ, Eq. (3.14) implies that [Mie98, KU00]

$$\operatorname{sign}(q_i - q_j)\left(h_{i,i}(\infty) - h_{j,j}(\infty)\right) > 0. \tag{3.18}$$

The pc generator sort the eigen values according to the number of QPs.

The pc generator (3.13) in the operator representation reads

$$\eta_{\mathrm{pc}}(\ell) = \sum_{i,j=0} \operatorname{sign}(i-j) H_{i:j}(\ell) \tag{3.19}$$

where i and j now run over different QP blocks and $H_{i:j}$ is the part of Hamiltonian which creates i QPs and annihilates j QPs.

3.1.4 Reduced Generator

The pc generator makes the Hamiltonian block diagonal in the sense that the final effective Hamiltonian conserves the number of QPs. If we are working in QP picture, the sectors with a small number of QPs describe the low-lying excitation spectrum of the system. Therefore,

[1] We have assumed $i < j$.

it is sufficient to decouple only the first few QP sectors from higher sectors in order to describe the low-lying excitation spectrum. The reduced generator, which allows us to decouple the first n quasiparticle sectors, reads [FDU10]

$$\eta_{\mathrm{p:n}}(\ell) = \sum_{i=0}^{n} \sum_{j>n} \left(H_{j:i}(\ell) - H_{i:j}(\ell) \right). \tag{3.20}$$

In comparison to Eq. (3.19), it is clear that only terms acting on the first n QP sectors contribute to the reduced generator (3.20). This generator is especially useful to describe QP decay in the framework of CUT [FDU10]. While the pc generator sorts the eigen values according to the number of QPs, the reduced generator allows, for example, the 1-QP dispersion to decay into the 2-QP continuum [FDU10]. The band-diagonality will not be preserved by the generator (3.20). However, it has the potential not only to avoid some divergences that occur in the flow, but also to increase the speed of calculations because less terms need to be considered as generator. The proof that the generator (3.20) vanishes in the limit $\ell \to \infty$, and the details about its properties can be found in Ref. [FDU10].

3.2 The deepCUT method

In order to illustrate the deepCUT method, we assume that the initial Hamiltonian can be decomposed into a local part (H_0) and a nonlocal part (V)[1]

$$H = H_0 + xV, \tag{3.21}$$

where x is an expansion parameter. In the following, we derive the general shape of the flow equations in the deepCUT framework. Next, we briefly discuss how to truncate these flow equations based on powers of the expansion parameter x if the first few QP sectors are targeted. With "targeted" sectors we mean the sectors which we are interested to calculate their coefficients up to order n. Such a truncation scheme allows us to use simplification rules which accelerate the speed of calculations. For the details about the truncation scheme and the simplification rules, we refer to the original paper in Ref. [KDU12].

3.2.1 Flow Equations

To switch to the QP representation, the Hamiltonian (3.21) is written in terms of creation and annihilation operators of H_0 in second quantization formalism. In this representation,

[1] We assume these conditions to describe the deepCUT method in simple terms. However, the method may work even if these conditions are not satisfied. See, for example, the application of the deepCUT to the transverse field Ising model in Ref. [FU13]. Another example is the Hubbard model with a n.n. interaction. In this case, both the Hubbard interaction and the n.n. interaction define the nonperturbative part and the hopping term defines the perturbation. The possible application of the deepCUT method in momentum space is also discussed, but this is beyond the scope of the present thesis.

H_0 counts the number of excitations present in the system[1]. For $x = 0$, these excitations are the *true* QPs of the system and vacuum is the ground state. However, for any finite values of x these QPs become dressed and the Hamiltonian (3.21) does not necessarily conserve the number of these excitations.

The Hamiltonian (3.21) in QP representation is given as a sum of monomials $\{A_i\}$ of creation and annihilation operators. Each monomial describes a specific interaction in real space and creates and annihilates a definite number of QPs. The transformed Hamiltonian $H(\ell)$ can then be expressed as

$$H(\ell) = \sum_i h_i(\ell) A_i, \tag{3.22}$$

where the coefficients $h_i(\ell)$ carry the ℓ-dependence of the Hamiltonian. Similarly, the pc generator (3.19) and the reduced generator (3.20) can be written as

$$\eta(\ell) = \sum_i \eta_i(\ell) A_i =: \sum_i h_i(\ell) \hat{\eta}[A_i], \tag{3.23}$$

where the superoperator $\hat{\eta}$ defines how a given monomial enters the generator. By the above representations (3.22) and (3.23) for the Hamiltonian and the generator, the flow equations (3.2) read

$$\partial_\ell h_i(\ell) = \sum_{jk} D_{ijk} h_j(\ell) h_k(\ell), \tag{3.24}$$

where the contributions D_{ijk} result from the expansion of the commutator in terms of the monomials

$$[\hat{\eta}[A_j], A_k] = \sum_i D_{ijk} A_i. \tag{3.25}$$

The contributions D_{ijk} are fractional numbers and depend on the algebra of the operators and the structure of the lattice.

The solution of the flow equation (3.2) requires two major steps:

- Finding the contributions D_{ijk} from Eq. (3.25).
- Solving the set of ordinary differential Eq. (3.24).

The first step is pure algebraic work which is already implemented in the framework of self-similar CUT (sCUT) [Rei06, Duf10, Fis11]. When the contributions D_{ijk} are calculated, the integration in the second part allows us to obtain the coefficients $\{h_i(\infty)\}$. In principle, however, the summation in Eq. (3.23) will contain an infinite number of monomials. Hence, the number of monomials has to be restricted in practice by defining a systematic truncation scheme for the flow equations.

[1] In the case that H_0 is composed of two or more terms, such as the IHM (2.1), this nonperturbative part of the Hamiltonian measures the local energy of the system.

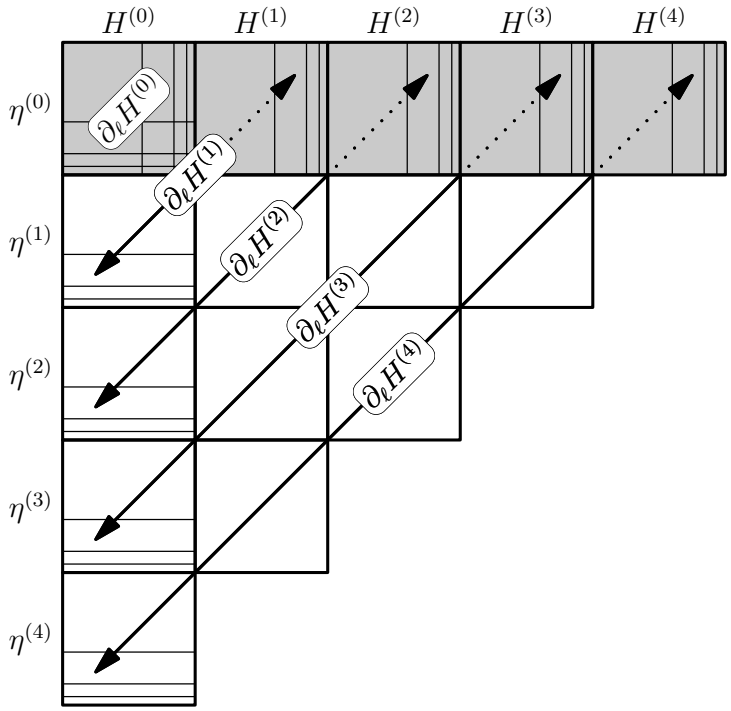

Figure 3.1: The generic algorithm for calculating the commutators between different generator $\eta^{(m)}$ and Hamiltonian $H^{(m)}$ blocks at order 4. The part $H^{(m)}$ ($\eta^{(m)}$) is defined to contain all the Hamiltonian (generator) monomials with minimal order m. The figure is taken from Ref. [KDU12] where the reader can find further details.

3.2.2 Truncation Scheme

Let us at first illustrate how to truncate the flow equations in order to obtain the final effective Hamiltonian as a series expansion in x up to order n. We append a minimal order to each monomial. This is defined to be the order in which the monomial appears for the first time during the calculations. Consequently, the Hamiltonian (3.22) and the generator (3.23) can be classified into different blocks

$$H(\ell) = \sum_{m=0}^{n} H^{(m)}, \tag{3.26a}$$

$$\eta(\ell) = \sum_{m=0}^{n} \eta^{(m)}, \tag{3.26b}$$

where $H^{(m)}$ and $\eta^{(m)}$ involve all the monomials with the minimal order m. The calculations of the commutators $\left[\eta^{(p)}, H^{(q)}\right]$ with $p+q \leq n$ provide the contributions D_{ijk} which are necessary for a perturbative analysis up to order n. The evaluation of the commutators begins from the lowest orders and the newly generated monomials are added to the Hamiltonian (3.22). The procedure for $n = 4$ is sketched schematically in Fig. 3.1. This figure is taken from Ref. [KDU12] where the reader can find the details of the generic algorithm. With the contributions D_{ijk} in hand, one can expand the prefactor $h_i(\ell)$ in powers of x and integrate the flow equations (3.24) perturbatively, see Ref. [KDU12]. In the limit $\ell \to \infty$, this leads to a series expansion up to order n for the prefactors of all the monomials present

in the effective Hamiltonian (3.22).

Usually, we are not interested in calculating all the prefactors of the final effective Hamiltonian up to order n. This is especially the case if we are working in QP representations. The prefactors of identity and bilinear operators, for instance, are sufficient to know the ground state energy and the 1-particle dispersion. This means that we need to obtain just the prefactors of some targeted monomials up to order n. The other monomials are relevant as far as they contribute to the targeted quantities in the hierarchy of flow equations. In this way, depending on the generator, some monomials can be completely neglected and some others need to be calculated only up to orders $\leq n$.

The maximal order $O_{\max}(A)$ is defined as the maximal order in which we have to calculate the monomial A in order to find the targeted quantities up to order n. The maximal orders of monomials can be determined from their minimal orders and the set of flow equations in an iterative way starting from the condition [KDU12]

$$O_{\max}(A_i) = \begin{cases} n & \text{if } A_i \text{ is targeted,} \\ 0 & \text{otherwise.} \end{cases} \tag{3.27}$$

For further details of the notion of the maximal order and how to determine it we refer to Ref. [KDU12] where concrete examples are provided. When the maximal orders are found, the monomials A_i with

$$O_{\max}(A_i) < O_{\min}(A_i) \tag{3.28}$$

can be completely discarded causing no effect on the targeted quantities up to order n. The contributions D_{ijk} with

$$O_{\max}(A_i) < O_{\min}(A_j) + O_{\min}(A_k) \tag{3.29}$$

are also irrelevant and can be ignored [KDU12]. In this ways, the flow equations (3.24) reduces to a unique set of differential equations which are necessary and sufficient to describe the targeted quantities up to order n.

The perturbative integration of the reduced flow equations in the limit $\ell \to \infty$ leads to a series expansion in x up to order n for the targeted quantities. This introduces a perturbative method that, in contrast to the pCUT [KU00, KSU03a], can work also for Hamiltonians whose non-perturbative part has a non-equidistant spectrum. This method, which is a generalization of the pCUT method, is called *enhanced perturbative CUT* (epCUT) [KDU12].

The numerical integration of the reduced flow equations, however, will lead to *renormalized* values for targeted quantities. This renormalization approach is called *directly evaluated epCUT* (deepCUT). Whenever the deepCUT results are presented, two facts have to be specified: (i) The order of calculations and (ii) the targeted quantities. In this way, we define a unique scheme for truncating the flow equations[1]. The deepCUT method has

[1] We estimate the minimal orders of monomials during the algebraic part of calculations. The real minimal orders are specified at the end of calculations when the flow equations are integrated. In some situations, it is possible that the minimal order of a monomial is estimated lower than its real value. This can happen due to some symmetries between different prefactors which cancel each other in the flow equations. This enlarges the set of flow equations, but will not have any effect on perturbative results. It affects, however, the deepCUT results, but within the range of accuracy of the method.

been successfully applied to the transverse field Ising model leading to reliable results for multiparticle excitation spectra and dynamical correlation functions [FU13].

3.2.3 Simplification Rules

The possibility to reduce the flow equations shows that not all the monomials appearing in the algebraic calculations have to be tracked. The terms which satisfy the condition (3.28) can safely be ignored leading to a substantive acceleration of the algorithm. Such an elimination, however, is not possible because the maximal orders are unknown during the algebraic step [KDU12].

The simplification rules (SRs) help us to find an upper bound for maximal orders of monomials during the algebraic part of the calculations [KDU12]. Such an estimate is based on the shape of the generator and on the structure of the monomials. Two kinds of SRs are introduced: *A-posteriori* and *a-priori* [KDU12]. The a-posteriori SRs are applied *after* calculating a commutator to the newly appeared monomials. It checks whether a monomial needs to be tracked or not by considering the criterion (3.28). The a-priori SRs are applied *before* a commutator is calculated. This kind of SR evaluates whether a commutator will result in any monomial which may pass the condition (3.28). The a-priori SRs prevent unnecessary commutators to be computed increasing the speed of algorithm. In practice, the a-posteriori and a-priori SRs are used together in order to reach the highest efficiency [KDU12]. In this thesis, we will just describe the SRs that we have implemented for the model under consideration. For the general aspects of SRs, we refer the reader to Ref. [KDU12].

3.2.4 Residual Off-Diagonality

In any CUT approach, there can occur some divergency in the flow equations. For the pc generator, this especially happens if the states with higher QP number lie energetically lower than the states with lower number of QPs.

The *residual off-diagonality* (ROD) is defined to measure the convergence of the flow equations. It reads

$$\mathrm{ROD}(\ell) = \sqrt{\sum_i |\eta_i(\ell)|^2}, \tag{3.30}$$

where the sum runs over all the monomials that appear in the generator. The coefficient $\eta_i(\ell)$ is the prefactor of the monomial A_i as is defined in Eq. (3.23). In the deepCUT analysis, the ROD can diverge due to the energetic overlap of different QP continua. In this case, decoupling sectors with lower number of QPs only may lead to convergence of the flow as it will be seen in the following chapters.

3.3 Few-Particle Problems

The idea in the CUT-based methods is to map a many-particle Hamiltonian to a few-particle problem by working in a suitable QP representation. At least the ground state in the final effective Hamiltonian is decoupled from higher QP sectors. Hence, the ground state coincides with the vacuum of QPs and we need to analyze the first few-QP sectors in order to calculate the low-energy excitation spectrum. We treat both fermionic and bosonic systems which contain at most four QPs. In this way, we have generalized the approach introduced in Ref. [FDU10] for bosonic problems with at most three particles.

Let us consider a general Hamiltonian of the form

$$\begin{aligned} H &= H_{0:0} + H_{1:1} + H_{2:2} + H_{3:3} + H_{4:4} \\ &\quad + (H_{2:1} + \text{h.c.}) + (H_{3:1} + \text{h.c.}) + (H_{4:1} + \text{h.c.}) \\ &\quad + (H_{3:2} + \text{h.c.}) + (H_{4:2} + \text{h.c.}) + (H_{4:3} + \text{h.c.}), \end{aligned} \tag{3.31}$$

where $H_{n:m}$ creates n and annihilates m number of QPs. We suppose that the ground state is already decoupled: There is no off-diagonal interaction linking the ground state to higher-QP states. If some additional interactions exist which act on higher QP sectors, they will be irrelevant in our analysis. Because we are going to consider a Hilbert space with at most four QPs.

3.3.1 Basis States

Because the ground state is already decoupled, it is possible to work directly in the thermodynamic limit. The excitations above the vacuum are spanned by the states with specific total momentum K, total spin S, and total magnetic number M

$$|K\rangle^{S,M} = \frac{1}{\sqrt{L}} \sum_r e^{iKr} |r\rangle^{S,M}, \tag{3.32a}$$

$$|K;d\rangle^{S,M} = \frac{1}{\sqrt{L}} \sum_r e^{iK\left(r+\frac{d}{2}\right)} |r;r+d\rangle^{S,M}, \tag{3.32b}$$

$$|K;d_1;d_2\rangle_\alpha^{S,M} = \frac{1}{\sqrt{L}} \sum_r e^{iK\left(r+\frac{2d_1+d_2}{3}\right)} |r;r+d_1;r+d_{12}\rangle_\alpha^{S,M}, \tag{3.32c}$$

$$|K;d_1;d_2;d_3\rangle_\alpha^{S,M} = \frac{1}{\sqrt{L}} \sum_r e^{iK\left(r+\frac{3d_1+2d_2+d_3}{4}\right)} |r;r+d_1;r+d_{12};r+d_{123}\rangle_\alpha^{S,M}, \tag{3.32d}$$

where d_1, d_2, and d_3 are the distances between the QPs, L is the lattice size, and the summation r runs over the lattice sites. We define $d_{12} := d_1 + d_2$ and $d_{123} := d_{12} + d_3$. The parameter α is an additional quantum number that specifies the spin configuration. It appears because there can be more than one spin configuration with specific total spin and total magnetic numbers. For instance, if all QPs are spin-1/2 fermions, there are two different spin configurations for the 3-QP states with total spin $S = \frac{1}{2}$. For the 4-QP states

with total spin $S = 0$ and $S = 1$, there are 2 and 3 different choices for the quantum number α, respectively.

In general, QPs in Eqs.(3.32) can be either fermionic or bosonic. We always deal with hardcore particles, *i.e.* $d \neq 0$.

3.3.2 Hamiltonian Matrix

The Hamiltonian matrix is constructed using the basis states (3.32) for fixed values of K, S, and M. Each element of the matrix will be labeled by the number of QPs[1], the distances between the QPs[2], and some additional quantum numbers such as α. The major step is to calculate the action of different parts of the Hamiltonian (3.31) on the 1-, 2-, 3-, and 4-QP states analytically.

The effect of $H_{1:1}$ on the 1-QP state (3.32a) is given by

$$H_{1:1}\,|K,\sigma\rangle = \sum_n \sum_\beta e^{iKn} \begin{matrix}\beta\\ \sigma\end{matrix}\left[\mathcal{C}_1^1\right]^n |K,\beta\rangle \tag{3.33}$$

with the definition

$$\begin{matrix}\beta\\ \sigma\end{matrix}\left[\mathcal{C}_1^1\right]^n = \langle r-n,\beta|\,H_{1:1}\,|r,\sigma\rangle\,. \tag{3.34}$$

If the 1-particle sector is decoupled from the remaining Hilbert space, the 1-particle dispersion $\omega(k)$ is given by

$$\omega(k) = c_0 + \sum_{n>0}^{d_{\max}} c_n \cos(nk), \tag{3.35}$$

where we have assumed $\begin{matrix}\beta\\ \sigma\end{matrix}\left[\mathcal{C}_1^1\right]^n = \delta_{\sigma\beta} c_n$ and $c_n = c_{-n}$. One can see immediately that a linear dispersion can never be captured by the relation (3.35) for $d_{\max} < \infty$.[3]

Applying $H_{1:1}$ to the 2-QP states, we obtain

$$\begin{aligned} H_{1:1}\,|K,\sigma_1;d,\sigma_2\rangle = \;& + \sum_{n>-d}\sum_{\beta_1} e^{iK\frac{n}{2}} \begin{matrix}\beta_1\\ \sigma_1\end{matrix}\left[\mathcal{C}_1^1\right]^n |K,\beta_1;+d+n,\sigma_2\rangle \\ & - \sum_{n<-d}\sum_{\beta_1} e^{iK\frac{n}{2}} \begin{matrix}\beta_1\\ \sigma_1\end{matrix}\left[\mathcal{C}_1^1\right]^n |K,\sigma_2;-d-n,\beta_1\rangle \\ & + \sum_{n<d}\sum_{\beta_2} e^{iK\frac{n}{2}} \begin{matrix}\beta_2\\ \sigma_2\end{matrix}\left[\mathcal{C}_1^1\right]^n |K,\sigma_1;+d-n,\beta_2\rangle \end{aligned}$$

[1] In the special case that there is no off-diagonal interaction between different QP sectors, the number of QPs will also be a constant of motion.

[2] The distances between the QPs have to be restricted in order to limit the size of the Hilbert space to be studied numerically.

[3] A simple example is the gapless spinon dispersion of the 1D Heisenberg model $\omega(k) = \frac{\pi}{2}\sin(k)$ which behaves linearly near the edge of BZ.

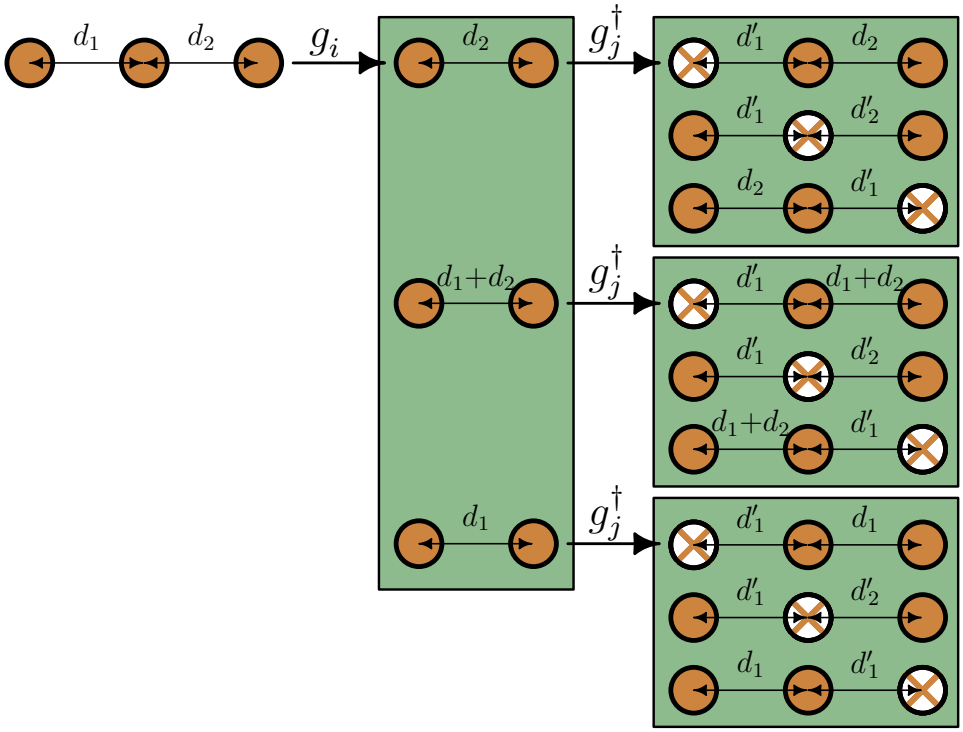

Figure 3.2: Schematic representation of the application of $H_{1:1} \equiv \sum_{i,j} g_j^\dagger g_i$ on the 3-QP state $|K; d_1; d_2\rangle$ defined in (3.32c). There are three different possibilities for the operator g_i to annihilate a QP and the operator $g_j^\dagger$ can create a QP in three distinct positions: To the left, between, and to the right of the two QPs already present. This leads to 9 different contributions.

$$-\sum_{n>d}\sum_{\beta_2} e^{iK\frac{n}{2}} {}^{\beta_2}_{\sigma_2}\left[\mathcal{C}_1^1\right]^n |K, \beta_2; -d+n, \sigma_1\rangle\,, \tag{3.36}$$

where the minus signs in front of the prefactors stem from the assumption that both QPs are fermions. These minus signs have to be omitted if the QPs are bosons. Similarly, for $H_{2:2}$ acting on the 2-QP states we have

$$H_{2:2}\,|K, \sigma_1; d, \sigma_2\rangle = -\sum_{n}\sum_{d'>0}\sum_{\beta_1\beta_2} e^{iK\left(n+\frac{d-d'}{2}\right)} {}^{\beta_1\beta_2}_{\sigma_1\sigma_2}\left[\mathcal{C}_2^2\right]_d^{nd'} |K, \beta_1; d', \beta_2\rangle\,, \tag{3.37}$$

with the definition

$${}^{\beta_1\beta_2}_{\sigma_1\sigma_2}\left[\mathcal{C}_2^2\right]_d^{nd'} = \langle r-n, \beta_1; r-n+d', \beta_2|\, H_{2:2}\,|r, \sigma_1; r+d, \sigma_2\rangle\,. \tag{3.38}$$

In order to fix the fermionic sign in the definition (3.38) it is assumed that in each monomial of $H_{2:2}$ the creation operators are placed in front of the annihilation operators and the creation and the annihilation parts are separately site-ordered[1]. Eqs. (3.36) and (3.37) are enough to describe the 2-QP sector in the absence of off-diagonal interactions. One just needs to include the appropriate Clebsch-Gordan coefficients and to set up the Hamiltonian matrix by varying the distance between QPs.

[1] With "site-ordered" we mean the operators are sorted according to their positions in the lattice.

The effect of $H_{1:1}$ and $H_{2:2}$ on the 2-QP state is evaluated in Eqs. (3.36) and (3.37). The effect of $H_{1:1}$ on the 2-QP state has 4 contributions, while it has 9 and 16 contributions for the 3- and the 4-QP states, respectively. The application of $H_{2:2}$ on the 3- and the 4-QP states leads to 9 and 36 different contributions. The numbers of contributions can be understood easily. For instance, $H_{1:1}$ has three different possibilities to annihilate a QP when it acts on a 3-QP state and it can also create a QP in three distinct positions (to the left, between, and to the right of the two QPs already present) leading to 9 contributions. The process is schematically shown in Fig. 3.2.

The full expressions for the action of different parts of the Hamiltonian (3.31) on the states (3.32) are calculated and reported in Appendix A. These expressions are general and can be used for all hardcore fermionic or bosonic problems. However, one has to omit all the fermionic minus signs in front of the prefactors for bosonic systems. In the next two chapters, we use these relations to analyze the effective Hamiltonians derived by various generators applying the deepCUT method.

3.4 Chapter Summary

This chapter reviews some methodological aspects of the present thesis. We begin with some basic concepts of the continuous unitary transformation (CUT) approach and discuss some generators of the flow such as the Wegner generator, the particle-conserving generator, and the reduced generator. The directly evaluated enhanced perturbative CUT (deepCUT) method is considered as a renormalization technique to derive effective Hamiltonians [KDU12]. The deepCUT method introduces a systematic way of truncating the flow equations based on the powers of an expansion parameter. The final effective Hamiltonians obtained from the deepCUT are analyzed by an exact diagonalization (ED) technique which is valid in the thermodynamic limit [FDU10]. This ED is illustrated in the last section 3.3 of this chapter and it is employed in different parts of this thesis to calculate the excitation spectrum of the ionic Hubbard model.

Chapter 4

Band Insulator Limit

In this chapter, the phase transitions of the 1D IHM and its excitation spectrum in the BI phase are investigated in the vicinity of the transition point U_{c1} where the transition from BI phase to SDI phase occurs. We use the deepCUT method [KDU12] in two consecutive steps to derive simpler effective Hamiltonians which facilitate a quantitative analysis of the dynamics of the excitations.

In the first step, we employ the deepCUT method to obtain an effective Hamiltonian describing the low-energy physics of the system for $\delta \approx U \gg t$. This corresponds to eliminating doubly occupied states on even sites and empty states on odd sites. This reduces the relevant energy scale from U to t. The dimension of the local Hilbert space is also reduced from four to three.

In the next step, the resulting low-energy Hamiltonian is mapped to various effective Hamiltonians using various generators in the deepCUT method. In this step, the processes creating particle-hole pairs from the vacuum or in addition to existing fermionic excitations are eliminated. The 1-particle dispersion and the dispersion of 2-particle bound states are obtained by the deepCUT in the BI phase. In addition, we aim at improving the accuracy of the results by analyzing the effective Hamiltonians obtained from the deepCUT by using the ED techniques which is valid in the thermodynamic limit and described in the previous chapter. For the charge gap, the exciton gap, and the spin gap, we compare our results to the extrapolated DMRG results of Ref. [MMNS04].

Finally, we use a BCS-type mean-field theory to describe the phase beyond the transition point U_{c1} which is signaled by vanishing the exciton gap. We can show that the SDI phase is indeed stable for $U > U_{c1}$.

The chapter is organized as follows: In the next section 4.1, we present the results of the application of deepCUT alone. In Sect. 4.2, the results obtained by a combination of deepCUT and ED are presented. The last-but-one section 4.3 is devoted to the analysis of the effective Hamiltonian on the mean-field level. Finally, the chapter is concluded in the last section.

4.1 A Pure deepCUT Analysis

In this section, the low-lying excitation spectrum of the IHM including the 1-QP dispersion, the 2-QP continuum, and possible singlet and triplet bound states in the 2-QP channel are discussed using the deepCUT. The results for the charge gap, the exciton gap, and the spin gap are compared to the DMRG results obtained by Manmana *et. al.* [MMNS04].

4.1.1 Preliminary Considerations

To apply the deepCUT method in the BI phase of the IHM, we put the local staggered potential and the Hubbard interaction in the IHM (2.1) into the local Hamiltonian H_0 and consider the hopping term as perturbation V. The unperturbed Hamiltonian H_0 has a unique ground state only for $U < \delta$. The energy gap for inserting a single fermion takes the value $\delta - U$ so that the dimensionless expansion parameter $t/(\delta - U)$ appears in the series expansion. In the limit $U \to \delta$, any purely perturbative analysis breaks down. Below, however, we will show that in the deepCUT approach the on-site energy is renormalized to larger values so that the BI phase is stabilized beyond $U = \delta$ and one can obtain H_{eff} for $U > \delta$ as well.

In the ground state of H_0 all odd sites are occupied and all even sites are empty. An electron hop from an odd site to an even site excites the system, see Fig. 4.1. In order to make the fermionic vacuum the ground state of H_0, we apply an electron-hole transformation to the odd sites. To be specific, we define

$$c_{i,\sigma} = h^\dagger_{i,\sigma}. \tag{4.1}$$

Due to this transformation the spin operators on odd sites change

$$S^z_i = \sum_\sigma \sigma c^\dagger_{i,\sigma} c_{i,\sigma} = -\sum_\sigma \sigma h^\dagger_{i,\sigma} h_{i,\sigma} := -\tilde{S}^z_i, \tag{4.2a}$$

$$S^+_i = c^\dagger_{i,\uparrow} c_{i,\downarrow} = -h^\dagger_{i,\downarrow} h_{i,\uparrow} := -\tilde{S}^-_i, \tag{4.2b}$$

$$S^-_i = c^\dagger_{i,\downarrow} c_{i,\uparrow} = -h^\dagger_{i,\uparrow} h_{i,\downarrow} := -\tilde{S}^+_i, \tag{4.2c}$$

and the spin operators on even sites remain unchanged. Hence the spin states that include a mixture of electrons and holes are different from the usual definitions. For instance, the singlet state of an electron-hole pair on adjacent sites reads

$$|\mathrm{e}-\mathrm{h}\rangle^{S=0} = \frac{1}{\sqrt{2}}(|\uparrow\uparrow\rangle + |\downarrow\downarrow\rangle), \tag{4.3}$$

where on an even site the arrow refers to the spin of an electron and on an odd site it refers to the spin of a hole. This point must be kept in mind in the considerations of this chapter. Although the electron-hole transformation (4.1) causes some inadequacies, it allows us to make our simplification rules spin-dependent increasing the efficiency of the deepCUT algorithm.

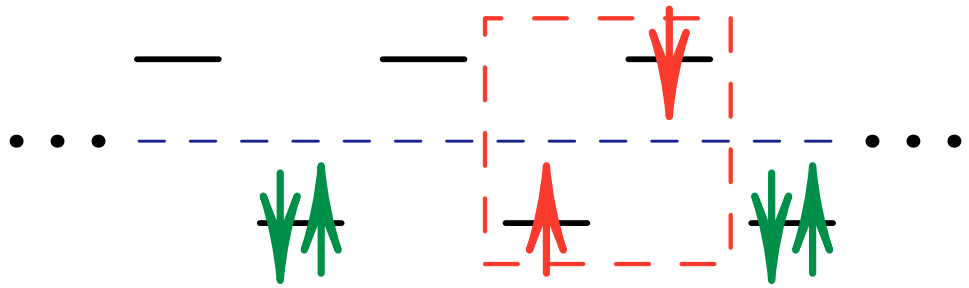

Figure 4.1: Schematic representation of excitations of the ionic Hubbard model in the band insulator phase. In the absence of hopping terms, the ground state for $U < \delta$ is characterized by occupied odd sites and empty even sites. A pair of excitations appears when an electron hops from an odd to an even site.

In order to unify all electron and hole operators, we define the fermionic operator

$$f_{i,\sigma} = \begin{cases} c_{i,\sigma} & \text{for } i \in \text{even} \\ h_{i,\sigma} & \text{for } i \in \text{odd} \end{cases}. \tag{4.4}$$

According to these definitions the Hamiltonian (2.1) reads

$$\begin{aligned} H = \frac{U-2\delta}{4}\sum_i \mathbb{1} \;&+\; \frac{\delta - U}{2}\sum_{i,\sigma} f^\dagger_{i,\sigma} f_{i,\sigma} \\ &+\; U\sum_i f^\dagger_{i,\uparrow} f^\dagger_{i,\downarrow} f_{i,\downarrow} f_{i,\uparrow} \\ &+\; t\sum_{i,\sigma} (-1)^i (f^\dagger_{i,\sigma} f^\dagger_{i+1,\sigma} + \text{h.c.}), \end{aligned} \tag{4.5}$$

it still has two sites per unit cell as the original Hamiltonian (2.1).

It is possible to restore full translational symmetry by applying a suitable local transformation on the fermionic operators

$$f^\dagger_{j,\sigma} \longrightarrow e^{-i\frac{\pi}{4}} e^{i\frac{\pi}{2}j} f^\dagger_{j,\sigma}. \tag{4.6}$$

This transformation leaves the first three terms in Eq. (4.5) unchanged and eliminates the prefactor $(-1)^i$ from the last term. Thereby, we reach

$$\begin{aligned} H = \frac{U-2\delta}{4}\sum_i \mathbb{1} \;&+\; \frac{\delta - U}{2}\sum_{i,\sigma} f^\dagger_{i,\sigma} f_{i,\sigma} \\ &+\; U\sum_i f^\dagger_{i,\uparrow} f^\dagger_{i,\downarrow} f_{i,\downarrow} f_{i,\uparrow} \\ &+\; t\sum_{i,\sigma} (f^\dagger_{i,\sigma} f^\dagger_{i+1,\sigma} + \text{h.c.}). \end{aligned} \tag{4.7}$$

The last term of this Hamiltonian is a Bogoliubov term which creates and annihilates a pair of QPs (originally an electron and a hole) with total spin *zero* on neighboring sites. In the rest of this chapter, the deepCUT method will be applied to this Hamiltonian.

The conservation of the original *electron* number in the representation (4.7) is not manifest. Thus we write down the operator of the total electron number $\widehat{N}$ in terms of f-operators

$$\widehat{N} := \sum_{i,\sigma} c^\dagger_{i,\sigma} c_{i,\sigma} = L + \sum_{i,\sigma} (-1)^i f^\dagger_{i,\sigma} f_{i,\sigma}, \tag{4.8}$$

where L is the number of sites in the chain. The difference between the number of QPs on even sites and on odd sites is a constant of motion. Thus the QPs are always created or annihilated in pairs with an *odd* distance between them.

4.1.2 Low-Energy Effective Hamiltonian

The interesting physics of the IHM happens at large values of the Hubbard interaction U approaching the first transition at U_{c1}. We focus on the case $U, \delta \gg t$ where the states with finite number of double occupancies (DOs) in the Hamiltonian (4.7) lie very high in energy. Thus the low-energy physics of the Hamiltonian (4.7) is governed by the Hilbert subspace without DOs. But the subspaces with and without DOs are linked by the Bogoliubov term.

In a first step, we decouple the low- and the high-energy parts of the Hilbert space. The same idea was first realized by Stein perturbatively for the Hubbard model on the square lattice [Ste97]. Extended calculations using self-similar CUTs (sCUT) were carried out at and away from half-filling [RMHU04, HDU10] to investigate the range of validity of the mapping from the Hubbard model to the t-J model. High-order perturbative calculations for the Hubbard model on the triangular lattice at half-filling have been performed by Yang and co-workers [YLMS10].

In the fermionic representation (4.7) of the IHM it is not evident how many DOs are created or annihilated by a term because this depends on the state to which the term is applied. Thus, we introduce a representation (Hubbard operators [Hub64]) of hard-core particles defined by

$$g^\dagger_{i,\sigma} := |\sigma\rangle_{i\,i}\langle 0| = (1 - n_{i,\bar{\sigma}}) f^\dagger_{i,\sigma} \tag{4.9a}$$

$$g^\dagger_{i,d} := |\uparrow\downarrow\rangle_{i\,i}\langle 0| = f^\dagger_{i,\uparrow} f^\dagger_{i,\downarrow} \tag{4.9b}$$

where $\bar{\sigma} = -\sigma$. The fermionic hard-core operator $g^\dagger_{i,\sigma}$ creates a fermion with spin σ at site i from the vacuum and the bosonic operator $g^\dagger_{i,d}$ creates a DO at site i from the vacuum. They obey the hard-core (anti-)commutation relation

$$\left[g_{i,\alpha}, g^\dagger_{j,\beta} \right]_\pm = \delta_{i,j} \left(\delta_{\alpha,\beta} \pm g^\dagger_{i,\beta} g_{i,\alpha} - \delta_{\alpha,\beta} \sum_{\gamma=\uparrow,\downarrow,d} g^\dagger_{i,\gamma} g_{j,\gamma} \right) \tag{4.10}$$

where the anticommutation $[\ ,\ ]_+$ is to be used if both operators are fermionic, otherwise the commutation $[\ ,\ ]_-$ is to be used. The above representation can be reversed to express the f-operators in terms of the g-operators

$$f^\dagger_{i,\sigma} = g^\dagger_{i,\sigma} + \mathrm{sign}(\sigma) g^\dagger_{i,d}\ g_{i,\bar{\sigma}}. \tag{4.11}$$

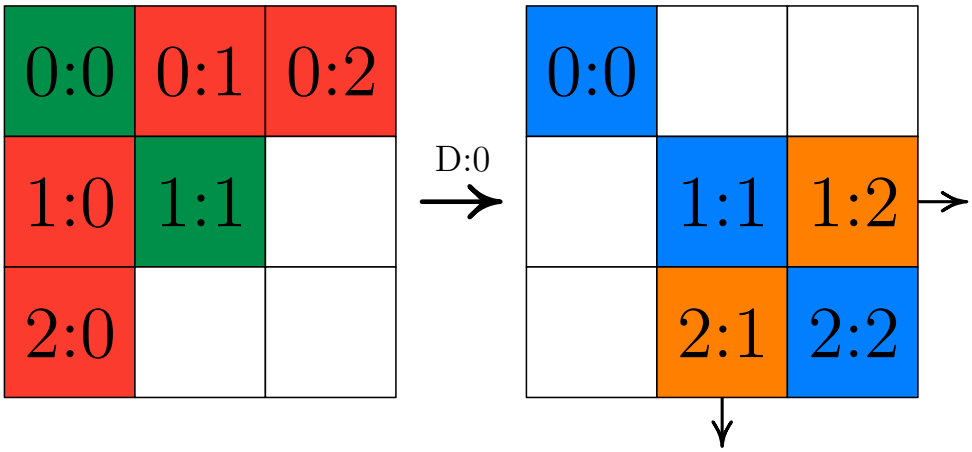

Figure 4.2: Schematic representation of the application of the generator $D:0$ to the initial Hamiltonian (4.12). Each part $H_{i:j}$ of the Hamiltonian is depicted by a block; the notation $i:j$ stands for the number of DOs which is first annihilated (j) and then created (i). The blank blocks indicate the absence of the correspond interaction in the Hamiltonian. In the final effective Hamiltonian the sector with zero number of DOs is decoupled and the coefficients in other blocks are renormalized as indicated by the change of color.

The IHM (4.7) in terms of the g-operators can be split into different parts which create and annihilate a specific number of DOs. Explicitly one has

$$H = H_{0:0} + H_{1:1} + H_{1:0} + H_{0:1} + H_{2:0} + H_{0:2}, \tag{4.12}$$

where $H_{i:j}$ creates i and annihilates j DOs. These parts are given by

$$H_{0:0} = \frac{U-2\delta}{4}\sum_i \mathbb{1} + \frac{\delta-U}{2}\sum_{i,\sigma} g^\dagger_{i,\sigma} g_{i,\sigma} + t\sum_{i,\sigma}(g^\dagger_{i,\sigma} g^\dagger_{i+1,\sigma} + \text{h.c.}), \tag{4.13a}$$

$$H_{1:1} = \delta\sum_i g^\dagger_{i,d} g_{i,d}, \tag{4.13b}$$

$$H_{1:0} = t\sum_{i,\sigma} \text{sign}(\sigma)(g^\dagger_{i,d} g_{i,\bar{\sigma}} g^\dagger_{i+1,\sigma} + g^\dagger_{i,\sigma} g^\dagger_{i+1,d} g_{i+1,\bar{\sigma}}) = (H_{0:1})^\dagger, \tag{4.13c}$$

$$H_{2:0} = t\sum_{i,\sigma} g^\dagger_{i,d} g_{i,\sigma} g^\dagger_{i+1,d} g_{i+1,\sigma} = (H_{0:2})^\dagger. \tag{4.13d}$$

These expressions indicate that for $U \approx \delta \gg t$, the low-energy physics takes place in the subspace without DOs. The reduced generator $\eta_{D:0}$ is applied to (4.12) to disentangle the subspace without any DOs from the remaining Hilbert space. The process is schematically shown in Fig. 4.2. The final low-energy effective Hamiltonian acts on a 3-dimensional local Hilbert space (no fermion present or an $\uparrow$ or $\downarrow$ fermion is present). The fermionic hard-core QPs can hop and they interact with one another. In Table 4.1, the relevant monomials A_j up to the minimal order $O_{\text{min}} \leq 2$ are given. Together with the prefactors $h_j(\infty)$ the monomials define the low-energy effective Hamiltonian after the first CUT

$$H^{\text{eff}}_{0:0} = \sum_{j=0} h_j(\infty) A_j. \tag{4.14}$$

j	A_j	$O_{\min}$
0	$\sum_i \mathbb{1}$	0
1	$\sum_{i,\sigma} g^\dagger_{i,\sigma} g_{i,\sigma}$	0
2	$\sum_{i,\sigma} \left(g^\dagger_{i,\sigma} g^\dagger_{i+1,\sigma} + \text{h.c.} \right)$	1
3	$\sum_{i,\sigma} g^\dagger_{i,\sigma} g_{i,\sigma} g^\dagger_{i+1,\sigma} g_{i+1,\sigma}$	2
4	$\sum_{i,\sigma} g^\dagger_{i,\sigma} g_{i,\sigma} g^\dagger_{i+1,\bar{\sigma}} g_{i+1,\bar{\sigma}}$	2
5	$\sum_{i,\sigma} g^\dagger_{i,\sigma} g_{i,\bar{\sigma}} g^\dagger_{i+1,\sigma} g_{i+1,\bar{\sigma}}$	2
6	$\sum_{i,\sigma} \left(g^\dagger_{i,\sigma} g^\dagger_{i+1,\bar{\sigma}} g_{i+1,\bar{\sigma}} g_{i+2,\sigma} + \text{h.c.} \right)$	2
7	$\sum_{i,\sigma} \left(g^\dagger_{i,\sigma} g^\dagger_{i+1,\sigma} g_{i+1,\bar{\sigma}} g_{i+2,\bar{\sigma}} + \text{h.c.} \right)$	2

Table 4.1: The operators A_j up to the minimal order $O_{\min} = 2$ present in the low-energy effective Hamiltonian (4.14). Note that we combined certain monomials which must have the same prefactor due to symmetries or hermitian conjugation.

In order to verify the convergence of the results, the prefactors of the monomials A_1, A_2, and A_3 are plotted versus U in panels (a), (b), and (c) of Fig. 4.3, respectively. In each panel, the results for the hopping parameters $t = 0.05\delta$ (solid line), $t = 0.10\delta$ (dashed line), and $t = 0.20\delta$ (dotted-dashed line) in three different orders 2 (green), 4 (blue), and 6 (red) are depicted. For $t = 0.05\delta$ the results in the different orders agree nicely for all the three prefactors. Fig. 4.3 also shows that for $t = 0.10\delta$, order 4 and 6 still coincide. But for $t = 0.20\delta$ we need to go to higher orders to obtain the effective Hamiltonian quantitatively. In the rest of this chapter, we fix the order of deepCUT in this first step to 4 in the hopping parameter t. This appears to be sufficient as long as we focus on low values of t.

The underlying idea to eliminate processes changing the number of DOs is similar to the one used in the well-known derivation of the t-J model from the Hubbard model [HL67, CSO77, Hir85, Faz99]. We stress that the obtained effective Hamiltonian here is a *renormalized* one and that it can be *systematically* improved by including higher orders in t/δ, see also Refs. [RMHU04, HDU10, YLMS10].

In Ref. [TNB09], Tincani *et al.* investigated the IHM by restricting the local Hilbert space to the three states without DOs. They deal directly with the Hamiltonian (4.13a) omitting the other processes completely. Their findings for the transition points tend towards the results of the IHM in the limit $U, \delta \gg t$ [TNB09]. In chapter 5, we will restrict the Hilbert space in the same way and use the dimer limit as the starting point in the deepCUT to study the excitation spectrum of the IHM in different phases.

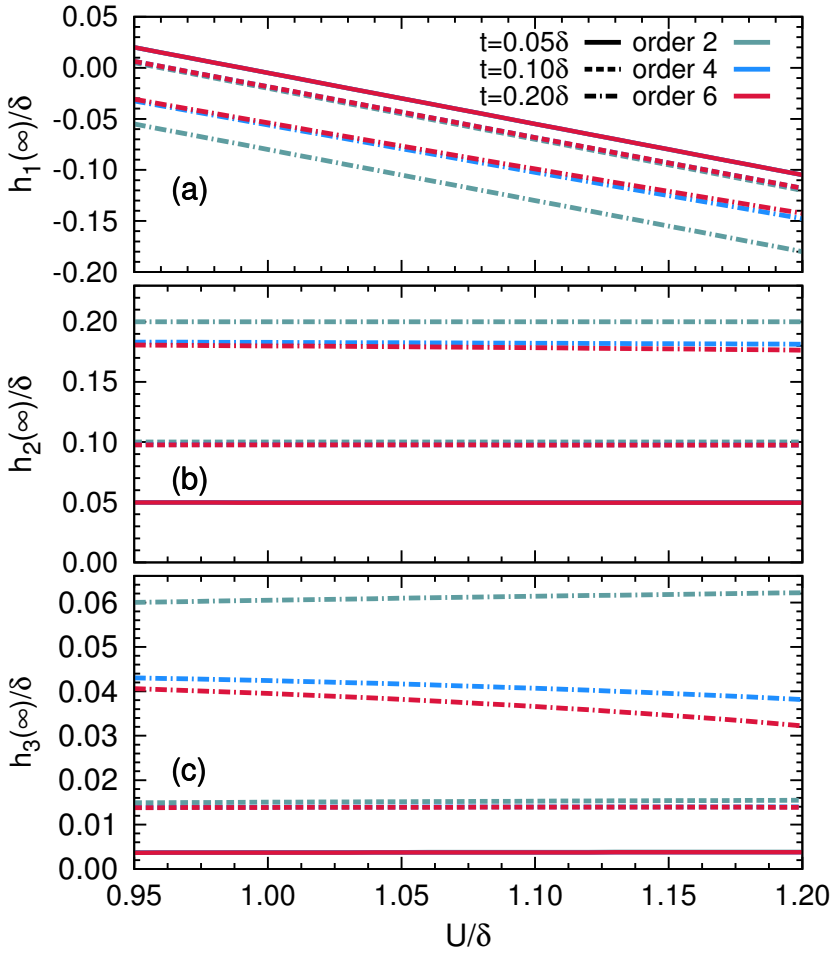

Figure 4.3: The coefficiens $h_1(\infty)/\delta$ (a), $h_2(\infty)/\delta$ (b), and $h_3(\infty)/\delta$ (c) defined in Eq. (4.14) plotted versus the Hubbard interaction U/δ. The results are obtained by applying the $D:0$ generator to the Hamiltonian (4.13). Each panel includes the results for the hopping parameters $t = 0.05\delta$ (solid line), $t = 0.10\delta$ (dashed line), and $t = 0.20\delta$ (dotted-dashed line) in three diferent orders 2 (green), 4 (blue), and 6 (red).

4.1.3 The 1-Quasiparticle Sector

The effective Hamiltonian derived in the previous subsection is still complicated. It includes various interactions between different QP sectors. These QPs are created and annihilated by the g-operators of spin $\uparrow$ and $\downarrow$. To determine the dispersion of a single quasiparticle (1QP), we need to decouple at least the zero- and 1-QP sectors from the sectors with more QPs. The reduced generator $\eta_{g:1}$ is required for this goal. Various symmetries and simplification rules are used in order to decrease the runtime and the memory requirement in the deepCUT algorithm so that the high orders can be reached.

We use the symmetries of reflection, spin flip, and the self-adjointness of the Hamiltonian to reduce the number of representative terms by about a factor 8. The various simplification rules we use are analogous to those introduced in the first paper on deepCUT [KDU12]. In addition, we exploit the fact that the Bogoliubov term in the low-energy effec-

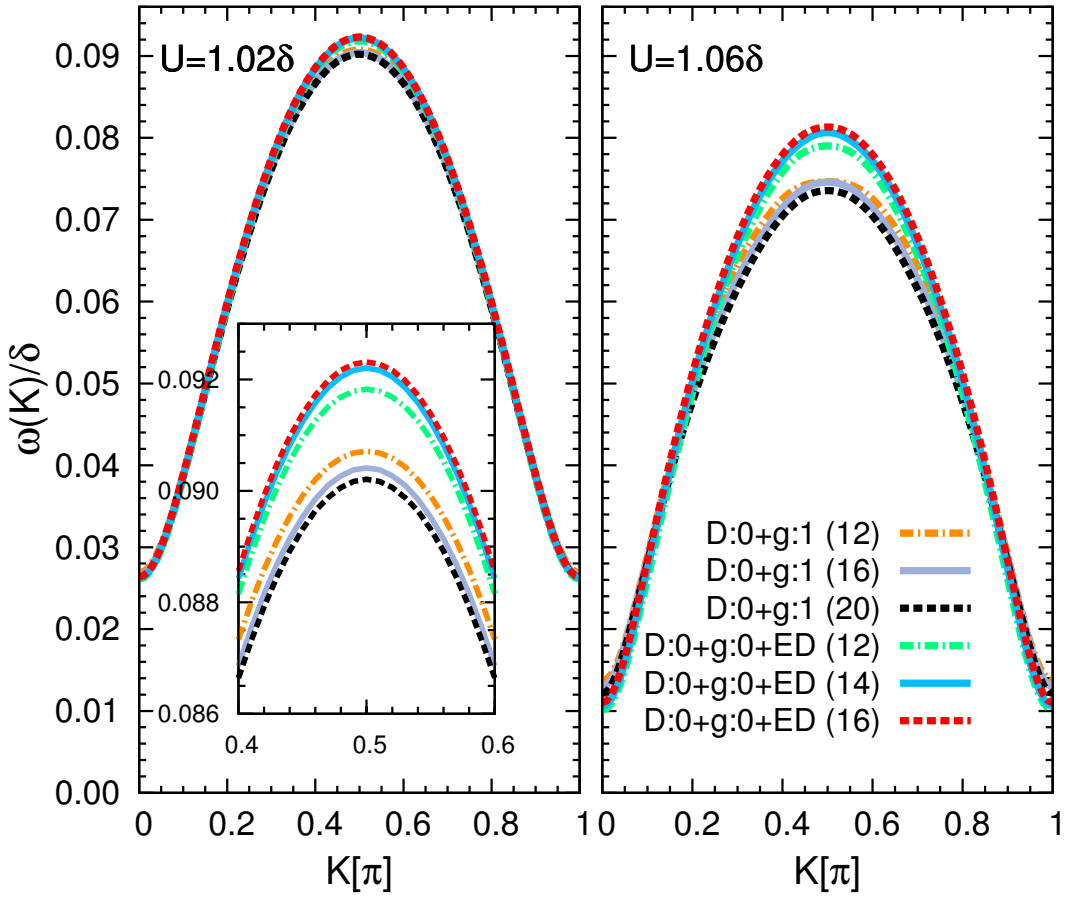

Figure 4.4: The 1-QP dispersion of the IHM for $t = 0.05\delta$ and $U = 1.02\delta$ (left panel) and $U = 1.06\delta$ (right panel). The 1-QP dispersion is obtained by a successive application of the generators $D:0$ and $g:1$, denoted by $D:0+g:1$. The order in $D:0$ step is fixed to 4 and the step $g:1$ is realized in order 12 (dotted-dashed line), 16 (solid line), and 20 (dashed line). The deviations between different orders are maximum close to $K = \frac{\pi}{2}$. In addition, the dispersion resulting from the combination of the deepCUT with ED, denoted $D:0+g:0+\mathrm{ED}$, see section 4.2, is depicted. The largest deviation between the two approaches occurs around $K = \frac{\pi}{2}$, i.e., at the maximum value of the dispersion.

tive Hamiltonian (4.14) creates and annihilates two QPs with the same spin. This allows us to make the simplification rules spin-dependent. For details about the implementation of the simplification rules we refer the reader to the Appendix B.1. In this way, we were able to reach order 20 in the hopping parameter t in the calculations for the 1QP dispersion. Up to this order no divergence in the numeric evaluation of the flow equations occurred in the investigated parameter regime.

The final effective Hamiltonian is translationally invariant so that the 1-QP sector is diagonalized by a Fourier transformation. The resulting 1-QP dispersion reads

$$\omega(k) = h_0 + 2\sum_{d=1}^{n} h_{2n}\cos(2nk) \tag{4.15}$$

where the prefactors h_d is the hopping element from site i to $i \pm d$. Only hopping elements

over *even* distances occur because odd hops would violate the conservation of the total particle number of original particles, see Eq. (4.8). All bilinear terms acting on odd distances are of Bogoliubov type.

The 1-QP dispersion (4.15) resulting from the consecutive application of the generators $D:0$ and $g:1$, denoted by $D:0+g:1$, is depicted in Fig. 4.4. The shorthand $D:0+g:1$ stands for a first application by applying the generator $\eta_{D:0}$. Then, the resulting effective Hamiltonian is block-diagonalized by applying the generator $\eta_{g:1}$. The left panel of Fig. 4.4 is for $U = 1.02\delta$ and the right panel is for $U = 1.06\delta$. The hopping prefactor t in Eq. (4.7) is fixed to 0.05δ. The 1-QP dispersion is presented for order 12 (dotted-dashed line), 16 (solid line), and 20 (dashed line) in the hopping prefactor t.

The left panel in Fig. 4.4 shows that the results of different orders 12, 16, and 20 coincide accurately in the whole range of momenta $0 \leq K < \pi$ demonstrating a good convergence of the deepCUT method. The largest deviation occurs around the momentum $K = \frac{\pi}{2}$ where the dispersion is maximum as shown in the inset.

The convergence for increasing order is worse at $U = 1.06\delta$ because we approach the transition point, $U_{c1} \approx 1.07\delta$. Again, the largest deviation between different orders occurs near the total momentum $K = \frac{\pi}{2}$. The 1-QP dispersion $\omega(k)$ shows a tendency to decrease on increasing order of calculations.

The charge gap Δ_c is defined as the energy necessary to add an electron plus the energy for taking an electron from the system, see Eq. (2.2). For our electron-hole symmetric Hamiltonian (2.1), it is twice the minimum of the 1-QP dispersion $\Delta_c = 2\omega_{\min}$.

The charge gap for different orders of the hopping prefactor t is plotted in the left panel of Fig. 4.5 as function of the Hubbard interaction U. The deepCUT results extrapolated by a linear fit in 1/order to infinite order are also depicted. The DMRG results, rescaled to the present units, are shown for comparison [MMNS04]. Data is given up to $U = 1.08\delta$ because around this point the phase transition to the SDI takes place (see next subsection) and the QP picture breaks down. Fig. 4.5 shows that the results of the deepCUT at high orders coincide very well for $U < 1.00\delta$. For $U > 1.00\delta$, especially close to the transition point, the different orders deviate indicating a poorer convergence. The difference between the extrapolated deepCUT results and the DMRG results is about 0.002δ. We draw the reader's attention to the accuracy of such data. The energy scale of the initial model before the renormalizing unitary transformations is $U + \delta \approx 2\delta$ so that the transformations are still precise on energy scales reduced by three orders of magnitude.

In the right panel of Fig. 4.5, the charge gap versus the inverse order is displayed for various values of U. The charge gap decreases on increasing order. The deepCUT results are extrapolated to infinite order by a linear fit to the last four points. This plot illustrates how the deepCUT calculations converge as function of the order in the hopping t. The deepCUT method as used in the present work is a renormalizing approach based on a truncation in real space. This means that processes are tracked only up to a certain range in real space. This range is determined by the order of the calculations interpreted as the maximum number of hops on the lattice. Thus it is clear that the approach as presented

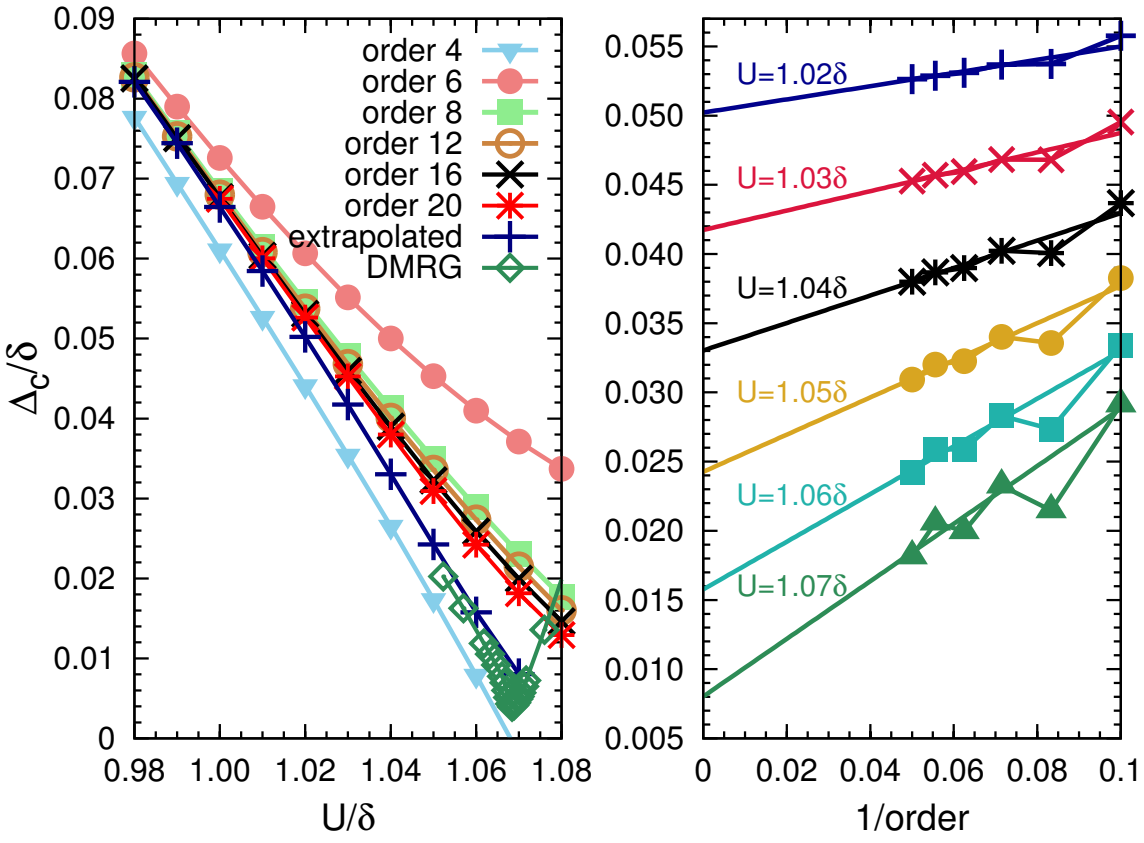

Figure 4.5: The charge gap of the ionic Hubbard model for the hopping parameter $t = 0.05\delta$. Left panel: The charge gap as a function of U/δ in various orders. The deepCUT results extrapolated to infinite order are also depicted. The extrapolated DMRG results [MMNS04] are shown for comparison. The deviation in our analysis at finite orders becomes large close to the transition point, $U_{c1} = 1.07\delta$. The difference between extrapolated deepCUT results and the extrapolated DMRG results is about 0.002δ. Right panel: The charge gap versus the inverse order for various values of the Hubbard interaction U. The deepCUT results are extrapolated to infinite order by a linear fit to the last four points in 1/order.

here runs into difficulties upon approaching continuous phase transitions where long-range processes become essential due to diverging correlation length.

4.1.4 The 2-Quasiparticle Sector

In the framework of CUTs, the treatment of sectors with higher number of QPs is also possible [KU00, WGN+01, KSGU01, KSU03b, SU05, FDU10, KDU12]. The 2-QP sector can be decoupled by using the reduced generator $\eta_{g:2}$. This generator yields an effective Hamiltonian that can be diagonalized for each combination of the total momentum K, total spin S, and total magnetic quantum number M. The 2-QP states with fixed K, S, and M is given in Eq. (3.32b). The distance d between the two QPs takes only positive values because the two constituting fermions are indistinguishable after the particle-hole transformation.

The Hamiltonian matrix in the 2-QP sector is composed of three different submatrices referring to different total charge. Both QPs can be original electrons, or holes, or one is an electron and the other a hole. Here we refer to the fermions before the particle-hole transformations. If the 2-QP state (3.32b) contains only odd distances d it consists of an electron and a hole. If the 2-QP state is made of two original electrons or two holes, the distances between them are even, cf. Eq. (4.8). Here we focus on the case of 2-QP states with one electron and one hole and discuss the possible triplet and singlet bound states.

The sector with two holes (or two electrons) is also very interesting in the context of superconductivity. A recent investigation of the IHM including NNN hopping terms on the honeycomb lattice found evidence for superconducting behavior upon hole doping [WI13]. A dynamic mean-field theory study of the model also indicates an interesting half-metallic behavior upon doping away from half-filling [GKR14]. But these issues are beyond the scope of the present thesis.

The Hamiltonian matrix can be constructed by applying the Hamiltonian parts $H_{1:1}$ and $H_{2:2}$ to the state $|K, \sigma_1; d, \sigma_2\rangle$. These actions are already computed and reported in Eqs. (3.36) and (3.37). The diagonalization of the Hamiltonian matrix in the singlet and the triplet channels provides information of the eigenvalues in the 2-QP sector.

The low-lying excitation spectra for $U = 1.02\delta$ and $U = 1.06\delta$ are depicted in the left and in the right panel of Fig. 4.6, respectively. The hopping t is fixed to 0.05δ. The order of the second CUT is 12. We cannot go beyond this order because the flow equations for the 2-QP sector do not converge in higher orders. As can be seen in the right panel, the 2-QP continuum lies within the 3-QP continuum. The lower edge of the 4-QP continuum (not shown) lies also close in energy to the lower edge of 2-QP continuum. This large overlap between continua of different number of QPs is the major reason of divergence of the flow equations [FDU10].

For both values of U in Fig. 4.6 there are two singlet and one triplet bound states. The singlet bound modes occur only near the total momentum $K = \pi$ and around $K = \frac{\pi}{2}$. The triplet bound mode becomes more and more symmetric about $K = \frac{\pi}{2}$ as the Hubbard interaction U is increased and approaches the transition point $U_{c1} \approx 1.07\delta$. We attribute the wiggling of the singlet mode for $U = 1.06\delta$ around the total momentum $K = \frac{\pi}{2}$ to the truncation of the flow equations. For $U = 1.06\delta$, the lowest excited state is the singlet bound state that appears at the total momentum $K = \pi$. This mode becomes soft, i.e, its energy vanishes, upon increasing the Hubbard interaction further indicating the first phase transition at U_{c1} from the BI to the SDI phase.

In our formalism, the exciton gap (2.3) is given by the lowest eigenvalue of the singlet channel of the 2-QP sector. The exciton gap is plotted versus the interaction U in Fig. 4.7 for different orders. Due to the divergence of the flow equations no values are reported in order 10 for $U > 1.04\delta$. For the same reason, orders higher than 12 were not accessible. The extrapolated DMRG results extracted from Ref. [MMNS04] and rescaled to the present units are also shown. The deepCUT results at high orders are very close to the DMRG results. The DMRG prediction of the transition point is 1.069δ. In our analysis in order 12 the exciton gap vanishes at $U_c = 1.072\delta$. The deepCUT results for the exciton gap

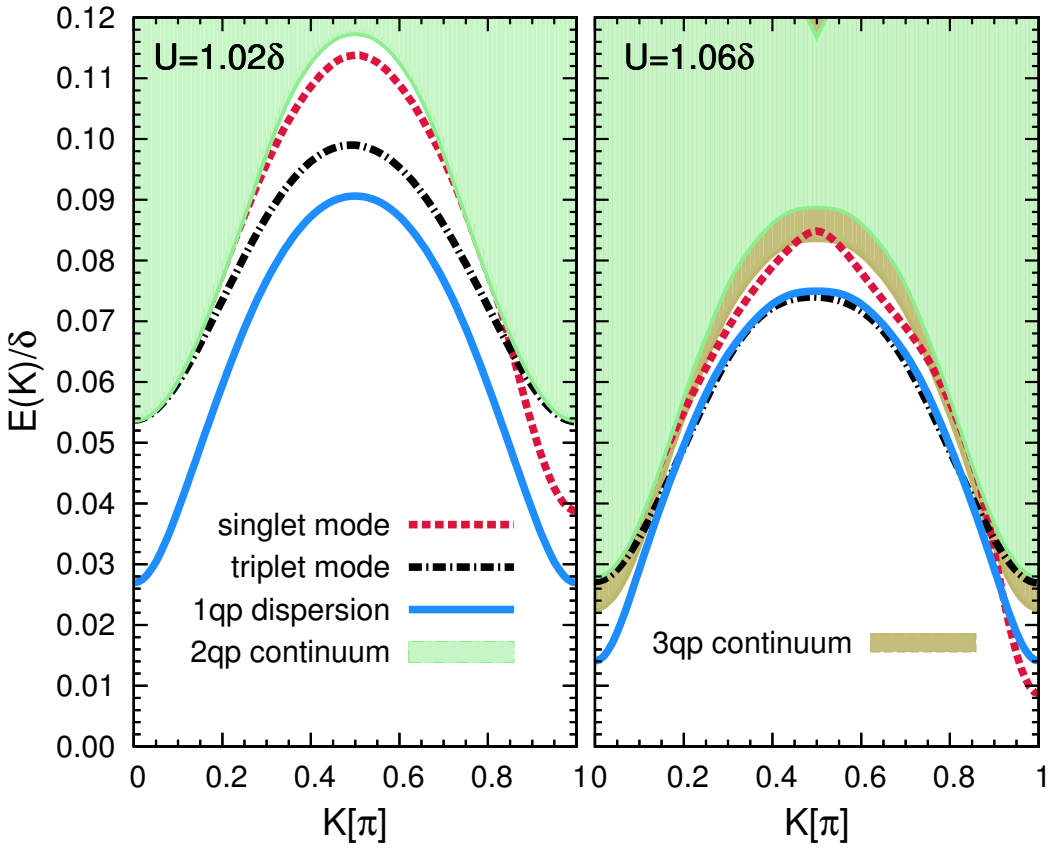

Figure 4.6: Low-lying excitation spectrum including 1-quasiparticle dispersion (solid line), 2-quasiparticle and 3-quasiparticle continuum (colored regions), singlet (dashed line) and triplet (dotted-dashed line) bound states. The results are obtained by consecutive application of the generators $D:0$ and $g:2$. The order of the transformation for $D:0$ is 4 and for $g:2$ it is 12 which is the highest converging order. The hopping element is $t = 0.05\delta$. The Hubbard interaction U is fixed to 1.02δ for the left panel and to $U = 1.06\delta$ for the right panel. There are two singlet bound states near the total momentum $K = \pi$ and around $K = \frac{\pi}{2}$. The triplet bound state is almost symmetric around $K = \frac{\pi}{2}$ and exists in the whole BZ. For $U = 1.06\delta$, the 2-quasiparticle continuum lies completely within the 3-quasiparticle continuum.

Δ_e converge better upon increasing order than the deepCUT results for the charge gap Δ_c shown in Fig. 4.5. We attribute this to the larger separation in energy from the closest continuum.

We studied the energy difference between the spin gap and the charge gap. This equals the binding energy of the triplet bound state at total momentum $K = \pi$, see Fig. 4.6. While this binding energy is finite in any finite order, it shows a tendency to vanish for $U \leq U_{c1}$ upon increasing the order of calculations. The difference between the charge gap and the spin gap is plotted in Fig. 4.8 versus the Hubbard interaction U. The hopping is fixed to $t = 0.05\delta$ in this figure. These findings are to be compared to previous DMRG data. Takada and Kido extrapolated the DMRG results to infinite system size and deduced that the spin gap and charge gap become different before the first transition point U_{c1} [TK01]. But, the equality of spin and charge gaps up to the first transition point is supported by other

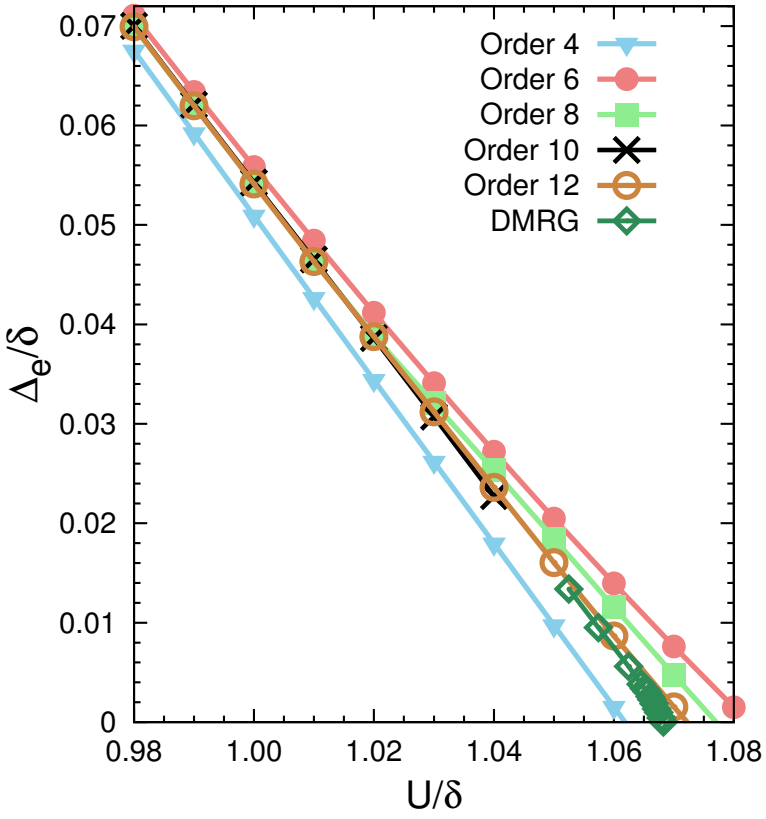

Figure 4.7: The exciton (or singlet) gap Δ_e versus the Hubbard interaction in various orders. The hopping is fixed to $t = 0.05\delta$. The exciton gap becomes soft at $U_{c1} = 1.072\delta$ in order 12. For comparison, the DMRG prediction of the first transition is $U_{c1} = 1.069\delta$ [MMNS04].

extrapolated DMRG calculations [MMNS04, LQX+03, KSJB03].

In the deepCUT approach realized in real space, the range of processes taken into account is proportional to the order of the calculation. Thus we expect the deepCUT method to provide accurate results as long as the order is larger than the correlation length ξ in units of the lattice spacing of the system. The correlation length can be estimated as [SA93, OAAY01]

$$\xi \approx \frac{v}{\Delta}, \tag{4.16}$$

where v is the velocity for vanishing gap and Δ is the gap present in the system. The relation (4.16) stems from the assumption that the low-energy physics of the model fulfills an (approximate) Lorentzian symmetry.

In the IHM, the exciton gap is the smallest gap and hence we set $\Delta = \Delta_e$. The fermionic velocity can be obtained by fitting $\omega(k) = v \sin(k)$ to the 1-QP dispersion. We find $\xi = \frac{0.09}{0.038} \approx 2.4$ for $U = 1.02\delta$, $\xi = \frac{0.07}{0.008} \approx 8.8$ for $U = 1.06\delta$, and $\xi = \frac{0.07}{0.0015} \approx 47$ for $U = 1.07\delta$. The rapid increase of ξ on approaching the transition point U_{c1} reflects the vanishing exciton gap Δ_e. This implies that the deepCUT approach parametrized in real space naturally becomes inaccurate on approaching U_{c1}.

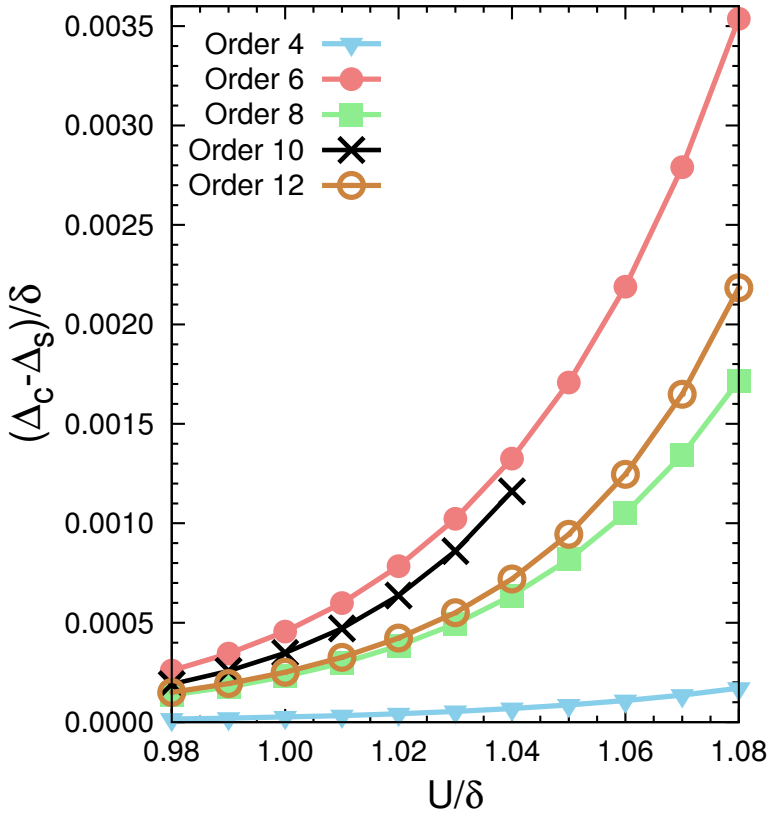

Figure 4.8: The energy difference between the charge gap Δ_c and the spin gap Δ_s versus the Hubbard interaction U in various orders. The hopping parameter is fixed to $t = 0.05\delta$.

4.2 Thermodynamic Exact Diagonalization

The deepCUT results close to the transition point are not quantitative, especially for the charge gap for reasons given above. In this section, we aim at improving the results by following the route used previously in Ref. [FDU10]. The goal of the deepCUT is chosen less ambitious, i.e., less terms are rotated away. This makes the deepCUT step less prone to inaccuracies and convergence can be achieved more easily. But the disadvantage is that the resulting effective Hamiltonian is not yet diagonal or block-diagonal so that the subsequent analysis becomes more demanding. Here we will employ exact diagonalization in restricted subspaces for this purpose.

4.2.1 Construction of the Hamiltonian Matrix

In order to take into account processes of longer range for the important *excited states*, we only decouple the ground state from the subspaces with finite number of QPs. This is achieved by applying the reduced generator $g : 0$. This generator keeps interactions and transitions between different excited states. Because the system under study is fermionic, there are only terms in the Hamiltonian with even number of fermionic operators. Thus

there is no process linking one QP and two QPs: $H_{2:1} = 0$. Therefore, the major off-diagonal interaction for 1-QP states is $H_{3:1} + H_{1:3}$ and for 2-QP states $H_{4:2} + H_{2:4}$ in addition.

After applying the generator $g:0$, the effective Hamiltonian has the following structure

$$\begin{aligned} H_{\text{eff}} &= H_{0:0} + H_{1:1} + H_{2:2} + H_{3:3} + H_{4:4} \\ &\quad + (H_{3:1} + \text{h.c.}) + (H_{4:2} + \text{h.c.}) \\ &\quad + \text{less important terms}, \end{aligned} \tag{4.17}$$

where the less important terms include the parts which involve states with more than four QPs. These interactions have much less effect than $H_{3:1}$ and $H_{4:2}$ on the low-energy spectrum given by the eigenvalues in the 1-QP and in the two QP sectors.

The effect of off-diagonal interactions between 1- and 3-QP states and between 2- and 4-QP states can be considered by restricting the Hilbert space to 4-QP states and performing an ED within this restricted Hilbert space. The effect of the Hamiltonian is stored in two separate matrices, one for the states that are built from one and three QPs and the other for the states built from two and four QPs. We stress that also states with four QPs have to be considered to be able to address modifications in the 2-QP spectrum.

Because the ground state is decoupled in the deepCUT step, we can work directly in the thermodynamic limit by introducing the states (3.32). The Hamiltonian matrix is constructed for each fixed set of total momentum K, total spin S, and total magnetic number M by restricting the distances between QPs as discussed in the previous chapter. The 2-, 3-, and 4-QP states with total spin $S = 0$ and $S = 1$, total magnetic number $M = 0$ and $M = 1$, and the additional label α are given in the Appendix C.1.

The idea that we have applied here is similar to what had been introduced in Ref. [FDU10] to describe QP decay with CUT. The main difference is that we have to take care of the fermionic minus sign and to consider also the states with four QPs. Including the 4-QP states not only leads to large analytic expressions, but also limits the maximum relative distances that can be treated numerically. For the following results, the Hamiltonian matrix has been constructed with maximum distances $d_1^{\max} = d_2^{\max} = d_3^{\max} = 24$.

4.2.2 Low-lying Excitation Spectrum

The charge and exciton gaps obtained by the combination of deepCUT and ED are depicted in Fig. 4.9. We denote this approach by $D:0 + g:0 + \text{ED}$ which means that the effective Hamiltonian is derived by the consecutive application of the generators $\eta_{D:0}$ and $\eta_{g:0}$. Then this effective Hamiltonian is analyzed by ED method as described above. Due to the restriction of the Hilbert space in the ED, its results *overestimate* the eigen values of the *effective Hamiltonian*, i.e., they provide upper bounds to them. But note that the effective Hamiltonian has only a limited accuracy due to the truncations in the course of the deepCUT $D:0+g:0$ so that the ED results cannot be taken as rigorous upper bounds. If we, however, assume that the inaccuracies introduced in the derivation of the effective Hamiltonian are

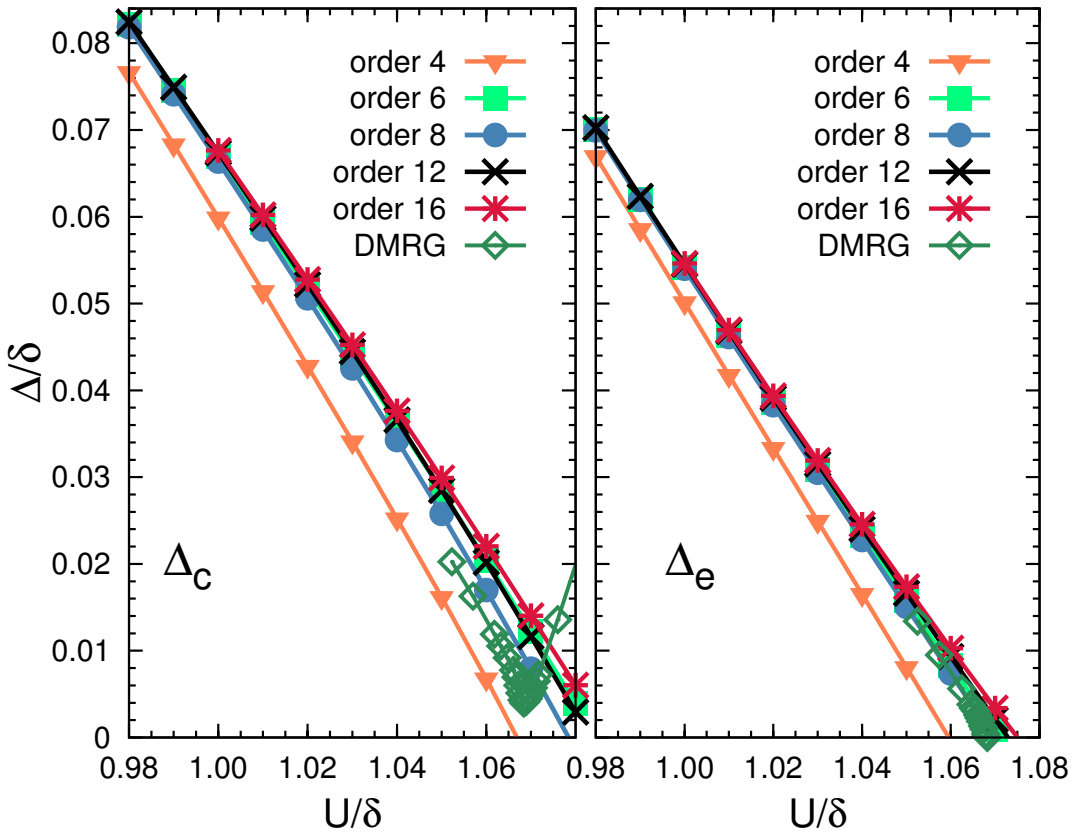

Figure 4.9: The charge gap (left panel) and the exciton gap (right panel) vs. U obtained by $D:0+g:0+$ED, see main text. The order of the $D:0$ step is 4 and $g:0$ is carried out in various orders, given in the legend. The data for the charge gap appears to be more robust in $D:0+g:0+$ED than in the pure deepCUT analysis $D:0+g:2$.

of minor importance, the ED results can be taken as an *upper* bound for the *true* excitation energies.

The left panel of Fig. 4.9 shows that the difference between the data obtained by $D:0+g:0+$ED and the DMRG results is smaller than the difference of the data of the pure application of the deepCUT to the DMRG results, cf. Fig. 4.5. For the charge gap close to the phase transition, the deviation between our results and the DMRG data is decreased from about 1% for the pure deepCUT to about 0.5% for the combination of deepCUT and ED.

In the right panel of Fig. 4.9, the exciton gap is plotted vs. the Hubbard interaction U. The results agree nicely with the DMRG results for all orders higher than 4. Inspecting the trend of the results for increasing order they appear to converge to values slightly higher than the DMRG results. We attribute this fact to the restriction of the Hilbert space in the ED treatment making it an upper bound.

The 1-QP dispersion obtained by the combination $D:0+g:0+$ED is plotted in Fig. 4.4 for the two different values of the Hubbard interaction $U = 1.02\delta$ (left panel) and $U = 1.06\delta$ (right panel). In this figure, we compare the results of pure deepCUT with the results of

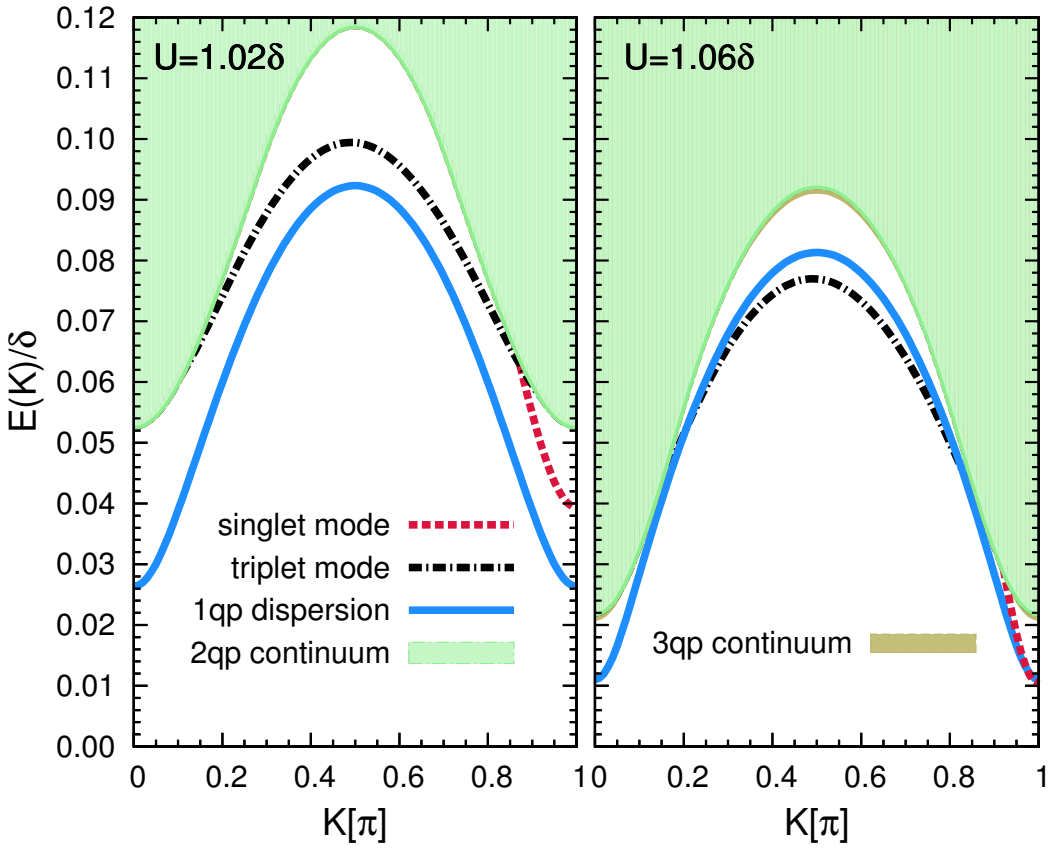

Figure 4.10: The low-energy spectrum of the IHM including 1-quasiparticle dispersion (solid line), 2- and 3-quasiparticle continuum (solid region), and singlet (dashed line) and triplet (dotted-dashed line) bound states. The results are obtained by $D:0+g:0+$ED. The deepCUT steps $D:0$ and $g:0$ are performed in orders 4 and 16, respectively. For the ED, the Hamiltonian matrix is constructed for maximum relative distances of 24. The hopping is fixed to $t = 0.05\delta$ for both panels; $U = 1.02\delta$ in the left panel and $U = 1.06\delta$ in the right panel. For $U = 1.06\delta$, the lower edge of 2- and 3-quasiparticle continuum are very close to each other. No singlet bound state is found near the total momentum $K = \pi/2$ in contrast to the pure deepCUT $D:0+g:2$, see Fig. 4.6.

the combination of deepCUT and ED. For $U = 1.02\delta$, both methods coincide nicely except very close to $K = \frac{\pi}{2}$ where the maximum deviation occurs. Around $K = \frac{\pi}{2}$ the results of deepCUT plus ED lie a bit higher in energy than those by pure deepCUT, see also inset. It is not clear whether the small difference is due to the restriction of the Hilbert space in ED implying a certain overestimation or whether it is due to the effect of long-range processes that are less well captured by the pure deepCUT.

Next, we focus on the right panel of Fig. 4.4 where $U = 1.06\delta$ close to the transition point. Here the difference between the two methods is larger. For the momenta near 0 and π the combination $D:0+g:0+$ED yields a dispersion with lower energies while for the momenta around $\frac{\pi}{2}$ the result from $D:0+g:2$ is the lower one. From the comparison with the extrapolated DMRG results for the charge gap we deduce that the dispersion of $D:0+g:0+$ED is more accurate near $K = 0$ and $K = \pi$. Thus we presume that also around $K = \frac{\pi}{2}$ the $D:0+g:0+$ED data is more accurate, but there is no data from alternative

approaches available to corroborate this conclusion.

Let us turn to Fig. 4.10 which shows the low-energy spectrum of the IHM obtained by $D:0+g:0+$ED with the orders 4 and 16 for the deepCUT steps $D:0$ and $g:0$, respectively. The left and right panels are again for $U = 1.02\delta$ and $U = 1.06\delta$. The lower edge of the 3-QP continuum for $U = 1.06\delta$ lies close to the lower edge of the 2-QP continuum. The major difference between this figure and the pure deepCUT results plotted in Fig. 4.6 is the absence of the singlet bound state around the total momentum $K = \pi/2$. This difference may arise from the restricted relative distances of QPs in the ED treatment. The singlet bound state mode near $K = \pi/2$ has a very small binding energy indicating that it is weakly bound and thus extending over large distances. Its extension is restricted due to computational limitations and the binding may be suppressed spuriously in the ED.

4.3 Beyond the Transition Point: A Mean Field Study

The deepCUT approach realized in the previous sections is based on the QPs of the BI, i.e., the more complicated, dressed excitations close to the transition to the SDI are continuously mapped to the simple QPs of the BI. The same quantum numbers are used in analogy to Fermi liquid theory which uses the same quantum numbers as the Fermi gas. As long as the system is located on the BI side of the phase transition, only a few-particle problem remains to be solved in a subsequent step to find the low-lying excitation spectrum. But this QP picture breaks down when a phase transition occurs. Beyond the transition point, a macroscopic number of QPs of the BI condenses forming the new phase. This new phase displays other types of elementary excitations.

Our analysis of the BI of the IHM in the previous sections showed that the exciton gap decreases on increasing the Hubbard interaction and vanishes at a critical value U_{c1}. This critical interaction was found to be $U_{c1} = 1.072\delta$ for $D:0+g:2$ in order 12, see Fig. 4.7. How can we proceed beyond the transition and still profit from the effective Hamiltonians obtained by deepCUT? The most systematic way would be to set up a CUT with respect to the ground state and the elementary excitations for $U > U_{c1}$. But there are two obstacles to this route. The first one is that one has to know and to characterize the SDI ground state sufficiently well to be able to set up a CUT. The second one is that this approach would require to implement another, completely different CUT which we postpone to the next chapter.

Thus we choose a slightly modified approach and continue to use the implemented CUT to derive an effective Hamiltonian by applying $D:0+g:2$ and to analyze this effective Hamiltonian subsequently by a mean-field approach. The guiding idea is that the terms driving the phase transition are small and can be treated perturbatively as long as the system is considered close to the phase transition. In this way, one continues to profit from the deepCUT implemented to obtain the effective Hamiltonians. We use the deepCUT $D:0+g:2$ in order 12 to derive the effective Hamiltonian.

For simplicity, we choose here a mean-field approximation as a first step of a perturbative treatment. Although this approach is not able to capture the correct critical behavior in low dimensions and underestimates the role of fluctuations, it provides us with an estimate which phases are lower in energy. Since the $S = 0$ exciton at $K = \pi$ becomes soft at U_{c1} the SDI can be seen as a condensate of $S = 0$ excitons. The electron-hole transformation (4.1) that we performed maps the original exciton into a bound state of two fermions, i.e., the exciton appears as Cooper pair. Thus we expect a BCS-type theory to describe the SDI phase transition.

The effective Hamiltonian is represented in terms of hardcore fermions $\{g_{i,\sigma}\}$ and it includes various interactions within and between sectors of different numbers of QPs. In the following, we consider this effective Hamiltonian up to quadrilinear interactions and ignore interaction terms acting on higher numbers of QPs. Hence the effective Hamiltonian takes the general form

$$H_{\text{eff}} = H_{0:0} + H_{1:1} + H_{2:2}, \tag{4.18a}$$

where

$$H_{0:0} = E_0 \mathbb{1}, \tag{4.18b}$$

$$H_{1:1} = \sum_{ij} \Gamma_{j;i}\; g_j^\dagger g_i\,, \tag{4.18c}$$

$$H_{2:2} = \sum_{ijkl} \Gamma_{kl;ij}\; g_k^\dagger g_l^\dagger g_i\, g_j\,. \tag{4.18d}$$

The prefactors $\Gamma_{j;i}$ and $\Gamma_{kl;ij}$ are nonzero up to an interaction range proportional to the order of the deepCUT calculation. The processes of longer range do not occur. Because the effective Hamiltonian (4.18a) is obtained by applying the reduced generator $g : 2$ no off-diagonal interactions such as $H_{3:1}$ appear.

In order to apply Wick's theorem, we neglect the hardcore property of the operators and treat them like usual fermions. Due to this approximation two fermions with different spin are allowed to occupy the same site. It is also possible to deal with the hardcore property by the slave-particle techniques, see Ref. [Vae11] and references therein, or by the Brueckner approach [KSWO98]. But such analyses are beyond the scope of present investigation.

For a self-consistent mean-field approximation the symmetries of the ground state are essential. In order to describe the SDI phase of the IHM, we take the possibility of a spontaneous symmetry breaking into account with nonzero anomalous expectation values (see below). The broken symmetry is the parity with respect to reflection about a site. Thus adjacent bonds may become different even though in the original Hamiltonian the (directed) bond from site 0 to 1 was identical to the one from 0 to -1. This is characteristic of the SDI as found in previous studies based on variational quantum Monte Carlo [WM01] and DMRG [LQX+03, KSJB03, MMNS04, LBS06, TNB09]. Thus, we assume for the expectation values

$$\langle g_{i,\sigma}^\dagger g_{i+m,\sigma}^\dagger \rangle \neq \langle g_{i+1,\sigma}^\dagger g_{i+m+1,\sigma}^\dagger \rangle \neq 0, \tag{4.19a}$$

$$\langle g_{i,\sigma}^\dagger g_{i+n,\sigma} \rangle = \langle g_{i+1,\sigma}^\dagger g_{i+n+1,\sigma} \rangle \neq 0, \tag{4.19b}$$

where m and n stand for odd and even distances, respectively. The maximum values of m and n depend on the order in which the deepCUT was performed. All the above expectation values are zero in the BI phase where the ground state is the vacuum of "g-particles", but they become finite as soon as the exciton begins to condense and the phase transition occurs.

For a transparent notation, we express the g-operators acting on even and odd sites by a- and b-operators, respectively. The resulting mean-field Hamiltonian takes the BCS-form

$$\begin{aligned} H_{\mathrm{BCS}} &= \frac{L}{2}(\epsilon_0^A+\epsilon_0^B) \\ &+ \sum_{r\in\mathrm{even},\sigma}\left(t_0^A : a_{r,\sigma}^\dagger a_{r,\sigma} : + \sum_{n=2,4,\cdots} t_n^A : a_{r,\sigma}^\dagger a_{r+n,\sigma} + \mathrm{h.c.} : \right) \\ &+ \sum_{r\in\mathrm{odd},\sigma}\left(t_0^B : b_{r,\sigma}^\dagger b_{r,\sigma} : + \sum_{n=2,4,\cdots} t_n^B : b_{r,\sigma}^\dagger b_{r+n,\sigma} + \mathrm{h.c.} : \right) \\ &+ \sum_{r\in\mathrm{even},\sigma}\sum_{m=1,3,\cdots} \Delta_m^A : a_{r,\sigma}^\dagger b_{r+m,\sigma}^\dagger : + \mathrm{h.c.} \\ &+ \sum_{r\in\mathrm{odd},\sigma}\sum_{m=1,3,\cdots} \Delta_m^B : b_{r,\sigma}^\dagger a_{r+m,\sigma}^\dagger : + \mathrm{h.c.} \end{aligned} \tag{4.20}$$

where we have divided the lattice into the two sublattices A and B of even sites and odd sites, respectively. The prefactors ϵ_0^A, ϵ_0^B, t_d^A, t_d^B, Δ_d^A, and Δ_d^B depend on the coefficients of the effective Hamiltonian, which stem from the flow equations, see Eq. (3.22), and on the expectation values introduced in Eq. (4.19). Due to the identity (4.19b), the hopping prefactors of the two sublattices are identical. So we unify them omitting the sublattice index $t_d^A = t_d^B =: t_d$.

The BCS Hamiltonian (4.20) is diagonalized by a Bogoliubov transformation in momentum space. The self-consistency equations to be solved are found after some lengthy, but standard calculations

$$\langle a_{r,\sigma}^\dagger a_{r+n,\sigma}\rangle = \langle b_{r,\sigma}^\dagger b_{r+n,\sigma}\rangle = \frac{1}{\pi}\int_0^{\frac{\pi}{2}} dk\, \frac{\lambda(k)-t(k)}{\lambda(k)}\cos(nk), \tag{4.21a}$$

$$\langle a_{r,\sigma}^\dagger b_{r+m,\sigma}^\dagger\rangle = \frac{1}{\pi}\int_0^{\frac{\pi}{2}} dk\, \frac{\mathrm{Im}(\Delta(k))\sin(mk)-\mathrm{Re}(\Delta(k))\cos(mk)}{\lambda(k)}, \tag{4.21b}$$

$$\langle b_{r,\sigma}^\dagger a_{r+m,\sigma}^\dagger\rangle = \frac{1}{\pi}\int_0^{\frac{\pi}{2}} dk\, \frac{\mathrm{Im}(\Delta(k))\sin(mk)+\mathrm{Re}(\Delta(k))\cos(mk)}{\lambda(k)}, \tag{4.21c}$$

where n and m take even and odd values, respectively. The functions $t(k)$, $\Delta(k)$, and $\lambda(k)$ are defined by

$$t(k) = t_0 + 2\sum_{n=2,4,\cdots} t_n\cos(nk), \tag{4.22a}$$

$$\Delta(k) = \sum_{m=1,3,\cdots}\left((\Delta_m^A-\Delta_m^B)\cos(mk) - i(\Delta_m^A+\Delta_m^B)\sin(mk)\right), \tag{4.22b}$$

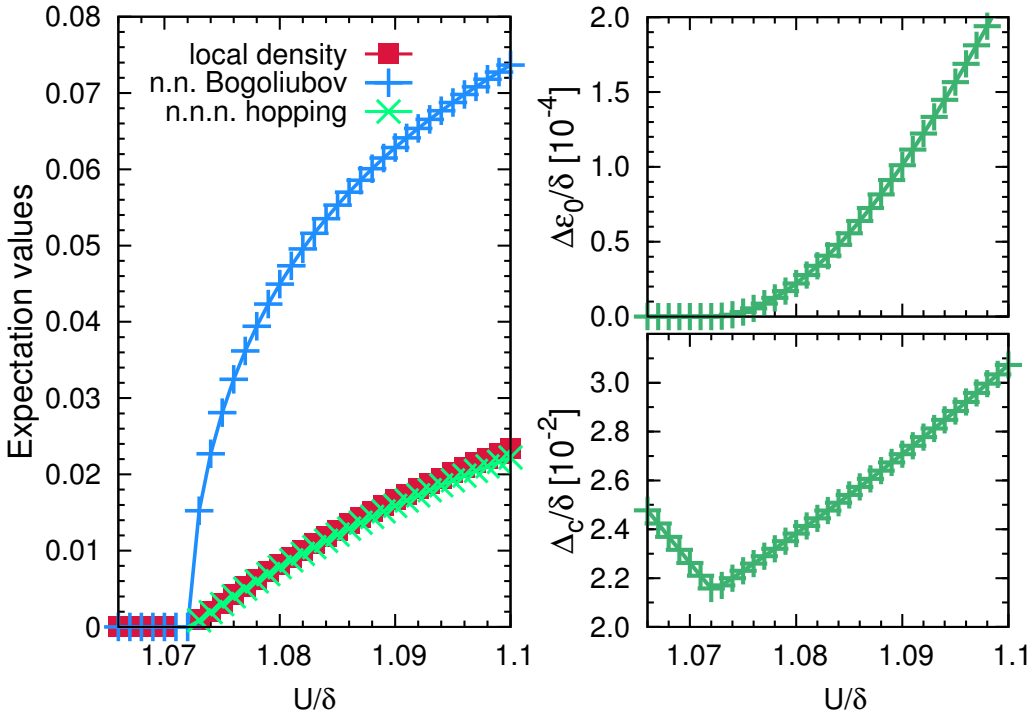

Figure 4.11: Analysis of the effective Hamiltonian obtained by $D:0+g:2$ in order 12 within the BCS-type approximation. The hopping prefactor t is 0.05δ. Left panel: Expectation values of the local density, the nearest-neighbor (NN) Bogoliubov term, and the next-nearest-neighbor (NNN) hopping term vs. the Hubbard interaction U. At the phase transition at $U_c = 1.072\delta$ the expectation values become finite. The Bogoliubov term shows a square root behavior near the transition point. Right panel: The condensation energy per site $\Delta\epsilon_0$ (upper panel) and the charge gap Δ_c (lower panel) vs. Hubbard interaction U. The charge gap starts to increase beyond the transition point $U > U_{c1}$.

$$\lambda(k) \;=\; \sqrt{t^2(k)+|\Delta(k)|^2}. \tag{4.22c}$$

Once the parameters t and U are specified, the mean-field equations (4.21) have to be solved self-consistently for the expectation values (4.19). The results are shown in Fig. 4.11. The left panel displays the expectation values of the local density operator, of the NN Bogoliubov term, and of the NNN hopping term. For $U \leq 1.072\delta$, all the expectation values are zero; they continuously increase starting from zero for $U \geq 1.072\delta$. This critical Hubbard interaction $U_c = 1.072\delta$ is precisely the value we found in our study of the BI phase in the previous sections based on the deepCUT $D:0+g:2$ in order 12, see Fig. 4.7. This demonstrates the global consistency of the approach used.

The two NN Bogoliubov terms in the unit cell are related to each other by a minus sign

$$\langle a^\dagger_{r,\sigma} b^\dagger_{r+1,\sigma}\rangle = -\langle b^\dagger_{r+1,\sigma} a^\dagger_{r+2,\sigma}\rangle; \quad r \in \text{even}. \tag{4.23}$$

Two equivalent solutions are possible corresponding to the two ground states. In one of them $\langle a^\dagger_{r,\sigma} b^\dagger_{r+1,\sigma}\rangle > 0$ holds and in the other $\langle a^\dagger_{r,\sigma} b^\dagger_{r+1,\sigma}\rangle < 0$. It is seen from the left panel

of Fig. 4.11 that the expectation values of the local density and of the NNN hopping term are close to each other and behave linearly in the vicinity of the transition point. The NN Bogoliubov term displays a square root behavior around the transition point. This square root behavior of the order parameter near the transition point is what one expects from a mean-field theory without spatial fluctuations, i.e., Landau theory, for transitions from a unique ground state to a state with spontaneously broken symmetry.

We define the condensation energy as the energy difference between the vacuum of "g-particles" and the mean-field ground state of the system. In the right panel of Fig. 4.11 the condensation energy per site $\Delta\epsilon_0$ and the charge gap are plotted vs. U. Of course, the condensation energy is zero in the BI phase and becomes finite when the condensation starts.

The mean-field analysis shows that the charge gap starts to increase as soon as the transition has taken place. The behavior of the charge gap beyond the first transition point U_{c1} has been discussed controversially in previous studies. Lou *et al.* [LQX+03] concluded by extrapolating DMRG results to infinite chain length that the charge gap continues to decrease beyond U_{c1} up to the second transition point U_{c2}, see Fig. 2.8. At this second transition point both charge and spin gaps vanish and for $U > U_{c2}$ the charge gap starts to increase while the spin gap remains zero [LQX+03]. The DMRG method employed by other groups show that the charge gap starts to increase just from the first transition point on [TK01, KSJB03, MMNS04], see Figs. 2.6, 2.9 and 2.10. Our findings clearly support the latter scenario.

Because the IHM can be mapped to the Heisenberg model in the limit $U - \Delta \gg t$, we expect a MI phase in the large U limit with a vanishing spin gap. However, the effective Hamiltonian analysed on the mean-field level shows no evidence for a second transition to the MI phase. But, as we discussed in chapter 2, there is strong evidence for a second transition to the MI phase obtained by field theoretical approach [FGN99, TAC01] and by DMRG [TK01, LQX+03, ZWL03, MMNS04, LBS06, TNB09] even though it appears to be difficult to determine it unambiguously [WM01, KSJB03].

The question arises why we do not see any evidence for the transition from SDI to MI. From the employed approach two sources are conceivable. The first source consists in errors in the mapping of the IHM to the effective Hamiltonian using $D:0+g:2$. We have already seen that this effective Hamiltonian includes some inaccuracies. This is seen, for instance, in the charge gap calculated from the effective Hamiltonian and compared to DMRG results in the left panel of Fig. 4.5. But this is only a quantitative discrepancy which can explain quantitative deviations and it is unlikely that the qualitative aspect of a mechanism driving the system from the SDI to the MI is completely missed.

The second source arises from the analysis of the effective Hamiltonian. The mean-field analysis can capture the essential aspects of the gaps of *single* fermionic excitations, but it is not powerful enough to provide information about binding phenomena. The physics of the MI is characterized by the massless excitations of a generalized Heisenberg model. In higher dimensions it would display magnetic long-range order. In 1D this order is reduced by quantum fluctuations to a quasi-long-range order with power law decay. Still we expect

that the transition SDI to MI is driven by the softening of a magnetic $S = 1$ excitation, i.e., a triplon. The condensation of such a triplon would indicate the transition to a phase dominated by magnetic fluctuations or with magnetic long-range order [SB90].

In terms of fermions, the triplon is an exciton with $S = 1$, in contrast to the exciton with $S = 0$ which signalled the BI to SDI transition. Thus we conclude that the second transition U_{c2} can only be found if the binding of $S = 1$ excitons formed by two fermionic excitations above the SDI ground state is analyzed. This issue will be addressed in the next chapter 5 where the dimer limit is used as the starting point in the deepCUT method.

4.4 Chapter Summary

In this chapter, we studied the ionic Hubbard model (IHM) at half-filling in one dimension in detail in order to understand the nature of its three phases: The band insulator (BI), the spontaneously dimerized insulator (SDI), and the Mott insulator (MI). We employed the deepCUT approach [KDU12] to derive effective Hamiltonians in a systematically controlled fashion. The deepCUT is applied in two consecutive steps. In the first step, a low-energy effective Hamiltonian is obtained in the limit $\delta \gg t$. This corresponds to eliminating the doubly occupied states from even sites and the empty states from odd sites. This reduces the energy scale in the system from $\delta \approx U$ to t. The obtained low-energy Hamiltonian in quasiparticle (QP) representation of the BI contains non-particle conserving interactions. These off-diagnoal interactions are rotated away by a second application of the deepCUT method using various generators. In the final effective Hamiltonian, the vacuum of QPs corresponds to the ground state of the IHM in the BI phase. The analysis of the derived effective Hamiltonian in the first few QP sectors provides the low-lying excitation spectrum of the system.

We quantitatively determined the dispersion of single fermionic excitation in the BI phase almost up to the first transition point U_{c1}. The convergence of the finite order calculations illustrates the accuracy of the results. The deepCUT outcomes become less accurate as we approach the tranistion point indicating the role of long-range processes which are neglected in our treatment. The dispersion at the total momentum $K = 0$ (or equivalently π) takes its minimum; this defines the charge gap. This is the only point of the BZ where DMRG results are available and we can compare our results. The deepCUT results for the charge gap at finite order are extrapolated to infinite order by a linear fit in the inverse order. We find a nice agreement between the extrapolated deepCUT results and the DMRG results obtained by Manmana *et. al.* [MMNS04].

In addition to the 1-QP dispersion, we have discussed the binding phenomena occuring in the singlet and in the triplet channels of the 2-QP sector. The dispersion of singlet and triplet bound states as well as 2- and 3-QP continua are computed in the whole BZ even close to the transition to the SDI phase. It is found that the transition from the BI to the SDI is signaled by vanishing a $S = 0$ exciton at $U_{c1} \simeq 1.07\delta$ for $t = 0.05\delta$. We emphasize that any bare perturbative series contains powers of $t/(\delta - U)$ and finally fails to reach the

point $U = \delta$ from below. We have been able to go near the transition point $U_{c1} \simeq 1.07\delta$ and beyond because of the renormalizing nature of the deepCUT method.

The electron-hole bound states in the BI phase appear as a Cooper pair in our QP representation of the IHM. The condensation of the $S = 0$ exciton beyond the first transition point U_{c1} is described by a mean-field BCS-type-theory. The dimerization parameter becomes finite in the new phase which indicates the stabilization of the SDI phase. This SDI phase remains stable upon increasing the Hubbard interaction and the mean-field solution shows no evidence for a second transition to the MI phase. We expect the transition from the SDI to the MI to be signaled by softening a $S = 1$ excitation known as triplon. This point will be addressed in the next chapter.

We mention that the phase diagram of the IHM in two dimensions is disputed [GKR06, PBH$^+$07, KD07, CZLW10]. The strategy introduced in this chapter has no conceptual problem to be applied in two dimensions. The mean-field analysis is expected to work better in higher dimensions. We want to emphasize that our approach correctly identifies the nature of the middle SDI phase even in the leading order.

The IHM doped with holes is another interesting problem [GKR14, WI13] which can be analyzed by the combination of deepCUT and mean-field theory. The deepCUT with the BI limit as starting point can be employed to investigate other Hamiltonians as well. An example would be the Hubbard model with the n.n. intercation which shows a competition between charge density wave and spin density wave phases [Nak00, EN07].

Chapter 5

Dimer Limit Analysis

In the previous chapter, the deepCUT method was applied in the BI phase of the IHM yielding reliable results for the excitation spectrum of the model even close to the transition point to the SDI phase. A mean-field BCS-type-theory was employed to describe the system beyond the BI-to-SDI transition point. The mean-field theory, however, can capture only the physics of 1-particle excitation above the ground state and in the previous chapter no second transition to the MI phase was found upon increasing the Hubbard interaction.

In this chapter, we explore the excitation spectrum and quantum phase transitions of the 1D IHM by using the dimer limit as starting point of the deepCUT method. In the dimer limit, the system is assumed to be composed of isolated dimers [OHZ06, DU11] and the effect of interdimer hopping is considered using the deepCUT method [KDU12]. The advantage of the dimer limit, compared to the BI limit considered in the previous chapter, is that it allows us to have access to all phases of the IHM.

In the first step, we restrict the size of the local Hilbert space in order to reduce the number of possible excitations on each local dimer. This restriction corresponds to eliminating the doubly occupied states from even sites and empty states from odd sites in the IHM in Eq. (2.1). In other words, we ignore to apply the $D:0$ step introduced in the previous chapter. A DMRG analysis by Tincani shows that the positions of the phase transitions for the restricted IHM matches the results of the full Hamiltonian fairly in the limit $\delta \gg t$ [TNB09]. We want to mention that the treatment of the full Hamiltonian within the deepCUT approach is also possible.

We address the phase transitions of the model by analyzing both the ground state energy and various gaps. The obtained positions for the transition points are compared with the DMRG results obtained by Tincani *et. al.* [TNB09]. In addition, we discuss the low-energy excitation spectrum of the model in the BI, in the SDI, and in the MI phases. In the BI phase, it is revealed that the dimer limit can satisfactorily reproduce the deepCUT results of the BI limit. In the MI phase, it is found that the low-energy physics of the IHM for large enough Hubbard interaction can be described by an effective Hamiltonian *purely* in terms of triplon operators. The analysis of this effective triplon Hamiltonian leads to quantitative

results for the gapless triplon dispersion of the IHM in the MI phase.

5.1 Preliminary Considerations

5.1.1 Restricted IHM

The IHM (2.1) has a four dimensional Hilbert space at each site: empty state, spin up and down states, and doubly occupied state. But, the empty states on odd sites and the doubly occupied states on even sites are very high in energy for $U, \delta \gg t$. In the following, we limit our analysis of the IHM to the case where $U, \delta \gg t$ and restrict the Hilbert space such that there is no empty state on odd sites and no doubly occupied state on even sites. We stress that such a restriction has no qualitative effect on the phase diagram of the IHM. In addition, a DMRG study shows that the position of the transition points of the IHM restricted in this way match the results of the full IHM in the limit $U, \delta \gg t$ [TNB09]. For $t = 0.05\delta$, for example, the position of the first transition point changes from $U_{c1} = 1.069\delta$ for the full IHM [MMNS04] to $U_{c1} = 1.065\delta$ for the restricted Hamiltonian [TNB09]. We studied the full IHM in the previous chapter and the BI limit predicted the first transition point to occur at $U_{c1} = 1.072\delta$.

In order to treat the odd and even sites in the same way, we apply an electron-hole transformation on the odd sites. The transformation reads[1]

$$c^\dagger_{i,\sigma} \to \eta_\sigma h_{i,\bar{\sigma}}, \tag{5.1}$$

where $\eta_\uparrow = 1$, $\eta_\downarrow = -1$, and $\bar{\sigma}$ shows the opposite direction of σ. Unifying all the electron and hole operators by a new fermion operator

$$f_{i,\sigma} := \begin{cases} c_{i,\sigma} & \text{for } i \in \text{even}, \\ h_{i,\sigma} & \text{for } i \in \text{odd}, \end{cases} \tag{5.2}$$

brings the Hamiltonian (2.1) to the form

$$\begin{aligned} H = \frac{U-2\delta}{4} \sum_i \mathbb{1} \quad &+ \quad \frac{\delta - U}{2} \sum_{i,\sigma} f^\dagger_{i,\sigma} f_{i,\sigma} \\ &+ \quad U \sum_i f^\dagger_{i,\uparrow} f^\dagger_{i,\downarrow} f_{i,\downarrow} f_{i,\uparrow} \\ &+ \quad t \sum_{i,\sigma} \eta_\sigma (f^\dagger_{i,\sigma} f^\dagger_{i+1,\bar{\sigma}} + \text{h.c.}) \end{aligned} \tag{5.3}$$

In this new operator representation, ignoring all the doubly occupied states is equivalent to throwing away the empty states from odd sites and doubly occupied states from even sites

[1] Here we use a slightly different electron-hole transformation rather than (4.1) in order to have the usual definitions for the triplet and singlet excitations on a dimer, see Table 5.1.

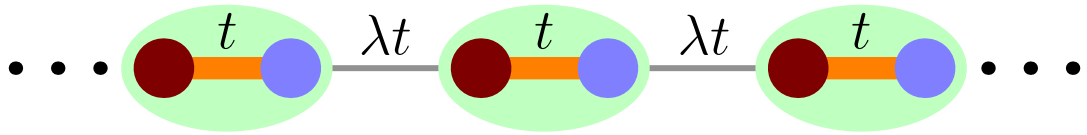

Figure 5.1: Schematic representation of the dimer limit expansion. The intradimer hopping parameter is shown by t. For $\lambda = 0$ the system is made of isolated dimers and for $\lambda = 1$ the uniform lattice is recovered.

in the original picture as we intended to do. The Hubbard operators are used to decompose the Hamiltonian (5.3) into the terms which create and annihilate specific numbers of double occupancies. The Hubbard operators are defined as

$$g^\dagger_{i,\sigma} := |\sigma\rangle_{i\,i}\langle e|, \tag{5.4a}$$

$$g^\dagger_{i,d} := |d\rangle_{i\,i}\langle e|, \tag{5.4b}$$

where d and e stand for doubly occupied state and empty state, respectively. The f-operator in terms of Hubbard operators is given by

$$f^\dagger_{i,\sigma} = g^\dagger_{i,\sigma} + \eta_\sigma g^\dagger_{i,d} g_{i,\bar{\sigma}}. \tag{5.5}$$

Finally, substituting Eq. (5.5) and its hermitian conjugate in the Hamiltonian (5.3) and considering only the sector with zero number of double occupancy leads to

$$\begin{aligned} H = \frac{U-2\delta}{4}\sum_i \mathbb{1} \;&+\; \frac{\delta - U}{2}\sum_{i,\sigma} g^\dagger_{i,\sigma} g_{i,\sigma} \\ &+\; t\sum_{i,\sigma} \eta_\sigma (g^\dagger_{i,\sigma} g^\dagger_{i+1,\bar{\sigma}} + \text{h.c.}). \end{aligned} \tag{5.6}$$

In the previous chapter we used the deepCUT step called $D:0$ to derive a low-energy effective Hamiltonian in the limit $\delta, U \gg t$. Here, however, we do not apply this first deepCUT and deal directly with the Hamiltonian (5.6). The IHM restricted in this way is studied by Tincani *et. al.* [TNB09] giving us the possibility to compare our findings with their DMRG results.

5.1.2 Dimer limit

We modify the Hamiltonian (5.6) so that it is suitable for the dimer limit expansion

$$\begin{aligned} H = \frac{U-2\delta}{4}\sum_i \mathbb{1} \;&+\; \frac{\delta - U}{2}\sum_{i,\sigma} g^\dagger_{i,\sigma} g_{i,\sigma} \\ &+\; t\sum_{i\in\text{even},\sigma} \eta_\sigma (g^\dagger_{i,\sigma} g^\dagger_{i+1,\bar{\sigma}} + \lambda g^\dagger_{i+1,\sigma} g^\dagger_{i+2,\bar{\sigma}} + \text{h.c.}), \end{aligned} \tag{5.7}$$

where λ is the perturbative parameter on which we truncate the flow equations in the deepCUT method [KDU12]. For $\lambda = 0$ the Hamiltonian is composed of isolated dimers and

#	Dimer Eigenstates	Eigenvalues
1	$\|0\rangle = -\beta \|e,e\rangle + \frac{\alpha}{\sqrt{2}}(\|\uparrow,\downarrow\rangle - \|\downarrow,\uparrow\rangle)$	ϵ_0
2	$\|t\rangle_{+1} = \|\uparrow,\uparrow\rangle$	$\epsilon_0 + \epsilon_t$
3	$\|t\rangle_0 = \frac{1}{\sqrt{2}}(\|\uparrow,\downarrow\rangle + \|\downarrow,\uparrow\rangle)$	$\epsilon_0 + \epsilon_t$
4	$\|t\rangle_{-1} = \|\downarrow,\downarrow\rangle$	$\epsilon_0 + \epsilon_t$
5	$\|f\rangle_{l,\uparrow} = \|\uparrow,e\rangle$	$\epsilon_0 + \epsilon_f$
6	$\|f\rangle_{l,\downarrow} = \|\downarrow,e\rangle$	$\epsilon_0 + \epsilon_f$
7	$\|f\rangle_{r,\uparrow} = \|e,\uparrow\rangle$	$\epsilon_0 + \epsilon_f$
8	$\|f\rangle_{r,\downarrow} = \|e,\downarrow\rangle$	$\epsilon_0 + \epsilon_f$
9	$\|s\rangle = +\alpha \|e,e\rangle + \frac{\beta}{\sqrt{2}}(\|\uparrow,\downarrow\rangle - \|\downarrow,\uparrow\rangle)$	$\epsilon_0 + \epsilon_s$

Table 5.1: Eigenstates and eigenvalues of a single dimer of Hamiltonian (5.7) for $\lambda = 0$. There are three different possible states on each site: empty state e, spin up state $\uparrow$, and spin down $\downarrow$ state. This leads to nine eigenstates on each dimer. The ground state has total spin zero and is shown by the vacuum $|0\rangle$. There are four fermionic and four bosonic excited states. The expressions ϵ_0, ϵ_t, ϵ_f, and ϵ_s are defined in Eq. (5.8) and the coefficients α and β are given in Eq. (5.9).

for $\lambda = 1$ the IHM (5.6) is retrieved. The dimer limit expansion is schematically shown in Fig. 5.1. The Hamiltonian (5.7) defines the starting point to analyze the IHM from the dimer limit.

For applying the deepCUT method, the Hamiltonian (5.7) needs to be expressed in terms of dimer excitation operators. In the absence of interdimer hopping, the system is made of independent dimers with a nine dimensional local Hilbert space. The nine eigenstates and eigenvalues of a single dimer are summarized in Table 5.1. The ground state energy ϵ_0, the triplon energy ϵ_t, the fermion energy ϵ_f, and the singlon energy ϵ_s are given by

$$\epsilon_0 = -\frac{1}{2}\left(\delta + \sqrt{(U-\delta)^2 + 8t^2}\right), \tag{5.8a}$$

$$\epsilon_t = +\frac{1}{2}\left(\delta - U + \sqrt{(U-\delta)^2 + 8t^2}\right), \tag{5.8b}$$

$$\epsilon_s = 2\epsilon_f = \sqrt{(U-\delta)^2 + 8t^2}. \tag{5.8c}$$

The coefficients α and β are given by

$$\alpha = \sqrt{\frac{1}{2} + \frac{U-\delta}{4\epsilon_f}}, \tag{5.9a}$$

$$\beta = \sqrt{\frac{1}{2} - \frac{U-\delta}{4\epsilon_f}}. \tag{5.9b}$$

For all values of the model parameters t, U, and δ, the state with lowest energy has total spin zero and is denoted as vacuum $|0\rangle$. There are four degenerate fermionic excited states corresponding to the fermion being on the left-site $|f\rangle_{l,\sigma}$ or on the right-site $|f\rangle_{r,\sigma}$, each one with two different spin states $\sigma = \uparrow, \downarrow$. Among the four bosonic excited states, there

is one state with total spin zero $|s\rangle$, called singlon henceforth, and three degenerate states with total spin one and different magnetic numbers $|t\rangle_{\pm1,0}$. It is seen from Eqs. (5.8b) and (5.8c) that the singlon energy ϵ_s is twice the fermion energy ϵ_f. The triplon energy ϵ_t and the fermion energy ϵ_f are also close to each other for $U \approx \delta$. This makes it difficult in the deepCUT method to decouple the 2-fermion sector, the 2-triplon sector, and the 1-singlon sector from one another.

The local hardcore dimer excitation operators at the *dimer* position j are defined as

$$f^\dagger_{j;p,\sigma} := |f\rangle_{j;p,\sigma\ j}\langle 0| \quad ; \quad p = l,r \tag{5.10a}$$

$$t^\dagger_{j;m} := |t\rangle_{j;m\ j}\langle 0| \quad ; \quad m = \pm1,0 \tag{5.10b}$$

$$s^\dagger_j := |s\rangle_{j\ j}\langle 0|. \tag{5.10c}$$

The interpretation of these operators is clear from the definition of the dimer states. The fermion operator $f^\dagger_{j;p,\sigma}$ creates one fermionic excitation at dimer j with spin σ and internal position $p = l,r$ from the vacuum. Similarly, the triplon operator $t^\dagger_{j;m}$ and the singlon operator $s^\dagger_j$ create a triplon with magnetic number m or a singlon at the dimer position j, respectively. The g-operators in terms of dimer excitation operators are given by

$$g^\dagger_{j;l,\sigma} = -\beta f^\dagger_{j;l,\sigma} + t^\dagger_{j;\eta_\sigma} f_{j;r,\sigma} + \alpha f^\dagger_{j;l,\sigma} s_j + \frac{1}{\sqrt{2}}\left(\eta_\sigma\alpha + t^\dagger_{j;0} + \eta_\sigma\beta s^\dagger_j\right) f_{j;r,\bar\sigma}, \tag{5.11a}$$

$$g^\dagger_{j;r,\sigma} = -\beta f^\dagger_{j;r,\sigma} - t^\dagger_{j;\eta_\sigma} f_{j;l,\sigma} + \alpha f^\dagger_{j;r,\sigma} s_j + \frac{1}{\sqrt{2}}\left(\eta_\sigma\alpha - t^\dagger_{j;0} + \eta_\sigma\beta s^\dagger_j\right) f_{j;l,\bar\sigma}, \tag{5.11b}$$

where $g^\dagger_{j;l,\sigma}$ and $g^\dagger_{j;r,\sigma}$ act on the left-site and on the right-site of dimer j. Finally, the Hamiltonian (5.7) in terms of dimer excitation operators reads

$$\begin{aligned} H = \epsilon_0 \sum_j \mathbb{1} \;&+\; \sum_j \epsilon_s\, s^\dagger_j s_j \\ &+\; \sum_j \sum_{m=\pm1,0} \epsilon_t\, t^\dagger_{j;m} t_{j;m} \\ &+\; \sum_j \sum_\sigma \sum_{p=l,r} \epsilon_f\, f^\dagger_{j;p,\sigma} f_{j;p,\sigma} \\ &+\; \lambda t \sum_{j,\sigma} \eta_\sigma \left(g^\dagger_{j;r,\sigma} g^\dagger_{j+1;l,\bar\sigma} + \text{h.c.} \right), \end{aligned} \tag{5.12}$$

where the summation j is now over dimers instead of sites. In the last term, the g-operators have to be replaced according to Eq. (5.11). Until there is no interdimer hopping, the dimer excitations are the true quasiparticles of the system. For any finite value of interdimer hopping λ, however, the dimer excitations start to propagate in the lattice and become dressed quasiparticles. In the next sections 5.2 and 5.3, the Hamiltonian (5.12) is mapped to effective Hamiltonians such that the dimer excitations can still be used as quasiparticles of the system even for $\lambda \neq 0$.

5.1.3 Technical Points

The general aspects of the deepCUT method were reviewed in chapter 3. Here we present just some points about the generator that we have employed to study the IHM from the dimer limit. Because the nonperturbative part of the Hamiltonian (5.12) has a non-equidistant spectrum, the change in local energy is used as criterion to decide about the sign of a term appearing in the generator.

Assume $H^{c_t,c_f,c_s}_{a_t,a_f,a_s}$ stands for the part of the Hamiltonian which creates c_t triplons, c_f fermions, and c_s singlons and annihilates a_t triplons, a_f fermions, and a_s singlons. Then this part contributes to the generator according to

$$\hat{\eta}\left[H^{c_t,c_f,c_s}_{a_t,a_f,a_s}(\ell)\right] = \operatorname{sign}(\epsilon(\ell))\, H^{c_t,c_f,c_s}_{a_t,a_f,a_s}(\ell), \tag{5.13}$$

where the local energy change $\epsilon(\ell)$ is defined by

$$\epsilon(\ell) = (c_t - a_t)\epsilon_t(\ell) + (c_f - a_f)\epsilon_f(\ell) + (c_s - a_s)\epsilon_s(\ell). \tag{5.14}$$

The functions $\epsilon_t(\ell)$, $\epsilon_f(\ell)$, and $\epsilon_s(\ell)$ are the onsite energies of triplon, fermion, and singlon excitations during the flow ℓ. The initial values are given in Eq. (5.8).

The symmetry group which is used in the dimer limit analysis comprises reflection, spin-flip, and self-adjointness saving a factor of about 8 in the number of representatives. In addition, we implemented simplification rules in order to increase the order of calculations in the deepCUT. The simplification rules employed in the dimer limit analysis are illustrated in Appendix B.2.

5.2 Ground Energy and Energy Gaps

5.2.1 Ground State Energy

To find the ground state energy (GSE), the sector with no singlon, no fermion, and no triplon has to be decoupled from the rest. We extended the definition of the reduced generator introduced in Eq. (3.20) to the case where different kind of excitations are present in the system. The ground state generator $\eta_{t:0;f:0;s:0}$ is given by

$$\eta_{t:0;f:0;s:0}(\ell) = \sum_{ijk}\left(\hat{\eta}\left[H^{i,j,k}_{0,0,0}(\ell)\right] - \text{h.c.}\right), \tag{5.15}$$

where the superoperator $\hat{\eta}$ is defined in Eq. (5.13). The generator (5.15) is used to decouple the sector with zero number of triplon, fermion, and singlon from higher quasiparticle sectors. We have been able to reach order 12 in the interdimer hopping for the dimer limit analysis of the GSE. The restricted IHM (4.13a) is also analyzed using the BI limit described in the previous chapter. We stress that the $D:0$ step is no longer required because the IHM

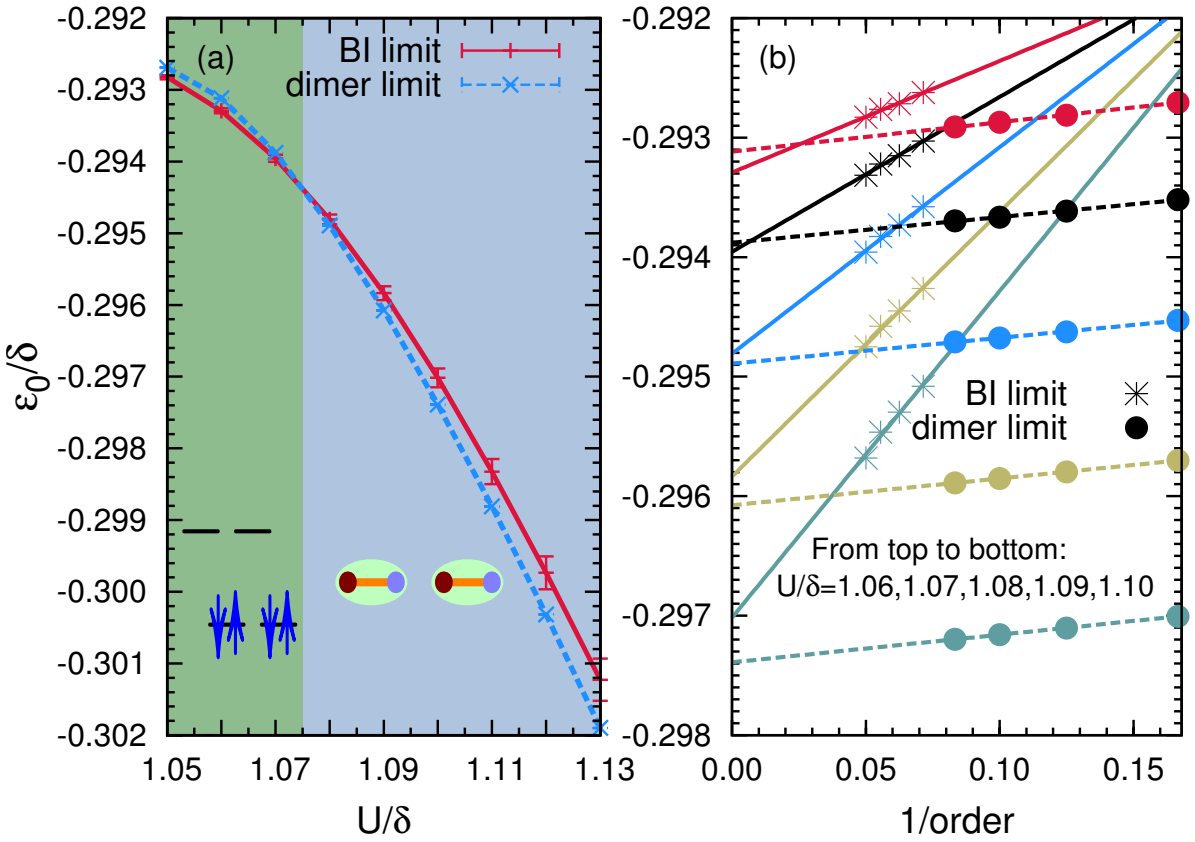

Figure 5.2: Ground state energy per site ϵ_0 of the restricted ionic Hubbard model (5.6) for $t = 0.05\delta$. The results obtained from both dimer limit and band insulator (BI) limit are displayed. In the left panel (a) the ground state energy per site extrapolated to infinite order is plotted versus the Hubbard interaction U/δ. For $U > U_{c1} = 1.075\delta$, the dimer limit produces a lower ground state energy compared to the band insulator limit. In the right panel (b), the ground state energy is depicted versus the inverse order for different values of the Hubbard interaction U. The finite order results are extrapolated to infinite order by performing a linear fit.

is already restricted to the sector with no double occupancy. We apply the $g : 0$ generator directly to the Hamiltonian (4.13a). For the BI limit, the GSE is obtained up to order 20 in the hopping parameter t.

The left panel of Fig. 5.2 indicates the GSE per site extrapolated to infinite order versus the Hubbard interaction U/δ for $t = 0.05\delta$. The right panel of Fig. 5.2 shows the extrapolation process where the GSE per site and the performed linear fit are depicted versus the inverse order. In the right panel, the model parameter $t = 0.05\delta$ and the Hubbard interaction $U = 1.06\delta$, 1.07δ, 1.08δ, 1.09δ, and 1.10δ from top to bottom for both the dimer limit (solid circles) and the BI limit (asterisks). The dimer limit results exhibit a faster convergence compared to the results of BI limit. It is seen from Fig. 5.2 that the ground energy obtained from the dimer limit produces a lower energy for $U > U_{c1} = 1.075\delta$. We recognize this point as the critical point where the transition from the BI phase to the SDI phase occurs. In principle, the results of GSE obtained from both the dimer limit and the BI limit must be identical in the BI phase, $U < 1.075\delta$. However, due to the approximative

nature of our treatment the dimer limit in the BI phase leads to a GSE which is slightly higher than the result of BI limit.

A DMRG study identified the first transition point of the restricted IHM (5.6) at $U = 1.065\delta$ [TNB09] indicating about 1% deviation in our analysis in the determination of the BI-to-SDI transition point. We remind the reader that the position of the first transition point for the full IHM (2.1) obtained by Manmana *et. al* using DMRG method was $U = 1.069\delta$ [MMNS04]. Thus the difference between the restricted IHM (5.6) and the full Hamiltonian is still less important than the truncation error in our approach.

5.2.2 Gaps to Excited States

The charge gap Δ_c, the exciton gap Δ_e, and the spin gap Δ_s are defined in order to measure the excitation energies to the charge and spin channels in the IHM. We refer the reader to Eqs. (2.2), (2.3), and (2.4) where explicit definitions of the gaps are given.

In our formalism, the charge gap is accessible by decoupling the ground state and, at least, the 1-fermion sector from the other quasiparticle sectors. The 1-fermion generator $\eta_{t:0;f:1;s:0}$, which separates the ground state and the 1-fermion sector from the rest, is given by

$$\eta_{t:0;f:1;s:0}(\ell) = \eta_{t:0;f:0;s:0}(\ell) + \eta^{p}_{t:0;f:1;s:0}(\ell), \tag{5.16}$$

where we have defined

$$\eta^{p}_{t:0;f:1;s:0}(\ell) \equiv \sum_{ijk} \left(\hat{\eta} \left[H^{i,j,k}_{0,1,0}(\ell) \right] - \text{h.c.} \right) X^{i,j,k}_{0,0,0}, \tag{5.17}$$

with

$$X^{i,j,k}_{i',j',k'} \equiv 1 - \delta_{i,i'}\delta_{j,j'}\delta_{k,k'}. \tag{5.18}$$

One needs to include the term $X^{i,j,k}_{0,0,0}$ in Eq. (5.17) in order to prevent the interaction $H^{0,0,0}_{0,1,0}$ to appear twice in the generator (5.16). In a similar way, the 1-triplon channel can be decoupled using the 1-triplon generator

$$\eta_{t:1;f:0;s:0}(\ell) = \eta_{t:0;f:0;s:0}(\ell) + \eta^{p}_{t:1;f:0;s:0}(\ell), \tag{5.19}$$

with the definition

$$\eta^{p}_{t:1;f:0;s:0}(\ell) = \sum_{ijk} \left(\hat{\eta} \left[H^{i,j,k}_{1,0,0}(\ell) \right] - \text{h.c.} \right) X^{i,j,k}_{0,0,0}. \tag{5.20}$$

The generator (5.19) provides an effective Hamiltonian whose 1-triplon sector can be diagonalized by a Fourier transformation yielding the triplon dispersion. Subsequently, the triplon gap can be found as the minimum of the triplon dispersion. The triplon gap is a spin-1 excitation. One must be cautious to call this excitation the spin gap. In the 2-fermion sector, there is a channel with total spin one and the spin gap (2.4) should be considered as the minimum of the spin-1 2-fermion excitation and the triplon gap. Of course, one can also imagine other possibilities for the spin gap but these two cases are the most probable

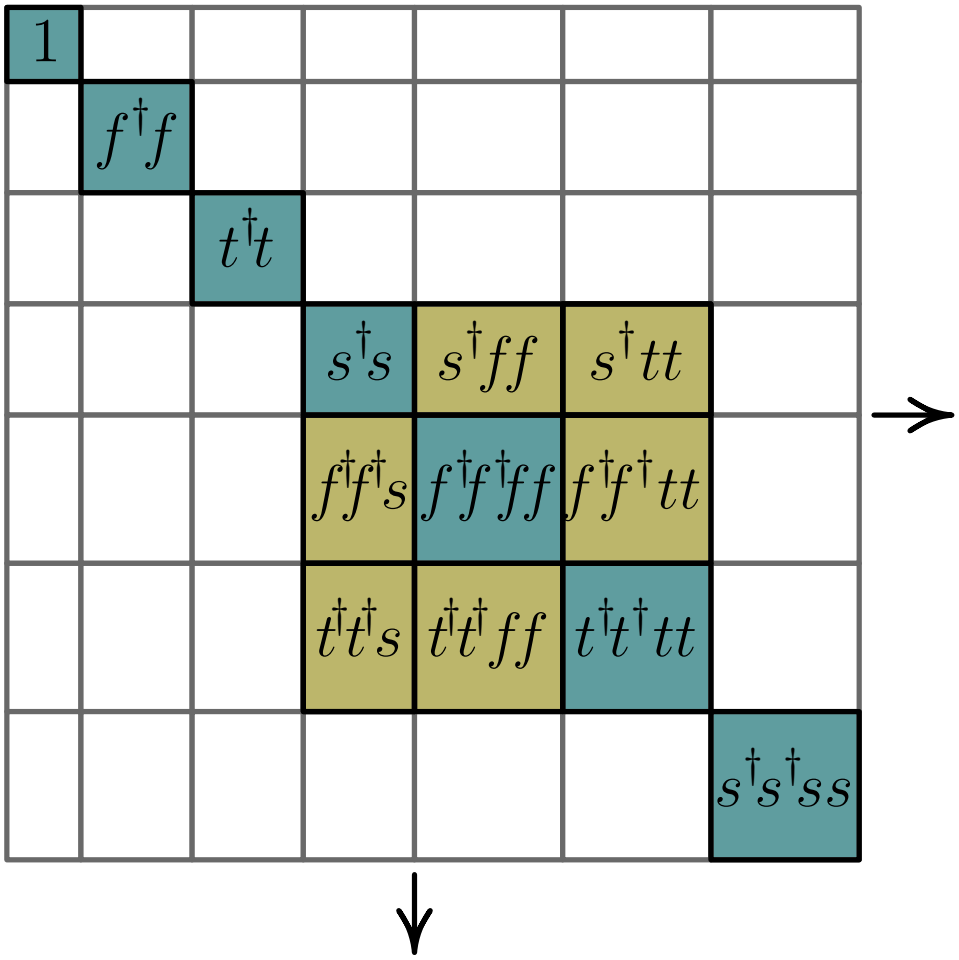

Figure 5.3: The general structure of the effective Hamiltonian derived by applying the generator $\eta_{t:2;f:2;s:1}$ to the initial Hamiltonian (5.12). The generator $\eta_{t:2;f:2;s:1}$ is defined in Eq. (5.21). It is seen that the ground state, 1-fermion, and 1-triplon sectors are completely decoupled from the rest. However, the interactions between 1-singlon and 2-fermion, 1-singlon and 2-triplon, and 2-triplon and 2-fermion sectors are still present in the final effective Hamiltonian.

ones. Because they involve only a small number of excitations. Our results show that the triplon gap is always identical or smaller than the spin-1 2-fermion excitation and hence the triplon gap is indeed the spin gap.

There are two similar possibilities for the $S = 0$ exciton gap. Because the singlon quasiparticle has total spin zero, the exciton gap can be either the singlon gap or the gap to the spin-0 2-fermion channel. It is found that there is a bound state in the singlet channel of 2-fermion sector which is indeed lower in energy than the singlon gap. Therefore the singlet bound state defines the $S = 0$ exciton gap.

It is not possible to decouple the 2-fermion sector from all other sectors. The exciton gap as well as the low-energy spectrum of the BI phase (see the next section) are calculated using the generator called $\eta_{t:2;f:2;s:1}$. This generator decouples the 2-fermion sector, the 2-triplon sector, and the 1-singlon sector as a whole from other quasiparticle sectors.

The off-diagonal interactions between these three sectors are present in the final effective Hamiltonian. This is due to the fact that the on-site energies of two fermions, two triplons, and one singlon are close to each other, see Eqs. (5.8b) and (5.8c). The structure of the final effective Hamiltonian is schematically shown in Fig. 5.3. The generator $\eta_{t:2;f:2;s:1}$ can be written down explicitly in the rather complicated form below

$$\begin{aligned}\eta_{t:2;f:2;s:1}(\ell) &= \eta_{t:0;f:0;s:0}(\ell)+\eta^{p}_{t:1;f:0;s:0}(\ell)+\eta^{p}_{t:0;f:1;s:0}(\ell)\\ &+\sum_{i+j+k\geq 2}\left(\hat{\eta}\left[H^{i,j,k}_{0,0,1}(\ell)\right]-\text{h.c.}\right)X^{i,j,k}_{2,0,0}X^{i,j,k}_{0,2,0}\\ &+\sum_{i+j+k\geq 2}\left(\hat{\eta}\left[H^{i,j,k}_{2,0,0}(\ell)\right]-\text{h.c.}\right)X^{i,j,k}_{0,2,0}\\ &+\sum_{i+j+k\geq 2}\left(\hat{\eta}\left[H^{i,j,k}_{0,2,0}(\ell)\right]-\text{h.c.}\right)X^{i,j,k}_{2,0,0},\end{aligned} \tag{5.21}$$

where the definitions (5.17) and (5.20) are used in the first line. It is seen that the off-diagonal interactions $H^{0,0,1}_{2,0,0}$, $H^{0,0,1}_{0,2,0}$, and $H^{2,0,0}_{0,2,0}$ are excluded from the generator (5.21) due to the definition (5.18).

The application of the generator (5.21) to the Hamiltonian (5.12) leads to an effective Hamiltonian with the general structure displayed in Fig. 5.3. The exciton gap is calculated by performing an exact diagonalization in the singlet channel of the Hilbert space composed of two fermions, two triplons, and one singlon. The employed exact diagonalization technique is valid in the thermodynamic limit and is described in Section 3.3. The basis states to construct the Hamiltonian matrix are given by

$$|K\rangle_s := \frac{1}{\sqrt{L}}\sum_r e^{iKr}\,|r\rangle_s \quad , \tag{5.22a}$$

$$|K,d\rangle^{S=0}_{tt} := \frac{1}{\sqrt{L}}\sum_r e^{iK\left(r+\frac{d}{2}\right)}\,|r,r+d\rangle^{S=0}_{tt}, \tag{5.22b}$$

$$|K,d\rangle^{S=0}_{f_lf_r} := \frac{1}{\sqrt{L}}\sum_r e^{iK\left(r+\frac{d}{2}\right)}\,|r,r+d\rangle^{S=0}_{f_lf_r}, \tag{5.22c}$$

$$|K,d\rangle^{S=0}_{f_rf_l} := \frac{1}{\sqrt{L}}\sum_r e^{iK\left(r+\frac{d}{2}\right)}\,|r,r+d\rangle^{S=0}_{f_rf_l}, \tag{5.22d}$$

where the lower index specifies that the state contains one singlon (s), two triplons (tt), or two fermions (f_lf_r or f_rf_l). The upper index $S=0$ specifies that the total spin of the state is zero. The distinguishability of the fermions f_l and f_r is taken into account in Eqs. (5.22c) and (5.22d). The spin states with total spin $S=0$ constructed from two fermions (2F) or two triplons (2T) are given by

$$|2F\rangle^{S=0} = \frac{1}{\sqrt{2}}\left(|f_\uparrow,f_\downarrow\rangle-|f_\downarrow,f_\uparrow\rangle\right), \tag{5.23a}$$

$$|2T\rangle^{S=0} = \frac{1}{\sqrt{3}}\left(|t_{+1},t_{-1}\rangle+|t_{-1},t_{+1}\rangle-|t_0,t_0\rangle\right), \tag{5.23b}$$

where $|f_{\sigma=\uparrow,\downarrow}\rangle$ and $|t_{m=0,\pm1}\rangle$ define the spin state of a single fermion and a single triplon, respectively. To construct the Hamiltonian matrix, one can again use the complete relations

reported in Appendix A paying attention to the fermionic minus sign. The Hamiltonian matrix is set up for the total momentum $K = 0$ where the minimum of the $S = 0$ exciton mode occurs (see Fig. 5.5).

Fig. 5.4 shows the behavior of the different gaps as functions of the Hubbard interaction U/δ for $t = 0.05\delta$. The results obtained from the BI limit are also included for comparison.[1] The results of BI limit are valid only up to the first transition point where the exciton gap closes. The charge gap Δ_c is calculated up to order 12 in the interdimer hopping from the dimerized limit and up to order 20 in the hopping parameter from the BI limit. Order 12 in the dimer limit corrsponds to a lattice spacing of 24 sites. The lattice spacing in the BI limit at order 20 is 20 sites. The finite order results are extrapolated to infinite order by performing a linear fit to the last four points similar to the right panel of Fig. 5.2 for the GSE per site. It is seen from Fig. 5.4 that the charge gap obtained from the dimer and BI limits are satisfactorily close to each other up to $U = 1.06\delta$ where the minimum of the charge gap of the dimer limit occurs. We take this minimum as an indication for the first transition point from BI phase to SDI phase [MMNS04].

Next, we focus on the exciton gap presented in Fig. 5.4. In the dimer limit analysis, order 6 is the maximum order that we can reach for this quantity. Higher orders are not accessible due to a divergence of the flow equations which arises from overlapping continua. The same problem appears for $U > 1.04\delta$. The results of the BI limit in order 12 in the hopping parameter are also shown for comparison. Again, the divergence of the flow equations prevents us to reach higher orders. The deviation between the two limits is expected to be mostly due to the low order calculations in the dimer limit. In both limits, the exciton gap is smaller than the charge gap indicating a singlet electron-hole bound state in the BI phase. The exciton gap obtained from BI limit vanishes at the critical interaction $U = 1.067\delta$ which is very close to the DMRG prediction of the first transition point 1.065δ [TNB09]. We expect, however, that the exciton gap of the dimer limit will just give us a non zero minimum near the transition point. This minimum will approach zero for high order calculations.

The spin gap (triplon gap) is obtained up to order 10 in the interdimer hopping parameter λt and plotted versus the interaction U in Fig. 5.4 for $t = 0.05\delta$. The results of order 8 almost coincide with the results of order 10 especially inside the BI phase. We have not extrapolated the spin gap because there is no clear linear behavior versus the inverse order up to order 10 for this quantity. Higher orders are necessary for an accurate extrapolation to infinite order.

It is seen from Fig. 5.4 that the spin gap and the charge gaps are very close up to $U = 1.05\delta$. The BI limit analysis identifies equal spin and charge gaps up to the transition point $U = 1.067\delta$. This allows us to estimate the error present in the finite order calculations of the spin gap. In fact, the spin gap at the transition point $U = 1.067\delta$ should be about 0.007δ smaller to match the BI limit results. If this amount of error for the spin gap is taken into account, one finds that the spin gap becomes soft at $U \simeq 1.10\delta$ which is close to the DMRG prediction of the second transition point, $U_{c2} \simeq 1.085\delta$ [TNB09].

[1] In the restricted IHM (4.13a), the sectors with finite number of double occupancies are already neglected and hence the BI limit analysis no longer requires the $D : 0$ step.

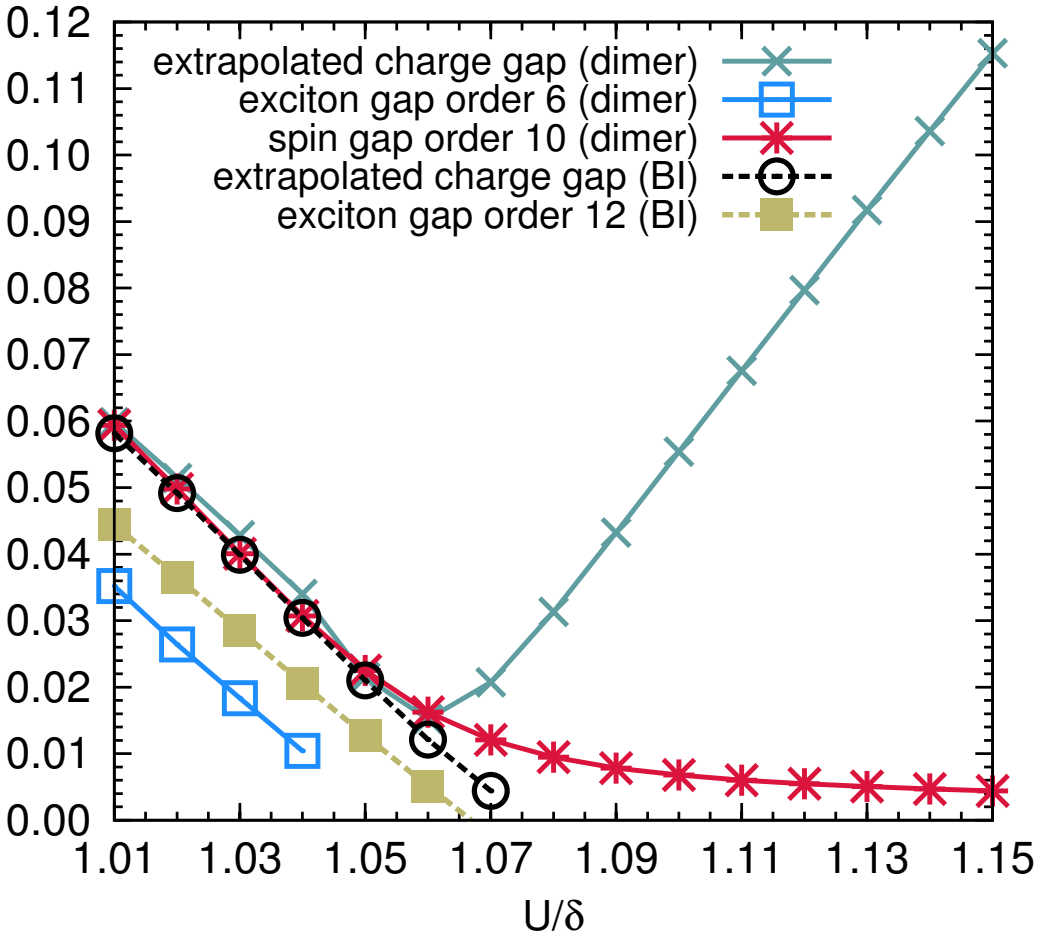

Figure 5.4: The charge gap, the exciton gap, and the spin (triplon) gap of the Hamiltonian (5.6) plotted versus the Hubbard interaction U/δ for the hopping parameter $t = 0.05\delta$. The results obtained from both band insulator (BI) limit (dashed lines) and the dimer limit (solid lines) are depicted for comparison.

Nevertheless, the spin gap in order 10 remains finite even for large values of the Hubbard interaction. This seems to contradict the fact that the MI phase stabilizes at the large-U limit [TNB09, MMNS04]. There is a manifest explanation for this finite spin gap that we find in the dimer limit analysis. The gapless MI phase in one dimension is unstable versus dimerization [Sch86]. Any finite dimerization will introduce a finite spin gap in the system [CF79]. The dimer limit analysis breaks the full translational symmetry of the initial Hamiltonian (5.6). This broken symmetry can never be restored in finite order calculations and consequently leads to a finite spin gap in the system. In the next section, we derive a low-energy effective Hamiltonian solely in terms of triplon operators for large values of the Hubbard interaction, $U \gtrsim 1.15\delta$. This low-energy Hamiltonian is analyzed using a second application of the deepCUT method. In this second deepCUT, we are able to calculate the spin gap up to orders much higher than 10. The finite order results plotted versus the inverse order show an obvious tendency towards zero.

5.3 Excitation Spectrum

The excitation spectrum of the IHM in the BI phase was discussed in the previous chapter from the BI limit. The BI limit, however, prevents us to have access to the SDI and to the MI phases of the model. In this section, using the dimer limit, we investigate the low-energy excitation spectrum of the restricted IHM (5.6) in the BI, in the SDI, and in the MI phases.

5.3.1 Band Insulator Phase

In the BI phase of the IHM, electrons and holes define the elementary excitations of the system. These fermionic quasiparticles can form singlet or triplet bound states. By starting from the dimer limit we have introduced three different kind of quasiparticles in the system: fermions, triplons, and singlons. It is interesting to see how well the deepCUT method starting from the dimer limit can reproduce the excitation spectrum of the BI phase.

The excitation spectrum of the restricted IHM (5.6) in the BI phase is obtained by using the generator (5.21) in the deepCUT method. As discussed in the previous section for the exciton gap, the generator $\eta_{t:2;f:2;s:1}$ maps the initial Hamiltonian (5.7) to an effective Hamiltonian with the general structure shown in Fig. 5.3. Because the 1-fermion and the 1-triplon sectors are decoupled from the remaining Hilbert space, the fermion and the triplon dispersions can be obtained by a simple Fourier transformation, see Eq. (3.35). In the derived effective Hamiltonian the 1-singlon, 2-fermion, and 2-triplon sectors as a whole are separated from all other sectors. But there are still off-diagonal interactions linking these three sectors to one another, see Fig. 5.3. The eigenvalues of the Hilbert space composed of the 1-singlon, 2-fermion, and 2-triplon subspaces are calculated by constructing the Hamiltonian matrix for each specific total momentum, total spin, and total magnetic number and performing an ED as explained in Section 3.3. For the channel with the total spin $S = 0$ this was described in the previous section in order to calculate the $S = 0$ exciton gap. The Hamiltonian matrix for the total spin $S = 1$ and the total magnetic numbers $M = 0, \pm 1$ is constructed from the 2-triplon state (5.22b) and the 2-fermion states (5.22c) and (5.22d). Clearly, the 1-singlon state (5.22a) is not needed for the triplet channel. The necessary 2-triplon spin states are given in Appendix C.2.

In Fig. 5.5, the low-energy excitation spectrum of the restricted IHM (5.6) for the parameters $U = 1.02\delta$ and $t = 0.05\delta$ is plotted versus the total momentum K. In this figure, the distance between two dimers, which is twice the distance between two sites, is considered as unit of length. The left panel of Fig. 5.5 shows the results obtained from the dimer limit. The BI limit results are depicted in the right panel for comparison[1]. We expect the BI limit results to be more accurate judging based on the convergence of different orders. We emphasize that in Fig. 4.6 the distance between two *sites* is considered as the unit of length. Therefore one needs to fold the excitation spectrum of the BI limit to the

[1]The BI limit results presented in the right panel of Fig. 5.5 are for the restricted IHM (4.13a) and therefore differ slightly from the left panel of Fig. 4.6 which is for the full IHM (4.12).

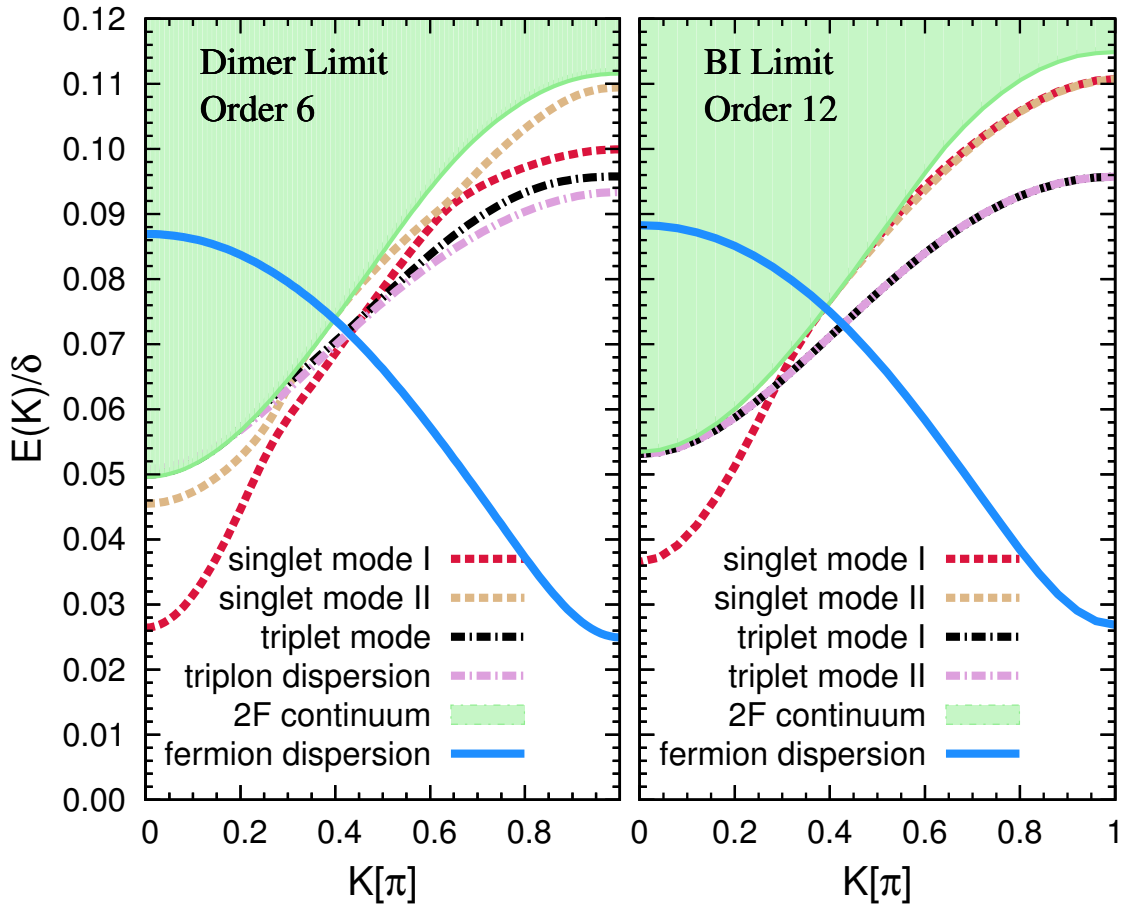

Figure 5.5: The low-energy excitation spectrum of Hamiltonian (5.6) for the hopping parameter $t = 0.05\delta$ and the Hubbard interaction $U = 1.02\delta$. For these values of the parameters, the system is in the band insulator phase. The green area indicates the 2-fermion (2F) continuum. The left panel shows the results calculated from the dimer limit analysis in order 6. In the right panel, the results of band insulator (BI) limit in order 12 is plotted for comparison. Two singlet bound states are found in both dimer limit and BI limit calculations. The two triplet modes I and II of the right panel are reproduced in the left panel as a triplet bound state and 1-triplon dispersion.

reduced BZ in order to make the comparison with the dimer limit results. Orders 12 and 6 are the maximum orders that we can reach in the BI limit and in the dimer limit analyses, respectively. The both analyses at these orders involve the same lattice extension. Because the range of processes taken into account in the BI limit is proportional to the order of calculations while it is twice the order in the dimer limit.

It is seen from the right panel of Fig. 5.5 that there are two singlet and two triplet bound states in the excitation spectrum obtained from the BI limit. The singlet mode II exists in the momentum range $\pi/2 \lesssim K \leq \pi$ and coincides with the singlet mode I. The two triplet bound states are on top of each other and exist almost in the whole range of momenta. The dimer limit yields also two singlet I and II bound states shown in the left panel of Fig. 5.5. The agreement of the BI limit and the dimer limit results is not perfect but remarkably good. The two singlet modes are not degenerate as in the BI limit findings. The

two triplet bound states I and II of the right panel are also reconstructed in the left panel. One of them has appeared as a triplet bound state between two fermions and the other is the triplon dispersion. The triplet bound state and the triplon dispersion are close to each other and the accuracy between the two limits is impressive in view of the very different starting points.

Because the Hamiltonian (5.6) has the full translational symmetry, the singlet modes I and II in the left panel of Fig. 5.5 must join in principle at the edge of BZ, $K = \pi$. The same statement is valid for the triplet bound state and the triplon dispersion in this panel. The energy differences which appear between the two triplet and between the two singlet modes at the total momentum $K = \pi$ in the left panel of Fig. 5.5 are a direct consequence of the broken translational symmetry at the starting point. The dimer limit breaks the translational symmetry which can never be recovered by an approximate treatment.

5.3.2 Spontaneously Dimerized Phase

The low-energy excitation spectrum of BI phase can be well-understood in terms of electron-hole pairs and their binding phenomena. In the MI phase, on the other hand, the charge degree of freedom is frozen and low-energy excitations are discussed in terms of spinons [FT81, dCP62] or triplons [SU03]. The competition between charge and spin degrees of freedom in the 1D IHM leads to the middle SDI phase. In this phase, both charge and spin excitations contribute to the low-energy spectrum of the system making it difficult to describe. The dimer limit that we consider in this chapter is especially suitable to investigate the SDI phase of the IHM. This is because the dimer limit takes the dimerization explicitly into account.

We present the results obtained by the deepCUT method for the fermion dispersion $\omega_f(K)$ and the triplon dispersion $\omega_t(K)$ in the SDI of the IHM. The fermion dispersion is obtained by use of the generator (5.16) targeting the ground state and the 1-fermion sector. Similarly, the triplon dispersion is calculated by the generator (5.19) targeting the ground state and the 1-triplon sector. The order of calculations is 12 for the fermion dispersion and it is 10 for the triplon dispersion in the interdimer hopping. The fermion dispersion (1F) and the triplon dispersion (1T) are plotted in Fig. 5.6. The 2-triplon (2T) continuum and the 2-fermion (2F) continuum are also shown. The hopping parameter and the Hubbard interaction in this figure are fixed to $t = 0.05\delta$ and $U = 1.08\delta$. The rescaled DMRG data presented in Ref. [TNB09] indicates that for $t = 0.05\delta$ the SDI phase exists from $U_{c1} = 1.065\delta$ to $U_{c2} \simeq 1.085\delta$. Therefore, for $U = 1.080\delta$ we expect to be inside the SDI phase of the IHM (5.6).

Fig. 5.6 shows that both the spin and the charge excitations contribute to the low-lying excitation spectrum of the system. In addition to the lower $\omega_{2T,-}(K)$ and the upper $\omega_{2T,+}(K)$ bands of the 2-triplon continuum we have also specified the lower band $\omega_{2F,-}(K)$ of the 2-fermion continuum which is inside the 2-triplon continuum. The fermion dispersion takes its minimum at the total momentum $K = \pi$. The fermion dispersion enters the 2-triplon continuum at $K \simeq 0.6\pi$ and it enters the 2-fermion continuum at $K \simeq 0.35\pi$. The triplon

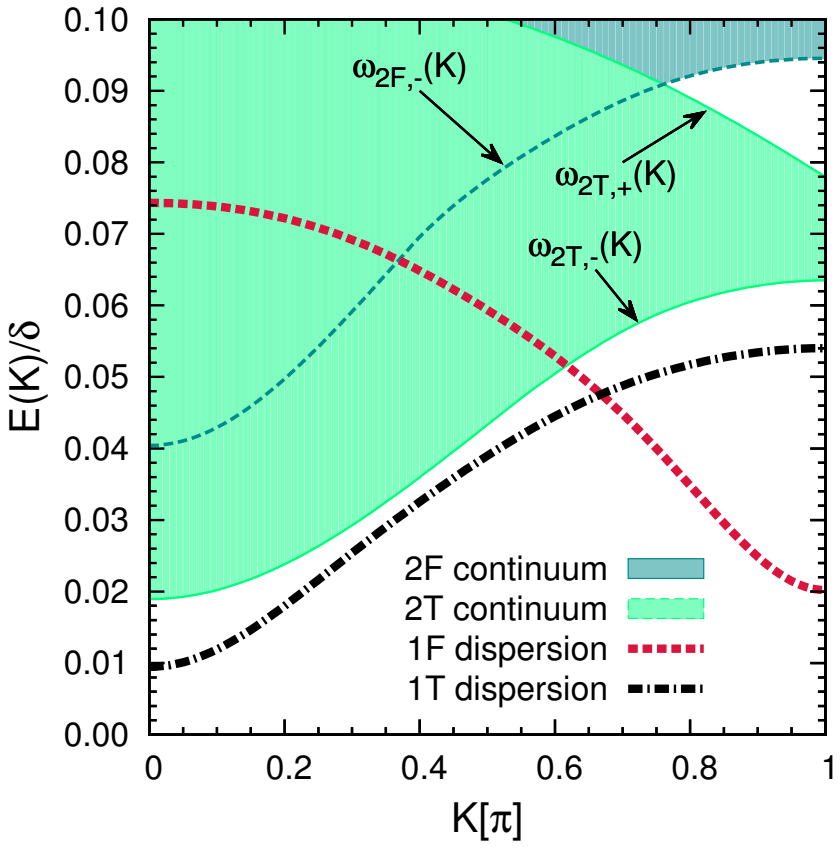

Figure 5.6: The low-energy spectrum of Hamiltonian (5.6) for the hopping parameter $t = 0.05\delta$ and the Hubbard interaction $U = 1.08\delta$. The order of calculations for the fermion (1F) dispersion is 12 and for the triplon (1T) dispersion it is 10. The 2-fermion (2F) continuum and the 2-triplon (2T) continuum are shown as solid region. We have also specified the lower $\omega_{2T,-}(K)$ and the upper band $\omega_{2T,+}(K)$ of the 2-triplon continuum as well as the lower band $\omega_{2F,-}(K)$ of the 2-fermion continuum.

dispersion is maximum at $K = \pi$ and stands always lower in energy than the 2-triplon continuum. Hence no quasiparticle decay occurs.

The contribution of the charge excitation to the low-energy spectrum in Fig. 5.6 indicates that the SDI phase is indeed very difficult to be described by a purely effective spin Hamiltonian either in terms of spinons or triplons. The electron-hole picture is also not suitable to explain the energy spectrum shown in Fig. 5.6. In the electron-hole language, the triplon dispersion has to appear as a $S = 1$ exciton bound state. One can see from Fig. 5.6 that this exciton mode has a large binding energy defined as the energy difference between the triplon dispersion and the lower band of the 2-fermion continuum $\omega_{2F,-}(K)$. This large binding energy indicates a strong electron-hole interaction, at least, in the $S = 1$ channel. In addition to the triplon dispersion, there are also some parts of the 2-triplon continuum in Fig. 5.6 lying below the 2-fermion continuum. This continuous region has also to be reproduced as $S = 0$ and $S = 1$ bound states between electrons and holes. All these points clarify the difficulties to describe the SDI phase of the IHM in terms of electrons and holes as elementary excitations of the system.

In the previous chapter we derived an effective Hamiltonian using the deepCUT method and described the SDI phase by a mean-field theory. In this approach we introduced fermionic QPs above the mean-field ground state. We focused on the 1-fermion sector to calculate the charge gap. It would be very interesting to analyze also the 2-fermion sector and see how these fermionic excitations can reproduce the results of Fig. 5.6. However, such an analysis is not considered the present thesis.

Beside the dimer representation, the SDI phase of the IHM can also be conveniently described in terms of spinons and holons. Spinons are spin-1/2 QPs and charge neutral. In contrast, holons carry total charge e but no spin. In this QP representation, the fermion dispersion in Fig. 5.6 appears as a bound state between a spinon and a holon. It is expected that 2-spinon will form a $S = 1$ bound state leading to the triplon dispersion in Fig. 5.6. This is an investigation which requires attention in the future.

5.3.3 Mott Insulator Phase

The excitation spectrum of the gapless MI phase in 1D is usually described in terms of spin-1/2 quasiparticles called spinons. But the triplon language is an alternative to investigate the MI phase [SU03]. Evidence is provided by the fact that about 99% of the spectral weight is concentrated in the sector with only two triplons [SU03], see Fig. 1.1. This contribution is even larger than the contribution of 2-spinon state to the spectral weight which is about 73% [KMB+97]. Hence, we proceed with the dimer limit to discuss the MI phase of the IHM as well.

It is seen from Fig. 5.4 that the energy difference between the charge gap and the spin gap increases upon increasing the Hubbard interaction beyond the first transition point. This suggests that at large values of the Hubbard interaction in the MI phase the charge fluctuations lie very high in energy and that the triplon fluctuations determine the low-energy physics of the system. Therefore, in a first step, it is convenient to derive an effective low-energy Hamiltonian describing the MI phase of the IHM. To this end, the generator $\eta_{f:0;s:0}(\ell)$ is defined to separate the sector with zero number of fermions *and* singlons from the sectors which contain a finite number of fermions and singlons. One should notice that the sector without singlon and fermion still includes triplon fluctuations. The generator $\eta_{f:0;s:0}(\ell)$ is given by

$$\eta_{f:0;s:0}(\ell) \equiv \sum_{j,k} \left(H^{j,k}_{0,0}(\ell) - H^{0,0}_{j,k}(\ell) \right), \tag{5.24}$$

where $H^{j,k}_{0,0}(\ell)$ stands for the part of the Hamiltonian which annihilates zero number of fermions and singlons and creates j fermions and k singlons without caring about the change in the number of triplons. The application of the generator (5.24) to the initial Hamiltonian (5.12) leads to an effective Hamiltonian whose low-energy part is decoupled from the high-energy sectors. The charge degree of freedom in the final effective Hamiltonian is separated from the low-energy physics of the IHM which is determined by a Hamiltonian only in terms of triplon operators.

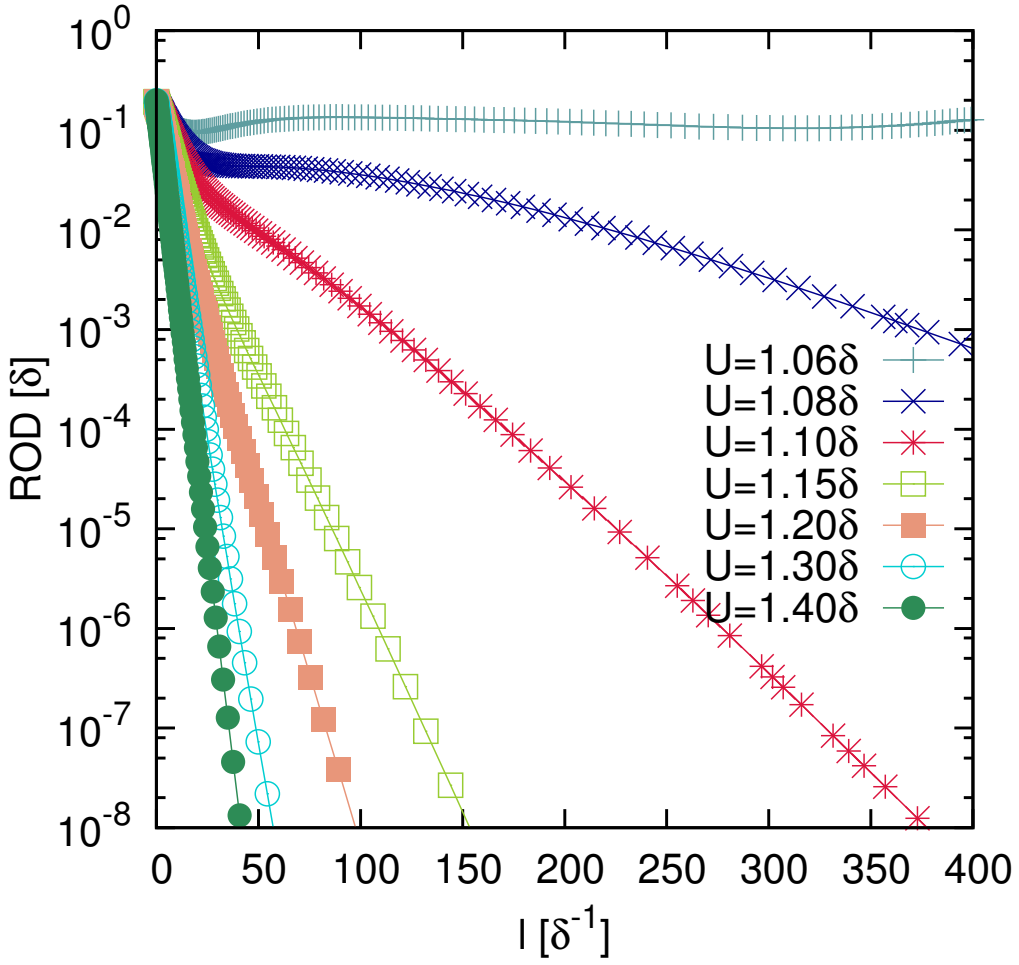

Figure 5.7: The residual off-diagonality (ROD) for the generator $\eta_{f:0;s:0}$ depicted versus the flow parameter ℓ for various values of the Hubbard interaction U. The hopping parameter $t = 0.05\delta$ and the expansion parameter $\lambda = 1.0$. The order of calculations is 6. It is seen that for larger values of the interaction U, a faster convergence in the flow equations is achieved.

In order to check the convergence of the flow equations for the generator (5.24), the residual off-diagonality (ROD) (3.30) is plotted in Fig. 5.7 versus the flow parameter ℓ for various values of the Hubbard interaction U. The hopping parameter in this figure is fixed to 0.05δ. The order of the calculations is 6 and we target all the monomials composed of triplon operators only. Fig. 5.7 shows that the convergence of the flow equations becomes faster by increasing the Hubbard interaction. This is due to the larger energy separation between the sector without singlons and fermions and the sectors containing a finite number of them. We expect the effective triplon Hamiltonian to be reliable for $U \gtrsim 1.15\delta$ where a very fast and robust convergence of ROD is found. For a more accurate statement, however, we need to reach high orders and check the convergence of the coefficients of the final effective Hamiltonian. The transition from the SDI to the MI phase is predicted by DMRG to take place at $U \simeq 1.085\delta$ [TNB09]. Therefore, the low-energy triplon Hamiltonian may fail to describe the system near the MI-to-SDI transition and remains valid only inside the MI phase.

#	Monomial	Order
0	$\sum_j \mathbb{1}$	0
1	$\sum_j t^\dagger_{j,0} t_{j,0}$	0
2	$\sum_{j,m} t^\dagger_{j,m} t_{j,m}$	0
3	$\sum_j \left(t^\dagger_{j,0} t_{j+1,0} + \text{h.c.} \right)$	2
4	$\sum_{j,m} \left(t^\dagger_{j,m} t_{j+1,m} + \text{h.c.} \right)$	2
5	$\sum_j \left(t^\dagger_{j,0} t^\dagger_{j+1,0} + \text{h.c.} \right)$	2
6	$\sum_{j,m} \left(t^\dagger_{j,m} t^\dagger_{j+1,\bar{m}} + \text{h.c.} \right)$	2
7	$\sum_{j,m} \left(t_{j,m} t^\dagger_{j+1,m} t_{j+1,0} - t_{j+1,m} t^\dagger_{j,m} t_{j,0} + \text{h.c.} \right)$	2
8	$\sum_{j,m} \left(t_{j,0} t^\dagger_{j+1,m} t_{j+1,m} - t_{j+1,0} t^\dagger_{j,m} t_{j,m} + \text{h.c.} \right)$	2
9	$\sum_{j,m} \left(t_{j,m} t^\dagger_{j+1,0} t_{j+1,\bar{m}} - t_{j+1,m} t^\dagger_{j,0} t_{j,\bar{m}} + \text{h.c.} \right)$	2
10	$\sum_{j,m} t^\dagger_{j,m} t_{j,m} t^\dagger_{j+1,m} t_{j+1,m}$	2
11	$\sum_j t^\dagger_{j,0} t_{j,0} t^\dagger_{j+1,0} t_{j+1,0}$	2
12	$\sum_{j,m} t^\dagger_{j,m} t_{j,m} t^\dagger_{j+1,\bar{m}} t_{j+1,\bar{m}}$	2
13	$\sum_{j,m} \left(t^\dagger_{j,m} t_{j,0} t^\dagger_{j+1,\bar{m}} t_{j+1,0} + \text{h.c.} \right)$	2
14	$\sum_{j,m} \left(t^\dagger_{j,m} t_{j,0} t^\dagger_{j+1,0} t_{j+1,m} + \text{h.c.} \right)$	2
15	$\sum_{j,m} \left(t^\dagger_{j,m} t_{j,m} t^\dagger_{j+1,0} t_{j+1,0} + t^\dagger_{j+1,m} t_{j+1,m} t^\dagger_{j,0} t_{j,0} \right)$	2

Table 5.2: All the monomials which appear in the effective triplon Hamiltonian up to minimal order 2 in the perturbative parameter λ. The summation j runs over dimers and the summation over m takes the two values $+1$ and -1. We define $\bar{m} = -m$. It is seen that in order 2 each monomial can affect at most two nearest-neighbor dimers.

We fix the order of calculations in the first step $\eta_{f:0;s:0}$ to 6 in the perturbative parameter λ. All the monomials appearing in the derived low-energy triplon Hamiltonian are of even order. In Table 5.2 they are listed up to order 2. The lattice extension of each monomial is equal or less than half of its minimal order. This means that, for example, all monomials with minimal order 2 can at most act on two nearest-neighbor dimers. This feature helps us to use the simplification rules implemented in Ref. [KDU12] in the subsequent deepCUT analysis of the effective triplon Hamiltonian. From now on, we switch the perturbative parameter from λ to $J := \lambda^2$ and present all results in orders of J.

The effective triplon Hamiltonian is mapped to a final effective Hamiltonian by a second application of the deepCUT method. In the final Hamiltonian the ground state and the 1-triplon sector are separated from higher triplon sectors. The triplon dispersion $\omega_t(K)$ is easy

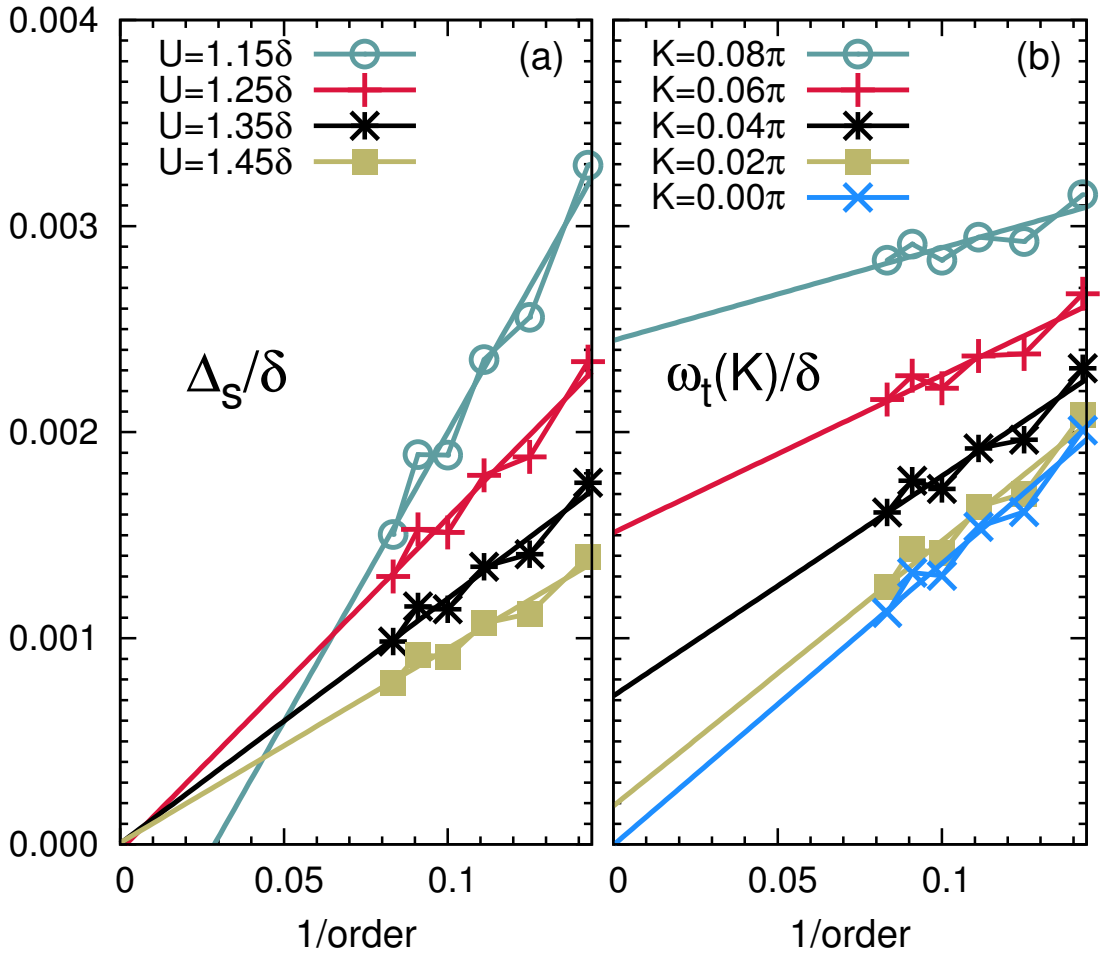

Figure 5.8: Left panel: The spin gap Δ_s versus the inverse order of $J := \lambda^2$ for different values of the Hubbard interaction U. Right panel: The triplon dispersion $\omega_t(K)$ for fixed values of the total momentum K versus the inverse order for the Hubbard interaction $U = 1.3\delta$. In both panels the hopping parameter is set to $t = 0.05\delta$ and the expansion parameter is $\lambda = 1.0$. The finite order results are extrapolated to infinite order by a linear fit to the last 6 points.

to read off. The minimum of the triplon dispersion occurs at the total momentum $K = 0$ and subsequently we find the spin (triplon) gap $\Delta_s = \omega_t(0)$. In this second step of the deepCUT, one needs to deal only with the triplon operators. This allows us to reach much higher orders compared to the case where all the dimer operators (5.10) were present. We have been able to reach order 12 in the expansion parameter J or equivalently 24 in λ. This maximum order is much higher than the order of calculations for the spin gap in Fig. 5.4.

In the left panel of Fig. 5.8, the spin gap Δ_s is plotted versus the inverse order in J for various values of the Hubbard interaction U. The hopping parameter is fixed to $t = 0.05\delta$ and $\lambda = 1.0$. The finite order results are extrapolated to infinite order by a linear fit. The extrapolated spin gap is lower than $10^{-4}\delta$ for the Hubbard interaction $U = 1.25\delta$ and lower than $10^{-5}\delta$ for the interactions $U = 1.35\delta$, and $U = 1.45\delta$. For $U = 1.15\delta$, however, the linear fit leads to a negative value for the spin gap. This inadequacy may stem from two origins. The first one is the linear extrapolation. As we decrease the Hubbard interaction

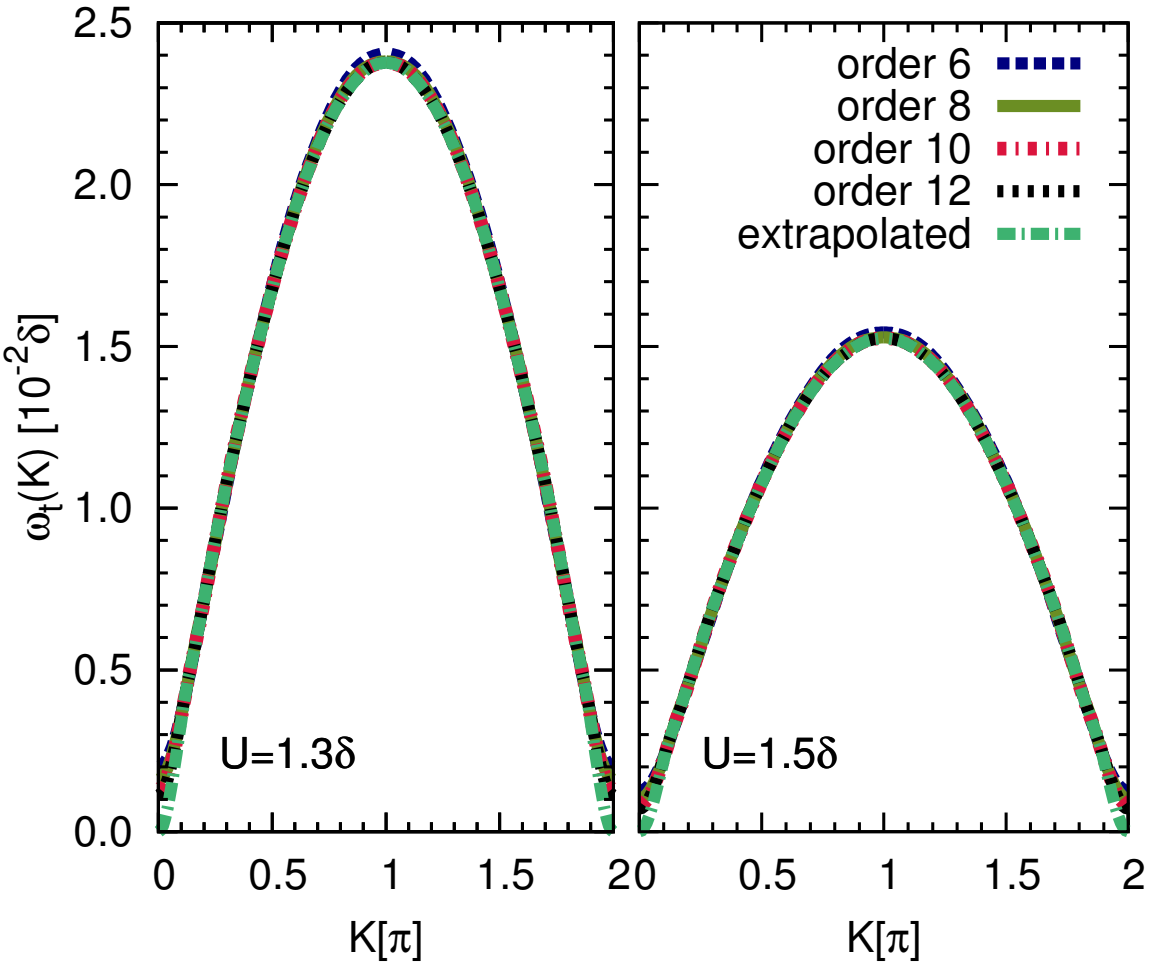

Figure 5.9: The triplon dispersion $\omega_t(K)$ plotted versus the total momentum K in the Brillouin zone. The hopping parameter is fixed to $t = 0.05\delta$ and the expansion parameter $\lambda = 1.0$. The left panel is for the Hubbard interaction $U = 1.3\delta$ and the right panel is for $U = 1.5\delta$. The largest deviation between different orders occurs at $K = 0$ and 2π. A gapless triplon dispersion is obtained by extrapolating the finite order results to infinite order.

and approach the MI-to-SDI transition point, the correlation length of the system becomes large. Hence near the transition point, one needs to reach orders high enough to obtain the linear behavior of the spin gap versus the inverse order. The maximum order 12 probably is not high enough to identify this linear behavior.

The error in the derivation of the low-energy triplon Hamiltonian is the second reason for finding the negative spin gap at $U = 1.15\delta$. We targeted a large number of monomials in the deepCUT method to derive the effective triplon Hamiltonian. A small error in this first application of the deepCUT may lead to a considerable error in the final spin gap. We believe that the latter effect is indeed dominating.

The triplon dispersion $\omega_t(K)$ for fixed values of the total momentum K is plotted versus the inverse order in the right panel of Fig. 5.8. The total momenta are chosen to be near $K = 0$ where the largest deviation between the results of different orders happens. The Hubbard interaction U is fixed to 1.3δ and the hopping parameter t is 0.05δ. Again a

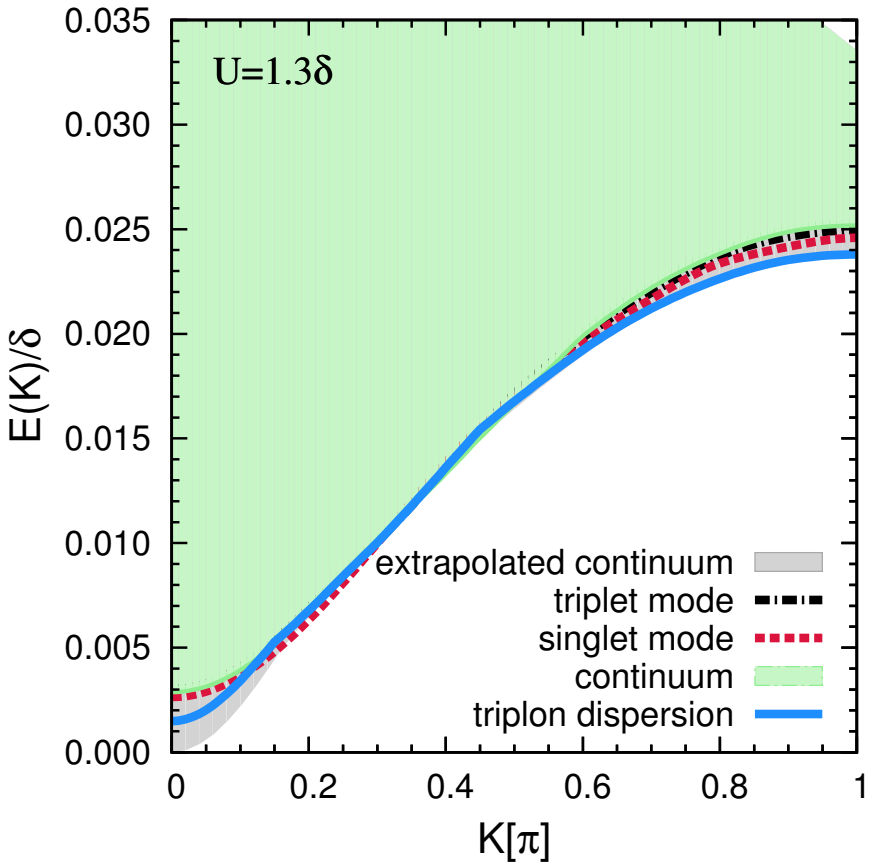

Figure 5.10: The low-energy spectrum of the restricted ionic Hubbard model (5.6) for $t = 0.05\delta$ and $U = 1.3\delta$. There is one singlet and one triplet bound state with very small binding energy. However, these bound states lie inside the 2-triplon continuum if it is constructed from the *extrapolated* triplon dispersion which is gapless at the total momentum $K = 0$, see Fig. 5.9.

linear fit is performed to extrapolate the triplon dispersion at fixed total momenta to infinite order. This extrapolation leads to a triplon dispersion which is gapless within the accuracy of the approach.

The triplon dispersion versus the total momentum K in the whole BZ is depicted in Fig. 5.9. The hopping parameter in this figure is $t = 0.05\delta$. The Hubbard interaction in the left panel and in the right panel is set to $U = 1.3\delta$ and $U = 1.5\delta$, respectively. In each panel, various finite order results and the extrapolated result are shown for comparison. The triplon dispersions at high orders are on top of each other except near the total momentum $K = 0$ and the equivalent point $K = 2\pi$. For these two total momenta, the finite order results always lead to a finite spin gap while the extrapolated result indicates a gapless mode. This gapless dispersion is what we expect in a MI phase. It is also interesting to notice the change in the bandwidth of the triplon dispersion in Fig. 5.9. As the Hubbard interaction decreases from $U = 1.5\delta$ in the right panel to $U = 1.3\delta$ in the left panel, the bandwidth of the triplon dispersion increases. This resembles the fact that the characteristic magnetic energy scale in the IHM is $\propto t^2/(U - \delta)$.

We analyzed the 2-triplon sector of the low-energy triplon Hamiltonian looking for possible bound states. We have not been able to decouple the 2-triplon sector completely due to a divergence in the flow equations. Instead, the 1-triplon sector is decoupled and the remaining off-diagonal interactions are taken into account by an exact diagonalization for the 2- and the 3-triplon states. The necessary spin states made from triplons with specific magnetic quantum numbers (5.10b) can be found in Appendix C.2. The low-energy spectrum including triplon dispersion, 2-triplon continuum, and singlet and triplet bound states are depicted in Fig. 5.10. The hopping parameter is fixed to $t = 0.05\delta$ and the Hubbard interaction $U = 1.3\delta$. The order of deepCUT is 8 in the perturbative parameter J. We have targeted diagonal interactions up to the 3-QP sector plus the off-diagonal interaction linking the 2- and 3-QP sectors. One singlet and one triplet bound state with very small binding energy is found. However, these bound states lie inside the 2-triplon continuum constructed from *extrapolated* triplon dispersion which is gapless at $K = 0$, see Fig. 5.9. The singlet and the triplet bound modes might appear as resonance states in a study of spectral densities.

The vanishing of the spin gap and the stabilization of the MI phase in the 1D IHM has been discussed somewhat ambiguously using Quantum Monte Carlo [WM01] and DMRG [KSJB03] methods, see Figs. 2.7 and 2.9 and the descriptions therein. Although the position of the second transition point from the SDI to the MI phase is not determined accurately in our investigation, it is found that the MI phase does stabilize in the large-U limit. In addition, we have obtained quantitative results for the excitation spectrum of the IHM in the MI phase. Our results suggest that the dimer limit can be used as a suitable starting point for CUT-based methods such as the deepCUT [KDU12], the perturbative CUT [KU00], and the graph-based CUT [YS11] to analyze the gapless MI phase in one dimension.

5.4 Chapter Summary

The ionic Hubbard model (IHM) is investigated by use of the deepCUT method starting from the dimer limit. The advantage of the dimer limit compared to the band insulator (BI) limit introduced in the previous chapter is that it enables us to describe all the three phases of the IHM. The IHM contains both spin and charge fluctuations which leads to a 16-dimensional Hilbert space on each dimer. For the range of model parameters $t \ll \delta, U$, the size of the local Hilbert space is reduced to 9 by ignoring the doubly occupied states on even sites and the empty states on odd sites. The restricted IHM involves eight local excitations above the vacuum: Four fermions, three triplons, and one singlon.

In a first step, we analyse the ground state energy of the system by decoupling the vacuum from all higher quasiparticle sectors. The comparison between the dimer limit and the BI limit results for the ground state energy suggests $U_{c1} = 1.075\delta$ for the transition point from the BI phase to the spontaneously dimerized insulator (SDI) phase. This is to be compared with the DMRG results $U_{c1} = 1.065\delta$ for the position of the first transition point [TNB09]. In the next step, we investigate the charge gap, the exciton gap, and the spin gap. The charge gap is obtained by decoupling the vacuum and the 1-fermion sector

from the remaining Hilbert space. The spin gap is found to be identical with the triplon gap accessible by decoupling the ground state and the 1-triplon sector from other sectors. It turns out that the exciton gap is given by a $S = 0$ bound state in the 2-fermion sector and not simply by the singlon gap. This requires to determine the eigenvalues in the 2-fermion subspace which are obtained by a combination of deepCUT and exact diagonalization.

The different gaps calculated from the dimer limit agree nicely with the BI limit results in the BI phase. Moreover, the dimer limit results are valid beyond the first transition point in the SDI and in the Mott insulator (MI) phases. The minimum of the charge gap, which indicates the first transition point, occurs at $U = 1.06\delta$ and the charge gap starts to increase beyond this point. The spin gap, on the other hand, continues to decrease and becomes very small for large values of the Hubbard interaction U. However, the finite order deepCUT results always yield a finite spin gap even in the large-U limit. This is interpreted as a consequence of the broken translational symmetry in the dimer limit analysis.

In addition to the ground state energy and energy gaps, the momentum-dependent excitation spectrum of the IHM in the BI, in the SDI, and in the MI phases are addressed in this chapter using the dimer limit analysis. In the BI phase, we are able to satisfactorily reproduce the excitation spectrum found from the BI limit. For instance, two triplet bound states found in the BI limit analysis are reproduced in the dimer limit. One of them appears as the triplon dispersion and the other as a 2-fermion bound state. In the SDI phase, both spin and charge excitations contribute to the low-energy spectrum. We present the results for the 1-fermion and for the 1-triplon dispersions in the SDI phase. For large values of the Hubbard interaction where the IHM is in the MI phase, we derive a low-energy effective Hamiltonian purely in terms of triplon operators. This effective triplon Hamiltonian is analyzed by a second step deepCUT. High order results extrapolated to infinite order indicate that the spin gap vanishes and that the MI phase stabilizes. We obtain reliable results for the gapless triplon dispersion in the MI phase.

Summary and Outlook

The description of strongly correlated materials is among the most difficult problems of physics today. The strong electron-electron interaction present in these systems hampers any perturbative analysis around the non-interacting limit. This calls for the development and application of new perturbative and renormalizing techniques. The continuous unitary transformations (CUT) method allows us to map a given initial Hamiltonian to final effective Hamiltonians in a systematic fashion [Weg94]. The CUT idea defines the cornerstone of various perturbative [KU00] and renormalizing [HU02, YS11] approaches in and out of equilibrium [HK09, TK11].

We use the recently developed *directly evaluated enhanced perturbative CUT* (deepCUT) method [KDU12] to study the excitation spectrum and quantum phase transitions in the one-dimensional (1D) ionic Hubbard model (IHM). The model is suggested as a minimal model to describe the neutral-ionic transition observed in mixed-stack organic charge-transfer compounds [NT86] as well as the ferroelectricity in transition metal oxides [EIT93]. The IHM consists of three terms: A nearest-neighbor (n.n.) hopping, the Hubbard interaction, and an ionic (staggered) potential separating the odd and even sites energetically. In one dimension, the model experiences two continuous phase transitions upon increasing the Hubbard interaction [FGN99, MMNS04]. The first transition occurs from the band insulator (BI) phase to the spontaneously dimerized insulator (SDI) phase. This transition lies in the Ising universality class where the gap behaves linearly up on approaching the transition point. The second transition takes place from the SDI to the quasi-long-range Mott insulator (MI) phase. The relevant gap vanishes exponentially slowly as in a the Kosterlitz-Thouless transition.

We study the IHM starting from two different limits by the deepCUT method. First, we consider the BI limit where electrons and holes are the relevant elementary excitations (quasiparticles, QPs). This BI limit is suitable to investigate the properties of the model in the BI phase. We obtain quantitative results for the fermion dispersion, 2- and 3-fermion continua, and singlet and triplet bound states almost up to the first transition point. We compare our results for the charge gap, the exciton gap, and the spin gap with DMRG results finding a nice agreement between the two approaches. The transition to the SDI phase is signaled by the softening of a $S = 0$ exciton mode. Beyond the transition point, the excitons begin to condense and the QP picture we started with breaks down. We analyze the effective Hamiltonian derived from the deepCUT by a BCS-type-theory to show the stabilization of the SDI phase. Unfortunately, this mean-field solution exhibits no second phase transition to the MI phase. We interpret this deficiency as the effect of strong quantum fluctuations

in one dimension which are neglected in mean-field analysis. In the mean-field treatment, we also ignore the hardcore property of the fermionic operators. This hardcore constraint can be satisfied either on average by a slave-particle mean-field theory [Vae11] or strictly by Brückner approach [KSWO98]. As an alternative to the mean-field theory, one can implement a new CUT step to describe the middle phase and its transition to the MI phase. This requires to identify the elementary excitations in the SDI phase. One possibility is to write the hardcore fermionic operators appearing in the effective Hamiltonian in terms of holons and spinons. Still the application of the CUT method in real space leads to difficulties due to the large correlation length of the system. A momentum space implementation is much more sophisticated. Treating spinons as QPs in the CUT method and the application of CUT in momentum space are both interesting projects which need attention in the future.

We emphasize that by the combination of deepCUT and mean-field approximation even in the leading order of the deepCUT we can correctly identify the nature of the middle phase in the IHM. This is remarkable because finite-size exact diagonalization requires at least 50 lattice sites to identify the SDI phase in the IHM as is pointed out in a quantum Monte Carlo (QMC) analysis [WM01]. Our strategy can be employed to investigate the nature of the intermediate phase of the IHM in two dimensions which is currently disputed [GKR06, PBH$^+$07, KD07, CZLW10]. It would be very interesting to see which excitation becomes soft in transition from the BI phase to the middle phase and at which momentum this happens. The mean-field part is expected to work even better in higher dimensions. The BI limit introduced in chapter 4 can also be used to study other Hamiltonians such as Hubbard models with n.n. interaction, 2-band Hubbard models, and so on.

We introduce the dimer limit analysis in order to describe the SDI and MI phases. This dimer limit allows us to access different phases in the IHM. We calculate the ground state energy and different gaps and discuss the phase transitions of the model. Moreover, we address the excitation spectrum of the IHM in the BI, in the SDI, and in the MI phases. We show that the dimer limit can reproduce the BI limit results of the BI phase. Quantitative results for the gapless triplon dispersion in the MI phase is reported. The high energy parts of the triplon dispersion converge quickly by increasing the order of calculations in the deepCUT. In contrast, the low-energy part of the dispersion becomes gapless only after extrapolating the finite order results to infinite order. We interpret the finite spin gap found in finite order calculations as a consequence of the instability of the quasi-long-range MI phase in one dimension versus dimerization.

The dimer limit as starting point of the deepCUT method can be used to investigate some other important problems as well. This dimer limit is especially useful to study the ladder structures. An example would be the $t-J$ model defined on 2-leg ladder which is an interesting issue in the context of superconductivity [Dag94, DR96]. The 1-hole dispersion of the model is already studied using the self-similar CUT (sCUT) method [DU11]. However, the evaluation of 2-hole sector is necessary in order to investigate the Cooper pair formation. The deepCUT method defines a much more systematic truncation scheme of the flow equations compared to the sCUT method especially if different kinds of excitations are present in the system. The deepCUT method by decoupling the 2-hole sector will yield effective Hamiltonians useful to describe the superconductivity in the $t-J$ model. In the next step, one can use these effective Hamiltonians to study the stripe-ordered superconductors

by linking 2-leg ladders via an additional interladder coupling [USG04].

Appendix A

Analysis of Effective Hamiltonians

In this section, the action of the different parts of the Hamiltonian (3.31) on the states (3.32) is presented. The results are obtained for a purely fermionic problem. However, they are in principle applicable to either bosonic or fermionic algebra or even to an algebra composed of both fermionic and bosonic operators. The user has to take care only about the fermionic signs which appear in front of the prefactors.

A.1 $H_{1:1}$

The action of the operator $H_{1:1}$ on the 1-QP state $|K\rangle$ is given by

$$H_{1:1}\,|K,\sigma\rangle = \sum_n \sum_\beta e^{iKn} \, {}^{\beta}_{\sigma}\Big[\mathcal{C}_1^1\Big]^n \,|K,\beta\rangle \tag{A.1}$$

with the definition

$${}^{\beta}_{\sigma}\Big[\mathcal{C}_1^1\Big]^n = \langle r-n,\beta|\,H_{1:1}\,|r,\sigma\rangle\,. \tag{A.2}$$

For the action of $H_{1:1}$ on the 2-QP state $|K,\sigma_1;d,\sigma_2\rangle$, we find

$$\begin{aligned} H_{1:1}\,|K,\sigma_1;d,\sigma_2\rangle = \;& + \sum_{n>-d}\sum_{\beta_1} e^{iK\frac{n}{2}} \, {}^{\beta_1}_{\sigma_1}\Big[\mathcal{C}_1^1\Big]^n \,|K,\beta_1;+d+n,\sigma_2\rangle \\ & - \sum_{n<-d}\sum_{\beta_1} e^{iK\frac{n}{2}} \, {}^{\beta_1}_{\sigma_1}\Big[\mathcal{C}_1^1\Big]^n \,|K,\sigma_2;-d-n,\beta_1\rangle \\ & + \sum_{n<d}\sum_{\beta_2} e^{iK\frac{n}{2}} \, {}^{\beta_2}_{\sigma_2}\Big[\mathcal{C}_1^1\Big]^n \,|K,\sigma_1;+d-n,\beta_2\rangle \\ & - \sum_{n>d}\sum_{\beta_2} e^{iK\frac{n}{2}} \, {}^{\beta_2}_{\sigma_2}\Big[\mathcal{C}_1^1\Big]^n \,|K,\beta_2;-d+n,\sigma_1\rangle\,. \end{aligned} \tag{A.3}$$

The action of $H_{1:1}$ on the 3-QP state $|K,\sigma_1;d_1,\sigma_2;d_2,\sigma_3\rangle$ leads to 9 contributions given below

$$
\begin{aligned}
&H_{1:1}\,|K,\sigma_1;d_1,\sigma_2;d_2,\sigma_3\rangle = \\
&+ \sum_{n>-d_1} \sum_{\beta_1} e^{iK\frac{n}{3}} \begin{matrix}\beta_1\\ \sigma_1\end{matrix}\Big[\mathcal{C}_1^1\Big]^n |K,\beta_1;+d_1+n,\sigma_2;+d_2,\sigma_3\rangle \\
&- \sum_{-(d_1+d_2)<n<-d_1} \sum_{\beta_1} e^{iK\frac{n}{3}} \begin{matrix}\beta_1\\ \sigma_1\end{matrix}\Big[\mathcal{C}_1^1\Big]^n |K,\sigma_2;-d_1-n,\beta_1;d_1+d_2+n,\sigma_3\rangle \\
&+ \sum_{n<-(d_1+d_2)} \sum_{\beta_1} e^{iK\frac{n}{3}} \begin{matrix}\beta_1\\ \sigma_1\end{matrix}\Big[\mathcal{C}_1^1\Big]^n |K,\sigma_2;+d_2,\sigma_3;-d_1-d_2-n,\beta_1\rangle \\
&+ \sum_{-d_2<n<d_1} \sum_{\beta_2} e^{iK\frac{n}{3}} \begin{matrix}\beta_2\\ \sigma_2\end{matrix}\Big[\mathcal{C}_1^1\Big]^n |K,\sigma_1;d_1-n,\beta_2;d_2+n,\sigma_3\rangle \\
&- \sum_{n<-d_2} \sum_{\beta_2} e^{iK\frac{n}{3}} \begin{matrix}\beta_2\\ \sigma_2\end{matrix}\Big[\mathcal{C}_1^1\Big]^n |K,\sigma_1;d_1+d_2,\sigma_3;-d_2-n,\beta_2\rangle \\
&- \sum_{n>d_1} \sum_{\beta_2} e^{iK\frac{n}{3}} \begin{matrix}\beta_2\\ \sigma_2\end{matrix}\Big[\mathcal{C}_1^1\Big]^n |K,\beta_2;-d_1+n,\sigma_1;d_1+d_2,\sigma_3\rangle \\
&+ \sum_{n<d_2} \sum_{\beta_3} e^{iK\frac{n}{3}} \begin{matrix}\beta_3\\ \sigma_3\end{matrix}\Big[\mathcal{C}_1^1\Big]^n |K,\sigma_1;d_1,\sigma_2;d_2-n,\beta_3\rangle \\
&- \sum_{d_2<n<(d_1+d_2)} \sum_{\beta_3} e^{iK\frac{n}{3}} \begin{matrix}\beta_3\\ \sigma_3\end{matrix}\Big[\mathcal{C}_1^1\Big]^n |K,\sigma_1;d_1+d_2-n,\beta_3;-d_2+n,\sigma_2\rangle \\
&+ \sum_{n>d_1+d_2} \sum_{\beta_3} e^{iK\frac{n}{3}} \begin{matrix}\beta_3\\ \sigma_3\end{matrix}\Big[\mathcal{C}_1^1\Big]^n |K,\beta_3;-d_1-d_2+n,\sigma_1;d_1,\sigma_2\rangle\,. \qquad \text{(A.4)}
\end{aligned}
$$

Finally, the application of $H_{1:1}$ on the 4-QP state $|K,\sigma_1;d_1,\sigma_2;d_2,\sigma_3;d_3,\sigma_4\rangle$ reads

$$
\begin{aligned}
&H_{1:1}\,|K,\sigma_1;d_1,\sigma_2;d_2,\sigma_3;d_3,\sigma_4\rangle = \\
&+ \sum_{-d_1<n} \sum_{\beta_1} e^{iK\frac{n}{4}} \begin{matrix}\beta_1\\ \sigma_1\end{matrix}\Big[\mathcal{C}_1^1\Big]^n |K,\beta_1;+d_1+n,\sigma_2;+d_2,\sigma_3;+d_3,\sigma_4\rangle \\
&- \sum_{-d_{12}<n<-d_1} \sum_{\beta_1} e^{iK\frac{n}{4}} \begin{matrix}\beta_1\\ \sigma_1\end{matrix}\Big[\mathcal{C}_1^1\Big]^n |K,\sigma_2;-d_1-n,\beta_1;d_{12}+n,\sigma_3;d_3,\sigma_4\rangle \\
&+ \sum_{-d_{123}<n<-d_{12}} \sum_{\beta_1} e^{iK\frac{n}{4}} \begin{matrix}\beta_1\\ \sigma_1\end{matrix}\Big[\mathcal{C}_1^1\Big]^n |K,\sigma_2;d_2,\sigma_3;-d_{12}-n,\beta_1;n+d_{123},\sigma_4\rangle \\
&- \sum_{n<-d_{123}} \sum_{\beta_1} e^{iK\frac{n}{4}} \begin{matrix}\beta_1\\ \sigma_1\end{matrix}\Big[\mathcal{C}_1^1\Big]^n |K,\sigma_2;d_2,\sigma_3;d_3,\sigma_4;-n-d_{123},\beta_1\rangle \\
&- \sum_{d_1<n} \sum_{\beta_2} e^{iK\frac{n}{4}} \begin{matrix}\beta_2\\ \sigma_2\end{matrix}\Big[\mathcal{C}_1^1\Big]^n |K,\beta_2;n-d_1,\sigma_1;d_{12},\sigma_3;d_3,\sigma_4\rangle \\
&+ \sum_{-d_2<n<d_1} \sum_{\beta_2} e^{iK\frac{n}{4}} \begin{matrix}\beta_2\\ \sigma_2\end{matrix}\Big[\mathcal{C}_1^1\Big]^n |K,\sigma_1;d_1-n,\beta_2;d_2+n,\sigma_3;d_3,\sigma_4\rangle \\
&- \sum_{-d_{23}<n<-d_2} \sum_{\beta_2} e^{iK\frac{n}{4}} \begin{matrix}\beta_2\\ \sigma_2\end{matrix}\Big[\mathcal{C}_1^1\Big]^n |K,\sigma_1;d_{12},\sigma_3;-d_2-n,\beta_2;d_{23}+n,\sigma_4\rangle
\end{aligned}
$$

$$
\begin{aligned}
&+ \sum_{n<-d_{23}} \sum_{\beta_2} e^{iK\frac{n}{4}} \left[\mathcal{C}_1^1\right]^n_{\sigma_2}{}^{\beta_2} |K,\sigma_1;d_{12},\sigma_3;d_3,\sigma_4;-d_{23}-n,\beta_2\rangle \\
&+ \sum_{d_{12}<n} \sum_{\beta_3} e^{iK\frac{n}{4}} \left[\mathcal{C}_1^1\right]^n_{\sigma_3}{}^{\beta_3} |K,\beta_3;n-d_{12},\sigma_1;d_1,\sigma_2;d_{23},\sigma_4\rangle \\
&- \sum_{d_2<n<d_{12}} \sum_{\beta_3} e^{iK\frac{n}{4}} \left[\mathcal{C}_1^1\right]^n_{\sigma_3}{}^{\beta_3} |K,\sigma_1;d_{12}-n,\beta_3;n-d_2,\sigma_2;d_{23},\sigma_4\rangle \\
&+ \sum_{-d_3<n<d_2} \sum_{\beta_3} e^{iK\frac{n}{4}} \left[\mathcal{C}_1^1\right]^n_{\sigma_3}{}^{\beta_3} |K,\sigma_1;d_1,\sigma_2;d_2-n,\beta_3;d_3+n,\sigma_4\rangle \\
&- \sum_{n<-d_3} \sum_{\beta_3} e^{iK\frac{n}{4}} \left[\mathcal{C}_1^1\right]^n_{\sigma_3}{}^{\beta_3} |K,\sigma_1;d_1,\sigma_2;d_{23},\sigma_4;-d_3-n,\beta_3\rangle \\
&- \sum_{d_{123}<n} \sum_{\beta_4} e^{iK\frac{n}{4}} \left[\mathcal{C}_1^1\right]^n_{\sigma_4}{}^{\beta_4} |K,\beta_4;n-d_{123},\sigma_1;d_1,\sigma_2;d_2,\sigma_3\rangle \\
&+ \sum_{d_{23}<n<d_{123}} \sum_{\beta_4} e^{iK\frac{n}{4}} \left[\mathcal{C}_1^1\right]^n_{\sigma_4}{}^{\beta_4} |K,\sigma_1;d_{123}-n,\beta_4;n-d_{23},\sigma_2;d_2,\sigma_3\rangle \\
&- \sum_{d_3<n<d_{23}} \sum_{\beta_4} e^{iK\frac{n}{4}} \left[\mathcal{C}_1^1\right]^n_{\sigma_4}{}^{\beta_4} |K,\sigma_1;d_1,\sigma_2;d_{23}-n,\beta_4;n-d_3,\sigma_3\rangle \\
&+ \sum_{n<d_3} \sum_{\beta_4} e^{iK\frac{n}{4}} \left[\mathcal{C}_1^1\right]^n_{\sigma_4}{}^{\beta_4} |K,\sigma_1;d_1,\sigma_2;d_2,\sigma_3;d_3-n,\beta_4\rangle\,, \qquad \text{(A.5)}
\end{aligned}
$$

where $d_{ij} := d_i + d_j$ and $d_{ijk} := d_i + d_j + d_k$.

A.2 $H_{2:2}$

The action of $H_{2:2}$ on the 2-QP state is given by

$$
H_{2:2}\,|K,\sigma_1;d,\sigma_2\rangle = -\sum_n \sum_{d'>0} \sum_{\beta_1\beta_2} e^{iK\left(n+\frac{d-d'}{2}\right)} \left[\mathcal{C}_2^2\right]^{nd'}_{d}{}^{\beta_1\beta_2}_{\sigma_1\sigma_2} |K,\beta_1;d',\beta_2\rangle\,, \qquad \text{(A.6)}
$$

with the definition

$$
\left[\mathcal{C}_2^2\right]^{nd'}_{d}{}^{\beta_1\beta_2}_{\sigma_1\sigma_2} = \langle r-n,\beta_1;r-n+d',\beta_2|\,H_{2:2}\,|r,\sigma_1;r+d,\sigma_2\rangle\,. \qquad \text{(A.7)}
$$

In order to fix the fermionic sign in Eqs. (A.6) and (A.7) we assume here and from now on that in $H_{2:2}$ all the annihilation operators are put to the right of the creation operators and annihilation and creation parts are site-ordered[1], separately.

For the action of $H_{2:2}$ on 3-QP state, we obtain

$$
H_{2:2}\,|K,\sigma_1;d_1,\sigma_2;d_2,\sigma_3\rangle = \sum_{d'>0} \Big\{
$$

[1] With "site-ordered" we mean that the operators are sorted according to their positions in the lattice.

$$
\begin{aligned}
&- \sum_{n<-d_{12}} \sum_{\beta_1\beta_2} e^{iK\left(\frac{2n+d_1-d'}{3}\right)} {}^{\beta_1\beta_2}_{\sigma_1\sigma_2}\Big[\mathcal{C}_2^2\Big]^{nd'}_{d_1} |K,\sigma_3;-n-d_{12},\beta_1;d',\beta_2\rangle \\
&- \sum_{d'-d_{12}<n} \sum_{\beta_1\beta_2} e^{iK\left(\frac{2n+d_1-d'}{3}\right)} {}^{\beta_1\beta_2}_{\sigma_1\sigma_2}\Big[\mathcal{C}_2^2\Big]^{nd'}_{d_1} |K,\beta_1;d',\beta_2;n+d_{12}-d',\sigma_3\rangle \\
&+ \sum_{-d_{12}<n<d'-d_{12}} \sum_{\beta_1\beta_2} e^{iK\left(\frac{2n+d_1-d'}{3}\right)} {}^{\beta_1\beta_2}_{\sigma_1\sigma_2}\Big[\mathcal{C}_2^2\Big]^{nd'}_{d_1} |K,\beta_1;n+d_{12},\sigma_3;d'-d_{12}-n,\beta_2\rangle \\
&+ \sum_{n<-d_1} \sum_{\beta_1\beta_3} e^{iK\left(\frac{2n+d_{12}-d'}{3}\right)} {}^{\beta_1\beta_3}_{\sigma_1\sigma_3}\Big[\mathcal{C}_2^2\Big]^{nd'}_{d_{12}} |K,\sigma_2;-n-d_1,\beta_1;d',\beta_3\rangle \\
&- \sum_{-d_1<n<d'-d_1} \sum_{\beta_1\beta_3} e^{iK\left(\frac{2n+d_{12}-d'}{3}\right)} {}^{\beta_1\beta_3}_{\sigma_1\sigma_3}\Big[\mathcal{C}_2^2\Big]^{nd'}_{d_{12}} |K,\beta_1;n+d_1,\sigma_2;d'-d_1-n,\beta_3\rangle \\
&+ \sum_{d'-d_1<n} \sum_{\beta_1\beta_3} e^{iK\left(\frac{2n+d_{12}-d'}{3}\right)} {}^{\beta_1\beta_3}_{\sigma_1\sigma_3}\Big[\mathcal{C}_2^2\Big]^{nd'}_{d_{12}} |K,\beta_1;d',\beta_3;n+d_1-d',\sigma_2\rangle \\
&+ \sum_{d_1<n<d_1+d'} \sum_{\beta_2\beta_3} e^{iK\left(\frac{2n+d_2-d'}{3}\right)} {}^{\beta_2\beta_3}_{\sigma_2\sigma_3}\Big[\mathcal{C}_2^2\Big]^{nd'}_{d_2} |K,\beta_2;n-d_1,\sigma_1;d_1+d'-n,\beta_3\rangle \\
&- \sum_{d_1+d'<n} \sum_{\beta_2\beta_3} e^{iK\left(\frac{2n+d_2-d'}{3}\right)} {}^{\beta_2\beta_3}_{\sigma_2\sigma_3}\Big[\mathcal{C}_2^2\Big]^{nd'}_{d_2} |K,\beta_2;d',\beta_3;n-d_1-d',\sigma_1\rangle \\
&- \sum_{n<d_1} \sum_{\beta_2\beta_3} e^{iK\left(\frac{2n+d_2-d'}{3}\right)} {}^{\beta_2\beta_3}_{\sigma_2\sigma_3}\Big[\mathcal{C}_2^2\Big]^{nd'}_{d_2} |K,\sigma_1;d_1-n,\beta_2;d',\beta_3\rangle \Big\}. \qquad \text{(A.8)}
\end{aligned}
$$

The result of the application of $H_{2:2}$ to the 4-QP state is given by

$$
\begin{aligned}
&H_{2:2}\,|K,\sigma_1;d_1,\sigma_2;d_2,\sigma_3;d_3,\sigma_4\rangle = \\
&- \sum_{d'>0} \sum_{\beta_1\beta_2} \sum_{d'-d_{12}<n} e^{iK\left(\frac{2n+d_1-d'}{3}\right)} {}^{\beta_1\beta_2}_{\sigma_1\sigma_2}\Big[\mathcal{C}_2^2\Big]^{nd'}_{d_1} |K,\beta_1;d',\beta_2;n+d_{12}-d',\sigma_3;d_3,\sigma_4\rangle \\
&+ \sum_{d'>d_3} \sum_{\beta_1\beta_2} \sum_{\substack{d'-d_{123}<n \\ d'-d_{12}>n}} e^{iK\left(\frac{2n+d_1-d'}{3}\right)} {}^{\beta_1\beta_2}_{\sigma_1\sigma_2}\Big[\mathcal{C}_2^2\Big]^{nd'}_{d_1} |K,\beta_1;n+d_{12},\sigma_3;d'-n-d_{12},\beta_2;n+d_{123}-d',\sigma_4\rangle \\
&- \sum_{d'>d_3} \sum_{\beta_1\beta_2} \sum_{\substack{-d_{12}<n \\ d'-d_{123}>n}} e^{iK\left(\frac{2n+d_1-d'}{3}\right)} {}^{\beta_1\beta_2}_{\sigma_1\sigma_2}\Big[\mathcal{C}_2^2\Big]^{nd'}_{d_1} |K,\beta_1;n+d_{12},\sigma_3;d_3,\sigma_4;d'-n-d_{123},\beta_2\rangle \\
&- \sum_{d'<d_3} \sum_{\beta_1\beta_2} \sum_{\substack{d'-d_{123}<n \\ -d_{12}>n}} e^{iK\left(\frac{2n+d_1-d'}{3}\right)} {}^{\beta_1\beta_2}_{\sigma_1\sigma_2}\Big[\mathcal{C}_2^2\Big]^{nd'}_{d_1} |K,\sigma_3;-n-d_{12},\beta_1;d',\beta_2;n+d_{123}-d',\sigma_4\rangle \\
&+ \sum_{d'<d_3} \sum_{\beta_1\beta_2} \sum_{\substack{-d_{123}<n \\ d'-d_{123}>n}} e^{iK\left(\frac{2n+d_1-d'}{3}\right)} {}^{\beta_1\beta_2}_{\sigma_1\sigma_2}\Big[\mathcal{C}_2^2\Big]^{nd'}_{d_1} |K,\sigma_3;-n-d_{12},\beta_1;n+d_{123},\sigma_4;d'-n-d_{123},\beta_2\rangle \\
&- \sum_{d'>0} \sum_{\beta_1\beta_2} \sum_{-d_{123}>n} e^{iK\left(\frac{2n+d_1-d'}{3}\right)} {}^{\beta_1\beta_2}_{\sigma_1\sigma_2}\Big[\mathcal{C}_2^2\Big]^{nd'}_{d_1} |K,\sigma_3;d_3,\sigma_4;-n-d_{123},\beta_1;d',\beta_2\rangle
\end{aligned}
$$

$$+\sum_{d'>0}\sum_{\beta_1\beta_3}\sum_{d'-d_1<n} e^{iK\left(\frac{2n+d_{12}-d'}{3}\right)}\,{}^{\beta_1\beta_3}_{\sigma_1\sigma_3}\left[\mathcal{C}_2^2\right]^{nd'}_{d_{12}}|K,\beta_1;d',\beta_3;d_1+n-d',\sigma_2;d_{23},\sigma_4\rangle$$

$$-\sum_{d'>0}\sum_{\beta_1\beta_3}\sum_{\substack{-d_1<n\\ d'-d_{123}<n\\ d'-d_1>n}} e^{iK\left(\frac{2n+d_{12}-d'}{3}\right)}\,{}^{\beta_1\beta_3}_{\sigma_1\sigma_3}\left[\mathcal{C}_2^2\right]^{nd'}_{d_{12}}|K,\beta_1;d_1+n,\sigma_2;d'-d_1-n,\beta_3;n+d_{123}-d',\sigma_4\rangle$$

$$+\sum_{d'>0}\sum_{\beta_1\beta_3}\sum_{\substack{-d_1<n\\ d'-d_{123}>n}} e^{iK\left(\frac{2n+d_{12}-d'}{3}\right)}\,{}^{\beta_1\beta_3}_{\sigma_1\sigma_3}\left[\mathcal{C}_2^2\right]^{nd'}_{d_{12}}|K,\beta_1;d_1+n,\sigma_2;d_{23},\sigma_4;d'-d_{123}-n,\beta_3\rangle$$

$$+\sum_{d'>0}\sum_{\beta_1\beta_3}\sum_{\substack{-d_1>n\\ d'-d_{123}<n}} e^{iK\left(\frac{2n+d_{12}-d'}{3}\right)}\,{}^{\beta_1\beta_3}_{\sigma_1\sigma_3}\left[\mathcal{C}_2^2\right]^{nd'}_{d_{12}}|K,\sigma_2;-d_1-n,\beta_1;d',\beta_3;n+d_{123}-d',\sigma_4\rangle$$

$$-\sum_{d'<d_{23}}\sum_{\beta_1\beta_3}\sum_{\substack{-d_{123}<n\\ d'-d_{123}>n}} e^{iK\left(\frac{2n+d_{12}-d'}{3}\right)}\,{}^{\beta_1\beta_3}_{\sigma_1\sigma_3}\left[\mathcal{C}_2^2\right]^{nd'}_{d_{12}}|K,\sigma_2;-d_1-n,\beta_1;n+d_{123},\sigma_4;d'-n-d_{123},\beta_3\rangle$$

$$+\sum_{d'>0}\sum_{\beta_1\beta_3}\sum_{-d_{123}>n} e^{iK\left(\frac{2n+d_{12}-d'}{3}\right)}\,{}^{\beta_1\beta_3}_{\sigma_1\sigma_3}\left[\mathcal{C}_2^2\right]^{nd'}_{d_{12}}|K,\sigma_2;d_{23},\sigma_4;-n-d_{123},\beta_1;d',\beta_3\rangle$$

$$-\sum_{d'>0}\sum_{\beta_1\beta_4}\sum_{d'-d_1<n} e^{iK\left(\frac{2n+d_{123}-d'}{3}\right)}\,{}^{\beta_1\beta_4}_{\sigma_1\sigma_4}\left[\mathcal{C}_2^2\right]^{nd'}_{d_{123}}|K,\beta_1;d',\beta_4;d_1+n-d',\sigma_2;d_2,\sigma_3\rangle$$

$$+\sum_{d'>d_2}\sum_{\beta_1\beta_4}\sum_{\substack{d'-d_1>n\\ d'-d_{12}<n}} e^{iK\left(\frac{2n+d_{123}-d'}{3}\right)}\,{}^{\beta_1\beta_4}_{\sigma_1\sigma_4}\left[\mathcal{C}_2^2\right]^{nd'}_{d_{123}}|K,\beta_1;d_1+n,\sigma_2;d'-d_1-n,\beta_4;n+d_{12}-d',\sigma_3\rangle$$

$$-\sum_{d'>0}\sum_{\beta_1\beta_4}\sum_{\substack{-d_1<n\\ d'-d_{12}>n}} e^{iK\left(\frac{2n+d_{123}-d'}{3}\right)}\,{}^{\beta_1\beta_4}_{\sigma_1\sigma_4}\left[\mathcal{C}_2^2\right]^{nd'}_{d_{123}}|K,\beta_1;d_1+n,\sigma_2;d_2,\sigma_3;d'-n-d_{12},\beta_4\rangle$$

$$-\sum_{d'>0}\sum_{\beta_1\beta_4}\sum_{\substack{-d_1>n\\ d'-d_{12}<n}} e^{iK\left(\frac{2n+d_{123}-d'}{3}\right)}\,{}^{\beta_1\beta_4}_{\sigma_1\sigma_4}\left[\mathcal{C}_2^2\right]^{nd'}_{d_{123}}|K,\sigma_2;-d_1-n,\beta_1;d',\beta_4;n+d_{12}-d',\sigma_3\rangle$$

$$+\sum_{d'<d_2}\sum_{\beta_1\beta_4}\sum_{\substack{-d_{12}<n\\ d'-d_{12}>n}} e^{iK\left(\frac{2n+d_{123}-d'}{3}\right)}\,{}^{\beta_1\beta_4}_{\sigma_1\sigma_4}\left[\mathcal{C}_2^2\right]^{nd'}_{d_{123}}|K,\sigma_2;-d_1-n,\beta_1;n+d_{12},\sigma_3;d'-n-d_{12},\beta_4\rangle$$

$$-\sum_{d'>0}\sum_{\beta_1\beta_4}\sum_{-d_{12}>n} e^{iK\left(\frac{2n+d_{123}-d'}{3}\right)}\,{}^{\beta_1\beta_4}_{\sigma_1\sigma_4}\left[\mathcal{C}_2^2\right]^{nd'}_{d_{123}}|K,\sigma_2;d_2,\sigma_3;-n-d_{12},\beta_1;d',\beta_4\rangle$$

$$-\sum_{d'>0}\sum_{\beta_2\beta_3}\sum_{d_1>n} e^{iK\left(\frac{2n+d_2-d'}{3}\right)}\,{}^{\beta_2\beta_3}_{\sigma_2\sigma_3}\left[\mathcal{C}_2^2\right]^{nd'}_{d_2}|K,\sigma_1;d_1-n,\beta_2;d',\beta_3;n+d_{23}-d',\sigma_4\rangle$$

$$+\sum_{d'>0}\sum_{\beta_2\beta_3}\sum_{\substack{d_1<n\\ d_1+d'>n}} e^{iK\left(\frac{2n+d_2-d'}{3}\right)}\,{}^{\beta_2\beta_3}_{\sigma_2\sigma_3}\left[\mathcal{C}_2^2\right]^{nd'}_{d_2}|K,\beta_2;n-d_1,\sigma_1;d_1+d'-n,\beta_3;n+d_{23}-d',\sigma_4\rangle$$

$$
\begin{aligned}
&- \sum_{d'>0} \sum_{\beta_2\beta_3} \sum_{\substack{d_1<n \\ d'-d_{123}>n}} e^{iK\left(\frac{2n+d_2-d'}{3}\right)} {}^{\beta_2\beta_3}_{\sigma_2\sigma_3}\left[\mathcal{C}_2^2\right]^{nd'}_{d_2} |K,\beta_2;n-d_1,\sigma_1;d_{123},\sigma_4;d'-n-d_{23},\beta_3\rangle \\
&- \sum_{d'>0} \sum_{\beta_2\beta_3} \sum_{d_1+d'<n} e^{iK\left(\frac{2n+d_2-d'}{3}\right)} {}^{\beta_2\beta_3}_{\sigma_2\sigma_3}\left[\mathcal{C}_2^2\right]^{nd'}_{d_2} |K,\beta_2;d',\beta_3;n-d_1-d',\sigma_1;d_{123},\sigma_4\rangle \\
&+ \sum_{d'>0} \sum_{\beta_2\beta_3} \sum_{\substack{d_1>n \\ -d_{23}<n \\ d'-d_{23}>n}} e^{iK\left(\frac{2n+d_2-d'}{3}\right)} {}^{\beta_2\beta_3}_{\sigma_2\sigma_3}\left[\mathcal{C}_2^2\right]^{nd'}_{d_2} |K,\sigma_1;d_1-n,\beta_2;n+d_{23},\sigma_4;d'-n-d_{23},\beta_3\rangle \\
&- \sum_{d'>0} \sum_{\beta_2\beta_3} \sum_{-d_{23}>n} e^{iK\left(\frac{2n+d_2-d'}{3}\right)} {}^{\beta_2\beta_3}_{\sigma_2\sigma_3}\left[\mathcal{C}_2^2\right]^{nd'}_{d_2} |K,\sigma_1;d_{123},\sigma_4;-n-d_{23},\beta_2;d',\beta_3\rangle \\
&+ \sum_{d'>0} \sum_{\beta_2\beta_4} \sum_{d_1+d'<n} e^{iK\left(\frac{2n+d_{23}-d'}{3}\right)} {}^{\beta_2\beta_4}_{\sigma_2\sigma_4}\left[\mathcal{C}_2^2\right]^{nd'}_{d_{23}} |K,\beta_2;d',\beta_4;n-d_1-d',\sigma_1;d_{12},\sigma_3\rangle \\
&- \sum_{d'>0} \sum_{\beta_2\beta_4} \sum_{\substack{d_1<n \\ d_1+d'>n \\ d'-d_2<n}} e^{iK\left(\frac{2n+d_{23}-d'}{3}\right)} {}^{\beta_2\beta_4}_{\sigma_2\sigma_4}\left[\mathcal{C}_2^2\right]^{nd'}_{d_{23}} |K,\beta_2;n-d_1,\sigma_1;d_1+d'-n,\beta_4;n+d_2-d',\sigma_3\rangle \\
&+ \sum_{d'>0} \sum_{\beta_2\beta_4} \sum_{\substack{d_1<n \\ d'-d_2>n}} e^{iK\left(\frac{2n+d_{23}-d'}{3}\right)} {}^{\beta_2\beta_4}_{\sigma_2\sigma_4}\left[\mathcal{C}_2^2\right]^{nd'}_{d_{23}} |K,\beta_2;n-d_1,\sigma_1;d_{12},\sigma_3;d'-n-d_2,\beta_4\rangle \\
&+ \sum_{d'>0} \sum_{\beta_2\beta_4} \sum_{\substack{d_1>n \\ d'-d_2<n}} e^{iK\left(\frac{2n+d_{23}-d'}{3}\right)} {}^{\beta_2\beta_4}_{\sigma_2\sigma_4}\left[\mathcal{C}_2^2\right]^{nd'}_{d_{23}} |K,\sigma_1;d_1-n,\beta_2;d',\beta_4;n+d_2-d',\sigma_3\rangle \\
&- \sum_{d'>0} \sum_{\beta_2\beta_4} \sum_{\substack{d_1>n \\ -d_2<n \\ d'-d_2>n}} e^{iK\left(\frac{2n+d_{23}-d'}{3}\right)} {}^{\beta_2\beta_4}_{\sigma_2\sigma_4}\left[\mathcal{C}_2^2\right]^{nd'}_{d_{23}} |K,\sigma_1;d_1-n,\beta_2;n+d_2,\sigma_3;d'-n-d_2,\beta_4\rangle \\
&+ \sum_{d'>0} \sum_{\beta_2\beta_4} \sum_{-d_2>n} e^{iK\left(\frac{2n+d_{23}-d'}{3}\right)} {}^{\beta_2\beta_4}_{\sigma_2\sigma_4}\left[\mathcal{C}_2^2\right]^{nd'}_{d_{23}} |K,\sigma_1;d_{12},\sigma_3;-n-d_2,\beta_2;d',\beta_4\rangle \\
&- \sum_{d'>0} \sum_{\beta_3\beta_4} \sum_{d'+d_{12}<n} e^{iK\left(\frac{2n+d_3-d'}{3}\right)} {}^{\beta_3\beta_4}_{\sigma_3\sigma_4}\left[\mathcal{C}_2^2\right]^{nd'}_{d_3} |K,\beta_3;d',\beta_4;n-d_{12}-d',\sigma_1;d_1,\sigma_2\rangle \\
&+ \sum_{d'>0} \sum_{\beta_3\beta_4} \sum_{\substack{d_{12}<n \\ d'+d_{12}>n \\ d'+d_2<n}} e^{iK\left(\frac{2n+d_3-d'}{3}\right)} {}^{\beta_3\beta_4}_{\sigma_3\sigma_4}\left[\mathcal{C}_2^2\right]^{nd'}_{d_3} |K,\beta_3;n-d_{12},\sigma_1;d_{12}+d'-n,\beta_4;n-d_2-d',\sigma_2\rangle \\
&- \sum_{d'>0} \sum_{\beta_3\beta_4} \sum_{\substack{d_{12}<n \\ d'+d_2>n}} e^{iK\left(\frac{2n+d_3-d'}{3}\right)} {}^{\beta_3\beta_4}_{\sigma_3\sigma_4}\left[\mathcal{C}_2^2\right]^{nd'}_{d_3} |K,\beta_3;n-d_{12},\sigma_1;d_1,\sigma_2;d_2+d'-n,\beta_4\rangle \\
&- \sum_{d'>0} \sum_{\beta_3\beta_4} \sum_{\substack{d_{12}>n \\ d'+d_2<n}} e^{iK\left(\frac{2n+d_3-d'}{3}\right)} {}^{\beta_3\beta_4}_{\sigma_3\sigma_4}\left[\mathcal{C}_2^2\right]^{nd'}_{d_3} |K,\sigma_1;d_{12}-n,\beta_3;d',\beta_4;n-d'-d_2,\sigma_2\rangle
\end{aligned}
$$

$$+\sum_{d'>0}\sum_{\beta_3\beta_4}\sum_{\substack{d_{12}>n\\ d_2<n\\ d_2+d'>n}} e^{iK\left(\frac{2n+d_3-d'}{3}\right)} {}^{\beta_3\beta_4}_{\sigma_3\sigma_4}\left[\mathcal{C}_2^2\right]^{nd'}_{d_3} |K,\sigma_1;d_{12}-n,\beta_3;n-d_2,\sigma_2;d_2+d'-n,\beta_4\rangle$$

$$-\sum_{d'>0}\sum_{\beta_3\beta_4}\sum_{d_2>n} e^{iK\left(\frac{2n+d_3-d'}{3}\right)} {}^{\beta_3\beta_4}_{\sigma_3\sigma_4}\left[\mathcal{C}_2^2\right]^{nd'}_{d_3} |K,\sigma_1;d_1,\sigma_2;d_2-n,\beta_3;d',\beta_4\rangle\,. \tag{A.9}$$

A.3 $H_{3:3}$

The effect of $H_{3:3}$ on the 3-QP state is given by

$$H_{3:3}\,|K,\sigma_1;d_1,\sigma_2;d_2,\sigma_3\rangle = -\sum_{d_1'd_2'}\sum_{\beta_1\beta_2\beta_3}\sum_{n} e^{iK\left(n+\frac{2(d_1-d_1')+(d_2-d_2')}{3}\right)} {}^{\beta_1\beta_2\beta_3}_{\sigma_1\sigma_2\sigma_3}\left[\mathcal{C}_3^3\right]^{nd_1'd_2'}_{d_1d_2} |K,\beta_1;d_1',\beta_2;d_2',\beta_3\rangle\,, \tag{A.10}$$

where d_1' and d_2' are positive integer values. We have also defined

$${}^{\beta_1\beta_2\beta_3}_{\sigma_1\sigma_2\sigma_3}\left[\mathcal{C}_3^3\right]^{nd_1'd_2'}_{d_1d_2} := \langle r-n,\beta_1;r-n+d_1',\beta_2;r-n+d_{12}',\beta_3|\,H_{3:3}\,|r,\sigma_1;r+d_1,\sigma_2;r+d_{12},\sigma_3\rangle\,, \tag{A.11}$$

where $d_{ij}' = d_i' + d_j'$.

The action of $H_{3:3}$ on the 4-QP state reads

$$\begin{aligned}
H_{3:3}\,|K,\sigma_1;d_1,\sigma_2;d_2,\sigma_3;d_3,\sigma_4\rangle = \sum_{d_1'd_2'>0}\Bigg\{ &\\
&-\sum_{n>d_{12}'-d_{123}} e^{iK\left(\frac{D_{33}}{4}\right)} \sum_{\beta_1\beta_2\beta_3} {}^{\beta_1\beta_2\beta_3}_{\sigma_1\sigma_2\sigma_3}\left[\mathcal{C}_3^3\right]^{nd_1'd_2'}_{d_1d_2} |K,\beta_1;d_1',\beta_2;d_2',\beta_3;n+d_{123}-d_{12}',\sigma_4\rangle\\
&+\sum_{\substack{n<d_{12}'-d_{123}\\ n>d_1'-d_{123}}} e^{iK\left(\frac{D_{33}}{4}\right)} \sum_{\beta_1\beta_2\beta_3} {}^{\beta_1\beta_2\beta_3}_{\sigma_1\sigma_2\sigma_3}\left[\mathcal{C}_3^3\right]^{nd_1'd_2'}_{d_1d_2} |K,\beta_1;d_1',\beta_2;n+d_{123}-d_1',\sigma_4;d_{12}'-n-d_{123},\beta_3\rangle\\
&-\sum_{\substack{n<d_1'-d_{123}\\ n>-d_{123}}} e^{iK\left(\frac{D_{33}}{4}\right)} \sum_{\beta_1\beta_2\beta_3} {}^{\beta_1\beta_2\beta_3}_{\sigma_1\sigma_2\sigma_3}\left[\mathcal{C}_3^3\right]^{nd_1'd_2'}_{d_1d_2} |K,\beta_1;n+d_{123},\sigma_4;d_1'-n-d_{123},\beta_2;d_2',\beta_3\rangle\\
&+\sum_{n<-d_{123}} e^{iK\left(\frac{D_{33}}{4}\right)} \sum_{\beta_1\beta_2\beta_3} {}^{\beta_1\beta_2\beta_3}_{\sigma_1\sigma_2\sigma_3}\left[\mathcal{C}_3^3\right]^{nd_1'd_2'}_{d_1d_2} |K,\sigma_4;-n-d_{123},\beta_1;d_1',\beta_2;d_2',\beta_3\rangle\\
&+\sum_{n>d_{12}'-d_{12}} e^{iK\left(\frac{D_{33}+d_3}{4}\right)} \sum_{\beta_1\beta_2\beta_4} {}^{\beta_1\beta_2\beta_4}_{\sigma_1\sigma_2\sigma_4}\left[\mathcal{C}_3^3\right]^{nd_1'd_2'}_{d_1d_{23}} |K,\beta_1;d_1',\beta_2;d_2',\beta_4;n+d_{12}-d_{12}',\sigma_3\rangle\\
&-\sum_{\substack{n<d_{12}'-d_{12}\\ n>d_1'-d_{12}}} e^{iK\left(\frac{D_{33}+d_3}{4}\right)} \sum_{\beta_1\beta_2\beta_4} {}^{\beta_1\beta_2\beta_4}_{\sigma_1\sigma_2\sigma_4}\left[\mathcal{C}_3^3\right]^{nd_1'd_2'}_{d_1d_{23}} |K,\beta_1;d_1',\beta_2;n+d_{12}-d_1',\sigma_3;d_{12}'-n-d_{12},\beta_4\rangle
\end{aligned}$$

$$
\begin{aligned}
&+\sum_{\substack{n<d_1'-d_{12}\\ n>-d_{12}}} e^{iK\left(\frac{D_{33}+d_3}{4}\right)} \sum_{\beta_1\beta_2\beta_4} {}^{\beta_1\beta_2\beta_4}_{\sigma_1\sigma_2\sigma_4}\Big[\mathcal{C}_3^3\Big]^{nd_1'd_2'}_{d_1d_{23}} |K,\beta_1;n+d_{12},\sigma_3;d_1'-n-d_{12},\beta_2;d_2',\beta_4\rangle\\
&-\sum_{n<-d_{12}} e^{iK\left(\frac{D_{33}+d_3}{4}\right)} \sum_{\beta_1\beta_2\beta_4} {}^{\beta_1\beta_2\beta_4}_{\sigma_1\sigma_2\sigma_4}\Big[\mathcal{C}_3^3\Big]^{nd_1'd_2'}_{d_1d_{23}} |K,\sigma_3;-n-d_{12},\beta_1;d_1',\beta_2;d_2',\beta_4\rangle\\
&-\sum_{n>d_{12}'-d_1} e^{iK\left(\frac{D_{33}+d_{23}}{4}\right)} \sum_{\beta_1\beta_3\beta_4} {}^{\beta_1\beta_3\beta_4}_{\sigma_1\sigma_3\sigma_4}\Big[\mathcal{C}_3^3\Big]^{nd_1'd_2'}_{d_{12}d_3} |K,\beta_1;d_1',\beta_3;d_2',\beta_4;n+d_1-d_{12}',\sigma_2\rangle\\
&+\sum_{\substack{n<d_{12}'-d_1\\ n>d_1'-d_1}} e^{iK\left(\frac{D_{33}+d_{23}}{4}\right)} \sum_{\beta_1\beta_3\beta_4} {}^{\beta_1\beta_3\beta_4}_{\sigma_1\sigma_3\sigma_4}\Big[\mathcal{C}_3^3\Big]^{nd_1'd_2'}_{d_{12}d_3} |K,\beta_1;d_1',\beta_3;n+d_1-d_1',\sigma_2;d_{12}'-n-d_1,\beta_4\rangle\\
&-\sum_{\substack{n<d_1'-d_1\\ n>-d_1}} e^{iK\left(\frac{D_{33}+d_{23}}{4}\right)} \sum_{\beta_1\beta_3\beta_4} {}^{\beta_1\beta_3\beta_4}_{\sigma_1\sigma_3\sigma_4}\Big[\mathcal{C}_3^3\Big]^{nd_1'd_2'}_{d_{12}d_3} |K,\beta_1;n+d_1,\sigma_2;d_1'-n+d_1,\beta_3;d_2',\beta_4\rangle\\
&+\sum_{n<-d_1} e^{iK\left(\frac{D_{33}+d_{23}}{4}\right)} \sum_{\beta_1\beta_3\beta_4} {}^{\beta_1\beta_3\beta_4}_{\sigma_1\sigma_3\sigma_4}\Big[\mathcal{C}_3^3\Big]^{nd_1'd_2'}_{d_{12}d_3} |K,\sigma_2;-n-d_1,\beta_1;d_1',\beta_3;d_2',\beta_4\rangle\\
&+\sum_{n>d_1+d_{12}'} e^{iK\left(\frac{D_{33}+d_{23}-2d_1}{4}\right)} \sum_{\beta_2\beta_3\beta_4} {}^{\beta_2\beta_3\beta_4}_{\sigma_2\sigma_3\sigma_4}\Big[\mathcal{C}_3^3\Big]^{nd_1'd_2'}_{d_2d_3} |K,\beta_2;d_1',\beta_3;d_2',\beta_4;n-d_1-d_{12}',\sigma_1\rangle\\
&-\sum_{\substack{n>d_1+d_1'\\ n<d_1+d_{12}'}} e^{iK\left(\frac{D_{33}+d_{23}-2d_1}{4}\right)} \sum_{\beta_2\beta_3\beta_4} {}^{\beta_2\beta_3\beta_4}_{\sigma_2\sigma_3\sigma_4}\Big[\mathcal{C}_3^3\Big]^{nd_1'd_2'}_{d_2d_3} |K,\beta_2;d_1',\beta_3;n-d_1-d_1',\sigma_1;d_1+d_{12}'-n,\beta_4\rangle\\
&+\sum_{\substack{n<d_1+d_1'\\ n>d_1}} e^{iK\left(\frac{D_{33}+d_{23}-2d_1}{4}\right)} \sum_{\beta_2\beta_3\beta_4} {}^{\beta_2\beta_3\beta_4}_{\sigma_2\sigma_3\sigma_4}\Big[\mathcal{C}_3^3\Big]^{nd_1'd_2'}_{d_2d_3} |K,\beta_2;n-d_1,\sigma_1;d_1+d_1'-n,\beta_3;d_2',\beta_4\rangle\\
&-\sum_{n<d_1} e^{iK\left(\frac{D_{33}+d_{23}-2d_1}{4}\right)} \sum_{\beta_2\beta_3\beta_4} {}^{\beta_2\beta_3\beta_4}_{\sigma_2\sigma_3\sigma_4}\Big[\mathcal{C}_3^3\Big]^{nd_1'd_2'}_{d_2d_3} |K,\sigma_1;d_1-n,\beta_2;d_1',\beta_3;d_2',\beta_4\rangle\Big\},
\end{aligned}
\tag{A.12}
$$

where $D_{33} := 2d_1 + 2d_1' + d_2 + d_2'$.

A.4 $H_{4:4}$

The action of $H_{4:4}$ on the 4-QP state is given by

$$
\begin{aligned}
&H_{4:4}\,|K,\sigma_1;d_1,\sigma_2;d_2,\sigma_3;d_3,\sigma_4\rangle =\\
&+\sum_{d_1'd_2'd_3'>0}\sum_{\substack{\beta_1\beta_2\\ \beta_3\beta_4}}\sum_{n} e^{iK\left(n+\frac{D_{44}}{4}\right)} {}^{\beta_1\beta_2\beta_3\beta_4}_{\sigma_1\sigma_2\sigma_3\sigma_4}\Big[\mathcal{C}_4^4\Big]^{nd_1'd_2'd_3'}_{d_1d_2d_3} |K,\beta_1;d_1',\beta_2;d_2',\beta_3;d_3',\beta_4\rangle\,,
\end{aligned}
\tag{A.13}
$$

where $D_{44} = 3(d_1 - d_1') + 2(d_2 - d_2') + (d_3 - d_3')$. We have also defined

$$\begin{aligned}
&{}^{\beta_1\beta_2\beta_3\beta_4}_{\sigma_1\sigma_2\sigma_3\sigma_4}\Big[\mathcal{C}_4^4\Big]^{nd_1'd_2'd_3'}_{d_1d_2d_3} := \\
&\langle r', \beta_1; r'+d_1', \beta_2; r'+d_{12}', \beta_3; r'+d_{123}', \beta_4 | H_{3:3} | r, \sigma_1; r+d_1, \sigma_2; r+d_{12}, \sigma_3; r+d_{123}, \sigma_4 \rangle ,
\end{aligned} \tag{A.14}$$

where $r' := r-n$ and $d_{ijk}' := d_i' + d_j' + d_k'$.

A.5 $H_{2:1}$

The action of the off-diagonal interaction $H_{2:1}$ on the 1-QP state is given by

$$H_{2:1} |K, \sigma\rangle = + \sum_{d'>0} \sum_{n} \sum_{\beta_1\beta_2} e^{iK\left(n - \frac{d'}{2}\right)} {}^{\beta_1\beta_2}_{\sigma}\Big[\mathcal{C}_1^2\Big]^{nd'} |K, \beta_1; d', \beta_2\rangle , \tag{A.15}$$

where

$${}^{\beta_1\beta_2}_{\sigma}\Big[\mathcal{C}_1^2\Big]^{nd'} := \langle r-n, \beta_1; r-n+d', \beta_2 | H_{2:1} | r, \sigma \rangle . \tag{A.16}$$

The action of $H_{2:1}$ on the 2-QP state leads to 6 contributions given here

$$\begin{aligned}
H_{2:1} |K, \sigma_1; d_1, \sigma_2\rangle = \sum_{d_1'>0} \Big\{ & \\
&+ \sum_{d_1'-d_1<n} \sum_{\beta_1\beta_3} e^{iK\left(\frac{4n+d_1-2d_1'}{6}\right)} {}^{\beta_1\beta_3}_{\sigma_1}\Big[\mathcal{C}_1^2\Big]^{nd_1'} |K, \beta_1; d_1', \beta_3; n+d_1-d_1', \sigma_2\rangle \\
&- \sum_{\substack{d_1'-d_1>n \\ -d_1<n}} \sum_{\beta_1\beta_3} e^{iK\left(\frac{4n+d_1-2d_1'}{6}\right)} {}^{\beta_1\beta_3}_{\sigma_1}\Big[\mathcal{C}_1^2\Big]^{nd_1'} |K, \beta_1; n+d_1, \sigma_2; d_1'-n-d_1, \beta_3\rangle \\
&+ \sum_{-d_1>n} \sum_{\beta_1\beta_3} e^{iK\left(\frac{4n+d_1-2d_1'}{6}\right)} {}^{\beta_1\beta_3}_{\sigma_1}\Big[\mathcal{C}_1^2\Big]^{nd_1'} |K, \sigma_2; -n-d_1, \beta_1; d_1', \beta_3\rangle \\
&- \sum_{d_1>n} \sum_{\beta_2\beta_3} e^{iK\left(\frac{4n-d_1-2d_1'}{6}\right)} {}^{\beta_2\beta_3}_{\sigma_2}\Big[\mathcal{C}_1^2\Big]^{nd_1'} |K, \sigma_1; d_1-n, \beta_2; d_1', \beta_3\rangle \\
&+ \sum_{\substack{d_1+d_1'>n \\ d_1<n}} \sum_{\beta_2\beta_3} e^{iK\left(\frac{4n-d_1-2d_1'}{6}\right)} {}^{\beta_2\beta_3}_{\sigma_2}\Big[\mathcal{C}_1^2\Big]^{nd_1'} |K, \beta_2; n-d_1, \sigma_1; d_1+d_1'-n, \beta_3\rangle \\
&- \sum_{d_1+d_1'<n} \sum_{\beta_2\beta_3} e^{iK\left(\frac{4n-d_1-2d_1'}{6}\right)} {}^{\beta_2\beta_3}_{\sigma_2}\Big[\mathcal{C}_1^2\Big]^{nd_1'} |K, \beta_2; d_1', \beta_3; n-d_1-d_1', \sigma_1\rangle \Big\}.
\end{aligned} \tag{A.17}$$

The application of $H_{2:1}$ on the 3-QP state is given by

$$H_{2:1} |K, \sigma_1; d_1, \sigma_2; d_2, \sigma_3\rangle = \sum_{d_1'>0} \Big\{$$

$$
\begin{aligned}
&+\sum_{d_1'-d_1<n}\sum_{\beta_1\beta_4} e^{iK\left(\frac{D_{21}}{12}\right)}{}^{\beta_1\beta_4}_{\sigma_1}\left[\mathcal{C}_1^2\right]^{nd_1'} |K,\beta_1;d_1',\beta_4;n+d_1-d_1',\sigma_2;d_2,\sigma_3\rangle\\
&-\sum_{\substack{d_1'-d_1>n\\-d_1<n\\d_1'-d_{12}<n}}\sum_{\beta_1\beta_4} e^{iK\left(\frac{D_{21}}{12}\right)}{}^{\beta_1\beta_4}_{\sigma_1}\left[\mathcal{C}_1^2\right]^{nd_1'} |K,\beta_1;n+d_1,\sigma_2;d_1'-n-d_1,\beta_4;n+d_{12}-d_1',\sigma_3\rangle\\
&+\sum_{\substack{d_1'-d_{12}>n\\-d_1<n}}\sum_{\beta_1\beta_4} e^{iK\left(\frac{D_{21}}{12}\right)}{}^{\beta_1\beta_4}_{\sigma_1}\left[\mathcal{C}_1^2\right]^{nd_1'} |K,\beta_1;n+d_1,\sigma_2;d_2,\sigma_3;d_1'-n-d_{12},\beta_4\rangle\\
&+\sum_{\substack{d_1'-d_{12}<n\\-d_1>n}}\sum_{\beta_1\beta_4} e^{iK\left(\frac{D_{21}}{12}\right)}{}^{\beta_1\beta_4}_{\sigma_1}\left[\mathcal{C}_1^2\right]^{nd_1'} |K,\sigma_2;-n-d_1,\beta_1;d_1',\beta_4;n+d_{12}-d_1',\sigma_3\rangle\\
&-\sum_{\substack{d_1'-d_{12}>n\\-d_1>n\\-d_{12}<n}}\sum_{\beta_1\beta_4} e^{iK\left(\frac{D_{21}}{12}\right)}{}^{\beta_1\beta_4}_{\sigma_1}\left[\mathcal{C}_1^2\right]^{nd_1'} |K,\sigma_2;-n-d_1,\beta_1;n+d_{12},\sigma_3;d_1'-d_{12}-n,\beta_4\rangle\\
&+\sum_{-d_{12}>n}\sum_{\beta_1\beta_4} e^{iK\left(\frac{D_{21}}{12}\right)}{}^{\beta_1\beta_4}_{\sigma_1}\left[\mathcal{C}_1^2\right]^{nd_1'} |K,\sigma_2;d_2,\sigma_3;-n-d_{12},\beta_1;d_1',\beta_4\rangle\\
&-\sum_{d_1+d_1'<n}\sum_{\beta_2\beta_4} e^{iK\left(\frac{D_{21}-3d_1}{12}\right)}{}^{\beta_2\beta_4}_{\sigma_2}\left[\mathcal{C}_1^2\right]^{nd_1'} |K,\beta_2;d_1',\beta_4;n-d_1-d_1',\sigma_1;d_{12},\sigma_3\rangle\\
&+\sum_{\substack{d_1+d_1'>n\\d_1'-d_2<n\\d_1<n}}\sum_{\beta_2\beta_4} e^{iK\left(\frac{D_{21}-3d_1}{12}\right)}{}^{\beta_2\beta_4}_{\sigma_2}\left[\mathcal{C}_1^2\right]^{nd_1'} |K,\beta_2;n-d_1,\sigma_1;d_1'+d_1-n,\beta_4;n+d_2-d_1',\sigma_3\rangle\\
&-\sum_{\substack{d_1'-d_2>n\\d_1<n}}\sum_{\beta_2\beta_4} e^{iK\left(\frac{D_{21}-3d_1}{12}\right)}{}^{\beta_2\beta_4}_{\sigma_2}\left[\mathcal{C}_1^2\right]^{nd_1'} |K,\beta_2;n-d_1,\sigma_1;d_{12},\sigma_3;d_1'-d_2-n,\beta_4\rangle\\
&-\sum_{\substack{d_1'-d_2<n\\d_1>n}}\sum_{\beta_2\beta_4} e^{iK\left(\frac{D_{21}-3d_1}{12}\right)}{}^{\beta_2\beta_4}_{\sigma_2}\left[\mathcal{C}_1^2\right]^{nd_1'} |K,\sigma_1;d_1-n,\beta_2;d_1',\beta_4;n+d_2-d_1',\sigma_3\rangle\\
&+\sum_{\substack{d_1'-d_2>n\\d_1>n\\-d_2<n}}\sum_{\beta_2\beta_4} e^{iK\left(\frac{D_{21}-3d_1}{12}\right)}{}^{\beta_2\beta_4}_{\sigma_2}\left[\mathcal{C}_1^2\right]^{nd_1'} |K,\sigma_1;d_1-n,\beta_2;d_2+n,\sigma_3;d_1'-n-d_2,\beta_4\rangle\\
&-\sum_{-d_2>n}\sum_{\beta_2\beta_4} e^{iK\left(\frac{D_{21}-3d_1}{12}\right)}{}^{\beta_2\beta_4}_{\sigma_2}\left[\mathcal{C}_1^2\right]^{nd_1'} |K,\sigma_1;d_{12},\sigma_3;-d_2-n,\beta_2;d_1',\beta_4\rangle\\
&+\sum_{d_{12}+d_1'<n}\sum_{\beta_3\beta_4} e^{iK\left(\frac{D_{21}-3d_{12}}{12}\right)}{}^{\beta_3\beta_4}_{\sigma_3}\left[\mathcal{C}_1^2\right]^{nd_1'} |K,\beta_3;d_1',\beta_4;n-d_{12}-d_1',\sigma_1;d_1,\sigma_2\rangle\\
&-\sum_{\substack{d_{12}+d_1'>n\\d_{12}<n\\d_1'+d_2<n}}\sum_{\beta_3\beta_4} e^{iK\left(\frac{D_{21}-3d_{12}}{12}\right)}{}^{\beta_3\beta_4}_{\sigma_3}\left[\mathcal{C}_1^2\right]^{nd_1'} |K,\beta_3;n-d_{12},\sigma_1;d_{12}+d_1'-n,\beta_4;n-d_2-d_1',\sigma_2\rangle
\end{aligned}
$$

$$
\begin{aligned}
&+\sum_{\substack{d_2+d_1'>n\\ d_{12}<n}}\sum_{\beta_3\beta_4} e^{iK\left(\frac{D_{21}-3d_{12}}{12}\right)} {}^{\beta_3\beta_4}_{\sigma_3}\Big[\mathcal{C}_1^2\Big]^{nd_1'} |K,\beta_3;n-d_{12},\sigma_1;d_1,\sigma_2;d_2+d_1'-n,\beta_4\rangle\\
&+\sum_{\substack{d_2+d_1'<n\\ d_{12}>n}}\sum_{\beta_3\beta_4} e^{iK\left(\frac{D_{21}-3d_{12}}{12}\right)} {}^{\beta_3\beta_4}_{\sigma_3}\Big[\mathcal{C}_1^2\Big]^{nd_1'} |K,\sigma_1;d_{12}-n,\beta_3;d_1',\beta_4;n-d_1'-d_2,\sigma_2\rangle\\
&-\sum_{\substack{d_2+d_1'>n\\ d_{12}>n\\ d_2<n}}\sum_{\beta_3\beta_4} e^{iK\left(\frac{D_{21}-3d_{12}}{12}\right)} {}^{\beta_3\beta_4}_{\sigma_3}\Big[\mathcal{C}_1^2\Big]^{nd_1'} |K,\sigma_1;d_{12}-n,\beta_3;n-d_2,\sigma_2;d_2+d_1'-n,\beta_4\rangle\\
&+\sum_{d_2>n}\sum_{\beta_3\beta_4} e^{iK\left(\frac{D_{21}-3d_{12}}{12}\right)} {}^{\beta_3\beta_4}_{\sigma_3}\Big[\mathcal{C}_1^2\Big]^{nd_1'} |K,\sigma_1;d_1,\sigma_2;d_2-n,\beta_3;d_1',\beta_4\rangle\Big\},
\end{aligned}
\tag{A.18}
$$

with $D_{21} := 6n + 2d_1 + d_2 - 3d_1'$.

A.6 $H_{3:1}$

The action of $H_{3:1}$ on the 1-QP state is given by

$$
H_{3:1}\,|K,\sigma\rangle = +\sum_{d_1'd_2'}\sum_{n}\sum_{\beta_1\beta_2\beta_3} e^{iK\left(n-\frac{2d_1'+d_2'}{3}\right)} {}^{\beta_1\beta_2\beta_3}_{\sigma}\Big[\mathcal{C}_1^3\Big]^{nd_1'd_2'} |K,\beta_1;d_1',\beta_2;d_2',\beta_3\rangle\,, \tag{A.19}
$$

where

$$
{}^{\beta_1\beta_2\beta_3}_{\sigma}\Big[\mathcal{C}_1^3\Big]^{nd_1'd_2'} := \langle r-n,\beta_1;r-n+d_1',\beta_2;r-n+d_{12}',\beta_3|\,H_{3:1}\,|r,\sigma\rangle\,. \tag{A.20}
$$

The action of $H_{3:1}$ on the 2-QP state is given by

$$
\begin{aligned}
H_{3:1}\,|K,\sigma_1;d_1,\sigma_2\rangle = &\sum_{d_1'd_2'}\Big\{\\
&+\sum_{n>d_{12}'-d_1} e^{iK\left(\frac{D_{31}}{4}\right)}\sum_{\beta_1\beta_3\beta_4} {}^{\beta_1\beta_3\beta_4}_{\sigma_1}\Big[\mathcal{C}_1^3\Big]^{nd_1'd_2'} |K,\beta_1;d_1',\beta_3;d_2',\beta_4;n+d_1-d_{12}',\sigma_2\rangle\\
&-\sum_{\substack{n<d_{12}'-d_1\\ n>d_1'-d_1}} e^{iK\left(\frac{D_{31}}{4}\right)}\sum_{\beta_1\beta_3\beta_4} {}^{\beta_1\beta_3\beta_4}_{\sigma_1}\Big[\mathcal{C}_1^3\Big]^{nd_1'd_2'} |K,\beta_1;d_1',\beta_3;n+d_1-d_1',\sigma_2;d_{12}'-n-d_1,\beta_4\rangle\\
&+\sum_{\substack{n<d_1'-d_1\\ n>-d_1}} e^{iK\left(\frac{D_{31}}{4}\right)}\sum_{\beta_1\beta_3\beta_4} {}^{\beta_1\beta_3\beta_4}_{\sigma_1}\Big[\mathcal{C}_1^3\Big]^{nd_1'd_2'} |K,\beta_1;d_1+n,\sigma_2;d_1'-n-d_1,\beta_3;d_2',\beta_4\rangle\\
&-\sum_{n<-d_1} e^{iK\left(\frac{D_{31}}{4}\right)}\sum_{\beta_1\beta_3\beta_4} {}^{\beta_1\beta_3\beta_4}_{\sigma_1}\Big[\mathcal{C}_1^3\Big]^{nd_1'd_2'} |K,\sigma_2;-d_1-n,\beta_1;d_1',\beta_3;d_2',\beta_4\rangle
\end{aligned}
$$

$$
\begin{aligned}
&+\sum_{n<d_1} e^{iK\left(\frac{D_{31}-2d_1}{4}\right)} \sum_{\beta_2\beta_3\beta_4} {}^{\beta_2\beta_3\beta_4}_{\sigma_2}\Big[\mathcal{C}_1^3\Big]^{nd_1'd_2'} |K,\sigma_1;d_1-n,\beta_2;d_1',\beta_3;d_2',\beta_4\rangle \\
&-\sum_{\substack{n>d_1\\ n<d_1+d_1'}} e^{iK\left(\frac{D_{31}-2d_1}{4}\right)} \sum_{\beta_2\beta_3\beta_4} {}^{\beta_2\beta_3\beta_4}_{\sigma_2}\Big[\mathcal{C}_1^3\Big]^{nd_1'd_2'} |K,\beta_2;n-d_1,\sigma_1;d_1+d_1'-n,\beta_3;d_2',\beta_4\rangle \\
&+\sum_{\substack{n>d_1+d_1'\\ n<d_1+d_{12}'}} e^{iK\left(\frac{D_{31}-2d_1}{4}\right)} \sum_{\beta_2\beta_3\beta_4} {}^{\beta_2\beta_3\beta_4}_{\sigma_2}\Big[\mathcal{C}_1^3\Big]^{nd_1'd_2'} |K,\beta_2;d_1',\beta_3;n-d_1-d_1',\sigma_1;d_1+d_{12}'-n,\beta_4\rangle \\
&-\sum_{n>d_1+d_{12}'} e^{iK\left(\frac{D_{31}-2d_1}{4}\right)} \sum_{\beta_2\beta_3\beta_4} {}^{\beta_2\beta_3\beta_4}_{\sigma_2}\Big[\mathcal{C}_1^3\Big]^{nd_1'd_2'} |K,\beta_2;d_1',\beta_3;d_2',\beta_4;n-d_1-d_{12}',\sigma_1\rangle \Big\}, \qquad \text{(A.21)}
\end{aligned}
$$

where $D_{31} := 3n + d_1 - 2d_1' - d_2'$.

A.7 $H_{4:1}$

The action of $H_{4:1}$ on the 1-QP state is given by

$$
H_{4:1}\,|K,\sigma\rangle = + \sum_{d_1'd_2'd_3'} \sum_{n} \sum_{\substack{\beta_1\beta_2\\ \beta_3\beta_4}} e^{iK\left(n-\frac{3d_1'+2d_2'+d_3'}{4}\right)} {}^{\beta_1\beta_2\beta_3\beta_4}_{\sigma}\Big[\mathcal{C}_1^4\Big]^{nd_1'd_2'd_3'} |K,\beta_1;d_1',\beta_2;d_2',\beta_3;d_3',\beta_4\rangle\,, \qquad \text{(A.22)}
$$

where

$$
{}^{\beta_1\beta_2\beta_3\beta_4}_{\sigma}\Big[\mathcal{C}_1^4\Big]^{nd_1'd_2'd_3'} := \langle r-n,\beta_1;r-n+d_1',\beta_2;r-n+d_{12}',\beta_3;r-n+d_{123}',\beta_4|\,H_{4:1}\,|r,\sigma\rangle\,. \qquad \text{(A.23)}
$$

A.8 $H_{3:2}$

The action of $H_{3:2}$ on the 2-QP state is given by

$$
H_{3:2}\,|K,\sigma_1;d_1,\sigma_2\rangle = -\sum_{d_1'd_2'} \sum_{n} \sum_{\beta_1\beta_2\beta_3} e^{iK\left(n+\frac{d_1}{2}-\frac{2d_1'+d_2'}{3}\right)} {}^{\beta_1\beta_2\beta_3}_{\sigma_1\sigma_2}\Big[\mathcal{C}_2^3\Big]^{nd_1'd_2'}_{d_1} |K,\beta_1;d_1',\beta_2;d_2',\beta_3\rangle\,, \qquad \text{(A.24)}
$$

where

$$
{}^{\beta_1\beta_2\beta_3}_{\sigma_1\sigma_2}\Big[\mathcal{C}_2^3\Big]^{nd_1'd_2'}_{d_1} := \langle r-n,\beta_1;r-n+d_1',\beta_2;r-n+d_{12}',\beta_3|\,H_{3:1}\,|r,\sigma_1;r+d_1,\sigma_2\rangle\,. \qquad \text{(A.25)}
$$

For the application of $H_{3:2}$ on the 3-QP state, we find

$$
\begin{aligned}
H_{3:2}\,|K,\sigma_1;d_1,\sigma_2;d_2,\sigma_3\rangle = \sum_{d_1' d_2'} \Big\{ \\
&+ \sum_{-d_{12}>n} e^{iK\left(\frac{D_{32}}{12}\right)} \sum_{\beta_1\beta_2\beta_4} {}^{\beta_1\beta_2\beta_4}_{\sigma_1\sigma_2}\Big[\mathcal{C}_2^3\Big]^{nd_1'd_2'}_{d_1} |K,\sigma_3;-n-d_{12},\beta_1;d_1',\beta_2;d_2',\beta_4\rangle \\
&- \sum_{\substack{d_1'-d_{12}>n\\ -d_{12}<n}} e^{iK\left(\frac{D_{32}}{12}\right)} \sum_{\beta_1\beta_2\beta_4} {}^{\beta_1\beta_2\beta_4}_{\sigma_1\sigma_2}\Big[\mathcal{C}_2^3\Big]^{nd_1'd_2'}_{d_1} |K,\beta_1;n+d_{12},\sigma_3;d_1'-n-d_{12},\beta_2;d_2',\beta_4\rangle \\
&+ \sum_{\substack{d_1'-d_{12}<n\\ d_{12}'-d_{12}>n}} e^{iK\left(\frac{D_{32}}{12}\right)} \sum_{\beta_1\beta_2\beta_4} {}^{\beta_1\beta_2\beta_4}_{\sigma_1\sigma_2}\Big[\mathcal{C}_2^3\Big]^{nd_1'd_2'}_{d_1} |K,\beta_1;d_1',\beta_2;n+d_{12}-d_1',\sigma_3;d_{12}'-n-d_{12},\beta_4\rangle \\
&- \sum_{d_{12}'-d_{12}<n} e^{iK\left(\frac{D_{32}}{12}\right)} \sum_{\beta_1\beta_2\beta_4} {}^{\beta_1\beta_2\beta_4}_{\sigma_1\sigma_2}\Big[\mathcal{C}_2^3\Big]^{nd_1'd_2'}_{d_1} |K,\beta_1;d_1',\beta_2;d_2',\beta_4;n+d_{12}-d_{12}',\sigma_3\rangle \\
&- \sum_{-d_1>n} e^{iK\left(\frac{D_{32}+3d_2}{12}\right)} \sum_{\beta_1\beta_3\beta_4} {}^{\beta_1\beta_3\beta_4}_{\sigma_1\sigma_3}\Big[\mathcal{C}_2^3\Big]^{nd_1'd_2'}_{d_{12}} |K,\sigma_2;-n-d_1,\beta_1;d_1',\beta_3;d_2',\beta_4\rangle \\
&+ \sum_{\substack{d_1'-d_1>n\\ -d_1<n}} e^{iK\left(\frac{D_{32}+3d_2}{12}\right)} \sum_{\beta_1\beta_3\beta_4} {}^{\beta_1\beta_3\beta_4}_{\sigma_1\sigma_3}\Big[\mathcal{C}_2^3\Big]^{nd_1'd_2'}_{d_{12}} |K,\beta_1;n+d_1,\sigma_2;d_1'-n-d_1,\beta_3;d_2',\beta_4\rangle \\
&- \sum_{\substack{d_{12}'-d_1>n\\ d_1'-d_1<n}} e^{iK\left(\frac{D_{32}+3d_2}{12}\right)} \sum_{\beta_1\beta_3\beta_4} {}^{\beta_1\beta_3\beta_4}_{\sigma_1\sigma_3}\Big[\mathcal{C}_2^3\Big]^{nd_1'd_2'}_{d_{12}} |K,\beta_1;d_1',\beta_3;n+d_1-d_1',\sigma_2;d_{12}'-n-d_1,\beta_4\rangle \\
&+ \sum_{d_{12}'-d_1<n} e^{iK\left(\frac{D_{32}+3d_2}{12}\right)} \sum_{\beta_1\beta_3\beta_4} {}^{\beta_1\beta_3\beta_4}_{\sigma_1\sigma_3}\Big[\mathcal{C}_2^3\Big]^{nd_1'd_2'}_{d_{12}} |K,\beta_1;d_1',\beta_3;d_2',\beta_4;n+d_1-d_{12}',\sigma_2\rangle \\
&- \sum_{d_1>n} e^{iK\left(\frac{D_{32}+3d_2-6d_1}{12}\right)} \sum_{\beta_2\beta_3\beta_4} {}^{\beta_2\beta_3\beta_4}_{\sigma_2\sigma_3}\Big[\mathcal{C}_2^3\Big]^{nd_1'd_2'}_{d_2} |K,\sigma_1;d_1-n,\beta_2;d_1',\beta_3;d_2',\beta_4\rangle \\
&+ \sum_{\substack{d_1<n\\ d_1+d_1'>n}} e^{iK\left(\frac{D_{32}+3d_2-6d_1}{12}\right)} \sum_{\beta_2\beta_3\beta_4} {}^{\beta_2\beta_3\beta_4}_{\sigma_2\sigma_3}\Big[\mathcal{C}_2^3\Big]^{nd_1'd_2'}_{d_2} |K,\beta_2;n-d_1,\sigma_1;d_1'+d_1-n,\beta_3;d_2',\beta_4\rangle \\
&- \sum_{\substack{d_1+d_1'<n\\ d_1+d_{12}'>n}} e^{iK\left(\frac{D_{32}+3d_2-6d_1}{12}\right)} \sum_{\beta_2\beta_3\beta_4} {}^{\beta_2\beta_3\beta_4}_{\sigma_2\sigma_3}\Big[\mathcal{C}_2^3\Big]^{nd_1'd_2'}_{d_2} |K,\beta_2;d_1',\beta_3;n-d_1-d_1',\sigma_1;d_{12}'+d_1-n,\beta_4\rangle \\
&+ \sum_{d_1+d_{12}'<n} e^{iK\left(\frac{D_{32}+3d_2-6d_1}{12}\right)} \sum_{\beta_2\beta_3\beta_4} {}^{\beta_2\beta_3\beta_4}_{\sigma_2\sigma_3}\Big[\mathcal{C}_2^3\Big]^{nd_1'd_2'}_{d_2} |K,\beta_2;d_1',\beta_3;d_2',\beta_4;n-d_1-d_{12}',\sigma_1\rangle \Big\}, \qquad \text{(A.26)}
\end{aligned}
$$

with $D_{32} := 9n + 5d_1 + d_2 - 6d_1' - 3d_2'$.

A.9 $H_{4:2}$

The action of $H_{4:2}$ on the 2-QP state is given by

$$H_{4:2}\,|K,\sigma_1;d_1,\sigma_2\rangle = \\ -\sum_{d_1'd_2'd_3'}\sum_{n}\sum_{\substack{\beta_1\beta_2\\ \beta_3\beta_4}} e^{iK\left(n+\frac{d_1}{2}-\frac{3d_1'+2d_2'+d_3'}{4}\right)}\,{}^{\beta_1\beta_2\beta_3\beta_4}_{\sigma_1\sigma_2}\Big[\mathcal{C}_2^4\Big]^{nd_1'd_2'd_3'}_{d_1}\,|K,\beta_1;d_1',\beta_2;d_2',\beta_3;d_3',\beta_4\rangle\,, \tag{A.27}$$

where we have defined

$${}^{\beta_1\beta_2\beta_3\beta_4}_{\sigma_1\sigma_2}\Big[\mathcal{C}_2^4\Big]^{nd_1'd_2'd_3'}_{d_1} := \langle r',\beta_1;r'+d_1',\beta_2;r'+d_{12}',\beta_3;r'+d_{123}',\beta_4|\,H_{4:2}\,|r,\sigma_1;r+d_1,\sigma_2\rangle\,, \tag{A.28}$$

with $r' := r-n$.

A.10 $H_{4:3}$

The action of $H_{4:3}$ on the 3-QP state is given by

$$H_{4:3}\,|K,\sigma_1;d_1,\sigma_2;d_2,\sigma_3\rangle = \\ -\sum_{d_1'd_2'd_3'}\sum_{n}\sum_{\substack{\beta_1\beta_2\\ \beta_3\beta_4}} e^{iK\left(n+\frac{2d_1+d_2}{3}-\frac{3d_1'+2d_2'+d_3'}{4}\right)}\,{}^{\beta_1\beta_2\beta_3\beta_4}_{\sigma_1\sigma_2\sigma_3}\Big[\mathcal{C}_3^4\Big]^{nd_1'd_2'd_3'}_{d_1d_2}\,|K,\beta_1;d_1',\beta_2;d_2',\beta_3;d_3',\beta_4\rangle\,, \tag{A.29}$$

where we have defined

$${}^{\beta_1\beta_2\beta_3\beta_4}_{\sigma_1\sigma_2\sigma_3}\Big[\mathcal{C}_3^4\Big]^{nd_1'd_2'd_3'}_{d_1d_2} := \\ \langle r',\beta_1;r'+d_1',\beta_2;r'+d_{12}',\beta_3;r'+d_{123}',\beta_4|\,H_{4:3}\,|r,\sigma_1;r+d_1,\sigma_2;r+d_{12},\sigma_3\rangle\,, \tag{A.30}$$

with $r' := r-n$.

Appendix B

Simplification Rules

The algebraic part of the deepCUT method requires to keep track of many monomials and to calculate their commutators. The number of monomials to be tracked can be substantially reduced if we are interested in sectors with only a few QPs and in processes up to a specific order n in the formal expansion parameter. For the bookkeeping [KDU12], we define two different orders for each monomial A_i. The first is the minimal order $O_{\min}(A_i)$ which is the order in which the monomial A_i appears for the first time.

The second is the maximal order $O_{\max}(A_i)$ which gives the order up to which the prefactor of the monomial A_i is needed to describe the targeted sector up to order n. By the term "targeted" we simply express that it is this sector that we want to know and to compute finally. The maximal orders of monomials can be determined from the minimal orders and the flow equations in an iterative way, see Ref. [KDU12] for details and examples. Finally, if $O_{\max}(A_i) < O_{\min}(A_i)$ holds the monomial A_i has no effect on the targeted quantities up to order n and we can discard it.

This omission of unnecessary monomials is possible only *after* determining the flow equations. The idea of *simplification rules* (SRs) is to find an *upper bound* $\widetilde{O}_{\max}$ for the maximal order of each monomial A_i *during* the algebraic part of the calculations. Then this bound $\widetilde{O}_{\max}$ is used to discard at least some of the unnecessary monomials in the algebraic calculations leading to an acceleration of the algorithm and to reduce memory requirements.

B.1 Simplification Rules for BI Limit

Here, we present the *a-posteriori* and *a-priori* SRs which are employed in our BI limit analysis of the IHM in Chapter 4. They are used in the second application of the deepCUT analysis where effective Hamiltonians are drived which preserve the number of fermionic QPs.

B.1.1 The *A-Posteriori* Simplification Rules

The a-posteriori SRs are applied *after* the calculation of each commutator. They check whether a monomial can be discarded or not. In the sequel, it is assumed that the order of calculations is n. First, we discuss the simplifications if the sector with zero QPs is targeted, i.e., the ground state, because this is the simplest case. But we also discuss what is necessary to target sectors with a finite number of QPs.

For an upper bound to the maximal order of the monomial A, let us assume that c_σ and a_σ are the number of creation and annihilation operators with spin σ which occur in A. We explain the idea for the creation operators. The annihilation operators can be treated in the same way.

The ground state energy is just a number so that its corresponding operator is the identity $\mathbb{1}$. For the monomial A to influence the ground state energy, all creation operators have to be cancelled in the commutation process. The generator η comprises the monomials

$$\eta^{(1)}_{\text{eff}} = \sum_{i,\sigma} \left(g^\dagger_{i,\sigma} g^\dagger_{i+1,\sigma} + \text{h.c.} \right) \tag{B.1}$$

in first order. In the process of commutation, this generator term can compensate two creation or two annihilation operators with the *same* spin. This is the key observation for the SR. We point out that the higher order terms in the generator may be able to compensate more than two operators, but the ratio between the number of compensated operators and the minimal order of the generator term is always equal or less than 2. Thus it is sufficient to consider just the first order term of the generator in our analysis [KDU12]. The minimal number of commutations needed to cancel all the creation operators reads

$$K^c_0 = \sum_\sigma \left\lceil \frac{c_\sigma}{2} \right\rceil \tag{B.2}$$

where the ceiling brackets stand for the smallest integer larger than the argument. A lower number of commutations is necessary if sectors with more QPs are targeted. If we want to target q QPs we denote the required minimal number of commutations by K^c_q. The number of commutations is minimized if these operators are chosen from spin channels with an odd number of operators. In this way, one can reach the sector with q quasiparticles by a minimum of

$$K^c_q = \max\left(K^c_0 - d_c - \left\lfloor \frac{q - d_c}{2} \right\rfloor, 0 \right) \tag{B.3}$$

commutations with $d_c := \min(q, \alpha_c)$. The floor brackets stand for the largest integer smaller than the argument. The parameter α_c is zero if both the numbers of creation operators with spin up and with spin down are even; it is one if one of them is even and the other odd; it is two if both of them are odd. Analogously, K^a_q for the annihilation part is defined.

Because each commutation with the generator (B.1) increases the order by one, we deduce from the above considerations the upper bound

$$\widetilde{O}_{\max}(A) = n - K^c_q - K^a_q \tag{B.4}$$

for the maximal order of the monomial A. The monomial A is safely omitted if $\widetilde{O}_{\max}(A) < O_{\min}(A)$. We refer to the described analysis for the maximal order as *basic a-posteriori SR*.

The above upper bound of the maximal order can be reduced further by considering the structure of the generator terms on the lattice. The term (B.1) contains two creation or annihilation operators with the same spin only on *adjacent* sites. This means that the compensation of two operators which do not act on neighboring sites needs at least two commutations leading to an increase by two in the maximal order.

We point out that there are also other terms in the generator with extended structure in real space, but they occur in higher minimal orders [KDU12] so that it is sufficient to focus on the first order term (B.1). To exploit structural aspects on the lattice, the clusters of creation and annihilation operators with spin σ are divided into different *linked* subclusters, see Ref. [KDU12]. We denote the number of creation and annihilation operators with spin σ in the subcluster labelled by i by $k_i^{c,\sigma}$ and $k_i^{a,\sigma}$, respectively [KDU12]. The number of commutations with (B.1) needed to compensate all the creation operators reads

$$K_0^c = \sum_{i,\sigma} \left\lceil \frac{k_i^{c,\sigma}}{2} \right\rceil . \tag{B.5}$$

This equation extends (B.2) by considering the real space structure of the monomials. In analogy to the basic a-posteriori SR, the relation (B.5) can be generalized to K_q^c if the sectors with q QPs are targeted. In order to minimize K_q^c, the q operators are taken first from subclusters with odd number of sites saving one commutation for each operator. Then the remaining operators are taken from even subclusters which needs at least two operators to save one commutation. Eventually, we obtain

$$K_q^c = \max\left(K_0^c - d_c - \left\lfloor \frac{q-d_c}{2} \right\rfloor , 0 \right) \tag{B.6}$$

where $d_c := \min(q, \alpha_c)$ and α_c is the number of odd-size linked subclusters present in *both* spin up and spin down creation clusters. Similarly, one can find the corresponding relation for annihilation yielding K_q^a. Replacing them for K_q^c and K_q^a in Eq. (B.4) leads to a maximal order which is lower than the estimate of the basic a-posteriori SR. This improved analysis for the maximal order which takes into account the real space structure of the monomials is called *extended a-posteriori SR*.

B.1.2 The *A-Priori* Simplification Rules

The a-priori SRs are applied *before* commutators are computed explicitly. Thus they make an additional speed-up possible. This type of SRs checks whether the result of the commutator $[T, D] = TD - DT$ leads to any monomial which can pass the a-posteriori SRs or not. Here T stands for any monomial from the generator and D for any monomial from the Hamiltonian. If all the monomials which may ensue from the studied commutator are unnecessary, one can ignore this commutator improving the computational speed. Two different basic and extended a-priori SRs can be defined corresponding to the basic and extended a-posteriori SRs.

In the basic a-priori SR, the minimal number of creation and annihilation operators with spin σ resulting from the products TD and DT are estimated separately. Then the basic a-posteriori SR is employed to obtain an upper bound for the maximal orders of TD and DT. We explain the method for TD; the product DT can be analyzed in the same way.

Let a_T^σ and c_T^σ be the numbers of creation and annihilation operators with spin σ in the monomial T. Similarly, we define a_D^σ and c_D^σ for the monomial D. Next, the product TD is normal-ordered, the creation operators are sorted left to the annihilation operators by appropriate commuations. In the course of this normal-ordering, the number $s_{TD}^\sigma := \min(a_T^\sigma, c_D^\sigma)$ from the creation and annihilation operators with spin σ may cancel at maximum. Therefore, the minimal number of creation and annihilation operators of the normal-ordered product TD is given by

$$c_{TD}^\sigma = c_T^\sigma + c_D^\sigma - s_{TD}^\sigma, \tag{B.7}$$
$$a_{TD}^\sigma = a_D^\sigma + a_T^\sigma - s_{TD}^\sigma. \tag{B.8}$$

Using these estimates, one can find the upper bound for the maximal order of the normal-ordered product TD. Eventually, we conclude that the commutator $[T, D]$ can be ignored if

$$\max\left(\widetilde{O}_{\max}(TD), \widetilde{O}_{\max}(DT)\right) < O_{\min}(T) + O_{\min}(D). \tag{B.9}$$

In the extended a-priori SR, similar to the extended a-posteriori SR, the lattice structure of monomials is considered as well. Using this property, one can manage to identify more unnecessary commutators before computing them. Again, we describe the method for TD; DT is treated in the same fashion. All we have to do is to evaluate the clusters of creation and annihilation operators of the normal-ordered product TD for up and down spins. Then, the method uses the extended a-posteriori SR to find the maximal order of TD based on the estimated clusters.

Because the operator algebra is local, only operators acting on the same sites can cancel in the normal-ordering. This means that the spin-σ creation operators of T and the spin-σ annihilation operators of D which are elements of the set

$$\mathbf{S}_{TD}^\sigma := \mathbf{A}_T^\sigma \cap \mathbf{C}_D^\sigma \tag{B.10}$$

may cancel in the normal-ordering. The sets $\mathbf{A}_X^\sigma$ and $\mathbf{C}_X^\sigma$ denote the spin-σ creation and annihilation clusters of operator X. Hence, the creation and annihilation clusters of TD are given by

$$\mathbf{C}_{TD}^\sigma = \mathbf{C}_T^\sigma \cup \left(\mathbf{C}_D^\sigma \setminus \mathbf{S}_{TD}^\sigma\right), \tag{B.11a}$$
$$\mathbf{A}_{TD}^\sigma = \mathbf{A}_D^\sigma \cup \left(\mathbf{A}_T^\sigma \setminus \mathbf{S}_{TD}^\sigma\right). \tag{B.11b}$$

Similar results can be obtained for the product DT. Using the extended a-posteriori SR, one obtains an upper bound for the maximal orders of TD and DT. The commutator $[T, D]$ is ignored finally if (B.9) is fulfilled.

Although the extended a-priori SR can cancel more commutators compared to the basic a-priori SR, it has a caveat. In contrast to the basic a-priori SR, the extended version has

to be applied individually to each element of the translation symmetry group, which is computationally expensive. Therefore, in order to reach the highest efficiency we use a combination of these a-priori SRs in practice [KDU12].

B.2 Simplification Rules for Dimer Limit

In this section, we discuss the simplification rules (SRs) that we employed in the dimer limit analysis of the IHM (5.12). We classify the dimer excitation operators (5.10) into boson and fermion groups. The boson group contains the singlon (5.10c) and the three triplon operators (5.10b). The fermion group includes the four fermion operators (5.10a) which act on the left site f_l and on the right site f_r of a dimer with two different spins. The off-diagonal elements in the Hamiltonian (5.12) contain various kinds of annihilation and creation processes between and among fermions and bosons. This makes it difficult to write efficient and flexible SRs especially when sectors with finite numbers of fermions and/or bosons are targeted. In the following, two kinds of simplification rules are introduced. The first one is a basic SR which is not very efficient but flexible. It works if sectors with any specific number of bosons and fermions are targeted. In the basic SR, only the number of creation and annihilation operators of each monomial is considered. In the second one called extended SR the lattice structure of the monomials is also taken into account. This extended SR can work efficiently for the ground state and to some extent for the 1-fermion sector. However, the present scheme needs to be generalized if higher quasiparticle sectors are targeted.

Before describing the basic and the extended SRs, let us consider the general structure of off-diagonal terms in the Hamiltonian (5.12). We emphasize that the first order generator terms are enough for writing the SRs although higher order terms with other structures also appear during the flow [KDU12]. Among the various kinds of the first order generator terms, only the three structures given below play a major role in the estimate of maximal orders

$$\eta^{(a)} \sim \sum_j f^\dagger_{j;l} f^\dagger_{j+1;r} + \text{h.c.}, \tag{B.12a}$$

$$\eta^{(b)} \sim \sum_j b^\dagger_j f_{j;p} f^\dagger_{j+1;p} + \text{h.c.} \quad ; \quad p = l, r, \tag{B.12b}$$

$$\eta^{(c)} \sim \sum_j b^\dagger_j b^\dagger_{j+1} f_{j;l} f_{j+1;r} + \text{h.c.}, \tag{B.12c}$$

where the boson operator $b^\dagger$ stands either for a singlon or a triplon operator and we omitted the spin indices of the fermion operators because they play no role in the following considerations.

B.2.1 The Basic Simplification Rule

In order to elucidate the basic SR, we focus first on the number of annihilation and creation operators which can be canceled via commutations with generator structures (B.12). The first term $\eta^{(a)}$ can cancel two fermion creation or annihilation operators only if they act on *different* internal positions. This internal position of a single dimer can be either left $p = l$ or right $p = r$. This is natural due to the conservation of the total charge in the system. Two creation or annihilation operators of the same type need at least two commutations with the generator $\eta^{(a)}$ to be canceled. This property allows us to make the SRs dependent on the fermion types "left" and "right". The net effect of the second term $\eta^{(b)}$ is to eliminate one boson operator. The third term $\eta^{(c)}$ transforms two boson operators into two fermion operators but with different types.

We try to find an upper bound for the maximal order of the monomial A if sectors up to q_b bosons *and* q_f fermions are targeted up to order n. We suppose that the creation part of monomial A includes c_b boson and c_f fermion operators. We will only examine the creation part of the monomial A. The annihilation part can be treated in the same way. It is more convenient to first discuss the situation where no fermion (but still q_b boson) operator is targeted. Then, we will keep q_f fermion operators of the monomial A such that the maximal order is overestimated. The number of boson operators which have to be canceled reads

$$c_b' \equiv \max(c_b - q_b, 0). \tag{B.13}$$

If c_b' is even, then we transform all of these boson operators into fermion operators using $\eta^{(c)}$. If c_b' is odd, the even number $c_b' - 1$ boson operators are transformed into fermion operators and the final boson operator is canceled via $\eta^{(b)}$. This procedure requires $\left\lceil \frac{c_b'}{2} \right\rceil$ commutations and produces $2\left\lfloor \frac{c_b'}{2} \right\rfloor$ additional fermion operators. Half of these additional fermion operators are of type f_l and half of them are of type f_r. Therefore the total number of fermion operators of type "left" and "right" which should be canceled read

$$c_{f_l}' = c_{f_l} + \left\lfloor \frac{c_b'}{2} \right\rfloor, \tag{B.14a}$$

$$c_{f_r}' = c_{f_r} + \left\lfloor \frac{c_b'}{2} \right\rfloor, \tag{B.14b}$$

where c_{f_l} and c_{f_r} are the initial number of fermion operators of type "left" and "right" present in the monomial A. The fermion operators can be canceled by commutations with the term $\eta^{(a)}$. This term always cancels two fermions of different types. Fermion operators of the same type need one commutation each. Hence, the number of commutations necessary to eliminate all the boson (B.13) and the fermion (B.14) operators is given by

$$K^c_{0,q_b} = \left\lceil \frac{c_b'}{2} \right\rceil + \max(c_{f_l}', c_{f_r}'). \tag{B.15}$$

This equation can be generalized to $K^c_{q_f,q_b}$ if sectors with up to q_b bosons and q_f fermions are targeted. In this case, one needs to keep q_f fermion operators of monomial A such

that the number of commutations $K^c_{q_f,q_b}$ is minimized. We divide the fermion operators into pairs. Each pair contains one "left" fermion and one "right" fermion. There will be some single fermions left if the number of fermions of type "left" and "right" are not equal. First we keep the single fermion operators. In this way, one can save one commutation for each fermion operator. The remaining fermion operators have to be kept from paired fermions saving one commutation for each two operators. Therefore, we obtain

$$K^c_{q_f,q_b} = K^c_{0,q_b} - d^c_1 - \left\lceil \frac{d^c_2}{2} \right\rceil, \tag{B.16}$$

where d^c_1 and d^c_2 are defined as

$$d^c_1 \equiv \min\left(q_f, \left|c'_{f_l} - c'_{f_r}\right|\right), \tag{B.17a}$$

$$d^c_2 \equiv \min\left(q_f - d^c_1, c'_{f_l} + c'_{f_r} - d^c_1\right). \tag{B.17b}$$

The annihilation part of monomial A can be analyzed in the same way and leads to $K^a_{q_f,q_b}$. Finally, the upper bound for the maximal order of the monomial A is given by [KDU12]

$$\widetilde{O}_{\max}(A) = n - K^c_{q_f,q_b} - K^a_{q_f,q_b}, \tag{B.18}$$

where n is the order of calculations. This basic *a-posteriori* SR prevents unnecessary monomials to be tracked.

As pointed out in the previous section, the *a-priori* SRs prevent unnesseccary commutators to be evaluated. We explain the basic a-priori SR for the commutator $[T, D] = TD - DT$. We focus on the product TD. The product DT can be treated in the same way. All we need to do is to estimate the minimum number of creation and annihilation operators which remain after normal-ordering. Suppose c^i_T and a^i_T are the numbers of creation and annihilation operators, respectively, of type i in the monomial T. The index i refers to the eight possible operators (singlon, triplons, and fermions) that can appear on a dimer. Similarly for the monomial D we assume c^i_D creation operators and a^i_D annihilation operators of type i. Only operators of the same type can cancel each other in the normal-ordering. Therefore, the minimum number of creation and annihilation operators of type i of the product TD can be estimated as

$$c^i_{TD} \geq \tilde{c}^i_{TD} := c^i_T + c^i_D - s^i_{TD}, \tag{B.19a}$$

$$a^i_{TD} \geq \tilde{a}^i_{TD} := a^i_D + a^i_T - s^i_{TD}, \tag{B.19b}$$

where $s^i_{TD} := \min\left(a^i_T, c^i_D\right)$. Subsequently, for the number of boson operators and the number of left and right fermion operators we find

$$c^b_{TD} \geq \tilde{c}^b_{TD} := \sum_{i \in \mathrm{b}} \tilde{c}^i_{TD}, \tag{B.20a}$$

$$c^{f_r}_{TD} \geq \tilde{c}^{f_r}_{TD} := \sum_{i \in f_r} \tilde{c}^i_{TD}, \tag{B.20b}$$

$$c^{f_l}_{TD} \geq \tilde{c}^{f_l}_{TD} := \sum_{i \in f_l} \tilde{c}^i_{TD}, \tag{B.20c}$$

where b stands for bosons and f_r and f_l stand for the right-type and the left-type fermions. Similar relations as (B.20) are valid for the annihilation parts of TD.

By having the numbers c^{b}_{TD}, $c^{f_r}_{TD}$, $c^{f_l}_{TD}$, a^{b}_{TD}, $a^{f_r}_{TD}$, and $a^{f_l}_{TD}$ in hand, we can estimate the maximal order of the product TD using the relation (B.18). Finally, the commutator $[T,D]$ has no effect on the targeted quantities up to order n and can be ignored if [KDU12]

$$\max\left(\widetilde{O}_{\max}(TD),\widetilde{O}_{\max}(DT)\right) < O_{\min}(T)+O_{\min}(D). \tag{B.21}$$

The basic a-priori SR is used, in addition to the a-posteriori SRs, in order to increase the speed of the deepCUT algorithm.

B.2.2 The Extended Simplification Rule

The upper bound (B.18) for the maximal order of the monomial A can be reduced by taking into account the lattice structure of the generator terms (B.12). The first term $\eta^{(a)}$ cancels two fermions of different types but only on nearest-neighbor (n.n.) dimers. The third term $\eta^{(c)}$ transforms two n.n. bosons into two n.n. fermions of different types. Special attention has to be paid to the second term $\eta^{(b)}$. This term can cancel one boson accompanied by a n.n. hopping process of a fermion. This additional hopping process makes it difficult to write an efficient extended SR like in the previous section B.1. In the following, we estimate the minimum number of commutations that we need to compensate all the fermion and boson creation operators of monomial A. The annihilation part of monomial A can be treated in the same way.

Similar to the previous section, we divide the creation cluster of monomial A into different *linked* subclusters. Assume $K[\mathcal{C}]$ denotes the number of commutations needed to cancel all operators of the linked subcluster $\mathcal{C}$. One requires a *lower* bound for this number of commutations in order to find an upper bound for the maximal order of monomial A. Hence, the size of each linked subcluster can be reduced based on the inequalities

$$K\left[\otimes\!-\!\oplus\!-\mathcal{C}'\right] \geq K[\otimes\!-\!\oplus]+K\left[\mathcal{C}'\right] \geq 1+K\left[\mathcal{C}'\right], \tag{B.22a}$$
$$K\left[\bullet\!-\!\bullet\!-\mathcal{C}'\right] \geq K[\bullet\!-\!\bullet]+K\left[\mathcal{C}'\right] \geq 2+K\left[\mathcal{C}'\right], \tag{B.22b}$$
$$K\left[\bullet\!-\!\otimes\!-\mathcal{C}'\right] \geq K[\bullet\!-\!\otimes]+K\left[\mathcal{C}'\right] \geq 2+K\left[\mathcal{C}'\right], \tag{B.22c}$$
$$K\left[\otimes\!-\!\bullet\!-\mathcal{C}'\right] \geq 1+K\left[\otimes\!-\mathcal{C}'\right], \tag{B.22d}$$
$$K\left[\otimes\!-\!\otimes\!-\mathcal{C}'\right] \geq 1+K\left[\otimes\!-\mathcal{C}'\right], \tag{B.22e}$$

where the symbols $\otimes$ and $\oplus$ denote the two possible fermion operators on a dimer, the symbol $\bullet$ stands for a boson operator on a dimer, and $\mathcal{C}'$ shows the remaining part of the initial subcluster. In the left-hand side of the first equation (B.22a), for instance, the two n.n. fermion operators of different types $\otimes\!-\!\oplus$ are linked to the remaining part $\mathcal{C}'$. The validity of Eqs. (B.22) can be realized based on the structure of the generator terms (B.12).

As an example, let us check why we can not cancel the linked fermion and boson operators $\otimes\!-\!\bullet$ in Eq. (B.22d). Consider a linked cluster of the form

$$\mathcal{C} = \otimes\!-\underbrace{\bullet\!-\!\bullet\!-\cdots-\!\bullet\!-\!\bullet}_{n}\!-\oplus, \tag{B.23}$$

where two different fermion operators on the two outermost dimers of the cluster $\mathcal{C}$ are linked via n boson operators. After n applications of the generator term (B.12b), one can cancel all the boson operators and bring the two fermion operators to n.n. dimers. This pair of n.n. fermion operators can also be canceled via one commutation with the generator term (B.12a). Hence, the total number of commutations that one needs to cancel operators in this cluster (B.23) is $n+1$.

The scheme introduced in Eqs. (B.22) reduces a linked subcluster of operators to at most one individual fermion or boson operator. A single individual boson operator needs two commutations and a single individual fermion operator needs one commutation to be canceled. In this manner, we can find the minimum number of commutations to remove all operators of a linked subcluster. Finally, the minimum number of commutations necessary to cancel all the creation operators of monomial A is given by

$$K^c_{0,0} = \sum_{\mathcal{C}} K[\mathcal{C}]\,, \tag{B.24}$$

where the summation runs over all creation linked subcluster of the monomial A. Similarly, we can analyze the annihilation part of the monomial A. The maximal order can be calculated via Eq. (B.18) if just the ground state is targeted.

The extended SR saves a factor of about 8 in the number of representatives compared to the basic SR if the ground state is targeted. We also used this extended SR to describe the 1-fermion sector making the simple estimate $K_{1,0} = K_{0,0} - 1$ for both creation and annihilation parts. This relation can always be used in Eq. (B.18) because a fermion operator costs at most one commutation to be canceled. For higher quasiparticle sectors, however, such a simple estimate can not work efficiently and it requires to be modified.

Appendix C

Spin States

In the first section C.1 of this Appendix the spin states which are used in the BI limits analysis in Chapter 4 to construct the Hamiltonian matrix, are presented. The spin states made from triplons with specific magnetic numbers are reported in the second section C.2.

C.1 Fermions

The electron-hole transformation (4.1) on the odd sites of the IHM affects the spin eigen states and makes them deviate from their standard form. For instance, the two-QP state $|K;d\rangle$ with total spin zero reads

$$|K;d\rangle^{S=0,M=0} = \begin{cases} \frac{1}{\sqrt{2}}\big(|K,+;d,+\rangle + |K,-;d,-\rangle\big) & \text{for } d \in \text{odd} \\ \frac{1}{\sqrt{2}}\big(|K,+;d,-\rangle - |K,-;d,+\rangle\big) & \text{for } d \in \text{even} \end{cases} \tag{C.1}$$

where d is the distance between the two QPs. For constructing the Hamiltonian matrix in the ED, it is more suitable to apply the transformation $g^{\dagger}_{i,\sigma} \to g^{\dagger}_{i,\bar{\sigma}}$ to the odd sites of the effective Hamiltonian derived from the deepCUT calculations. The aim of this transformation is to make the spin eigen states independent of relative distances up to a sign factor.

The 1-, 2-, 3-, and 4-QP states with total spins $S = 0, \frac{1}{2}, 1$ and corresponding total magnetic numbers $M = 0, \frac{1}{2}, 1$ are presented in Table C.1. These relations are used for the construction of the Hamiltonian matrix in the ED treatment in Chapter 4.

C.2 Triplons

The spin states with the total spin $S = 0, 1$ and the corresponding total magnetic number $M = 0, 1$ which can be constructed from 1-triplon (1T), 2-triplon (2T), and 3-triplon (3T)

$\lvert K\rangle^{S=1/2,M=1/2}$	$\lvert K+\rangle$
$\lvert K;d_1\rangle^{S=1,M=1}$	$\lvert K+;d+\rangle$
$\lvert K;d_1\rangle^{S=0,M=0}$	$\frac{1}{\sqrt{2}}\Big(\lvert K+;d_1-\rangle-(-1)^{d_1}\lvert K-;d_1+\rangle\Big)$
$\lvert K;d_1;d_2\rangle_a^{S=1/2,M=1/2}$	$\frac{1}{\sqrt{2}}\Big(\lvert K+;d_1-;d_2+\rangle-(-1)^{d_1}\lvert K-;d_1+;d_2+\rangle\Big)$
$\lvert K;d_1;d_2\rangle_b^{S=1/2,M=1/2}$	$\frac{1}{\sqrt{6}}\Big(\lvert K-;d_1+;d_2+\rangle + (-1)^{d_1}\lvert K+;d_1-;d_2+\rangle - 2(-1)^{d_1+d_2}\lvert K+;d_1+;d_2-\rangle\Big)$
$\lvert K;d_1;d_2;d_3\rangle_a^{S=1,M=1}$	$\frac{1}{\sqrt{2}}\Big(\lvert K+;d_1+;d_2+;d_3-\rangle-(-1)^{d_3}\lvert K+;d_1+;d_2-;d_3+\rangle\Big)$
$\lvert K;d_1;d_2;d_3\rangle_b^{S=1,M=1}$	$\frac{1}{\sqrt{2}}\Big(\lvert K+;d_1-;d_2+;d_3+\rangle-(-1)^{d_1}\lvert K-;d_1+;d_2+;d_3+\rangle\Big)$
$\lvert K;d_1;d_2;d_3\rangle_c^{S=1,M=1}$	$\frac{1}{2}\Big(\lvert K+;d_1+;d_2+;d_3-\rangle + (-1)^{d_3}\lvert K+;d_1+;d_2-;d_3+\rangle - (-1)^{d_2}\lvert K-;d_1+;d_2+;d_3+\rangle - (-1)^{d_1+d_2}\lvert K+;d_1-;d_2+;d_3+\rangle\Big)$
$\lvert K;d_1;d_2;d_3\rangle_a^{S=0,M=0}$	$\frac{1}{2}\Big(\lvert K+;d_1-;d_2+;d_3-\rangle + (-1)^{d_1+d_3}\lvert K-;d_1+;d_2-;d_3+\rangle - (-1)^{d_3}\lvert K+;d_1-;d_2-;d_3+\rangle - (-1)^{d_1}\lvert K-;d_1+;d_2+;d_3-\rangle\Big)$
$\lvert K;d_1;d_2;d_3\rangle_b^{S=0,M=0}$	$\frac{1}{2\sqrt{3}}\Big(\lvert K-;d_1+;d_2+;d_3-\rangle - 2(-1)^{d_2}\lvert K+;d_1+;d_2-;d_3-\rangle - 2(-1)^{d_2}\lvert K-;d_1-;d_2+;d_3+\rangle + (-1)^{d_1}\lvert K+;d_1-;d_2+;d_3-\rangle + (-1)^{d_3}\lvert K-;d_1+;d_2-;d_3+\rangle + (-1)^{d_1+d_3}\lvert K+;d_1-;d_2-;d_3+\rangle\Big)$

Table C.1: One-, two-, three-, and four-QP states with total spin S and total magnetic number M employed in the ED analysis for constructing the Hamiltonian matrix in different sectors of total S and M.

states are expressed in Table C.2.

$\|1T\rangle^{S=1,M=1}$	$\|t_{+1}\rangle$
$\|1T\rangle^{S=1,M=0}$	$\|t_0\rangle$
$\|2T\rangle^{S=1,M=1}$	$\frac{1}{\sqrt{2}}\Big(\|t_{+1},t_0\rangle - \|t_0,t_{+1}\rangle\Big)$
$\|2T\rangle^{S=1,M=0}$	$\frac{1}{\sqrt{2}}\Big(\|t_{+1},t_{-1}\rangle - \|t_{-1},t_{+1}\rangle\Big)$
$\|2T\rangle^{S=0,M=0}$	$\frac{1}{\sqrt{3}}\Big(\|t_{+1},t_{-1}\rangle + \|t_{-1},t_{+1}\rangle - \|t_0,t_0\rangle\Big)$
$\|3T\rangle_a^{S=1,M=1}$	$\frac{1}{\sqrt{3}}\Big(\|t_{+1},t_{-1},t_{+1}\rangle + \|t_{-1},t_{+1},t_{+1}\rangle - \|t_0,t_0,t_{+1}\rangle\Big)$
$\|3T\rangle_b^{S=1,M=1}$	$\frac{1}{2}\Big(\|t_{+1},t_0,t_0\rangle + \|t_{-1},t_{+1},t_{+1}\rangle - \|t_0,t_{+1},t_0\rangle - \|t_{+1},t_{-1},t_{+1}\rangle\Big)$
$\|3T\rangle_c^{S=1,M=1}$	$\sqrt{\frac{1}{60}}\Big(2\|t_0,t_0,t_{+1}\rangle + 6\|t_{+1},t_{+1},t_{-1}\rangle + \|t_{+1},t_{-1},t_{+1}\rangle + \|t_{-1},t_{+1},t_{+1}\rangle - 3\|t_{+1},t_0,t_0\rangle - 3\|t_0,t_{+1},t_0\rangle\Big)$
$\|3T\rangle_a^{S=1,M=0}$	$\frac{1}{\sqrt{3}}\Big(\|t_{+1},t_{-1},t_0\rangle + \|t_{-1},t_{+1},t_0\rangle - \|t_0,t_0,t_0\rangle\Big)$
$\|3T\rangle_b^{S=1,M=0}$	$\frac{1}{2}\Big(\|t_{+1},t_0,t_{-1}\rangle + \|t_{-1},t_0,t_{+1}\rangle - \|t_0,t_{+1},t_{-1}\rangle - \|t_0,t_{-1},t_{+1}\rangle\Big)$
$\|3T\rangle_c^{S=1,M=0}$	$\sqrt{\frac{1}{60}}\Big(3\|t_0,t_{-1},t_{+1}\rangle + 3\|t_{-1},t_0,t_{+1}\rangle + 3\|t_{+1},t_0,t_{-1}\rangle + 3\|t_0,t_{+1},t_{-1}\rangle - 4\|t_0,t_0,t_0\rangle - 2\|t_{+1},t_{-1},t_0\rangle - 2\|t_{-1},t_{+1},t_0\rangle\Big)$
$\|3T\rangle^{S=0,M=0}$	$\frac{1}{\sqrt{6}}\Big(\|t_{+1},t_0,t_{-1}\rangle + \|t_0,t_{-1},t_{+1}\rangle + \|t_{-1},t_{+1},t_0\rangle - \|t_0,t_{+1},t_{-1}\rangle - \|t_{-1},t_0,t_{+1}\rangle - \|t_{+1},t_{-1},t_0\rangle\Big)$

Table C.2: 1-triplon (1T), 2-triplon (2T), and 3-triplon (3T) states with total spin S and total magnetic number M constructed from the single triplon states $|t_m\rangle$ with specific magnetic number $m = 0, \pm 1$.

Bibliography

[AM76] Neil W. Ashcroft and David N. Mermin. *Solid state physics*. Thomson Learning, Toronto, first edition, January 1976.

[Anu01] Anusooya-Pati, Y. and Soos, Z. G. and Painelli, A. Symmetry crossover and excitation thresholds at the neutral-ionic transition of the modified hubbard model. *Phys. Rev. B*, 63:205118, May 2001.

[Bet31] Hans Albrecht Bethe. Zur Theorie der Metalle; 1, Eigenwerte und Eigenfunktionen der linearen Atomkette. *Z. Phys.*, 71:205–226, 1931.

[BPH+07] K. Bouadim, N. Paris, F. Hébert, G. G. Batrouni, and R. T. Scalettar. Metallic phase in the two-dimensional ionic hubbard model. *Phys. Rev. B*, 76:085112, Aug 2007.

[CAN00] S. Caprara, M. Avignon, and O. Navarro. Spin and charge ordering in the dimerized hubbard model. *Phys. Rev. B*, 61:15667–15675, Jun 2000.

[CF79] M. C. Cross and Daniel S. Fisher. A new theory of the spin-peierls transition with special relevance to the experiments on ttfcubdt. *Phys. Rev. B*, 19:402–419, Jan 1979.

[CLH+08] L. Craco, P. Lombardo, R. Hayn, G. I. Japaridze, and E. Müller-Hartmann. Electronic phase transitions in the half-filled ionic hubbard model. *Phys. Rev. B*, 78:075121, Aug 2008.

[CPK+95] R. Chitra, Swapan Pati, H. R. Krishnamurthy, Diptiman Sen, and S. Ramasesha. Density-matrix renormalization-group studies of the spin-1/2 heisenberg system with dimerization and frustration. *Phys. Rev. B*, 52:6581–6587, Sep 1995.

[CSO77] K A Chao, J Spalek, and A M Oles. Kinetic exchange interaction in a narrow s-band. *Journal of Physics C: Solid State Physics*, 10(10):L271, 1977.

[CZLW10] Hui-Min Chen, Hui Zhao, Hai-Qing Lin, and Chang-Qin Wu. Bond-located spin density wave phase in the two-dimensional (2d) ionic hubbard model. *New Journal of Physics*, 12(9):093021, 2010.

[Dag94] Elbio Dagotto. Correlated electrons in high-temperature superconductors. *Rev. Mod. Phys.*, 66:763–840, Jul 1994.

[Daw12] Matthew Dawber. Electrons weigh in on ferroelectricity. *Physics*, 5:63, Jun 2012.

[dCP62] Jacques des Cloizeaux and J. J. Pearson. Spin-wave spectrum of the antiferromagnetic linear chain. *Phys. Rev.*, 128:2131–2135, Dec 1962.

[DR96] Elbio Dagotto and T. M. Rice. Surprises on the way from one- to two-dimensional quantum magnets: The ladder materials. *Science*, 271(5249):618–623, 1996.

[DU04] Sebastien Dusuel and Götz S. Uhrig. The quartic oscillator: a non-perturbative study by continuous unitary transformations. *Journal of Physics A: Mathematical and General*, 37(39):9275, 2004.

[DU11] S. Duffe and G.S. Uhrig. Hole dispersions for antiferromagnetic spin-$\frac{1}{2}$ two-leg ladders by self-similar continuous unitary transformations. *The European Physical Journal B*, 84(3):475–490, 2011.

[Duf10] Sebastian Duffe. *Effective Hamiltonians for Undoped and Hole-Doped Antiferromagnetic Spin-*$1/2$ *Ladders by Self-Similar Continuous Unitary Transformations in Real Space*. PhD thesis, Technische Universität Dortmund, 2010.

[EFG+05] Fabian H. L. Essler, Holger Frahm, Frank Göhmann, Andreas Klümper, and Vladimir E. Korepin. *The One-Dimensional Hubbard Model*. Cambridge University Press, Cambridge, 2005.

[Egg96] Sebastian Eggert. Numerical evidence for multiplicative logarithmic corrections from marginal operators. *Phys. Rev. B*, 54:R9612–R9615, Oct 1996.

[EIT93] T. Egami, S. Ishihara, and M. Tachiki. Lattice effect of strong electron correlation: Implication for ferroelectricity and superconductivity. *Science*, 261(5126):1307–1310, 1993.

[EN07] Satoshi Ejima and Satoshi Nishimoto. Phase diagram of the one-dimensional half-filled extended hubbard model. *Phys. Rev. Lett.*, 99:216403, Nov 2007.

[Faz99] P. Fazekas. *Lecture Notes on Electron Correlation and Magnetism*. Series in modern condensed matter physics. World Scientific, 1999.

[FDU10] Tim Fischer, Sebastian Duffe, and Götz S. Uhrig. Adapted continuous unitary transformation to treat systems with quasi-particles of finite lifetime. *New Journal of Physics*, 12(3):033048, 2010.

[FGN99] Michele Fabrizio, Alexander O. Gogolin, and Alexander A. Nersesyan. From band insulator to mott insulator in one dimension. *Phys. Rev. Lett.*, 83:2014–2017, Sep 1999.

[Fis11] Tim Fischer. *Description of quasiparticle decay by continuous unitary transformations*. PhD thesis, Technische Universität Dortmund, 2011.

[FT81] L.D. Faddeev and L.A. Takhtajan. What is the spin of a spin wave? *Physics Letters A*, 85(6-7):375 – 377, 1981.

[FU13] Benedikt Fauseweh and Götz S. Uhrig. Multiparticle spectral properties in the transverse field ising model by continuous unitary transformations. *Phys. Rev. B*, 87:184406, May 2013.

[GKR06] Arti Garg, H. R. Krishnamurthy, and Mohit Randeria. Can correlations drive a band insulator metallic? *Phys. Rev. Lett.*, 97:046403, Jul 2006.

[GKR14] Arti Garg, H.R. Krishnamurthy, and Mohit Randeria. Doping a correlated band insulator: A new route to half-metallic behavior. *Phys. Rev. Lett.*, 112:106406, Mar 2014.

[GKS+09] Gianluca Giovannetti, Sanjeev Kumar, Alessandro Stroppa, Jeroen van den Brink, and Silvia Picozzi. Multiferroicity in ttf-ca organic molecular crystals predicted through *Ab Initio* calculations. *Phys. Rev. Lett.*, 103:266401, Dec 2009.

[GP00] G. Grosso and G.P. Parravicini. *Solid State Physics*. Elsevier Science, 2000.

[GSB01] Sanjay Gupta, Shreekantha Sil, and Bibhas Bhattacharyya. Ground state of a chemically modulated hubbard chain at half filling. *Phys. Rev. B*, 63:125113, Mar 2001.

[GST00] N. Gidopoulos, S. Sorella, and E. Tosatti. Born effective charge reversal and metallic threshold state at a band insulator-mott insulator transition. *The European Physical Journal B - Condensed Matter and Complex Systems*, 14(2):217–226, 2000.

[Gut63] Martin C. Gutzwiller. Effect of correlation on the ferromagnetism of transition metals. *Phys. Rev. Lett.*, 10:159–162, Mar 1963.

[GW93] Stanisław D. Głazek and Kenneth G. Wilson. Renormalization of hamiltonians. *Phys. Rev. D*, 48:5863–5872, Dec 1993.

[HA11] Mohsen Hafez and M.R. Abolhassani. Dynamics in the one-dimensional extended ionic hubbard model. *Journal of Physics: Condensed Matter*, 23(24):245602, 2011.

[HDU10] Simone A. Hamerla, Sebastian Duffe, and Götz S. Uhrig. Derivation of the *t-j* model for finite doping. *Phys. Rev. B*, 82:235117, Dec 2010.

[Hir85] J. E. Hirsch. Attractive interaction and pairing in fermion systems with strong on-site repulsion. *Phys. Rev. Lett.*, 54:1317–1320, Mar 1985.

[HJ10] M. Hafez and S. A. Jafari. Excitation spectrum of one-dimensional extended ionic hubbard model. *The European Physical Journal B*, 78(3):323–333, 2010.

[HJA09] Mohsen Hafez, S.A. Jafari, and M.R. Abolhassani. Flow equations for the ionic hubbard model. *Physics Letters A*, 373(48):4479 – 4483, 2009.

[HK09] A. Hackl and S. Kehrein. A unitary perturbation theory approach to real-time evolution problems. *Journal of Physics: Condensed Matter*, 21(1):015601, 2009.

[HL67] A. Brooks Harris and Robert V. Lange. Single-particle excitations in narrow energy bands. *Phys. Rev.*, 157:295–314, May 1967.

[Hon99] A. Honecker. Strong-coupling approach to the magnetization process of polymerized quantum spin chains. *Phys. Rev. B*, 59:6790–6794, Mar 1999.

[HU02] C.P. Heidbrink and G.S. Uhrig. Renormalization by continuous unitary transformations: one-dimensional spinless fermions. *The European Physical Journal B - Condensed Matter and Complex Systems*, 30(4):443–459, 2002.

[Hub63] J. Hubbard. Electron correlations in narrow energy bands. *Proceedings of the Royal Society of London. Series A. Mathematical and Physical Sciences*, 276(1365):238–257, 1963.

[Hub64] J. Hubbard. Electron correlations in narrow energy bands. ii. the degenerate band case. *Proceedings of the Royal Society of London. Series A. Mathematical and Physical Sciences*, 277(1369):237–259, 1964.

[IFT98] Masatoshi Imada, Atsushi Fujimori, and Yoshinori Tokura. Metal-insulator transitions. *Rev. Mod. Phys.*, 70:1039–1263, Oct 1998.

[Kan63] Junjiro Kanamori. Electron correlation and ferromagnetism of transition metals. *Progress of Theoretical Physics*, 30(3):275–289, 1963.

[KD07] S. S. Kancharla and E. Dagotto. Correlated insulated phase suggests bond order between band and mott insulators in two dimensions. *Phys. Rev. Lett.*, 98:016402, Jan 2007.

[KDU12] H. Krull, N. A. Drescher, and G. S. Uhrig. Enhanced perturbative continuous unitary transformations. *Phys. Rev. B*, 86:125113, Sep 2012.

[Keh06] S. Kehrein. *The Flow Equation Approach to Many-Particle Systems*. Springer Tracts in Modern Physics, Vol. 217. Berlin:Springer, 2006.

[KHK+12] Kensuke Kobayashi, Sachio Horiuchi, Reiji Kumai, Fumitaka Kagawa, Youichi Murakami, and Yoshinori Tokura. Electronic ferroelectricity in a molecular crystal with large polarization directing antiparallel to ionic displacement. *Phys. Rev. Lett.*, 108:237601, Jun 2012.

[KMB+97] Michael Karbach, Gerhard Müller, A. Hamid Bougourzi, Andreas Fledderjohann, and Karl-Heinz Mütter. Two-spinon dynamic structure factor of the one-dimensional $s = \frac{1}{2}$ heisenberg antiferromagnet. *Phys. Rev. B*, 55:12510–12517, May 1997.

[KSGU01] C. Knetter, K. P. Schmidt, M. Grüninger, and G. S. Uhrig. Fractional and integer excitations in quantum antiferromagnetic spin 1/2 ladders. *Phys. Rev. Lett.*, 87:167204, Oct 2001.

[KSJB03] A P Kampf, M Sekania, G I Japaridze, and Ph Brune. Nature of the insulating phases in the half-filled ionic hubbard model. *Journal of Physics: Condensed Matter*, 15(34):5895, 2003.

[KSU03a] C. Knetter, K.P. Schmidt, and G.S. Uhrig. High order perturbation theory for spectral densities of multi-particle excitations: $S = \frac{1}{2}$ two-leg heisenberg ladder. *The European Physical Journal B - Condensed Matter and Complex Systems*, 36(4):525–544, 2003.

[KSU03b] Christian Knetter, Kai P Schmidt, and Götz S. Uhrig. The structure of operators in effective particle-conserving models. *Journal of Physics A: Mathematical and General*, 36(29):7889, 2003.

[KSWO98] V. N. Kotov, O. Sushkov, Zheng Weihong, and J. Oitmaa. Novel approach to description of spin-liquid phases in low-dimensional quantum antiferromagnets. *Phys. Rev. Lett.*, 80:5790–5793, Jun 1998.

[KU00] C. Knetter and G.S. Uhrig. Perturbation theory by flow equations: dimerized and frustrated s = 1/2 chain. *The European Physical Journal B - Condensed Matter and Complex Systems*, 13(2):209–225, 2000.

[LBS06] Ö. Legeza, K. Buchta, and J. Sólyom. Unified phase diagram of models exhibiting a neutral-ionic transition. *Phys. Rev. B*, 73:165124, Apr 2006.

[LNW06] Patrick A. Lee, Naoto Nagaosa, and Xiao-Gang Wen. Doping a mott insulator: Physics of high-temperature superconductivity. *Rev. Mod. Phys.*, 78:17–85, Jan 2006.

[LQX+03] Jizhong Lou, Shaojin Qin, Tao Xiang, Changfeng Chen, Guang-Shan Tian, and Zhaobin Su. Transition from band insulator to mott insulator in one dimension: critical behavior and phase diagram. *Phys. Rev. B*, 68:045110, Jul 2003.

[LW68] Elliott H. Lieb and F. Y. Wu. Absence of mott transition in an exact solution of the short-range, one-band model in one dimension. *Phys. Rev. Lett.*, 20:1445–1448, Jun 1968.

[LW96] Peter Lenz and Franz Wegner. Flow equations for electron-phonon interactions. *Nuclear Physics B*, 482(3):693 – 712, 1996.

[MG69] Chanchal K. Majumdar and Dipan K. Ghosh. On next-nearest-neighbor interaction in linear chain. i. *Journal of Mathematical Physics*, 10(8):1388–1398, 1969.

[Mie98] A. Mielke. Flow equations for band-matrices. *The European Physical Journal B - Condensed Matter and Complex Systems*, 5(3):605–611, 1998.

[MMNS04] S. R. Manmana, V. Meden, R. M. Noack, and K. Schönhammer. Quantum critical behavior of the one-dimensional ionic hubbard model. *Phys. Rev. B*, 70:155115, Oct 2004.

[Mot90] N.F. Mott. *Metal-Insulator Transitions*. Taylor & Francis Group, 1990.

[Nak00] Masaaki Nakamura. Tricritical behavior in the extended hubbard chains. *Phys. Rev. B*, 61:16377–16392, Jun 2000.

[NT86] Naoto Nagaosa and J. Takimoto. Theory of neutral-ionic transition in organic crystals. i. monte carlo simulation of modified hubbard model. *Journal of the Physical Society of Japan*, 55(8):2735–2744, 1986.

[OAAY01] K. Okunishi, Y. Akutsu, N. Akutsu, and T. Yamamoto. Universal relation between the dispersion curve and the ground-state correlation length in one-dimensional antiferromagnetic quantum spin systems. *Phys. Rev. B*, 64:104432, Aug 2001.

[OHZ06] Jaan. Oitmaa, Chris. Hamer, and Weihong. Zheng. *Series Expansion Methods for Strongly Interacting Lattice Models*. Cambridge University Press, 2006.

[ON92] Kiyomi Okamoto and Kiyohide Nomura. Fluid-dimer critical point in $s = \frac{1}{2}$ antiferromagnetic heisenberg chain with next nearest neighbor interactions. *Physics Letters A*, 169(6):433 – 437, 1992.

[ON05] Hiromi Otsuka and Masaaki Nakamura. Ground-state phase diagram of the one-dimensional hubbard model with an alternating chemical potential. *Phys. Rev. B*, 71:155105, Apr 2005.

[OOMC96] Gerardo Ortiz, Pablo Ordejón, Richard M. Martin, and Guillermo Chiappe. Quantum phase transitions involving a change in polarization. *Phys. Rev. B*, 54:13515–13528, Nov 1996.

[PBH+07] N. Paris, K. Bouadim, F. Hébert, G. G. Batrouni, and R. T. Scalettar. Quantum monte carlo study of an interaction-driven band-insulator–to–metal transition. *Phys. Rev. Lett.*, 98:046403, Jan 2007.

[Rei06] Alexander A. Reischl. *Derivation of Effective Models using Self-Similar Continuous Unitary Transformations in Real Space*. PhD thesis, Universität zu Köln, 2006.

[RMHU04] Alexander Reischl, Erwin Müller-Hartmann, and Götz S. Uhrig. Systematic mapping of the hubbard model to the generalized t-j model. *Phys. Rev. B*, 70:245124, Dec 2004.

[RS95] R. Resta and S. Sorella. Many-body effects on polarization and dynamical charges in a partly covalent polar insulator. *Phys. Rev. Lett.*, 74:4738–4741, Jun 1995.

[SA93] Erik S. Sørensen and Ian Affleck. Large-scale numerical evidence for bose condensation in the S =1 antiferromagnetic chain in a strong field. *Phys. Rev. Lett.*, 71:1633–1636, Sep 1993.

[SB90] Subir Sachdev and R. N. Bhatt. Bond-operator representation of quantum spins: Mean-field theory of frustrated quantum heisenberg antiferromagnets. *Phys. Rev. B*, 41:9323–9329, May 1990.

[Sch86] H. J. Schulz. Phase diagrams and correlation exponents for quantum spin chains of arbitrary spin quantum number. *Phys. Rev. B*, 34:6372–6385, Nov 1986.

[SKU04] Kai P. Schmidt, Christian Knetter, and Götz S. Uhrig. Spectral properties of the dimerized and frustrated $s = 1/2$ chain. *Phys. Rev. B*, 69:104417, Mar 2004.

[SM78] Z. G. Soos and S. Mazumdar. Neutral-ionic interface in organic charge-transfer salts. *Phys. Rev. B*, 18:1991–2003, Aug 1978.

[SS70] Paul J. Strebel and Zoltán G. Soos. Theory of charge transfer in aromatic donor-acceptor crystals. *The Journal of Chemical Physics*, 53(10):4077–4090, 1970.

[Ste97] Jürgen Stein. Flow equations and the strong-coupling expansion for the hubbard model. *Journal of Statistical Physics*, 88(1-2):487–511, 1997.

[SU03] Kai P. Schmidt and Götz S. Uhrig. Excitations in one-dimensional $s = \frac{1}{2}$ quantum antiferromagnets. *Phys. Rev. Lett.*, 90:227204, Jun 2003.

[SU05] Kai P. Schmidt and Götz S. Uhrig. Spectral properties of magnetic excitations in cuprate two-leg ladder systems. *Modern Physics Letters B*, 19(24):1179–1205, 2005.

[SW99] Rajiv R. P. Singh and Zheng Weihong. Dynamical transition from triplets to spinon excitations: A series expansion study of the $j_1 - j_2 - \delta$ spin-$\frac{1}{2}$ chain. *Phys. Rev. B*, 59:9911–9915, Apr 1999.

[TAC01] M. E. Torio, A. A. Aligia, and H. A. Ceccatto. Phase diagram of the hubbard chain with two atoms per cell. *Phys. Rev. B*, 64:121105, Sep 2001.

[TGM$^+$81] J. B. Torrance, A. Girlando, J. J. Mayerle, J. I. Crowley, V. Y. Lee, P. Batail, and S. J. LaPlaca. Anomalous nature of neutral-to-ionic phase transition in tetrathiafulvalene-chloranil. *Phys. Rev. Lett.*, 47:1747–1750, Dec 1981.

[TH87] Takashi Tonegawa and Isao Harada. Ground-state properties of the one-dimensional isotropic spin-1/2 heisenberg antiferromagnet with competing interactions. *Journal of the Physical Society of Japan*, 56(6):2153–2167, 1987.

[TK01] Yasutami Takada and Manabu Kido. Effect of electron correlation on the bragg reflection. *Journal of the Physical Society of Japan*, 70(1):21–24, 2001.

[TK11] C. Tomaras and S. Kehrein. Scaling approach for the time-dependent kondo model. *EPL (Europhysics Letters)*, 93(4):47011, 2011.

[TNB09] L. Tincani, R. M. Noack, and D. Baeriswyl. Critical properties of the band-insulator-to-mott-insulator transition in the strong-coupling limit of the ionic hubbard model. *Phys. Rev. B*, 79:165109, Apr 2009.

[TVML81] J. B. Torrance, J. E. Vazquez, J. J. Mayerle, and V. Y. Lee. Discovery of a neutral-to-ionic phase transition in organic materials. *Phys. Rev. Lett.*, 46:253–257, Jan 1981.

[UN98] G. S. Uhrig and B. Normand. Magnetic properties of $vo_2p_2o_7$ from frustrated interchain coupling. *Phys. Rev. B*, 58:R14705–R14708, Dec 1998.

[USG04] G. S. Uhrig, K. P. Schmidt, and M. Grüninger. Unifying magnons and triplons in stripe-ordered cuprate superconductors. *Phys. Rev. Lett.*, 93:267003, Dec 2004.

[Vae11] A. Vaezi. *Slave particle study of the strongly correlated electrons*. PhD thesis, Massachusetts Institute of Technology, 2011.

[WA96] Steven R. White and Ian Affleck. Dimerization and incommensurate spiral spin correlations in the zigzag spin chain: Analogies to the kondo lattice. *Phys. Rev. B*, 54:9862–9869, Oct 1996.

[Weg94] Franz Wegner. Flow-equations for hamiltonians. *Annalen der Physik*, 506(2):77–91, 1994.

[WGN+01] M. Windt, M. Grüninger, T. Nunner, C. Knetter, K. P. Schmidt, G. S. Uhrig, T. Kopp, A. Freimuth, U. Ammerahl, B. Büchner, and A. Revcolevschi. Observation of two-magnon bound states in the two-leg ladders of $(ca,la)_{14}cu_{24}o_{41}$. *Phys. Rev. Lett.*, 87:127002, Aug 2001.

[WI13] Tsutomu Watanabe and Sumio Ishihara. Band and mott insulators and superconductivity in honeycomb-lattice ionic-hubbard model. *Journal of the Physical Society of Japan*, 82(3):034704, 2013.

[WM01] Tim Wilkens and Richard M. Martin. Quantum monte carlo study of the one-dimensional ionic hubbard model. *Phys. Rev. B*, 63:235108, May 2001.

[YLMS10] Hong-Yu Yang, Andreas M. Läuchli, Frédéric Mila, and Kai Phillip Schmidt. Effective spin model for the spin-liquid phase of the hubbard model on the triangular lattice. *Phys. Rev. Lett.*, 105:267204, Dec 2010.

[YS11] H. Y. Yang and K. P. Schmidt. Effective models for gapped phases of strongly correlated quantum lattice models. *EPL (Europhysics Letters)*, 94(1):17004, 2011.

[ZWL03] Y. Z. Zhang, C. Q. Wu, and H. Q. Lin. Inducement of bond-order wave due to electron correlation in one dimension. *Phys. Rev. B*, 67:205109, May 2003.